

San Antonio Field Study Analysis

Final Report

Grant Number: 582-18-81339

Grant Activities Description No.: 582-22-33351-024

Tracking No. 2022-15

Prepared for the Texas Commission on Environmental Quality (TCEQ)

Principal Investigators:

Shan Zhou, University of Houston

James Flynn, University of Houston

Yuxuan Wang, University of Houston

Rob Griffin, Roger Williams University

Rebecca Sheesley, Baylor University

Sascha Usenko, Baylor University

May 31, 2023

Table of Content

1	INTRODUCTION	6
2	METHODS	7
2.1	Sampling Site and Instrumentation	7
2.2	Air Mass Back Trajectories	8
2.3	WRF-GC Model	8
2.4	NASA Langley Research Center (LaRC) Zero-dimensional Model	9
3	TASK RESULTS	11
3.1	Task 1: GAD	11
3.2	Task 2: Progress Reports	11
3.3	Task 3: Cybersecurity Training	11
3.4	Task 4: Ozone Chemistry and Dynamics	11
3.4.1	Summary and Key Findings	11
3.4.2	Methodology	12
3.4.2.1	Observational data	12
3.4.2.2	LaRC results analysis	12
3.4.3	Results	13
3.5	Task 5: Characterization of Volatile Organic Compounds (VOC) from 2021 Field Study Observations	17
3.5.1	Summary and Key Findings	17
3.5.2	Methodology	18
3.5.3	Results	18
3.6	Task 6: Analyze Aerosol Composition and Optical Properties from 2021 Field Study Observations	18
3.6.1	Summary and Key Findings	18
3.6.2	Methodology	19
3.6.2.1	HR-ToF-AMS data processing	19
3.6.2.2	Positive Matrix Factorization of Organic Aerosol Matrix and Combined Organic and Inorganic Aerosol Matrices	20
3.6.2.3	Aerosol optical parameters	21
3.6.3	Results	22
3.6.3.1	Overview of aerosol characteristics	22
3.6.3.2	Size-resolved aerosol composition	25
3.6.3.3	Organic Aerosol Sources and Processes	27
3.6.3.3.1	Primary Organic Aerosols (POA)	28
3.6.3.3.2	Secondary Organic Aerosols (SOA)	30
3.6.3.4	Comparisons of aerosol composition and diurnal profiles at two locations in San Antonio	33
3.6.3.5	Aerosol optical properties	36
3.7	Task 7: Compare and Contrast 2021 Measurements to 2017 datasets at Traveler’s World Site	37
3.7.1	Summary and Key Findings	37
3.7.2	Methodology	38
3.7.3	Results	40
3.7.3.1	Meteorological conditions and inorganic trace gases	40
3.7.3.2	Volatile organic compounds	43
3.7.3.2.1	VOC categories and diurnal profiles	43
3.7.3.2.2	Wind rose and polar plots of VOCS at TW during 2017 and 2021	46
3.7.3.2.3	Climatological differences between 2017 and 2021	47
3.7.3.3	Chemistry and dynamics of ozone	48
3.7.3.4	Aerosol composition and chemistry	53
3.8	Task 8: Spatial Distribution and Characterization of Air Pollutants (Ozone, Trace Gas, VOC, and Aerosols) from 2021 Field Study Observations	54
3.8.1	Summary and Key Findings	54
3.8.2	Methodology	55
3.8.2.1	Emission inventory	55
3.8.2.2	State-Informed Background Removal (SIBaR) analysis	55

3.8.3	Results	55
3.8.3.1	Inorganic trace gases	55
3.8.3.2	VOCs	63
3.8.3.3	Aerosol composition and chemistry	81
3.8.3.4	Aerosol optical properties	92
3.9	Task 9: Modeling Analysis to Aid the Observational Analysis	99
3.9.1	Summary and Key Findings	99
3.9.2	Methodology	99
3.9.2.1	Observations data	99
3.9.2.2	Model experiments	100
3.9.3	Results	101
3.9.3.1	Observed ozone interannual variability in San Antonio	101
3.9.3.2	Model evaluation	103
3.9.3.2.1	<i>Simulation of ozone</i>	103
3.9.3.2.2	<i>Simulation of trace gases</i>	106
3.9.3.2.3	<i>Simulation of VOCs</i>	109
3.9.3.2.4	<i>Simulation of meteorological variable</i>	113
3.9.3.3	Modeled ozone changes between 2017 and 2021	115
3.9.3.3.1	<i>Impact of anthropogenic emission changes on ozone</i>	116
3.9.3.3.2	<i>Impact of meteorological changes on ozone</i>	120
4	RECOMMENDATIONS FOR FUTURE WORK	122
5	REFERENCES	123

Executive Summary

To better understand air quality drivers in emerging Texas cities, the San Antonio Field Study (SAFS) 2017 investigated ambient concentration and sources of VOCs and trace gases, and physical and chemical processes that control O₃ (Anderson et al., 2019; Guo et al., 2021; Shrestha et al., 2022). Results from the SAFS 2017 study highlighted the need to characterize the influence of upwind sources and long-range transport on air quality in San Antonio. To address these outstanding questions from SAFS 2017, the Corpus Christi and San Antonio (CCSA) Field Study was conducted in Spring 2021. Key findings from this study include:

- SAFS 2021 was slightly cooler compared to 2017, but solar UV was comparable in both years. During this study, ambient O₃ was lower in 2021 compared to 2017 although NO_x and NO_y were higher. Biogenic VOCs contributed a larger fraction of the total in 2021 compared to 2017. Average isoprene concentration was enhanced by ~1.8 times and average monoterpene concentration enhanced by ~8 times. As a result, the total OH reactivity of VOCs increased by ~80% (3.7.1).
- Using the WRF-GC air quality models, we found that the regional mean ozone in May 2021 is 2.39 ± 0.99 ppbv lower than in May 2017. Anthropogenic emission-induced ozone changes account for an upward change of 1.13 ± 0.28 ppbv, while meteorology-induced changes account for a downward change of -0.64 ± 0.83 ppbv over 2017-2021. (3.9.1).
- Modeling results indicate that highways and urban centers (VOC-sensitive regions) are the major reasons for a positive ozone response to reduced anthropogenic NO_x emissions in 2021 compared to 2017. Lower temperature, higher humidity, stronger Bermuda High, etc., are the meteorological reasons for lower ozone in 2021 than in 2017 (3.9.1).
- The total OH reactivity of VOCs was dominated by alkenes (~ 43%) and isoprene (~ 32%) while the fractional contributions of all the rest of the VOC reactivities were below 10% (3.4.1).
- During the period at San Antonio Traveler's World (TW) Site, 66% of the ozone formation was in the NO_x-sensitive regime while 28% of the period was in the VOC-sensitive regime. The remaining 6% fell in the transitional regime. The transition between NO_x-sensitive and VOC-sensitive tended to occur between 1-2 ppbv of NO (3.4.1).
- The mass concentration of non-refractory submicron aerosols (NR-PM₁) was on average $15.7 (\pm 9.0)$ $\mu\text{g m}^{-3}$ during the entire study period, reaching up to $300 \mu\text{g m}^{-3}$ when sampling relatively fresh vehicular emissions (3.6.1).

- Aerosol composition on study average was dominated by organics followed by sulfate. Aerosol composition varied as a function of size. Larger particles were more enriched in sulfate than smaller particles (3.6.1).
- Organic aerosols were overall oxidized, suggestive of aged and processed aerosols. Primary organic factors together contributed 22% of the total organic aerosol mass, whereas the secondary factors accounted for 78% of organic aerosol mass (3.6.1).

1 Introduction

Although Texas is the second-most populous state in the US, with multiple industrial and economic urban centers, previous air quality studies have focused primarily on the Houston-Galveston-Brazoria and Dallas-Fort Worth areas. To better understand air quality drivers in emerging Texas cities, the San Antonio Field Study (SAFS) 2017 investigated ambient concentration and sources of VOCs and trace gases, and physical and chemical processes that control O₃ (Anderson et al., 2019; Guo et al., 2021; Shrestha et al., 2022). Results from the SAFS 2017 study highlighted the need to characterize the influence of upwind sources and long-range transport on air quality in San Antonio. To address these outstanding questions from SAFS 2017, the Corpus Christi and San Antonio (CCSA) Field Study was conducted in spring 2021 and collected a rich air quality dataset using the Mobile Air Quality Laboratory 2 (MAQL2). The MAQL2 was deployed successfully during the 2021 SAFS in the stationary mode at Traveler's World, as well as in the mobile mode sampling across the areas upwind and downwind of San Antonio. Measurements were performed for meteorological parameters, inorganic trace gases relevant to both particulate matter and ozone formation (including carbon monoxide, carbon dioxide, nitrogen oxides, total reactive nitrogen, sulfur dioxide, and ozone itself), VOC, and particulate matter composition, concentration, and optical properties.

The main objective of this project is to understand air quality in San Antonio area by analyzing the air quality data collected during 2021 SAFS and comparing air quality data collected from field studies in 2017 and 2021. The analyses will contribute to the understanding of ozone formation and any changes in air quality in San Antonio metropolitan area from 2017 to 2021. This project will also provide comprehensive descriptions of air quality and meteorological events in San Antonio. Analysis of the data in this project will support air quality modeling for the State Implementation Plan (SIP) and will also provide information regarding ozone formation over San Antonio.

2 Methods

2.1 Sampling Site and Instrumentation

We performed a field campaign using a combination of stationary and mobile measurements in the San Antonio area from April 23 to May 19, 2021:

- April 23 – 29: mobile measurements upwind (to the southeast) of San Antonio.
- April 29 – May 12: stationary measurements at the Traveler’s World RV Park (urban core)
- May 13 – 19, 2021: mobile measurements downwind (to the northwest) of San Antonio.

The sampling location of the Traveler’s World site and the routes of mobile measurements in the San Antonio area during this field study is shown in **Figure 2.1**. From April 23 through April 29, The Traveler’s World RV Park was used as the overnight location for sampling, but during the day, mobile sampling upwind of San Antonio was performed. This location was also used as the location for stationary sampling from April 29 until May 12. For the final week, Traveler’s World was used as the home base at night while sampling occurred downwind of San Antonio in mobile mode during the day, including stationary measurements at the campus of the University of Texas at San Antonio (UTSA), for comparison to 2017 SAFS data.

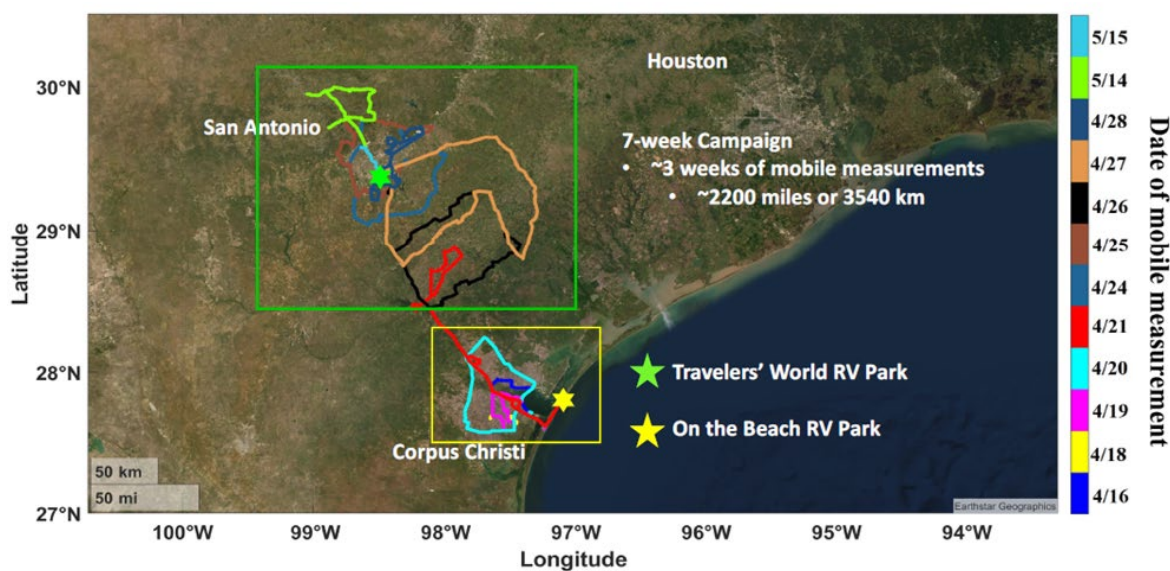


Figure 2.1: Sampling location (green star) and mobile sampling trajectories (in the green box) during the 2021 San Antonio Field Study among the greater 7-week 2021 San Antonio-Corpus Christi Field Campaign that included both the Corpus Christi and San Antonio area.

We took measurements using the Baylor University /Rice University/ University of Houston Mobile Air Quality Laboratory 2 (MAQL2). MAQL2 is comprised of a trailer and a truck to tow the equipment trailer. The trailer is air-conditioned and insulated with $\sim 22 \text{ m}^3$ of interior volume. Operating in stationary mode, aerosol and gas sample inlets are attached to a 10-m telescoping tower that is fully extended. The ambient trace gas sample air was drawn through an inlet box that houses valves, converters, and power supplies for sampler configuration and calibration. The

aerosol inlet has a 2.5 μm cyclone and uses 3/8-in. copper tubing to connect to aerosol instrumentation. The MAQL2 was equipped with wired and wireless network, dual 4G cellular internet connections to enable remote monitoring of instrumentation. The truck that towed this trailer is a 2015 Ford F250. The truck and trailer were wired to distribute power from either a generator while in motion or from a 50-A recreational vehicle (RV) power outlet for stationary measurements.

The generator was carried in the bed of the truck. The inlet associated with the instrumentation was forward of the generator and truck exhaust to avoid self-sampling when in motion. When operating in stationary mode, the truck was placed facing into the wind (if it was strong enough), and an exhaust hose was used to increase the distance between the truck and generator exhaust and the sampling inlets. When wind was not strong enough, for extended periods of stationary measurements, the MAQL2 was transferred to utility power and the truck/generator was detached. A telescoping tower was attached to the trailer to allow sampling from a greater height (10 m) when in stationary mode.

We deployed a suite of aerosol and gas instruments on the MAQL2, including an HR-ToF-AMS (referred to as HR-AMS) (Aerodyne) for size-resolved chemical characterization of non-refractory submicron aerosols (NR-PM₁), i.e., organics (Org), sulfate (SO₄), nitrate (NO₃), ammonium (NH₄), and chloride (Chl); a Tricolor Absorption Photometer (TAP; Brechtel model 2091) and a nephelometer (TSI model 3563) for measuring fine aerosol (PM_{2.5}) light absorption and scattering coefficients, respectively, a proton-transfer-reaction mass spectrometer (PTR-MS) for measuring volatile organic compounds (VOCs); and a suite of instruments for measuring inorganic trace gases including carbon monoxide (CO), carbon dioxide (CO₂), nitrogen oxides (NO_x), total reactive nitrogen (NO_y; the sum of NO_x and other nitrogen oxides referred to as NO_z), ozone (O₃), and sulfur dioxide (SO₂). We also measured meteorological parameters (temperature, relative humidity, wind speed and direction), boundary layer height, and the photolysis rate constants of NO₂ (j_{NO_2}).

2.2 Air Mass Back Trajectories

Developed by NOAA's Air Resources Laboratory, the Hybrid Single-Particle Lagrangian Integrated Trajectory model (HYSPLIT) was utilized to determine the origin of the air masses influencing the sampling sites. 72-hour backward trajectories were run at 500 meters above ground level, and new trajectories were started every 6 hours. The trajectories were downloaded and imported to MathWorks MATLAB (version R2021b 9.11.0.1769968 (64-bit)) for evaluation with the HMS fire and smoke output to determine possible biomass burning influences. Back trajectories can be computed at https://ready.arl.noaa.gov/HYSPLIT_traj.php.

2.3 WRF-GC Model

WRF-GC v2.0 is a regional air quality model (Feng et al., 2021; Lin et al., 2020) that couples the Weather Research and Forecasting (WRF) meteorological model (v3.9.1.1) with the GEOS-Chem atmospheric chemistry model (v12.7.2). The WRF and GEOS-Chem versions are benchmarks of

WRF-GC v2.0 with the proven performance of meteorology and chemistry in Feng et al. (2021) and Lin et al. (2020). We set up three domains with different horizontal resolutions of 25 km (d01), 5 km (d02), and 1 km (d03), respectively (**Figure 2.2**). All domains have identical vertical resolutions with 50 hybrid sigma-eta vertical levels spanning from the surface to 10 hPa.

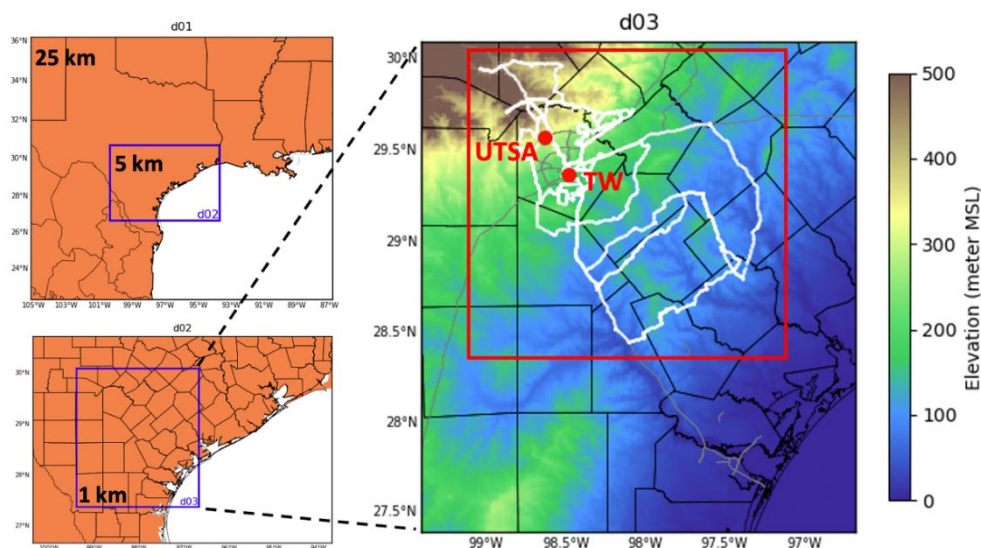


Figure 2.2: WRF-GC nested domains and their horizontal resolutions. Two stationary stations including the urban Travelers' World Recreational Vehicle Park (TW) and the suburban University of Texas at San Antonio (UTSA) are labeled as red dots. Mobile measurements during the 2021 field campaign are shown in white. The red box represents the greater San Antonio region used in the analysis below.

WRF-GC used the most updated full O_x-NO_x-VOC-halogen-aerosol chemistry from GEOS-Chem. The anthropogenic emissions were the TCEQ emission inventory for southeastern Texas at 4 km horizontal resolution (1 km for on-road emissions) and the 2013 National Emission Inventory for the rest of the US at 0.1° horizontal resolution. The TCEQ emissions were originally in 2019 but scaled to 2017 and 2021 based on scaling factors derived from the TROPOMI-derived emissions (Liu et al., 2023) in San Antonio and Corpus Christi. Biomass burning emissions are from the 2019 Global Fire Emissions Database (GFED). Biogenic emissions are from the Model of Emissions of Gases and Aerosols from Nature (MEGAN) (Guenther et al., 2012). Soil NO_x (Hudman et al., 2012) and lightning NO_x (Murray et al., 2012) emissions are also included.

2.4 NASA Langley Research Center (LaRC) Zero-dimensional Model

Ozone (O₃) formation and destruction rates and OH reactivity of VOCs were calculated by the NASA LaRC zero-dimensional model (Crawford et al., 1999; Olson et al., 2006) for both SAFS 2017 and 2021 field campaigns. A comparison of several model mechanisms including LaRC based on the Texas-II Radical and Aerosol Measurement Project (TRAMP) campaign can be found in Chen et al. (2010). The model is run in a time-dependent mode assuming a diurnal steady state with standard constraints and formaldehyde as of its latest application in the San Antonio Field Studies in 2017 (SAFS 2017) (Guo et al., 2021). Among the model inputs, trace gases,

meteorological parameters, photolysis rate of NO₂, and designated VOCs are from real-time measurements, while a subset of VOCs required but unmeasured by the PTR-MS are ratioed based on correlations derived from SAFS 2017.

3 Task Results

3.1 Task 1: GAD

This task was completed on May 27, 2022.

3.2 Task 2: Progress Reports

This task was completed each month, a total of 10 submitted by May 15, 2023

3.3 Task 3: Cybersecurity Training

This task was completed.

3.4 Task 4: Ozone Chemistry and Dynamics

3.4.1 Summary and Key Findings

- This task was completed. We investigated the chemistry and dynamics of ozone formation during SAFS 2021 at the Traveler's World site. We calculated the ozone production rate using NASA LaRC time-dependent box model, noted major formation and destruction pathways. We analyzed concentrations and reactivities of VOC measured by the PTR-MS for relationships to low and high ozone concentrations, specifically, isoprene, benzene, toluene, xylene, styrene, methyl vinyl ketone + methacrolein, methyl ethyl ketone, monoterpenes, acetone, acetaldehyde, acetonitrile, hydroxyacetone, dimethyl sulfide and formaldehyde (HCHO). We investigated factors affecting or indicative of ozone formation. The final data set was submitted to the TCEQ on April 15, 2023.
- The median of the hourly-averaged ozone formation rate was 34.0 ± 32.0 ppbv h⁻¹ for 6:00 to 19:00 CST with a noon to early afternoon peak between 11:00 and 15:00 CST averaging about 63.0 ppbv h⁻¹. Ozone destruction rate averaged 1.4 ± 1.2 ppbv h⁻¹ and was smaller than ozone formation rate by an order of magnitude, leading to a potentially high rate of net ozone production.
- The total OH reactivity of VOCs (9.1 ± 2.8 s⁻¹) was dominated by alkenes (3.9 ± 1.3 s⁻¹, 43%) and isoprene (2.9 ± 1.2 s⁻¹, 32%) while the fractional contributions of all the rest of the VOC reactivities were below 10%. The large contribution of isoprene reactivity also underscores the importance of biogenic VOC. Common oil and gas extraction indicators, such as ethane (C₂H₆), and petrochemical industry emission indicators, such as aromatics and BTEX, made only limited contributions (about 7% for aromatics, 1% for ethane, 2% for propane, 5% for alkanes other than ethane, and less than 1% for benzene).
- During the LaRC modeled period at San Antonio Traveler's World (TW) Site, 66% of the ozone formation was in the NO_x-sensitive regime, with an average NO of 1.2 ppbv and P(O₃) of 34.1 ppbv hr⁻¹, while 28% of the period was in the VOC-sensitive regime, with an

average NO of 7.1 ppbv and lower average P(O₃) of 30.4 ppbv hr⁻¹. Approximately 6% of the period was in the transitional regime with an average NO of 1.6 ppbv, consistent with the qualitative evaluation of the NO turning over point between 1 and 2 ppbv. The net ozone production rate was 35.0 ± 25.9 ppbv hr⁻¹ throughout the daytime and was most active from 11:00 to 15:00 CST when the ozone formation regime was NO_X-sensitive.

3.4.2 Methodology

3.4.2.1 Observational data

A suite of inorganic gas analyzers was used to measure trace gases in real-time at a high resolution (30 s). In situ O₃ measurements were collected with a 2B Technologies (Boulder, CO) model 205 dual beam O₃ ultraviolet photometric gas analyzer and a model 42C from Thermo Environmental, Inc. Ambient levels of carbon monoxide (CO) were measured with a Los Gatos Research (San Jose, CA) CO Analyzer, model F-CO-23r using laser-based off-axis integrated cavity output spectroscopy. The nitric oxide (NO) was measured by an Air Quality Design (Golden, CO) custom chemiluminescent analyzer. The nitrogen dioxide (NO₂) was measured by an Air Quality Design custom chemiluminescent analyzer that utilizes a Blue Light Converter (BLC) from Air Quality Design (Golden, CO) for photolytic conversion of NO₂ to NO (Lefer et al., 2010). Total reactive nitrogen (NO_Y) measurements (including HNO₃) were conducted using a modified Thermo Scientific Model 42C chemiluminescence analyzer with a 300°C molybdenum converter at the sample inlet. The NO_X reaction products are collectively calculated as NO_Z (where NO_Z = NO_Y – NO_X). Sulfur dioxide (SO₂) was measured by a Thermo Scientific Model 43C-TLE with the pulsed ultraviolet fluorescence technique. A quadrupole PTR-MS (Q300; Ionicon Analytik, Austria) was used to measure a set of VOCs and OVOCs (detailed in Section 3.5). Meteorological parameters including temperature, relative humidity, and pressure were measured by an RM Young weather station. Wind speed and direction were measured by an RM Young 2-D sonic anemometer. A Vaisala CL-31 ceilometer was used to measure the planetary boundary layer (PBL) height. The photolysis rate of NO₂ (jNO₂) is measured by a MetCon GmbH filter radiometer.

3.4.2.2 LaRC results analysis

Based on the observational data described above, daytime (6:00–19:00 CST) O₃ formation and destruction rates and OH reactivity of VOCs were calculated by the LaRC zero-dimensional model (detailed in Section 2.4). O₃ formation rate (F(O₃)) is calculated from three main NO₂ generating pathways in the LaRC model output: HO₂+NO, RO₂+NO, and CH₃O₂+NO (where CH₃O₂ is specifically the methyl peroxy radical, which is not included in the RO₂ parameter), as subsequent NO₂ photolysis and the association of O(³P) with O₂ are sufficiently fast and non-rate-limiting. O₃ destruction rate (D(O₃)) is calculated from a combination of five main OH production reactions (O(¹D)+H₂O), HO_X-driven O₃-depleting chain reactions (HO₂+O₃, OH+O₃) under lower-NO_X conditions, the termination of both NO_X and HO_X in forming HNO₃ (NO₂+OH) under higher-NO_X

conditions, and the reactions of O_3 with specific VOCs (O_3 +NMHC), particularly those with carbon-carbon double bonds. Net $P(O_3)$ is calculated as the difference between $F(O_3)$ and $D(O_3)$.

The relative importance of a specific VOC (or lumped VOC) with respect to the formation of secondary O_3 is determined by its atmospheric abundance and how quickly it reacts with OH. The reactivity of a VOC species (VOCR) is defined as the product of its concentration and reaction rate constant (k) with OH and is also calculated from the LaRC model output.

The quantification of O_3 - NO_x -VOC sensitivity and O_3 formation regimes (e.g., Kleinman, 1994; Sillman et al., 1995; Kleinman, 2005) was performed (Guo et al., 2021) based on the “ LRO_x/LNO_x ” metric recommended by Schroeder et al. (2017), in which O_3 formation is thought to be NO_x -sensitive when HO_x radical loss via $OH + NO_2$ accounts for less than half of total HO_x radical loss. In specific, the radical termination reaction of OH with NO_x to form HNO_3 is referred to as LNO_x , and radical-radical reactions (including RO_2 and RO_2 self-reactions, RO_2 and HO_2 reactions, and RO_2 reactions with a different RO_2) resulting in stable peroxide formation are referred to as LRO_x ($RO_x = RO_2 + HO_2$). The ratio of radical termination rate from LRO_x to LNO_x will provide a good indicator of NO_x -sensitive ($LRO_x/LNO_x > \sim 0.5$, which corresponds to $Ln/Q < 2/3$, where $Ln = LNO_x$ and $Q = LNO_x + LRO_x$), VOC-sensitive ($LRO_x/LNO_x < \sim 0.3$), and transitional ($0.3 < LRO_x/LNO_x < 0.5$) O_3 formation regimes (Kleinman et al., 2005; Mazzuca et al., 2016; Schroeder et al., 2017).

3.4.3 Results

The temporal patterns of meteorological conditions, jNO_2 , inorganics trace gases, and VOCs are presented in Section 3.5 (Task 5) and 3.7 (Task 7). At San Antonio Traveler’s World Site (TW) during SAFS 2021, the hourly-averaged median $F(O_3)$ was 34.0 ± 32.0 ppbv h^{-1} for 6:00 to 19:00 CST with a noon to early afternoon peak between 11:00 and 15:00 CST averaged about 63.0 ppbv h^{-1} (**Figure 3.1**, left). $RO_2 + NO$ (14.7 ± 13.8 ppbv h^{-1}) was the largest contributor (43%) to $F(O_3)$ followed by $HO_2 + NO$ (14.0 ± 13.2 ppbv h^{-1} , 41%) and $CH_3O_2 + NO$ (5.3 ± 5.0 ppbv h^{-1} , 16%). For components of $D(O_3)$ (**Figure 3.1**, right), $NO_2 + OH$ and was the dominant pathway, followed by $O(^1D) + H_2O$, $O_3 + NMHC$ and $HO_2 + O_3$. Specifically, $NO_2 + OH$ (1.0 ± 1.0 ppbv h^{-1} , 67%) was significant throughout the early morning to late afternoon, while $O(^1D) + H_2O$ (0.3 ± 0.5 ppbv h^{-1} , 22%), $O_3 + NMHC$ (0.3 ± 0.2 ppbv h^{-1} , 19%) and $HO_2 + O_3$ (0.1 ± 0.2 ppbv h^{-1} , 9%) became noticeable in early afternoon. In general, $D(O_3)$ averaged 1.4 ± 1.2 ppbv h^{-1} and was smaller than $F(O_3)$ by an order of magnitude, leading to a potential high rate of net ozone production $P(O_3)$.

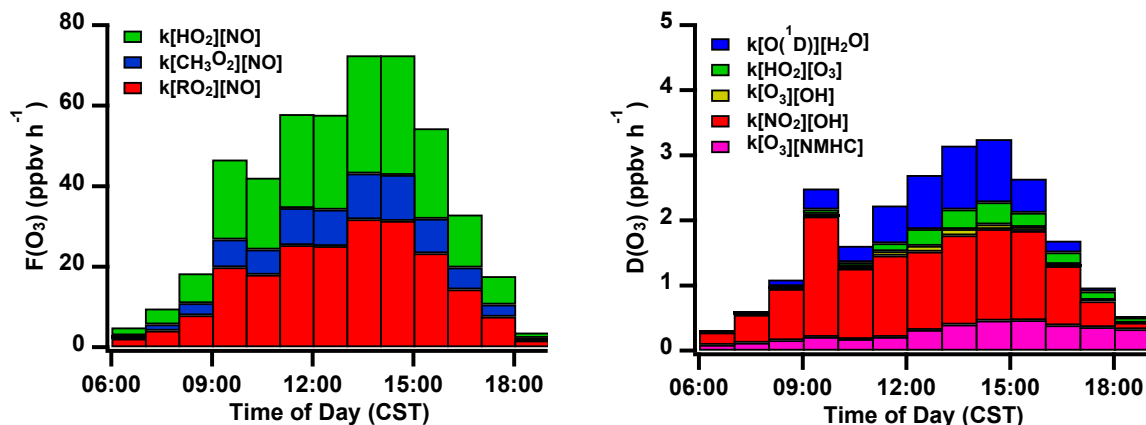


Figure 3.1: Median daytime profiles of ozone formation rate ($F(O_3)$; left) and ozone destruction rate ($D(O_3)$; right) estimated at the San Antonio Traveler's World Site during SAFS 2021 using the LaRC model.

The total OH reactivity of VOCs ($9.1 \pm 2.8 \text{ s}^{-1}$) was dominated by alkenes ($3.9 \pm 1.3 \text{ s}^{-1}$, 43%) and isoprene ($2.9 \pm 1.2 \text{ s}^{-1}$, 32%) during SAFS 2021, while the fractional contributions of all the rest of the VOC reactivities were below 10% (Figure 3.2). Formaldehyde only took account of approximately 6% ($0.5 \pm 0.2 \text{ s}^{-1}$) of total OH reactivity, which is consistent with the increased role of isoprene and alkenes, which indicates local emission sources and limited secondary processing. The large contribution of isoprene reactivity also underscores the importance of biogenic VOC. Common oil and gas extraction indicators, such as ethane (C_2H_6), and petrochemical industry emission indicators, such as aromatics and BTEX, made only limited contributions (about 7% for aromatics, 1% for ethane, 2% for propane, 5% for alkanes other than ethane, and less than 1% for benzene).

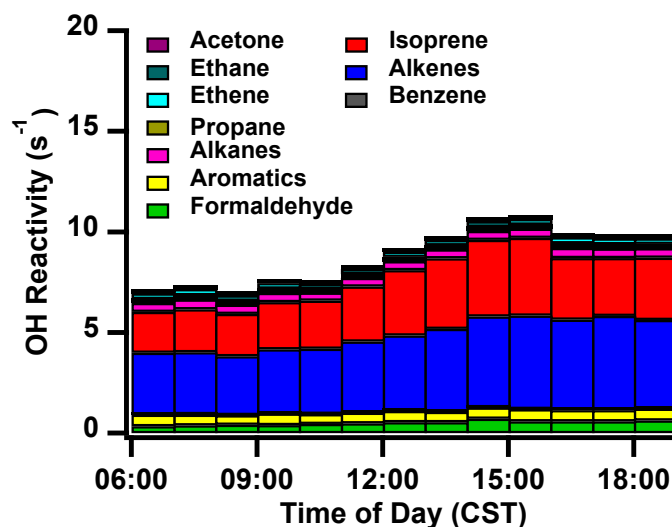


Figure 3.2 The OH reactivity of VOCs estimated at SA TW site using the LaRC model in SAFS 2021.

The NO_x or VOC-sensitive ozone formation regimes were estimated from the LaRC model qualitatively by the relationship between the net ozone production rate ($P(\text{O}_3)$) and NO (**Figure 3.3**) and quantitatively by the $\text{LRO}_x/\text{LNO}_x$ metric (**Figure 3.5**). In **Figure 3.3**, a turning-over point of net ozone production rate ($P(\text{O}_3)$) was observed at an NO concentration of approximately 1~2 ppbv, indicating a transition from the NO_x -sensitive regime (in which the increase of NO leads to an increased O_3 production rate) to the VOC-sensitive regime (in which the further increase of NO results in limited O_3 production rate).

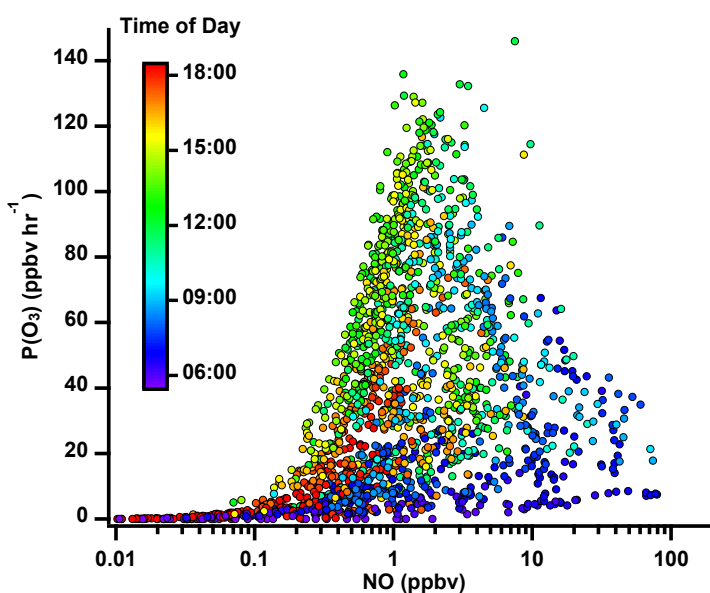


Figure 3.3: Modeled net ozone production rate ($P(\text{O}_3)$) versus NO concentration colored by time of day (CST) at SA TW in SAFS 2021.

Compared to **Figure 3.4**, in which $P(\text{O}_3)$ generally increased with the total OH reactivity of VOCs and photolytic activity, the highest $P(\text{O}_3)$ occurrence did not coincide with the highest total OH reactivity of VOCs. Instead, $P(\text{O}_3)$ peaked at a moderately high total OH reactivity of VOCs ($\sim 10 \text{ s}^{-1}$) where an intense photolytic activity existed ($j\text{NO}_2 > 0.015 \text{ s}^{-1}$).

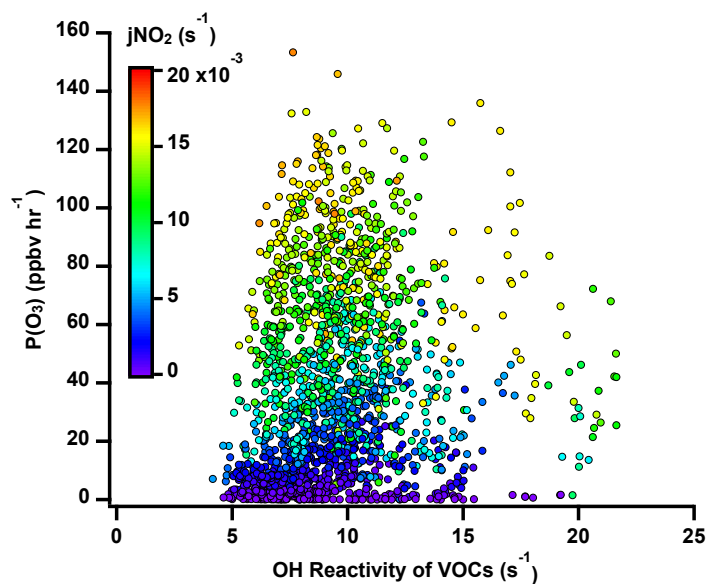


Figure 3.4: Modeled net ozone production rate ($P(O_3)$) versus the total OH reactivity of VOCs colored by the total photolysis rate of NO_2 at SA TW in SAFS 2021.

Based on the LRO_X/LNO_X ratio (**Figure 3.5**), 28% of the LaRC modeled period was in VOC-sensitive regime, with an average NO of 7.1 ppbv and $P(O_3)$ of 30.4 ppbv hr⁻¹, while 66% of the period was in a NO_X -sensitive regime, with an average NO of 1.2 ppbv and a higher average $P(O_3)$ of 34.1 ppbv hr⁻¹ at TW during the modeling period in SAFS 2021. Approximately 6% of the period was in the transitional regime with an average NO of 1.6 ppbv and $P(O_3)$ of 32.4 ppbv hr⁻¹. The average of 1.6 ppbv NO of the transitional regime was consistent with the NO turning-over point indicated in **Figure 3.3**. The diurnal variation of LRO_X/LNO_X indicated that $P(O_3)$ initiated in NO_X -sensitive regime between 6:00 and 7:00 CST in the early morning, but quickly shifted to VOC-sensitive regime between 7:00 and 9:00 CST, likely due to the addition of NO_X from morning traffic. Then the ozone formation lingered around the transitional regime between 9:00 and 11:00 CST, until it stabilized and stayed in NO_X -sensitive from 11:00 CST throughout the afternoon. Notice that a shift from NO_X - to VOC-sensitive regime during the afternoon traffic hour was not observed, likely due to the accumulation of VOCs throughout the day. The peak $P(O_3)$ was observed around early noon- 70.0 ppbv hr⁻¹ during 13:00–15:00 CST. On average, the net ozone production rate was 35.0 ± 25.9 ppbv hr⁻¹ throughout the daytime and was most active from 11:00 to 15:00 CST. During the elevated $P(O_3)$ period, the ozone formation regime stayed NO_X -sensitive, with an average $P(O_3)$ at 63.0 ± 8.7 ppbv hr⁻¹.

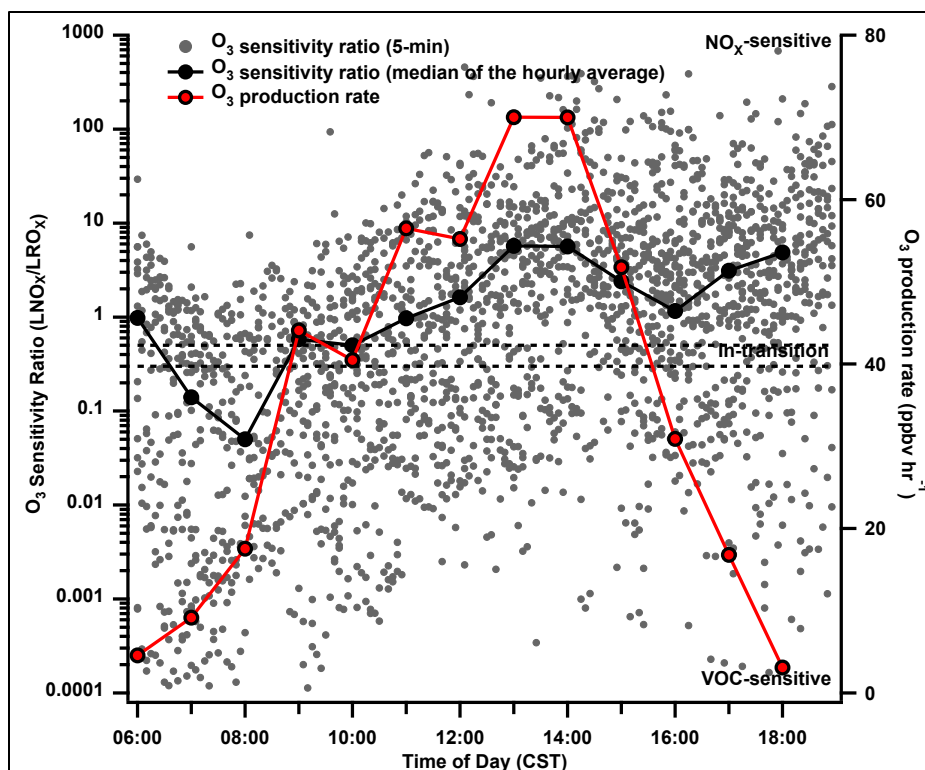


Figure 3.5: The 5-min (grey points) and median of the hourly average (black line with markers) daytime profiles of O₃ sensitivity ratio (LRO_x/LNO_x) on the left axis, and the modeled net ozone production rate ($P(O_3)$, red line with markers) on the right axis. The two horizontal dash lines on the left axis at values of 0.3 and 0.5 indicate the transition regime between NO_x- and VOC-sensitive regimes for SAFS 2021.

3.5 Task 5: Characterization of Volatile Organic Compounds (VOC) from 2021 Field Study Observations

3.5.1 Summary and Key Findings

- This task was completed. We characterized VOC data, including formaldehyde, from SAFS 2021 for its importance to ozone formation and biomass burning impacts. We analyzed VOC data to determine the influence of anthropogenic (AVOC), biogenic (BVOC), or biomass burning (BBVOC) sources from tracers such as toluene and benzene, isoprene and monoterpene, and acetaldehyde and acetonitrile, respectively. We estimated regional background concentrations of VOC, analyzed temporal trends, and identified possible sources of VOC emissions that play an important role in ozone formation. The final data set was submitted to the TCEQ on April 15, 2023.

3.5.2 Methodology

A quadrupole PTR-MS (Q300; Ionicon Analytik, Austria) was used to measure select VOCs and OVOCs. Details of the PTR-MS and its operation are discussed elsewhere (de Gouw and Warneke, 2007; Lindinger et al., 1998). Briefly, target gas molecules are ionized by proton transfer from protonated water (H_3O^+), and the ionized material is then detected and quantified using a quadrupole mass spectrometer. The ambient air is continuously drawn through a PFA Teflon-lined manifold at the flow rate of 8 lpm from which a subsample of 100 sccm is drawn by the PTR-MS. A sample drying system similar to that used by Jobson and McCoskey (2010) was implemented to reduce any effects of water vapor that can occur with operating the drift tube of the PTR-MS at a lower E/N (i.e., 100 Td).

The PTR-MS was operated in select ion mode. Operation in this manner allowed for detection during hydronium reagent ion of formaldehyde (HCHO, m/z 31) (which requires the cold trap sample conditioner developed in previous work), acetonitrile (m/z 42), acetaldehyde (m/z 45), acetone (m/z 59), dimethyl sulfide (DMS, m/z 63), isoprene (m/z 69), methyl vinyl ketone plus methacrolein (MVK+MACR, m/z 71), hydroxyacetone (m/z 75), benzene (m/z 79), toluene (m/z 93), styrene (m/z 105), C2-alkylbenzenes (m/z 107), C3-alkylbenzenes (m/z 121), C4-alkylbenzenes (m/z 135), and monoterpenes (m/z 137). A cold trap sample conditioner was built to reduce water content in the sample to a -30°C dew point, allowing for better sensitivity and quantification of HCHO i.e., lighter and water-soluble VOCs.

3.5.3 Results

The fractional contribution of VOC groups including anthropogenic, biogenic, oxidized, biomass burning, acetone, and HCHO for stationary periods at TW and UTSA are presented in Section 3.7 (Task 7). The diurnal variability, wind rose, and polar plots are also present under Task 7. The mobile observations of VOCs are presented in Section 3.8 (under Task 8).

3.6 Task 6: Analyze Aerosol Composition and Optical Properties from 2021 Field Study Observations

3.6.1 Summary and Key Findings

- This task was completed. We analyzed and evaluated the temporal profiles of the size-resolved mass concentrations of speciated submicron aerosols (e.g., organics, sulfate, nitrate, ammonium, and chloride), bulk submicron aerosol composition, elemental ratios of organic aerosols, and scattering and absorption coefficients. We used these analyses and others, as appropriate, to determine sources and processes of high aerosol pollution episodes using aerosol data from the high-resolution time-of-flight aerosol mass

spectrometer (HR-ToF-AMS). We integrated the aerosol and VOC data to improve source identification (e.g., biomass burning using aerosol optical properties, aerosol composition and VOC tracers). The final data set was submitted to the TCEQ on April 15, 2023.

- The mass concentration of non-refractory submicron aerosols (NR-PM₁) was on average 15.7 (± 9.0) µg m⁻³ during the entire study period, reaching up to 300 µg m⁻³ due to fresh vehicular emissions (primary aerosols directly emitted from the tailpipe or newly formed particles in the exhaust gas upon mixing with the ambient air).
- Aerosol composition on study average was dominated by organics followed by sulfate. Aerosol composition varied as a function of size. Larger particles were more enriched in sulfate than smaller particles. We saw bi-model size distributions with an additional prominent Aiken mode at the smaller particle sizes for organics and key organic mass fragments, which suggest a substantial potential contribution from fresh vehicular emissions and biomass burning emissions on aerosol concentration and composition.
- Organic aerosols were overall oxidized, suggestive of aged and processed aerosols. Source apportionment analysis based on Positive Matrix Factorization (PMF) identified 7 organic aerosol types associated with different sources and processes. Primary organic factors together contributed 22% of the total OA mass, whereas the secondary factors accounted for the majority (78%) of OA mass.
- The successful deployment of a tricolor absorption photometer (TAP) and nephelometer during the 2021 field campaign allowed for the improved assessment of aerosols across the SAFS domain, specifically their aerosol optical properties.

3.6.2 Methodology

3.6.2.1 HR-ToF-AMS data processing

We analyzed the size-resolved mass concentration and chemical composition of non-refractory submicron aerosols (NR-PM₁) using the standard high-resolution time-of-flight aerosol mass spectrometer (HR-ToF-AMS) data analysis toolkit (SQUIRREL v1.64 and PIKA v1.24). We used default relative ionization efficiency (RIE) values for organics (1.4), nitrate (1.1), and chloride (1.3), while an RIE value of 4.06 was determined for ammonium and 0.8 for sulfate following the analysis of pure NH₄NO₃ and (NH₄)₂SO₄, respectively. A Nafion dryer was placed upstream of the AMS to eliminate potential RH effect on particle collection efficiency (CE) at the vaporizer (Middlebrook et al., 2012). We applied a time- and composition-dependent collection efficiency (CDCE) and performed time-dependent gas-phase CO₂⁺ subtraction (Collier and Zhang, 2013; Middlebrook et al., 2012). Determination of atomic oxygen-to-carbon (O/C) and hydrogen-to-carbon (H/C) ratios of organic aerosols used the Aiken-ambient (AA) method (Aiken et al., 2008).

3.6.2.2 Positive Matrix Factorization of Organic Aerosol Matrix and Combined Organic and Inorganic Aerosol Matrices

To investigate the sources and processes of organic aerosols (OA), we performed positive matrix factorization (PMF) analysis on the high-resolution mass spectra (HRMS) of 1) organics only and 2) the combined spectral matrices of organic and inorganic species, respectively using the PMF2 algorithm in robust mode (Paatero and Tapper, 1994). We first generated the ion-speciated HRMS matrix and the corresponding error matrix from PIKA, and then analyzed using the PMF Evaluation Tool v3.06B (Ulbrich et al., 2009). We did PMF analysis on the entire sampling period from April 2 to May 19 covering both the stationary measurements and the mobile measurements.

For the organic PMF analysis, the OA data and error matrices were refined prior to PMF analysis according to the protocol summarized previously (Ulbrich et al., 2009; Zhang et al., 2011). Ions with m/z up to 190 were included in the PMF analysis. Isotopes were removed to avoid giving excess weight to their parent ions. Noisy ions were removed from the data matrix. These treatments largely improved the OA factorization, but had negligible impact on the mass concentrations. A minimum error was introduced for each ion. The “bad” ions with S/N ratio < 0.2 were downweighted by increasing their error values by a factor of 10, while the “weak” ions with S/N between 0.2 and 2 were downweighted a factor of 2 as described by [Ulbrich et al., 2009]. O^+ , OH^+ , H_2O^+ , and CO^+ ions were also downweighted to avoid additional weight to CO_2^+ , as their signals were all scaled to that of CO_2^+ . PMF solutions were tested from 2 to 7 factors, and the rotational forcing parameter, f_{Peak} , was varied between -1 and 1 (step = 0.2).

We also performed PMF analysis on the combined spectral matrices of organic and inorganic species of the HR-AMS (Paatero and Tapper, 1994; Zhang et al., 2011; Zhou et al., 2017). PMF is commonly applied to the organic mass spectral matrix to determine distinct OA factors (Zhang et al., 2011). However, conducting PMF analysis on the combined spectra of organic and inorganic aerosols allows for the derivation of additional information. In this study, we performed PMF analysis on the combined HR spectral matrices of organic and inorganic species. Organic ions at m/z 12 – 180 and major inorganic ions, i.e., SO^+ , SO_2^+ , HSO_2^+ , SO_3^+ , HSO_3^+ , and $H_2SO_4^+$ for sulfate; NO^+ and NO_2^+ for nitrate; NH^+ , NH_2^+ , and NH_3^+ for ammonium; and Cl^+ and HCl^+ for chloride were included, and the ion signals were expressed in nitrate-equivalent concentrations. The error matrix was pretreated the same as the PMF analysis of organic matrix only. After PMF analysis, the mass concentration of each OA factor was derived from the sum of organic signals in the corresponding mass spectrum after applying the default RIE for organics (1.4) and the time-dependent CDCE. The solutions for two to nine factors were explored at a fixed rotational parameter ($F_{PEAK} = 0$). We performed similar evaluation procedures as to the organic PMF analysis and chose the seven-factor solution as the optimum solution for the combined PMF analysis.

Following the procedures listed in Table 1 of Zhang et al. (2011), all PMF solutions have been evaluated by investigating the key diagnostic plots, mass spectra, correlations with external tracers and diurnal profiles. We selected the seven-factor solution with $f_{Peak} = 0$ from the PMF analysis

of the combined matrices as the optimum solution. The solution is presented and discussed in detail in Section 3.6.3.

3.6.2.3 Aerosol optical parameters

The aerosol light absorption coefficients (σ_{abs}) were measured using a 3 λ tricolor absorption photometer (TAP, Brechtel Inc., Hayward, CA) at wavelengths 365, 520, and 640 nm. The TAP is the commercially available version of NOAA's continuous light absorption photometer (CLAP) (Ogren et al., 2017). The TAP consecutively samples through eight sample filter spots and two reference filter spots. During the field campaign, the TAP was set to rotate to the next filter spot when a filter spot's transmission reached 50 %.

The light scattering coefficients (σ_{scat}) was measured using an integrating nephelometer (model 3563, TSI Inc., Shoreview, MN) at wavelengths 450, 550, and 700 nm. The measured values were corrected for angular scattering and truncation error (Anderson and Ogren, 1998; Bond et al., 2009) using the relationship: $\sigma_{\text{corrected}} = \text{correction factor (C)} \times \sigma_{\text{neph}}$ where C is the correction factor, σ_{neph} is the scattering coefficient reported by the instrument, and $\sigma_{\text{corrected}}$ is the corrected scattering coefficient (Shrestha et al., 2018). During the campaign the TSI nephelometer was calibrated against the filtered air and CO₂ (Anderson and Ogren, 1998).

Using 5-min averages, AAE and SAE were calculated as the negative slope of the linear fit of the optical parameter versus the wavelengths on a log-log plot (Bergstrom et al., 2007; Bond and Bergstrom, 2006; Kirchstetter et al., 2004). AAE and SAE provide information about the wavelength dependence of absorption and scattering, respectively (Schmeisser et al., 2017). For example, AAE values around 1 characterize BC, whereas BrC and mineral oxides show strong preferential light absorption in the UV range resulting in an enhancement in AAE values with respect to BC. SAE values are inversely related to the particle size, generally, $\text{SAE} < 1$ indicates larger particles and $\text{SAE} > 2$ indicates finer particles dominated the scattering aerosol. In this study, AAE above 1.2 (i.e. average non-BB influenced AAE + 2 times standard deviation) is used to indicate the periods of biomass burning influence (discussed in Section 3.3.1). This threshold is used to identify events that lie above the baseline AAE for a given site.

Single Scattering Albedo (SSA) is the ratio of σ_{scat} to extinction coefficient ($\sigma_{\text{scat}} + \sigma_{\text{abs}}$), which provides information about the absorbing or scattering nature of the sampled aerosol. The SSA value greater than 0.95 represents aerosol with a net effect of cooling whereas less than 0.85 will have a warming effect. The SSA values in between 0.85 and 0.95 may represent a warming or cooling effect depending upon surface albedo and cloud cover (Ramanathan et al., 2001). The wavelengths for σ_{scat} and σ_{abs} were not the same, so to calculate SSA at 550 nm, the σ_{abs} measured at 540 nm was converted to 550 nm using the equation below:

$$\sigma_{\text{abs}}^{550} = \sigma_{\text{abs}}^{540} \times \left(\frac{\lambda_{540}}{\lambda_{550}} \right)^{\text{AAE}_{365-640}}$$

3.6.3 Results

3.6.3.1 Overview of aerosol characteristics

Figure 3.6 presents an overview of the meteorological conditions and concentrations of gas-phase species and non-refractory PM_{10} (NR- PM_{10}) species during the sampling period from April 22 to May 19 2021. The weather during this campaign was relatively hot (average temperature = $23.0 \pm 4.5^{\circ}C$) and humid (average RH = $68.3 \pm 7.8\%$). NR- PM_{10} varied dynamically with the 2.5 min average concentration ranging from 0.5 to $307.3 \mu g m^{-3}$. The SA campaign averaged NR- PM_{10} was $15.7 (\pm 9.0) \mu g m^{-3}$. Large spikes and concentrations that approached above $100 \mu g m^{-3}$ were observed, which were associated with primary PM emissions from combustion sources, although more typical concentrations are below $40 \mu g m^{-3}$.

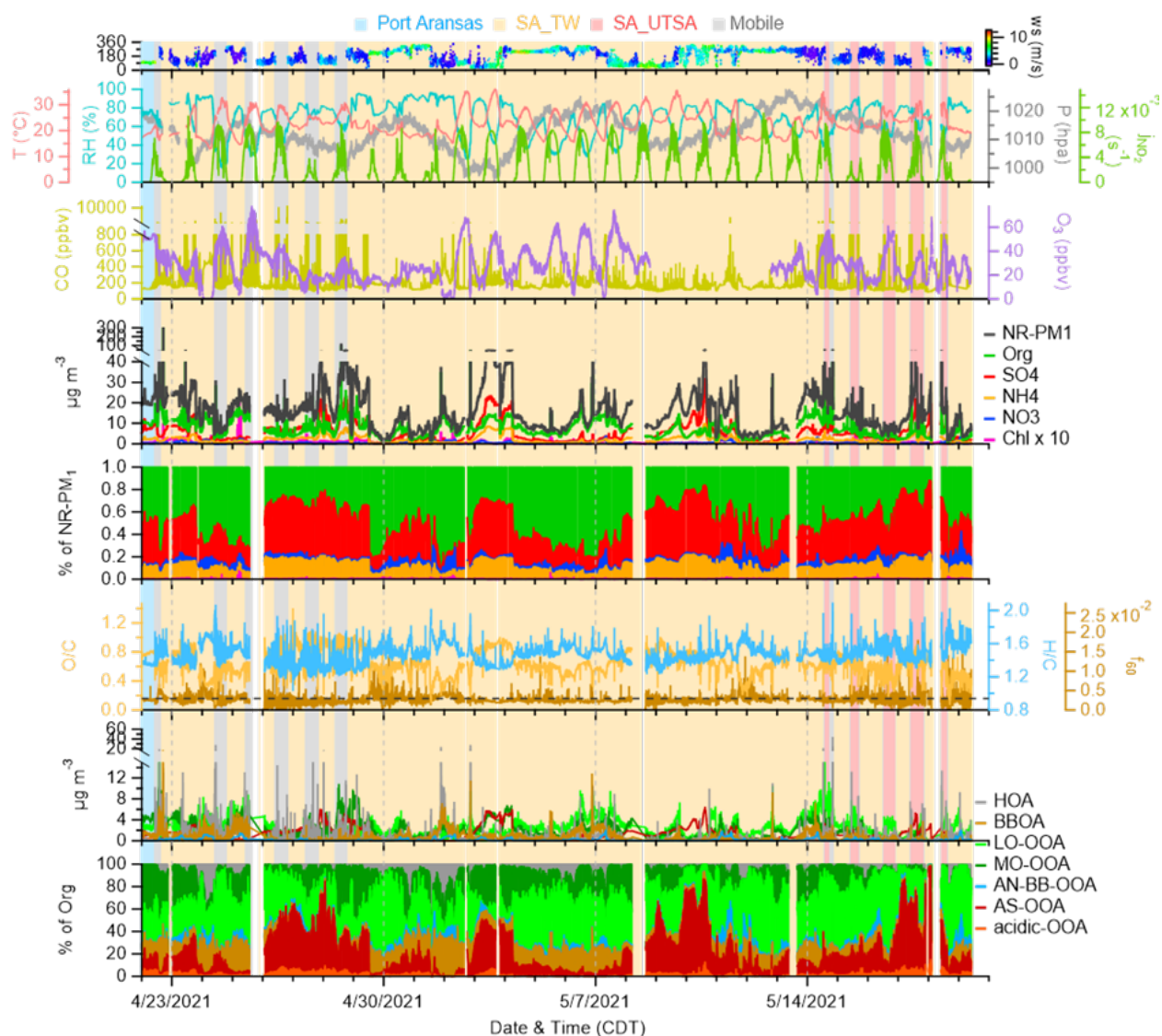


Figure 3.6: Time series of meteorological variables including 15-min wind direction (wd) colored by wind speed (ws), temperature (T), relative humidity (RH), pressure (P), NO_2 photolysis rate (j_{NO_2}), mixing ratios of select trace gases including CO and O_3 , mass concentrations of submicron aerosols species and

OA factors derived from the combined PMF analysis, elemental ratios of OA and the AMS biomass burning tracer - f_{60} (i.e., signals at m/z 60 to total OA), as well as the percentage contribution of the submicron aerosols species to the total NR-PM₁ mass and the percentage contribution of OA factors to total OA mass. The shaded regions indicate mode of sampling, either stationary at the Corpus Christi beachfront site (Port Aransas), the Traveler's World RV site in San Antonio (SA_TW), and University of Texas San Antonio (UTSA), or mobile measurements in the greater San Antonio region (mobile).

We also saw time dependent aerosol composition, where NR-PM₁ was dominated by organics or sulfate depending on time. On campaign average, organics dominated the composition, making up 45% of the total mass, followed by sulfate (38%), ammonium (13%), nitrate (3%), and chloride (1%). We saw a few high sulfate periods (e.g., April 26–29, May 3–4, and May 9–11) where sulfate was the predominant component. We plan to look into the source origin of air masses of these high sulfate events. The biomass burning tracer, AMS f_{60} ($= C_2H_4O_2^+ (m/z\ 60)/OA$) was generally at the threshold of 0.3%, suggesting the potential ubiquitous presence of biomass burning influences on aerosol composition during the entire sampling period.

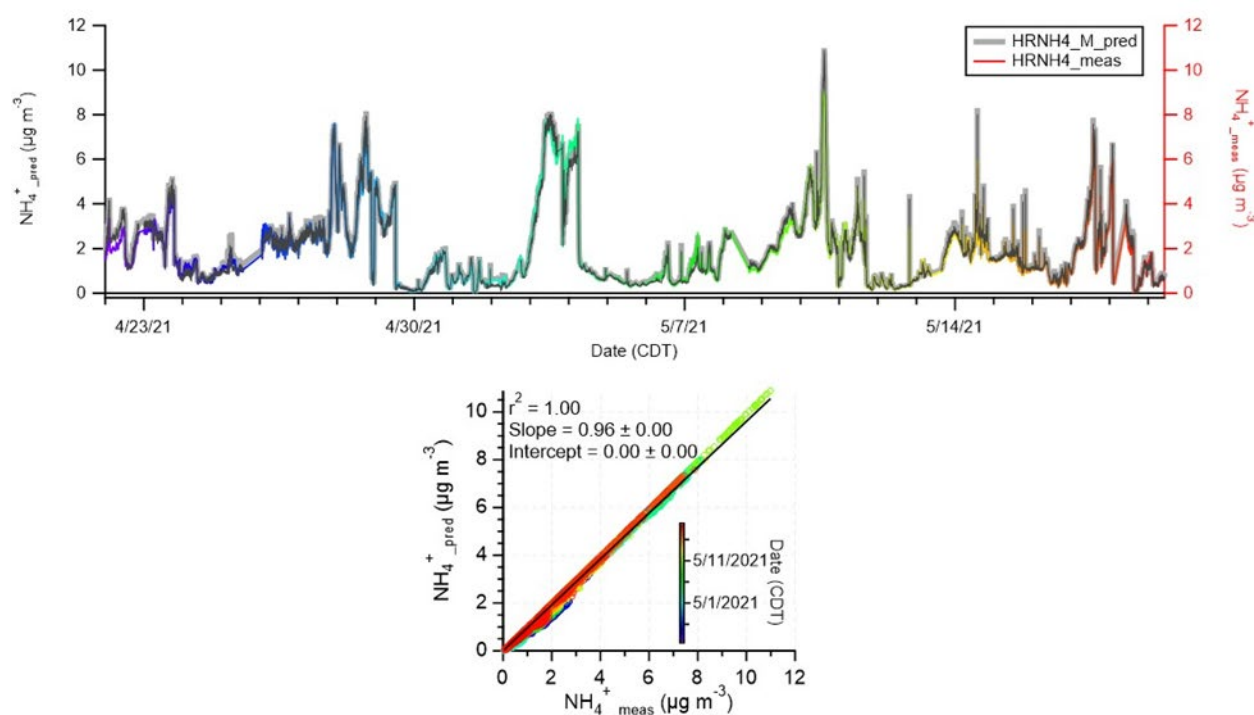


Figure 3.7: Time series of predicted NH_4^+ ($= 2 \times 18/96 \times [SO_4^{2-}] + (18/62 \times [NO_3^-]) + [18/35.5 \times [Cl^-]]$) and the measured NH_4^+ (upper panel) and the scatter plot between them colored by time. Data fitting was performed using the orthogonal distance regression (ODR).

The stoichiometric neutralization for NR-PM₁ was examined by comparing the ammonium concentrations needed to fully neutralize the AMS-measured concentrations of anionic species, i.e., sulfate, nitrate, and chloride measured by the AMS ($NH_4^+_{pred}$) to those measured ($NH_4^+_{meas}$). Aerosols with a ratio of 1 represents fully neutralized particles, whereas a ratio of 2 reflects the formation of ammonium bisulfate (NH_4HSO_4), and a ratio of >2 indicates presence of sulfuric acid. **Figure 3.7** shows that the predicted ammonium concentration followed the trend of the measured

nically. We observed a tight correlation between the two ($r^2 = 1$) and yielded a slope of 0.96, very close to 1. This observation suggests that the particles we measured in the San Antonio area during this field study were generally neutralized.

There are indications that a significant fraction of the nitrate measured by the AMS during this study was attributed to organonitrate. The average ratio of the signals for the two largest nitrate fragments, NO^+ ($m/z = 30$) and NO_2^+ ($m/z = 46$), was 4.19 during the campaign (**Figure 3.8**), substantially higher than the $\text{NO}^+/\text{NO}_2^+$ ratio measured for pure ammonium nitrate particles (R_{AN}) during this study (2.38). Previous studies reported that the ratio for organonitrates (R_{ON}) can be 2–4 times higher than for NH_4NO_3 (Fry et al., 2013; Fry et al., 2009). In addition, we observed significant amounts of ion fragments from the $\text{C}_x\text{H}_y\text{O}_z\text{N}_p^+$ family in the HRMS, providing further evidence for the presence of organonitrates.

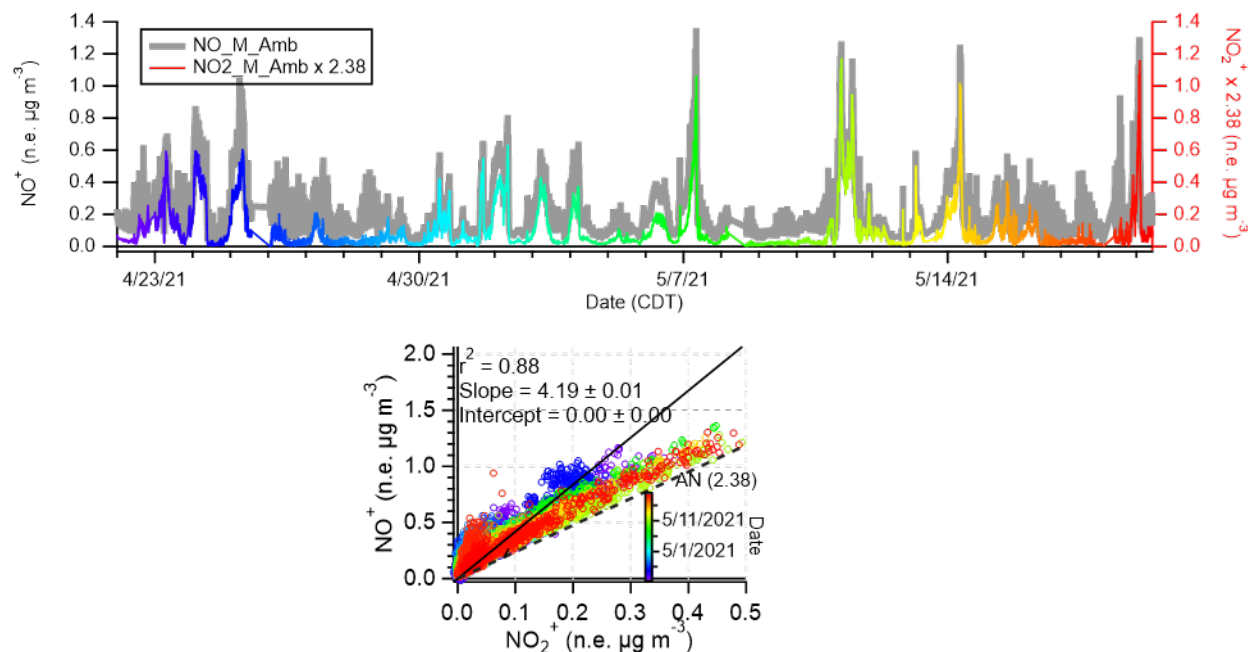


Figure 3.8: Time series of measured NO^+ and NO_2^+ ions and the scatter plot between them colored by time. Data fitting was performed using the orthogonal distance regression (ODR).

Assuming that the ratio of the ratios ($R_{\text{ON}}/R_{\text{AN}}$) is stable, based on equation (1) in Farmer et al. [2010], we calculated the nitrate concentration attributable to organonitrates and thus the nitrate signal from ammonium nitrate. **Figure 3.9** shows the time series of the $\text{NO}^+/\text{NO}_2^+$ ratio we observed (R_{obs}) during the sampling period. R_{obs} varied greatly. This suggests that nitrate composition varied greatly two; several episodes had R_{obs} values greater than 20, suggestive of significant contribution of organonitrates. **Figure 3.9** shows that organonitrates were observed throughout the campaign. During periods with lower concentrations of total nitrate were predominantly organonitrate while ammonium nitrate had an increasing contribution to the total nitrate mass concentration during periods with high total nitrate concentration. On study average,

89% of observed nitrate concentration can be attributable to organonitrates. Assuming that organonitrate molecules on average contain one $-\text{ONO}_2$ functional group per molecule and have an average molecular weight of 230 g mol^{-1} (Fry et al., 2009), we estimated that the average concentration of organonitrates was $1.24 (\pm 1.08) \mu\text{g m}^{-3}$ and accounted for 19% of the total OA mass during this study.

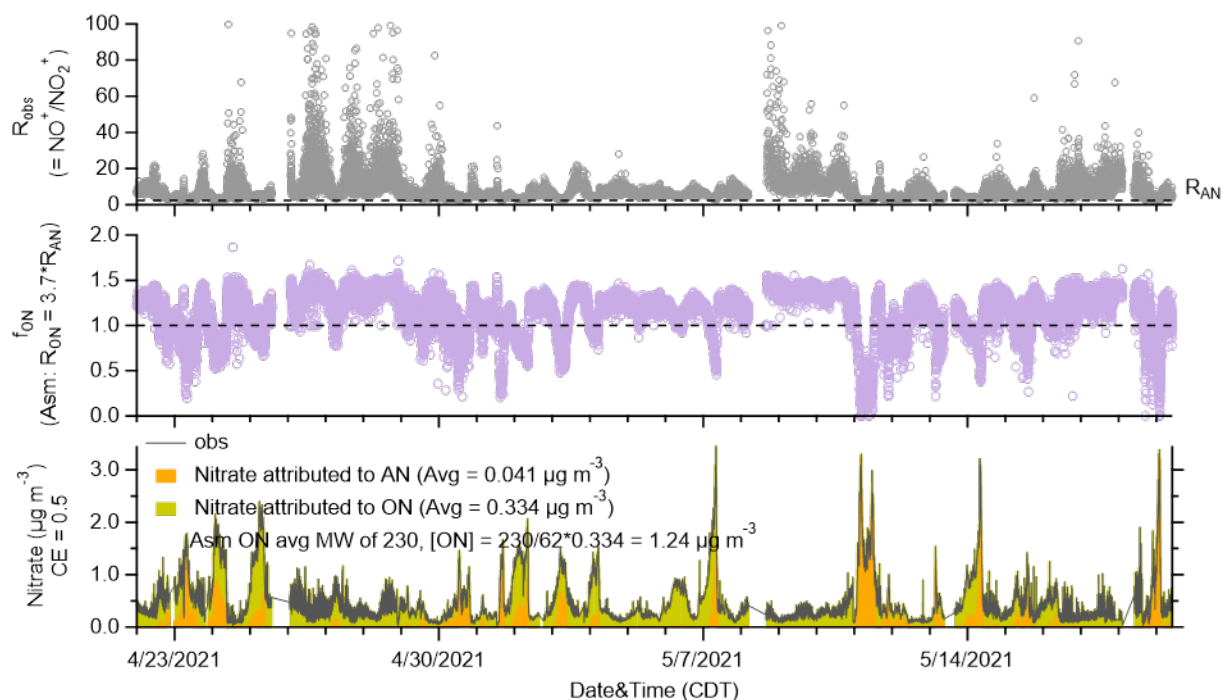


Figure 3.9: Time series of observed NO^+ -to- NO_2^+ ratio (R_{obs}), the fractional contribution of nitrate signal from organonitrate to total measured nitrate (f_{ON}) assuming the NO^+ -to- NO_2^+ ratio for organonitrates (R_{ON}) is 3.7 times that for ammonium nitrate (R_{AN}), and the stacked concentration of nitrate signals contributable to ammonium nitrate (AN) and organonitrate (ON), as well as the observed total nitrate signal (obs).

3.6.3.2 Size-resolved aerosol composition

The campaign-averaged size distributions of NR- PM_{10} species and size-resolved aerosol composition are shown in **Figure 3.10**. The average mass-based size distribution of NR- PM_{10} displayed a broad feature extending from 100 to 1000 nm in vacuum aerodynamic diameter (Dva). All species showed an overlapping accumulation mode peaking at $\sim 400 \text{ nm}$ (Dva), which was indicative of internally mixed regional particles. Aerosol composition varied as a function of size with larger particles more enriched in sulfate than smaller particles. Nitrate exhibited a second condensational mode extending to smaller sizes below 250 nm, suggestive of formation and growth of nitrate by gas-to-particle partitioning. In contrast, aged aerosol species, including sulfate and Org44 (organic mass at m/z 44; **Figure 3.11**), showed the narrowest size distribution with the prevalence of a droplet accumulation mode peaking at $\sim 500 \text{ nm}$. Particles with mass median

aerodynamic diameters of $\sim 0.4\text{--}1\ \mu\text{m}$ have been formed primarily via aqueous-phase reactions in clouds and wet aerosols, whereas gas-to-particle partitioning of secondary species formed from gas-phase reactions mostly modifies the condensation mode particles ($<0.2\ \mu\text{m}$) (Ervens et al., 2011). Given the humid weather during the campaign, where RH was frequently above 80% at night (**Figure 3.6**), this observation indicates that the formation and aging of sulfate and SOA likely was influenced by aqueous-phase reactions.

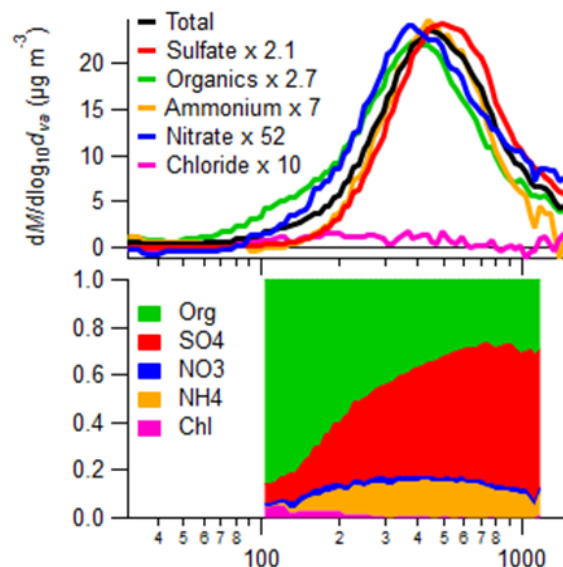


Figure 3.10: Average size distributions of (top) NR-PM1 (total) and individual species and (bottom) size-resolved mass fractional composition of NR-PM1.

The mass-based size distributions of total organics showed a prominent Aitken mode peaking at $\sim 120\text{--}200\ \text{nm}$. This indicates that primary emission sources made a non-negligible contribution to the observed aerosol concentration and composition, which is consistent with the urban nature of San Antonio. **Figure 3.11** shows the average size distributions of select key organic fragments. Organic signal at $m/z\ 57$ (Org57) is a prominent peak composed nearly completely of C_4H_9^+ in the mass spectra of primary organic aerosols from vehicle emissions [Collier et al., 2015] and has been used as an AMS spectral tracer for hydrocarbon-like OA (HOA) in urban environments. Org57 showed a clear bimodal distribution with greater contribution from the smaller Aitken mode ($< 200\ \text{nm}$) than the accumulation mode ($> 300\ \text{nm}$). This suggests significant contribution of primary vehicular emissions. Similar bi-modal distributions were observed in Org55 and Org71, where fragments of saturated hydrocarbon compounds were also the dominant signals at these m/z s. In addition, organic signal at $m/z\ 60$, where the levoglucosan fragment of $\text{C}_2\text{H}_4\text{O}_2^+$ dominated, also showed a broadened size distribution extending into the smaller size range. These features in the size distributions suggest that primary aerosol emissions from local combustion sources, including local vehicular exhaust and biomass burning contributed to the aerosol concentration and composition in San Antonio.

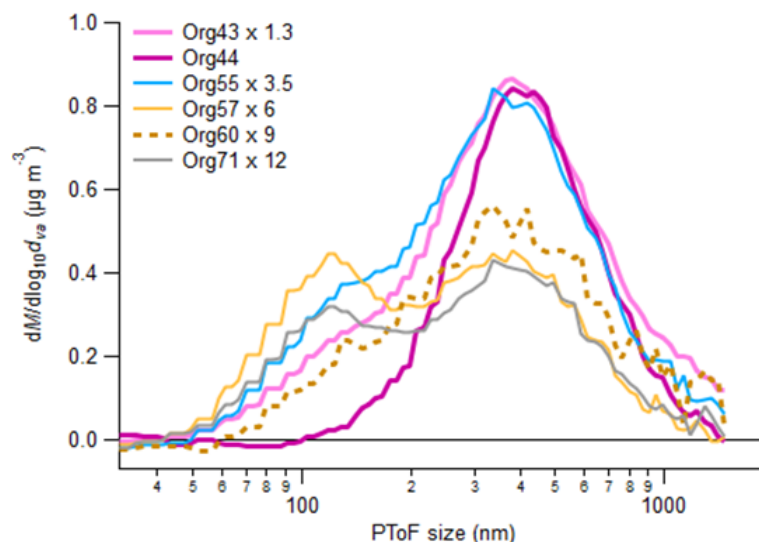


Figure 3.11: Average size distributions of key organic m/z s.

3.6.3.3 Organic Aerosol Sources and Processes

Figure 3.12 shows the average mass spectrum of bulk OA during the entire campaign period in the San Antonio area. Organics were overall oxidized with an average $O/C = 0.55$ and $OM/OC = 1.87$. In order to further elucidate the sources and processes of organic aerosols, we performed multiple PMF analyses of the AMS dataset. PMF analysis of AMS data sets has proved to be a useful method for extracting distinct OA factors that are associated with different sources and atmospheric processes (Zhou et al., 2017; Zhou et al., 2019; Zhou et al., 2016). Our analysis of the HRMS of OA identified seven factors, most of which were secondary in nature, as discussed below.

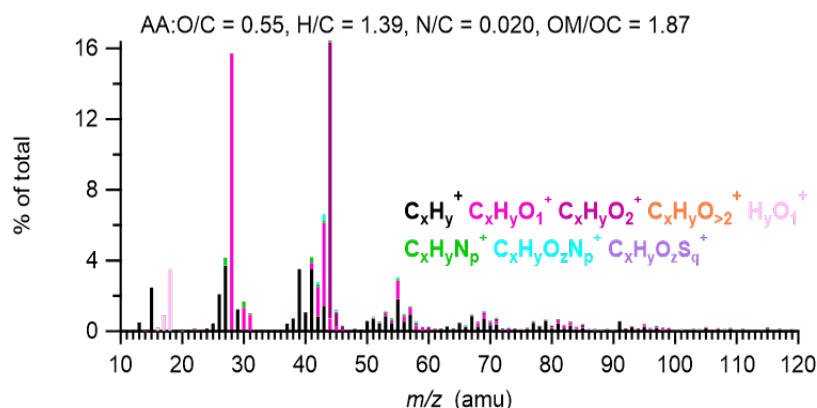


Figure 3.12: Average organic aerosol (OA) spectrum, colored by the contributions of seven ion categories for the San Antonio field study period. The average elemental and OM/OC ratios of OA calculated using Ambient-Aitken method (AA) are shown in the legend.

After a detailed evaluation of temporal trends (**Figure 3.13**), mass spectral profiles (**Figure 3.14** and **Figure 3.15**), and correlations with ions (not shown), we identified seven distinct OA factors.

These seven factors are: 1) hydrocarbon-like organic aerosol (HOA) that is associated with traffic-related primary emissions (contributing on average 10% of total organic aerosol mass; **Figure 3.16**), 2) biomass burning organic aerosol (BBOA; 12%) associated with campfires as well as regional transported wildfire plumes, 3) less-oxidized oxygenated organic aerosol (LO-OOA) representing less processed and fresher secondary organic aerosol (SOA) ($O/C = 0.51$; 30%), 4) more-oxidized OOA (MO-OOA) possibly representing more processed and aged SOA ($O/C = 1.22$; 30%), 5) an OOA that was associated with ammonium nitrate and biomass burning (AN-BB-OOA; 3%), 6) a highly oxidized OOA associated with ammonium sulfate (AS-OOA; 13%), and 7) a highly oxidized OOA associated with acidic sulfate (acidic-OOA; 3%).

Three of these factors had inorganic signals in the mass spectra, and were associated with neutralized ammonium nitrate, neutralized ammonium sulfate, and acidic sulfate signals, respectively. On average, organic aerosol was dominated by secondary organic aerosol (SOA), which together accounted for 78% of total OA mass. MO-OOA, which represented the highly oxidized and more aged SOA, made up the largest fraction. Below are discussions on individual OA factors.

3.6.3.3.1 Primary Organic Aerosols (POA)

The two primary OA sources identified for this campaign are HOA and BBOA. The mass spectrum of the HOA profile was characterized by the presence of ion signal peaks at m/z 43, 55, 57, 69, 71 etc, which corresponds to hydrocarbons ($C_xH_y^+$) associated with combustion of lubricant oils, e.g., traffic emissions, engine combustion etc. HOA had a low O/C ratio of 0.09 and a high H/C ratio of 1.85, which are consistent with HOA factors previously observed. The HOA profile correlates well with the reference HOA spectrum, and the time series showed sporadic spikes featuring fresh emissions. HOA accounted for 10% of the total measured organic mass during the campaign.

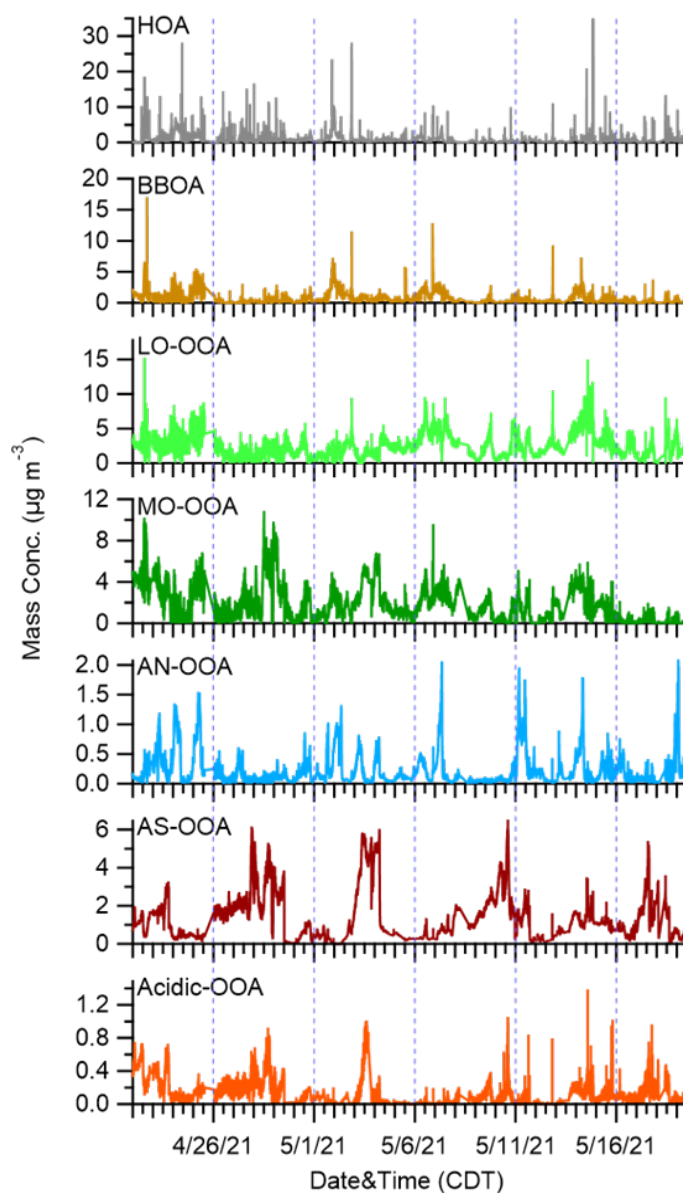


Figure 3.13: Time series of OA factors.

The BBOA factor accounted for 12% of the total OA mass. It was characterized by the peak signal intensities at m/z 60 and 73 (Figure 3.14 and Figure 3.15), which are fragments for biomass combustion. These two ion fragments indicate the sugars such as levoglucosan that are released during the wood-burning process. The fraction of m/z 44 (f_{44}) corresponding to BBOA mass spectra was low and the calculated O/C ratio was 0.12, while the H/C ratio was 1.56. Compared to previously observed BBOA factors representing different degrees of processing and aging, these chemical features suggest that the BBOA observed during this campaign are likely less aged and fresh emissions. The mass spectrum of BBOA was also characterized by elevated NO^+ signal at m/z 30 yet negligible NO_2^+ signal at m/z 46. This suggests that the BBOA factor was associated

with a significant amount of organonitrates, which is consistent with previous field and laboratory findings. BBOA presented throughout the campaign period and the temporal profiles showed both sporadic spikes featuring fresh emissions and episodic plumes with elevated mass concentrations over the course of a few hours and/or days. The exact sources of BBOA warrant further investigation. Both domestic wood-burning and trash burning could be potential contributors.

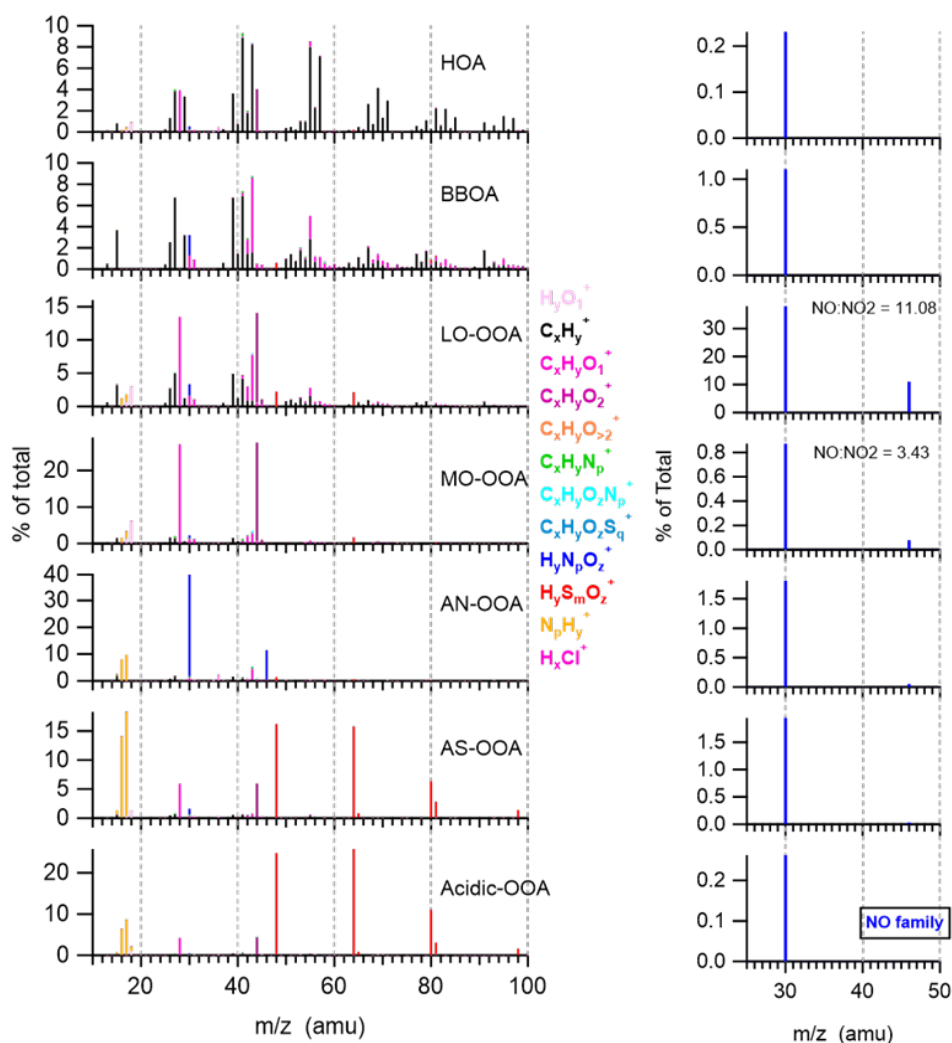


Figure 3.14: (Left) HR mass spectra of individual OA factors colored by ion categories. Inorganic ions associated with each OA factor are also shown. (Right) NO and NO_2^+ signals associated with each OA factor.

3.6.3.3.2 Secondary Organic Aerosols (SOA)

The secondary OA sources identified during the campaign are two OA types with less association with inorganics (LO-OOA, MO-OOA) and three OA types associated with inorganic signals (AN-OOA, AS-OOA, and acidic-OOA). Each OA type has distinct temporal profiles (**Figure 3.13**) and their spectra are distinguished by the presence and abundance of inorganic ions and characteristic peaks at m/z 43 and 44.

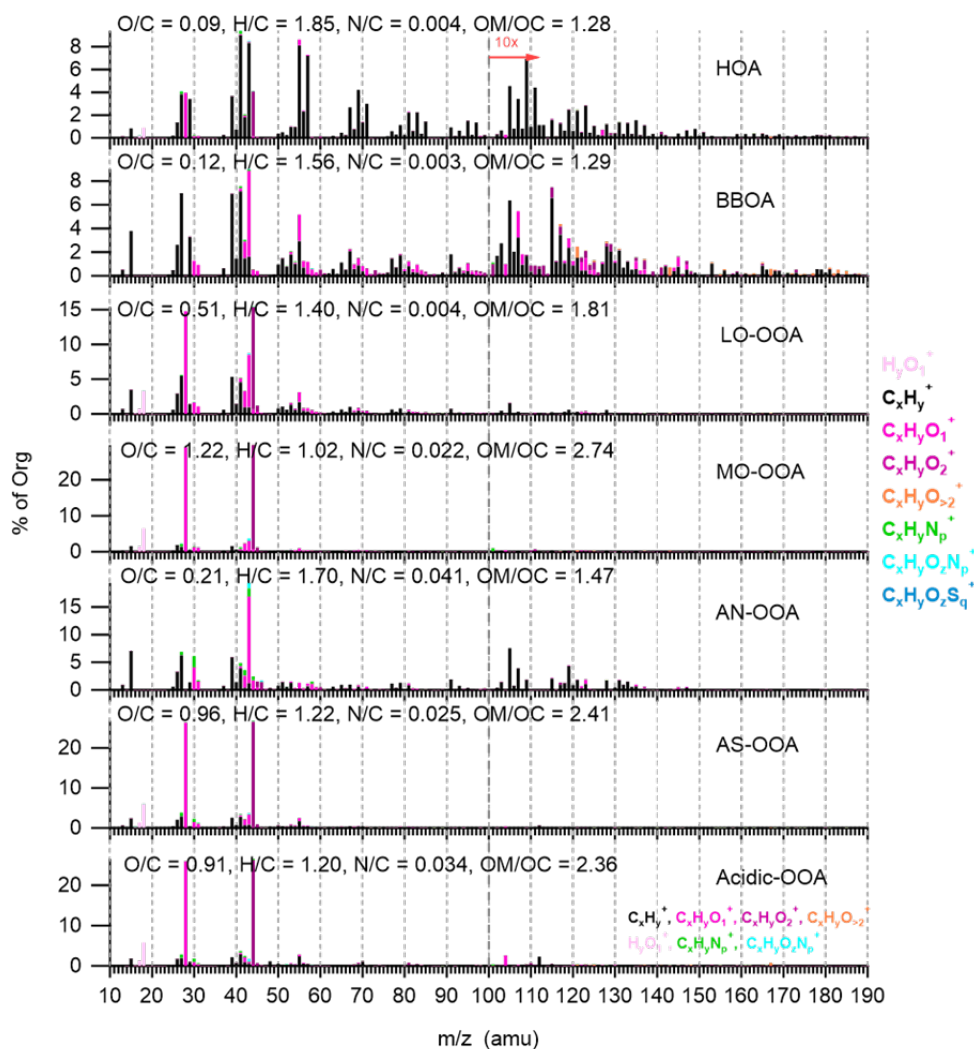


Figure 3.15: HR organic mass spectra of individual OA factors colored by ion categories. The elemental ratios of the organic signals of each factor (calculated with the Aiken-ambient method) are shown in the legends.

The mass spectrum of LO-OOA was characterized by the presence of higher f_{43} (ratio of m/z 43 to total organic spectra) and lower f_{44} indicating less oxidized species relative to MO-OOA. The LO-OOA profile is very similar to the reference SV-OOA (semivolatile-OOA), supporting the secondary nature. The average O/C calculated for the LO-OOA was 0.51 (**Figure 3.15**), within the range of O/C values of SV-OOA observed worldwide (Jimenez et al., 2009; Ng et al., 2010). In addition, the temporal profile of SV-OOA correlated tightly with the time series of $C_xH_y^+$ and $C_xH_yO^+$ ions, suggesting that this factor was mainly composed of oxygenated compounds containing hydrocarbon moieties. LO-OOA was associated with some inorganic signals, including ammonium, nitrate, and sulfate (**Figure 3.14**). Further analysis suggests that all nitrate signals associated with this factor could be attributed to organonitrates. The amount of ammonium needed to neutralize sulfate signal in this factor was twice the ammonium signal associated with the factor. This suggests that LO-OOA was associated with somewhat acidic sulfate particles, likely in the

form of a mixture of ammonium sulfate and ammonium bisulfate. LO-OOA represented an average 23% of the total OA mass during this study (**Figure 3.16**).

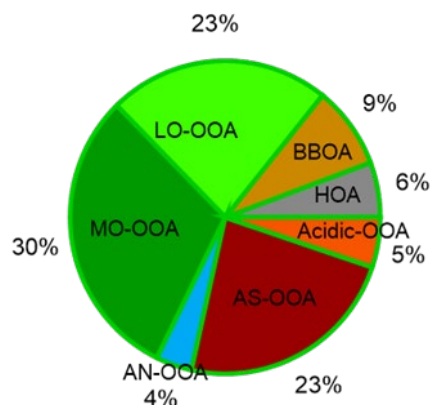


Figure 3.16: A pie chart of the average mass fractional contribution of the OA factors (organic signals only) during the entire study.

MO-OOA represented the largest component of OA, making up an average of 30% of the total OA mass (**Figure 3.16**), and had a mass spectrum that was characterized by negligible inorganic peaks and a dominant peak at m/z 44 (CO_2^+), a high O/C ratio of 1.22 and a low H/C of 1.02. The abundant CO_2^+ ion suggests a relatively high mass fraction of carboxylic functional groups and thus a significant contribution from carboxylic acid to MO-OOA composition.

The mass spectrum of AN-OOA was characterized by a significant amount of nitrate signals. Since nitrate is a secondary aerosol species, the association of AN-OOA with nitrate suggests that this factor was also secondary in nature. The $\text{NO}^+/\text{NO}_2^+$ in this factor was greater than the ratio for pure ammonium nitrate, suggesting the association with organonitrates. In addition, neutralization analysis of this factor showed a ratio of 1 between the calculated ammonium that is needed to neutralize the nitrate signals and the associated ammonium signals. This suggests the presence of ammonium nitrate. Furthermore, the f_{60} value of this factor was similar to that of the BBOA factor (0.54% vs. 0.53%), both well above the threshold of 0.3% where particles with f_{60} greater than 0.3% indicate biomass burning influences, likely more aged BB aerosols. AN-OOA on average only accounted for 4% of the total OA mass.

Both AS-OOA and acidic-OOA were characterized by significant sulfate signals in the combined mass spectra (**Figure 3.14**) and oxidized with a calculated O/C ratio of 0.96 and 0.91, respectively, suggesting the processed and aged nature of these two OA types. They are distinguished by the abundance of ammonium signal in the mass spectra (**Figure 3.14**). Neutralization analysis shows that the predicted ammonium (from sulfate signal) was comparable to the ammonium signal in the AS-OOA factor, yet much higher (22 times) for the acidic-OOA. This suggests that AS-OOA was mostly associated with neutralized ammonium sulfate, whereas the acidic-OOA was associated with a mixture of ammonium sulfate, ammonium bisulfate, and sulfuric acid. The average mass

fractional contribution of AS-OOA and acidic-OOA to total OA mass was 23% and 5%, respectively.

3.6.3.4 Comparisons of aerosol composition and diurnal profiles at two locations in San Antonio

In addition to the Traveler's World RV Park (TW), stationary measurements were also made for extended periods of time on multiple days (May 15–May 18) at the University of Texas at San Antonio (UTSA), which is ~25 km northwest of the TW site. We compared aerosol characteristics during the stationary measurement periods at these two different locations. As shown in **Figure 3.17**, the average NR-PM₁ mass concentrations were comparable for the TW and UTSA site, although the secondary aerosol species including sulfate, ammonium, LO-OOA, and SO₄-OOA had much greater fractional contribution to total NR-PM₁ at the UTSA site. This likely indicates more processed aerosols downwind of the San Antonio urban core.

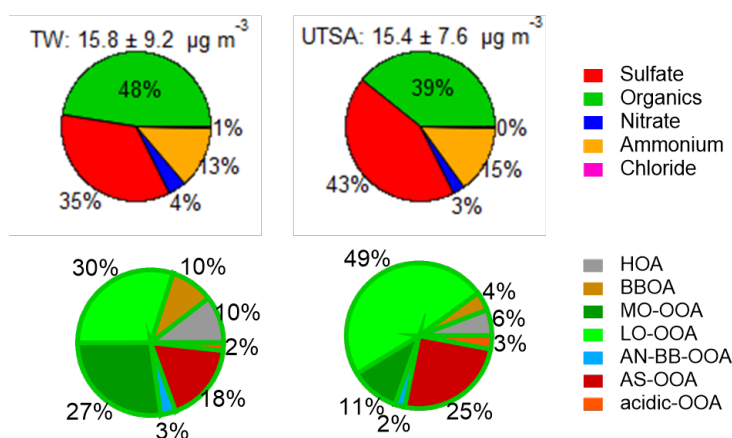


Figure 3.17: Pie charts of NR-PM₁ composition (first row) and OA composition (2nd row) during the stationary measurement periods at Traveler's World RV park (TW; left column) and the University of Texas at San Antonio (UTSA; right column), respectively. The average mass concentration of NR-PM₁ and standard deviation at each site are shown at the top of the pies. Percentages represent the mass fractional contribution of each component.

We also examined the diurnal variations of speciated submicron aerosols, bulk submicron aerosol composition, elemental ratios of organic aerosols, and OA factors during the stationary measurement periods at these two locations (TW and UTSA), as shown in **Figure 3.18–Figure 3.20**. The diurnal profiles between these two locations seemed to be different for almost all examined aerosol chemistry parameters and the UTSA site appeared to have more variable aerosols. There might be several reasons for the observed profiles. First, all sampling made at UTSA occurred during the day. We don't have data for a complete diel cycle. Comparing the diurnal profiles with partial data may be skewed. Second, sampling at TW and UTSA took place on different days. MAQL2 was only able to measure at one location at a time. TW's data shown in **Figure 3.18–Figure 3.20** were collected mostly during the first two weeks of May and lasted more than two weeks, whereas those for UTSA were in mid-May and only for several days. Many variables such

as meteorological conditions, emissions, and chemical processing environment might be different and lead to different aerosol concentrations and compositions. Lastly, the UTSA site is located much closer to major highways (e.g., ~200 m south of Texas State Highway Loop 1604) compared to the TW site (e.g., 1.5 km southwest of I-37) and likely had a strong influence from traffic emissions, and therefore led to more dynamic changes in aerosol concentration and composition. For example, we saw much elevated H/C values and HOA concentrations around 8–9 pm at UTSA, co-occurring with greatly decreased O/C and f_{43} values, which suggests primary aerosols from vehicular emissions.

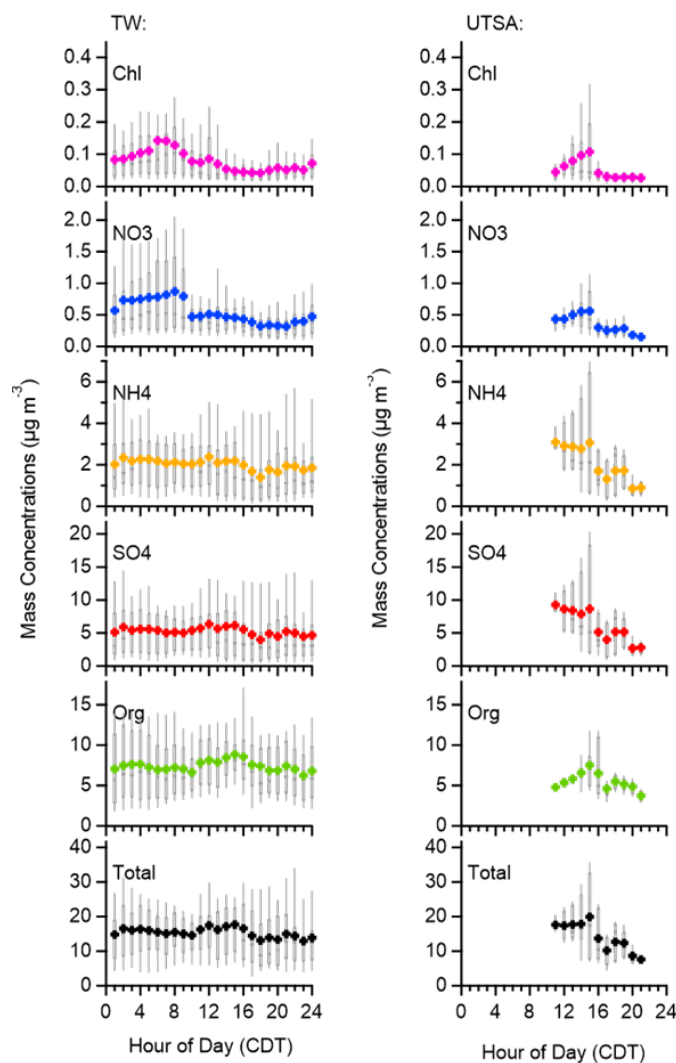


Figure 3.18: Diurnal variations of NR-PM₁ species and total mass concentrations during the stationary measurement periods at TW and UTSA, respectively. The whiskers indicate the 90th and 10th percentiles, the upper and lower boundaries indicate the 75th and 25th percentiles, the lines in the boxes indicate the median values, and the markers indicate the mean values.

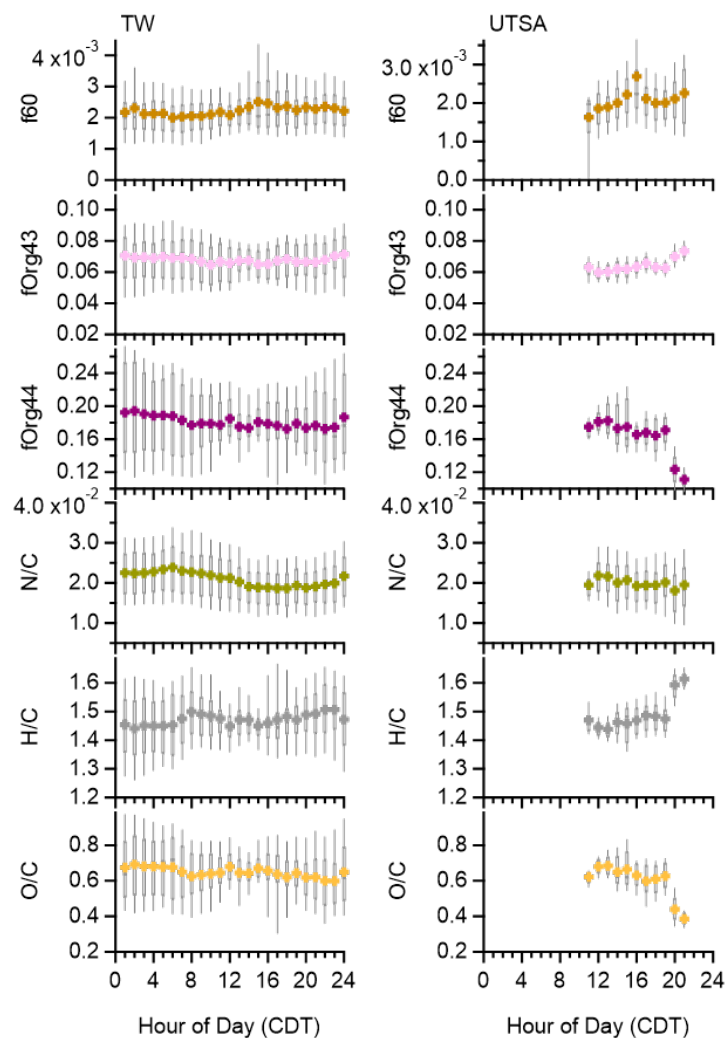


Figure 3.19: Diurnal variations of key OA tracers – f_{60} for biomass burning influences, f_{Org43} (i.e., f_{43}) for less oxidized and aged secondary aerosols, and f_{Org44} (i.e., f_{44}) for more oxidized and aged components, as well as OA elemental ratios during the stationary measurement periods at TW and UTSA, respectively. The whiskers indicate the 90th and 10th percentiles, the upper and lower boundaries indicate the 75th and 25th percentiles, the lines in the boxes indicate the median values, and the markers indicate the mean values.

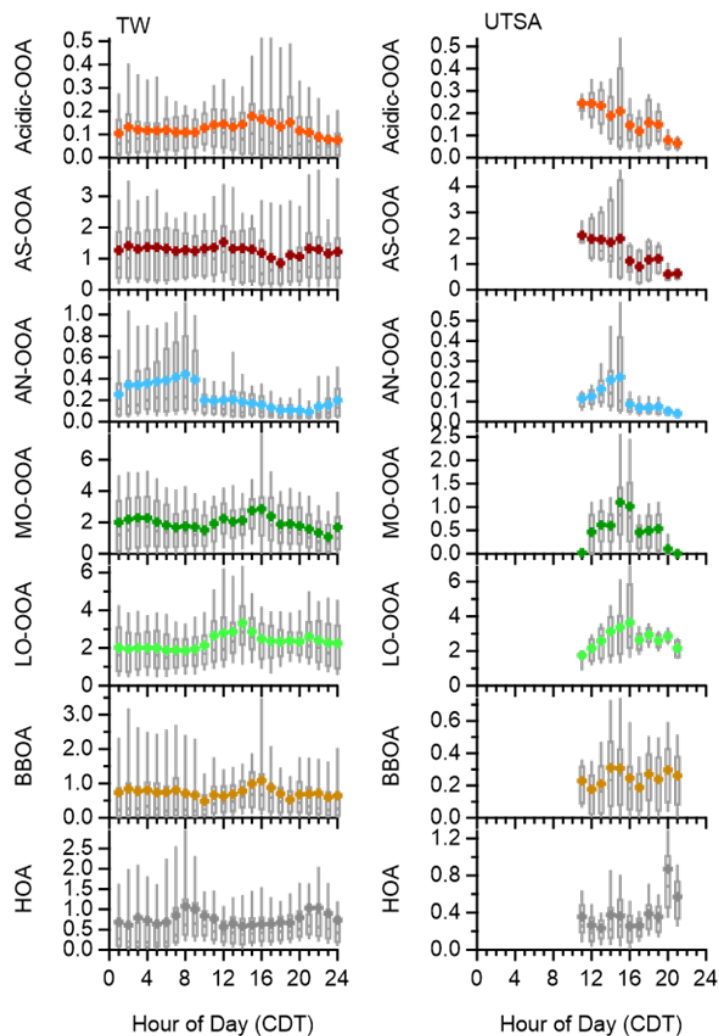


Figure 3.20: Diurnal variations of individual OA factors during the stationary measurement periods at TW and UTSA, respectively. The whiskers indicate the 90th and 10th percentiles, the upper and lower boundaries indicate the 75th and 25th percentiles, the lines in the boxes indicate the median values, and the markers indicate the mean values.

3.6.3.5 Aerosol optical properties

The TAPs and Nephelometer were successfully deployed for more than four weeks, including stationary and mobile measurements. The sampling resolution provided by the TAP and Nephelometer were high enough to characterize specific point sources during mobile operations. Aerosol absorption (TAP) and scattering (Nephelometer) instrumentation were robust and provided over 95% sampling collection completeness. The absorption coefficients and scattering coefficients provide insight into the aerosol loading across the domain. Additionally, these measurements can serve as tracers for influence of dust and biomass burning (e.g., AAE and SAE).

3.7 Task 7: Compare and Contrast 2021 Measurements to 2017 datasets at Traveler's World Site

3.7.1 Summary and Key Findings

- This task was completed. We analyzed and compared data from SAFS 2017 and SAFS 2021 to identify and evaluate changes in air quality. We compared various metrics for air quality which included ozone formation chemistry, VOC sources and concentration magnitudes, NO_X sources and concentration magnitudes, and aerosol concentration, composition, and sources, . In addition, we compared the meteorological conditions such as temperature, relative humidity, wind speed and direction, pressure, and synoptic weather conditions. The final data set was submitted to the TCEQ on April 15, 2023.
- SAFS 2021 was slightly cooler compared to 2017, but photolysis rates were comparable in both years.
- Ambient O₃ exhibited the known typical photo-oxidation mechanism of production in both years, but the O₃ level was lower in 2021 compared to 2017. In contrast, NO_X and NO_Y levels were higher in 2021 than in 2017; biogenic VOCs and oxidation products were also higher in 2021 than in 2017.
 - The sum of the average concentrations of total measured VOCs increased in 2021 (23.91 ± 9.11 ppbv) compared to 2017 (11.18 ± 5.63 ppbv).
 - The fraction of biogenic VOCs (isoprene and monoterpene) to the total VOC concentration at TW was significantly higher in 2021 compared to 2017 (**Figure 3.25**). Average isoprene concentration enhanced by ~1.8 times and average monoterpene concentration enhanced by ~8 times in 2021 compared to 2017.
 - Isoprene showed a strong photochemical trend during both years. Acetaldehyde, acetone, and the oxidation product of isoprene: methyl vinyl ketone and methacrolein (MVK+MACR) and methyl ethyl ketone (MEK) showed daytime photochemical peak at TW only in 2021. This indicates increased biogenic emissions and oxidation of these VOCs in 2021.
 - Ambient oxidized VOCs, HCHO, and acetone concentrations were higher at TW in 2021. The fraction of oxidized VOCs, HCHO, and acetone to the total VOC concentration at TW remained fairly similar during 2017 and 2021.
 - Benzene showed fairly consistent concentration at TW throughout the day in both years. Toluene peaked at known periods of high traffic peaks.
- Local ozone formation was dominated by the RO₂+NO pathway in 2021, whereas in 2017 was HO₂+NO. The peak of local ozone formation shifted from noon in 2017 to early afternoon in 2021.

- The predominant local ozone destruction pathway was $\text{NO}_2 + \text{OH}$ throughout the day in both years, followed by $\text{O}(^1\text{D}) + \text{H}_2\text{O}$ which became moderately significant during the early afternoon. In both years, local ozone destruction rate is one order of magnitude smaller than the local ozone formation rate, leading to a potentially high rate of net ozone production.
- The absolute total OH reactivity of VOCs increased by ~80% from 2017 to 2021. The most active VOC species in 2017 were formaldehyde and isoprene, whereas in 2021 were alkenes and isoprene.
- The ozone formation regime shifted from VOC-sensitive in the early morning to NO_x -sensitive around 9 a.m. for both years, but it remained in the transitional regime longer in 2021 (till ~ 11 am vs 10 am in 2017). While the ozone destruction rate was comparable between the two years, we saw much higher daytime ozone formation rate in 2021 and the peak delayed from around noon in 2017 to early afternoon in 2021 and nearly doubled in 2021. We saw higher net production rate of ozone and yet lower ozone mixing ratios in 2021. This indicates that the regional background ozone levels might be different between the two years and that it was likely lower in 2021 than in 2017.
- Both the total NR-PM_{10} and the speciated aerosol mass concentrations (including the primary and secondary species) were higher in 2021. Different diurnal patterns were observed and require further investigation.

3.7.2 Methodology

The SAFS campaigns took place in 2017 (May 2–31) and 2021 (April 22–May 19), respectively. During SAFS 2017, stationary measurements were taken at two sites, the Travelers' World Recreational Vehicle Park (TW, 29.374°N, 98.482°W, from May 2–31) ~ 7 km south of downtown San Antonio, and on the University of Texas at San Antonio (UTSA) main campus (29.579°N, 98.629°W, from May 6–31). During SAFS 2021, mobile measurements were taken by the Mobile Air Quality Laboratory (MAQL) in addition to the stationary measurements at either TW (April 29–May 12, and nighttime of April 22–29 and May 12–19) or UTSA (during daytime of May 15–18). A similar suite of instrumentation was carried out to measure gases (O_3 , NO_x , NO_y , CO, SO_2 , and selected VOCs), aerosol concentration, composition, and optical properties, as well as meteorological conditions during both SAFS campaigns. This section focuses on the comparisons of meteorological and air quality measurements made at the TW site between the two campaigns.

The temperature, pressure, and relative humidity were measured by RM Young (Traverse City, MI 41382); wind direction and speed were measured by an RM Young 2-D sonic anemometer; the jNO_2 were measured by MetCon GmbH filter radiometers (Koenigstein, Germany) for both years. The filter radiometers were calibrated against a diode-array actinic flux spectroradiometer (DAFS) before and after the two campaigns. For both campaigns O_3 was measured by a 2B Technology

(Boulder, CO) Model 205 dual beam O₃ ultraviolet photometric gas analyzer; NO was measured by an Air Quality Design (Golden, CO) custom chemiluminescent analyzer and NO₂ was measured by an Air Quality Design custom chemiluminescent analyzer with a Blue Light Converter for photolytic conversion of NO₂ to NO. NO_Y was measured by a Thermo Scientific (Franklin, MA) Model 42C chemiluminescent analyzer with a Thermo molybdenum oxide catalytic converter at 300°C for conversion of odd nitrogen to NO. CO was measured by a Los Gatos Research (San Jose, CA) CO analyzer, model F-CO-23r using laser-based off-axis integrated cavity output spectroscopy. SO₂ was measured by a Thermo Scientific Model 43C-TLE with the pulsed ultraviolet fluorescence technique. A PTR-MS was deployed for measuring select VOCs, and an HR-ToF-AMS was deployed for size-resolved chemical characterization of NR-PM₁.

Ozone (O₃) formation and destruction rates and OH reactivity of VOCs are calculated by the NASA LaRC zero-dimensional model (Crawford et al., 1999; Olson et al., 2006) for both SAFS 2017 and 2021 field campaigns. A comparison of several model mechanisms including LaRC based on the Texas-II Radical and Aerosol Measurement Project (TRAMP) campaign can be found in Chen et al. (2010). The model is run in time-dependent mode assuming a diurnal steady state with standard constraints and formaldehyde as of its latest application in the San Antonio Field Studies in 2017 (SAFS 2017) (Guo et al., 2021). Among the model inputs, trace gases, meteorological parameters, photolysis rate of NO₂, and designated VOCs are from real-time measurements, while a subset of VOCs required but unmeasured by the PTR-MS is ratioed based on correlations derived from SAFS 2017.

O₃ formation rate (F(O₃)) is calculated from three main NO₂ generating pathways in the LaRC model output: HO₂+NO, RO₂+NO, and CH₃O₂+NO (where CH₃O₂ is specifically the methyl peroxy radical, which is not included in the RO₂ parameter), as subsequent NO₂ photolysis and the association of O(³P) with O₂ are sufficiently fast and non-rate-limiting. O₃ destruction rate (D(O₃)) is calculated from a combination of five main OH production reactions (O(¹D)+H₂O), HO_X-driven O₃-depleting chain reactions (HO₂+O₃, OH+O₃) under lower-NO_X conditions, the termination of both NO_X and HO_X in forming HNO₃ (NO₂+OH) under higher-NO_X conditions, and the reactions of O₃ with specific VOCs (O₃+NMHC), particularly those with carbon-carbon double bonds. Net P(O₃) is calculated as the difference between F(O₃) and D(O₃).

The relative importance of a specific VOC (or lumped VOC) with respect to the formation of secondary O₃ is determined by its atmospheric abundance and how quickly it reacts with OH. The reactivity of a VOC species (VOCR) is defined as the product of its concentration and reaction rate constant (k) with OH and is also calculated from the LaRC model output.

The quantification of O₃-NO_X-VOC sensitivity and O₃ formation regimes (e.g., Kleinman, 1994; Sillman et al., 1995; Kleinman, 2005) was performed (Guo et al., 2021) based on the “LRO_X/LNO_X” metric recommended by Schroeder et al. (2017), in which O₃ formation is thought to be NO_X-sensitive when HO_X radical loss via OH + NO₂ accounts for less than half of total HO_X radical loss. In specific, the radical termination reaction of OH with NO_X to form HNO₃ is referred to as LNO_X, and radical-radical reactions (including RO₂ and RO₂ self-reactions, RO₂ and HO₂

reactions, and RO₂ reactions with a different RO₂) resulting in stable peroxide formation are referred to as LRO_X (RO_X = RO₂+HO₂). The ratio of radical termination rate from LRO_X to LNO_X will provide a good indicator of NO_X-sensitive ($LRO_X/LNO_X > \sim 0.5$, which corresponds to $L_n/Q < 2/3$, where $L_n = LNO_X$ and $Q = LNO_X + LRO_X$), VOC-sensitive ($LRO_X/LNO_X < \sim 0.3$), and transitional ($0.3 < LRO_X/LNO_X < 0.5$) O₃ formation regimes (Kleinman et al., 2005; Schroeder et al., 2017).

3.7.3 Results

3.7.3.1 Meteorological conditions and inorganic trace gases

We observed higher temperatures (by ~2.4 °C) and lower pressure (by ~24.0 mbar) during SAFS 2017 than during SAFS 2021. The diurnal patterns (**Figure 3.21**) showed that these differences occurred throughout the day. Relative humidity (RH) and the photolysis rate of NO₂ (j_{NO_2}) were generally compared between the two field campaigns (**Figure 3.21**); the median diurnals also trended closely to each other, indicating that the photochemical conditions were overall comparable.

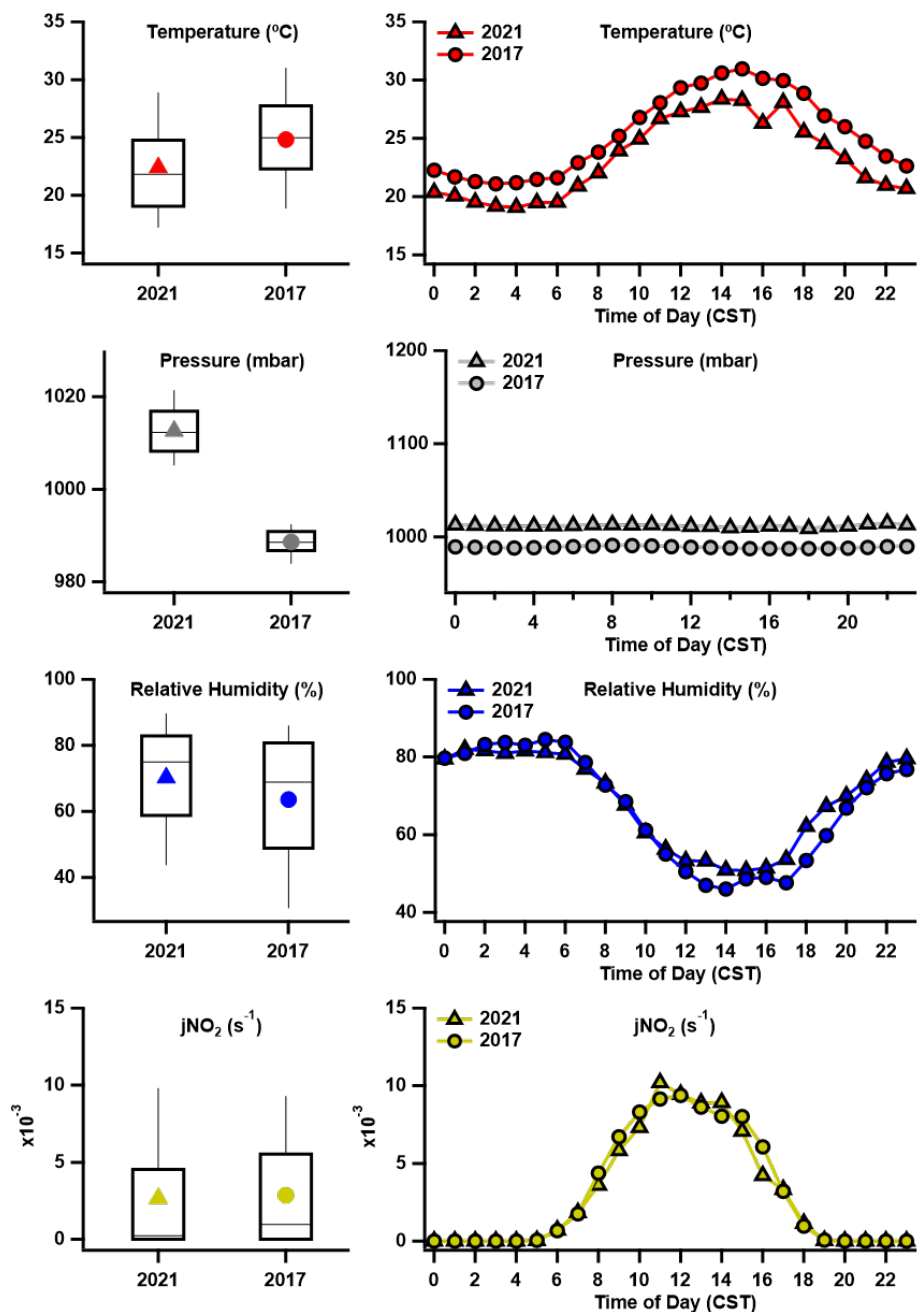


Figure 3.21: Box plots (left) and mean diurnal profiles (right) of temperature, pressure, relative humidity, and photolysis rate of NO_2 (j_{NO_2}) measured at the Travelers' World RV Park site (TW) during SAFS 2021 and 2017 campaigns.

Ambient ozone levels exhibited the known typical photo-oxidation mechanism of production (peak in the afternoon) in both years, but the O_3 level was lower in SAFS 2021 compared to 2017 (by ~ 10 ppbv on study average), which indicates improved air quality over the years. The decrease in O_3 concentrations was observed throughout the day, as shown in the diurnal profiles in **Figure 3.22**. However, we saw higher levels of NO , NO_2 , and NO_Y during SAFS 2021 than those during SAFS 2017 (**Figure 3.23**); increased NO occurred mostly during the nighttime and NO_2 during the day,

whereas NO_Y was elevated throughout the day. These observations imply potential changes in ozone formation pathway. CO levels were slightly higher during SAFS 2021, if not comparable (Figure 3.24). Since the majority of the SO_2 measurements were below the detection limit for both study campaigns, we did not show the comparisons.

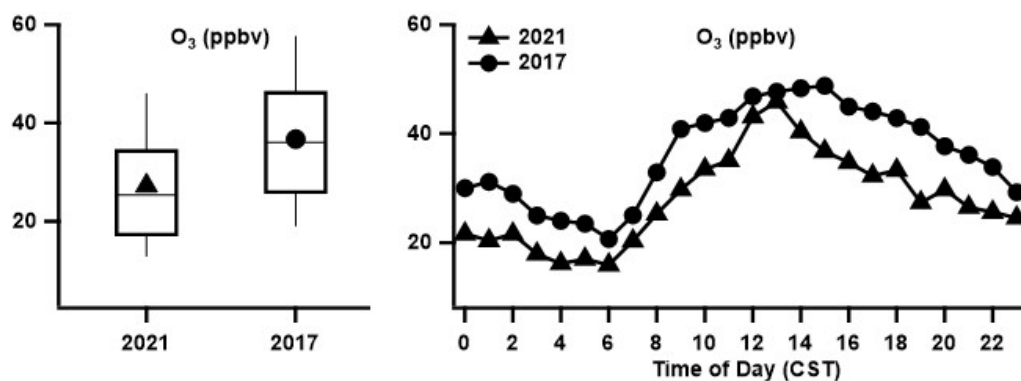


Figure 3.22: Box plots (left) and mean diurnal profiles (right) of ozone (O_3) measured at the TW during SAFS 2021 and 2017 campaigns.

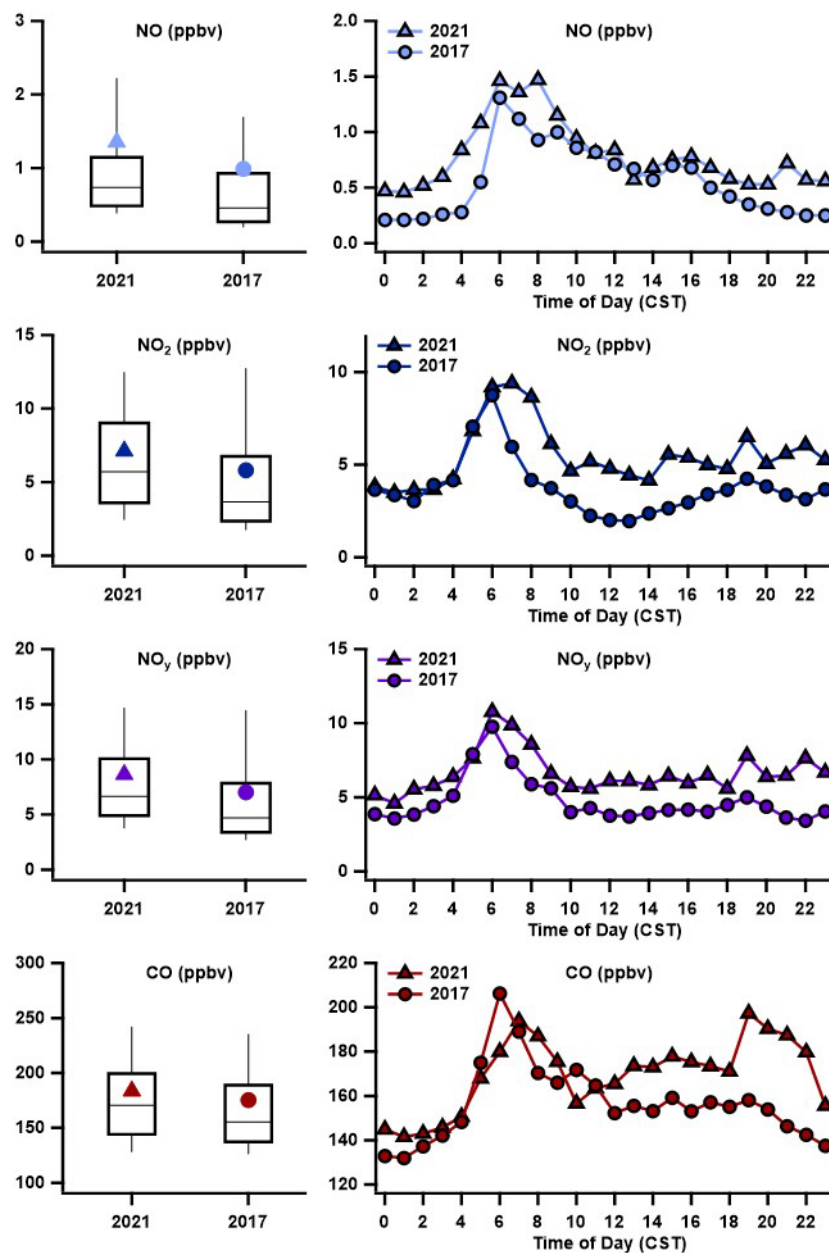


Figure 3.23: Box plots (left) and mean diurnal profiles (right) of nitrogen species and CO measured at the TW during SAFS 2021 and 2017 campaigns.

3.7.3.2 Volatile organic compounds

3.7.3.2.1 VOC categories and diurnal profiles

The successful deployment of the PTR-MS during the 2017 and 2021 SAFS field campaigns allows for the temporal comparison in VOCs at TW and UTSA. This comparison includes a wide range of VOCs (see methods section), which here are grouped as anthropogenic, biogenic, oxidized, biomass burning, acetone, and HCHO (**Figure 3.24**). This comparison examined VOCs as a fraction of the total as well as diurnal variability. Overall, the sum of the average ambient

concentration of total measured VOCs increased in 2021 (23.91 ± 9.11 ppbv) compared to 2017 (11.18 ± 5.63 ppbv). This increase in ambient VOC concentrations in 2021 over 2017 was driven by isoprene, monoterpenes, acetaldehyde, acetone, MEK, MVK+MACR, and to a lesser extent toluene (**Figure 3.25**).

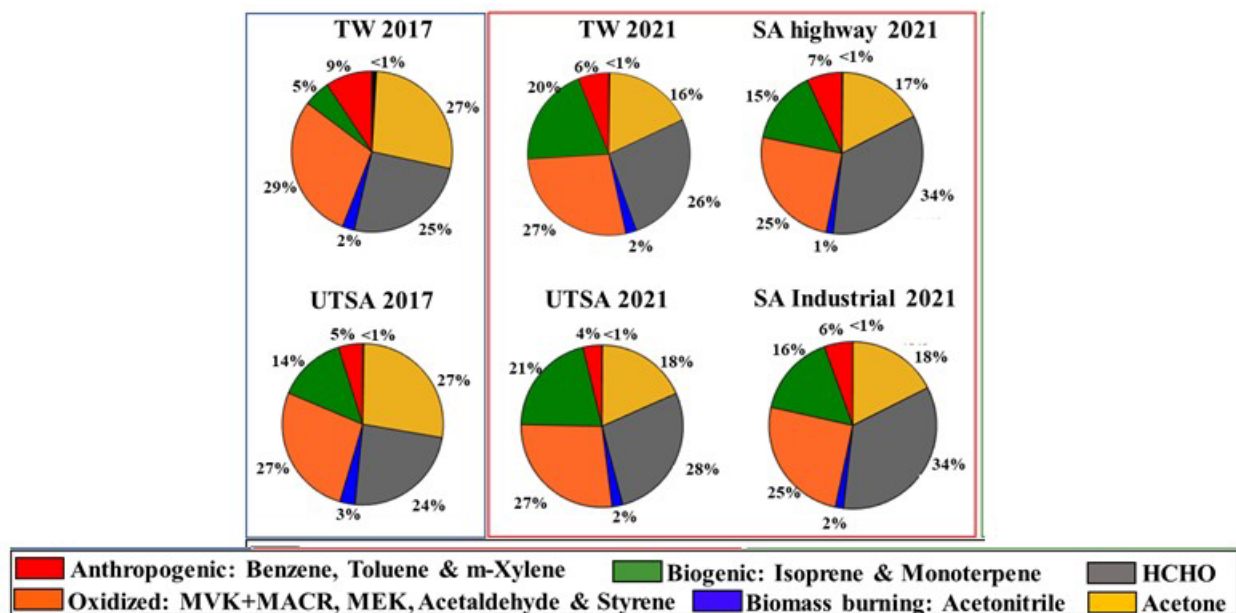


Figure 3.24: Pie chart showing contribution of different category of VOCs (anthropogenic, biogenic, oxidized, biomass burning, HCHO and acetone) to total VOC concentration during stationary measurement at San Antonio during SA FS 2017; stationary and mobile measurements in San Antonio in 2021. The stationary measurements in San Antonio were conducted at TW and UTSA. The mobile measurement is categorized as highway, urban, and industrial areas.

The fraction of biogenic VOCs (i.e. isoprene and monoterpene) to the total VOC concentration was significantly higher at TW, San Antonio in 2021 compared to 2017 (**Figure 3.25 c and d**). Average isoprene concentration was enhanced by ~1.8 times and average monoterpene concentration was enhanced by ~8 times in 2021 compared to 2017. It is important to note that isoprene diurnal variability showed a strong photochemical signature (i.e. peaking during midday) during both years, which suggests that the increase in isoprene in 2021 was driven by a change in the biogenic emissions. Nighttime nonzero isoprene was observed at TW in both the years, possibly due to the unreacted residual biogenic isoprene from the daytime emissions. The nighttime baseline was ~2 times higher in 2021. Interestingly, the nighttime baseline just moves up at the same increment as the daytime peak. A distinct diurnal profile of monoterpene showing daytime maxima was evident only in 2021. Acetaldehyde, acetone, and the oxidation product of isoprene: methyl vinyl ketone and methacrolein (MVK+MACR) and methyl ethyl ketone (MEK) showed daytime photochemical peak at TW only in 2021. This indicates increased biogenic emissions and oxidation of these VOC in 2021. The peak monoterpene emission was observed later in the day than isoprene or O₃. The potential sources of this biogenic VOC increase are

examined below and will be the focus of a Shrestha et al peer-reviewed publication, which is currently in preparation.

In addition to the BVOCs, observed oxidized VOCs, HCHO, and acetone ambient concentrations were also high in 2021 at TW. Interestingly, with the increase in BVOCs, the fraction of oxidized VOCs, HCHO, and acetone was very similar between the two years. For example, the fraction of oxidized VOCs to the total at TW in 2017 was 29%, and 27% at TW in 2021. The fraction of oxidized VOCs at UTSA in 2017 and 2021 were both 27%. This is in stark contrast to the BVOC fraction observed at TW which was 15% higher in 2021, with an increase from 5% to 20%.

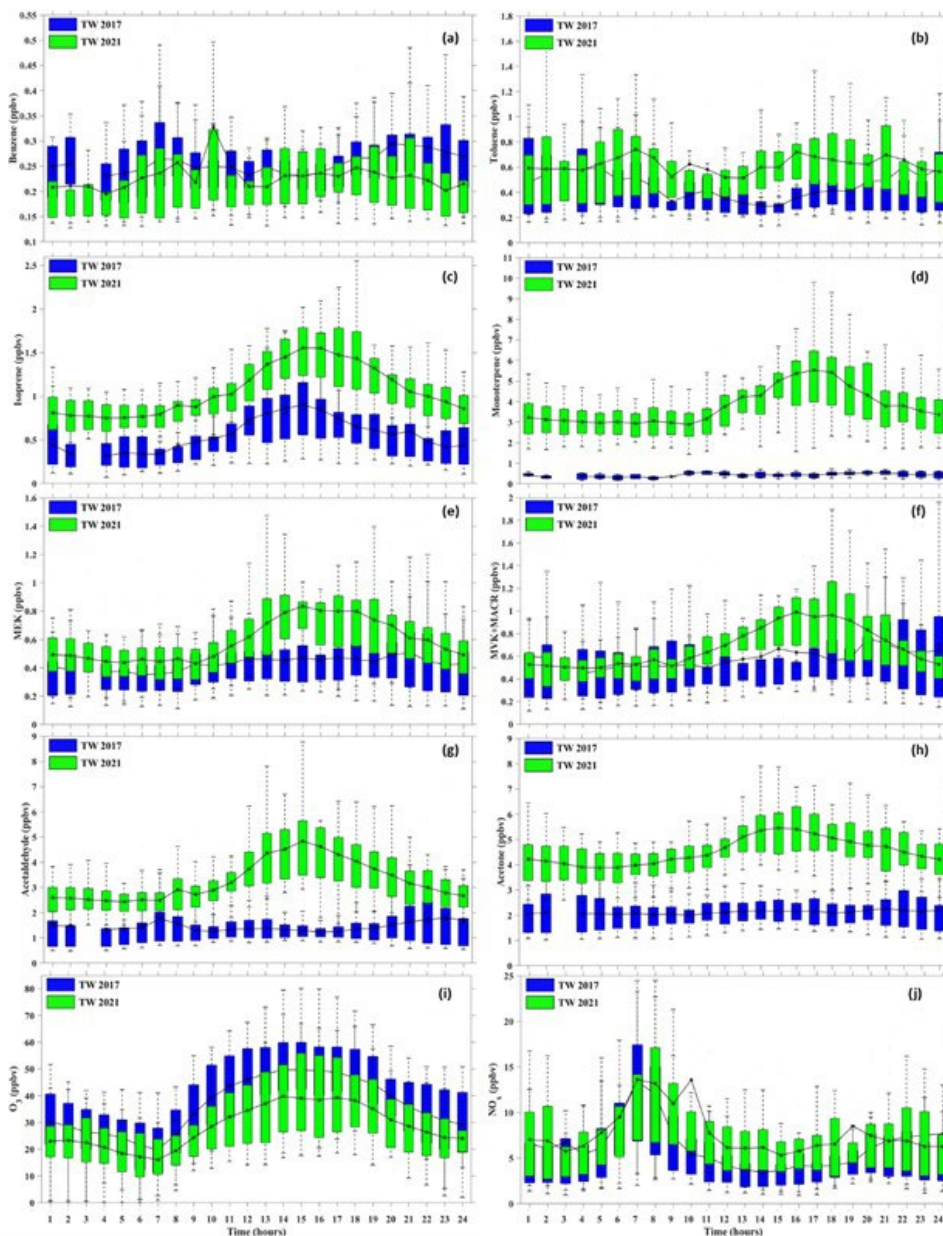


Figure 3.25: Diurnal variability of select VOCs, inorganic trace gases and meteorological parameters at TW during SAFS 2017 and 2021 campaigns.

3.7.3.2.2 *Wind rose and polar plots of VOCS at TW during 2017 and 2021*

The wind rose from SAFS in 2017 was uniquely consistent with a strong SE direction. This consistency in wind direction and directionally was in contrast to 2021, where the prominent wind direction was N and NE, but included the SE (Figure 3.26). Building on the BVOC concentrations, the isoprene, monoterpenes, MEK, and MVK+MACR polar plots show a strong source region in the SE and SW of TW. Note: polar plots utilize wind rose to illustrate ambient VOC concentration trends as a function of wind speed and direction. Interestingly, the acetaldehyde polar plots were similar to isoprene, monoterpenes, MEK, and MVK+MACR. All combined these VOCs showed a strong spatial overlap with O₃, highlighting the regional source of O₃ to be located in the SE and SW.

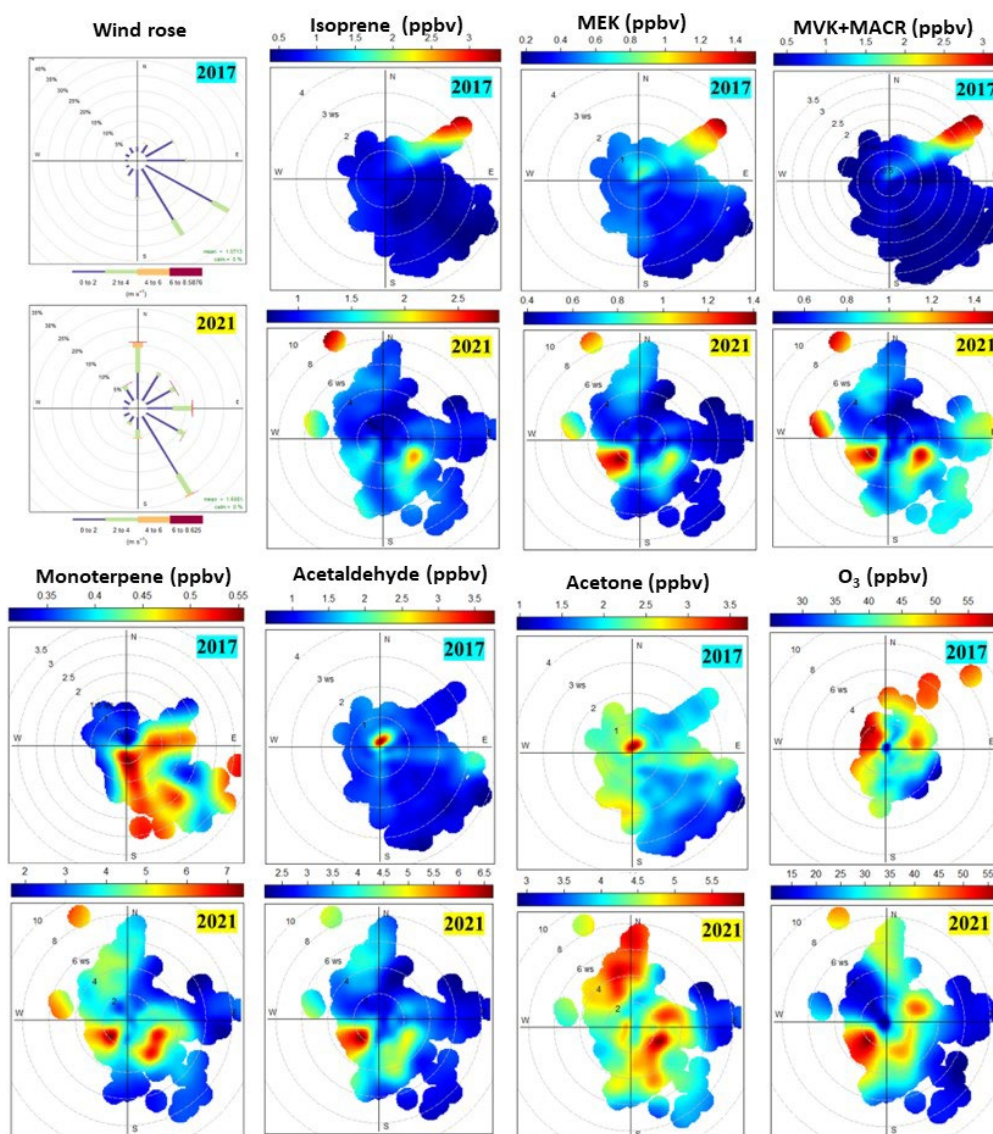


Figure 3.26: Wind rose plot and polar plots select-VOCs and O₃ at the TW site during SAFS 2017 and 2021.

3.7.3.2.3 *Climatological differences between 2017 and 2021*

Climate extremes such as droughts can cause disruptions to the functioning of ecosystems and emissions of VOCs (Pegoraro et al., 2004). Reported isoprene and monoterpene emission responses to drought are highly variable and dependent on the individual plant, making emission inventories uncertain. A recent study that conducted a controlled drought and rewetting experiment reported the monoterpene concentration enhanced during severe drought by ten times compared to the early drought period (Byron et al., 2022). With the transition into severe drought, the maxima of the α -pinene and β -pinene diurnal cycles shifted progressively later in the day. Within that study, the response of isoprene to drought had a threshold level: the isoprene enhanced parallel to monoterpene in the early drought but decreased during the severe drought period to pre-drought levels.

The drought severity and coverage index (DSCI) for Bexar County (that includes our sampling site in San Antonio) from January to May 2021 was significantly higher as compared to the same period in 2017 (**Figure 3.27**). This suggests that the elevated ambient concentrations of BVOCs (i.e. isoprene and monoterpenes) in 2021 (as compared to 2017; **Figure 3.25**) may have been a biological response to the ongoing 2021 drought. These scientific findings will be further explored and published by Shrestha et al.

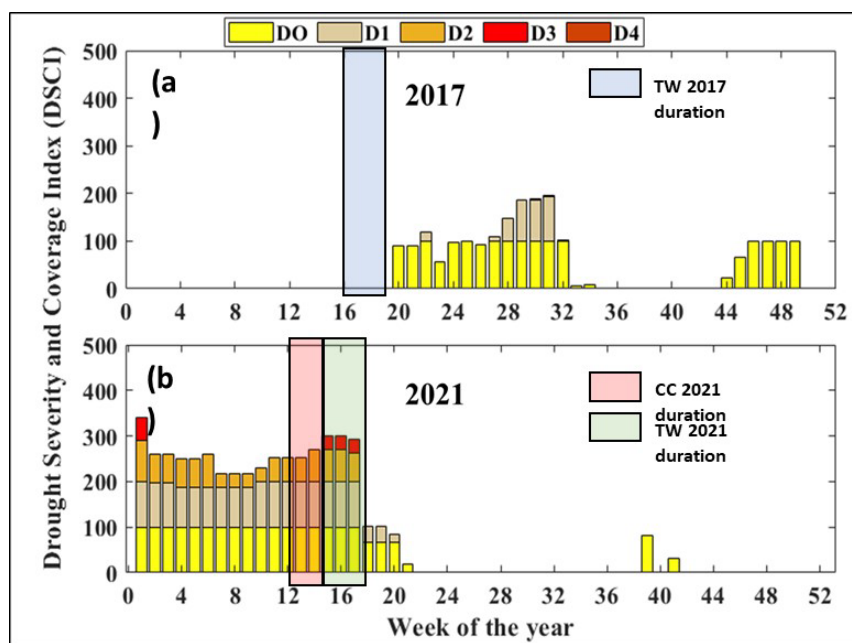


Figure 3.27. Comparison of Drought Severity and Coverage Index (DSCI) for Bexar County, TX during (a) 2017 and (b) 2021. The sampling periods during 2017 and 2021 are highlighted in the plot. (Data Source: <https://droughtmonitor.unl.edu>). Drought Monitor map identifies areas of drought and labels them by intensity (D0 through D4). D0 areas are experiencing abnormally dry condition, while D1 is experiencing a drought at the least intense levels and D4 the most intense.

3.7.3.3 Chemistry and dynamics of ozone

At San Antonio Traveler's World Site (TW) during SAFS 2021, the hourly-averaged median $F(O_3)$ was 34.0 ± 32.0 ppbv h^{-1} for 6:00 to 19:00 CST with a noon to early afternoon peak between 11:00 and 15:00 CST averaged about 63.0 ppbv h^{-1} (**Figure 3.28**, left). RO_2+NO (14.7 ± 13.8 ppbv h^{-1}) was the largest contributor (43%) to $F(O_3)$ followed by HO_2+NO (14.0 ± 13.2 ppbv h^{-1} , 41%) and CH_3O_2+NO (5.3 ± 5.0 ppbv h^{-1} , 16%). For components of $D(O_3)$ (**Figure 3.28**, right), NO_2+OH and was the dominant pathway, followed by $O(^1D)+H_2O$, O_3+NMHC and HO_2+O_3 . Specifically, NO_2+OH (1.0 ± 1.0 ppbv h^{-1} , 67%) was significant throughout the early morning to late afternoon, while $O(^1D)+H_2O$ (0.3 ± 0.5 ppbv h^{-1} , 22%), O_3+NMHC (0.3 ± 0.2 ppbv h^{-1} , 19%) and HO_2+O_3 (0.1 ± 0.2 ppbv h^{-1} , 9%) became noticeable in early afternoon. In general, $D(O_3)$ averaged 1.4 ± 1.2 ppbv h^{-1} and was smaller than $F(O_3)$ by an order of magnitude, leading to a potential high rate of net ozone production $P(O_3)$.

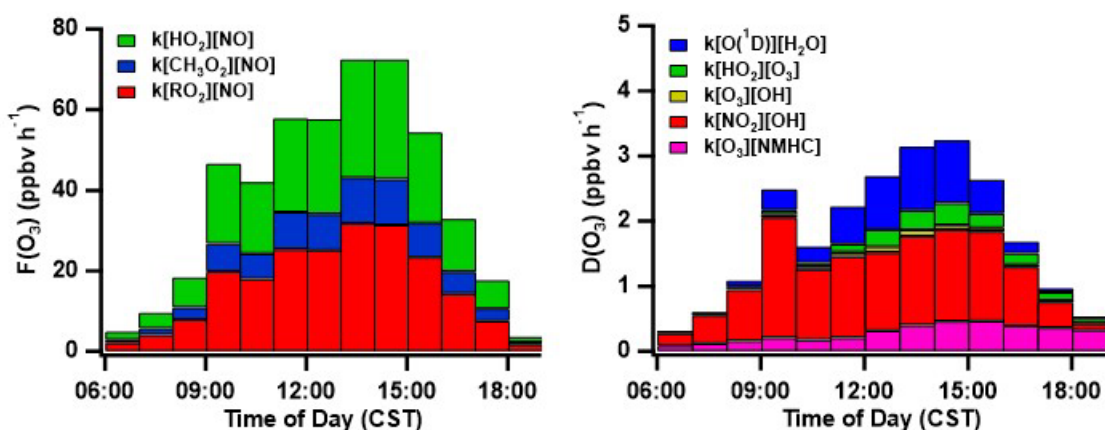


Figure 3.28: Median daytime profiles of $F(O_3)$ (left) and $D(O_3)$ (right) estimated at San Antonio Traveler's World Site using the LaRC model in SAFS 2021.

At San Antonio Traveler's World Site (TW) during SAFS 2017, the hourly-averaged median $F(O_3)$ was 22.7 ± 12.6 ppbv h^{-1} for 7:00 to 19:00 CST with a peak around 12:00 CST of 40.8 ppbv h^{-1} (**Figure 3.29** left). HO_2+NO (10.8 ± 6.0 ppbv h^{-1}) was the largest contributor (47%) to $F(O_3)$ followed by RO_2+NO (9.0 ± 5.0 ppbv h^{-1} , 39%) and CH_3O_2+NO (2.9 ± 1.5 ppbv h^{-1} , 13%). For components of $D(O_3)$ (**Figure 3.29**, right), NO_2+OH and was the dominant pathway, followed by $O(^1D)+H_2O$ and HO_2+O_3 . Specifically, NO_2+OH (0.6 ± 0.2 ppbv h^{-1} , 42%) was significant throughout the daytime, while $O(^1D)+H_2O$ (0.5 ± 0.5 ppbv h^{-1} , 29%) dominated at noon with additional contributions from HO_2+O_3 (0.2 ± 0.2 ppbv h^{-1} , 13%). In general, $D(O_3)$ averaged 1.5 ± 0.9 ppbv h^{-1} and was smaller than $F(O_3)$ by an order of magnitude, leading to a potential high rate of net ozone production $P(O_3)$.

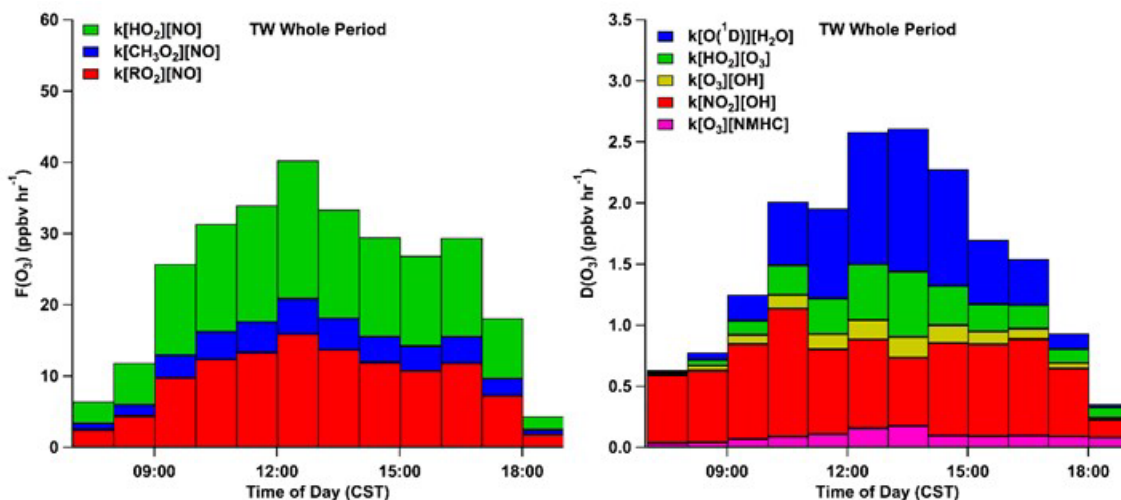


Figure 3.29: Median daytime profiles of $F(O_3)$ (left) and $D(O_3)$ (right) estimated at San Antonio Traveler's World Site using the LaRC model in SAFS 2017.

The total OH reactivity of VOCs ($9.1 \pm 2.8 \text{ s}^{-1}$) was dominated by alkenes ($3.9 \pm 1.3 \text{ s}^{-1}$, 43%) and isoprene ($2.9 \pm 1.2 \text{ s}^{-1}$, 32%) during SAFS 2021. The alkenes represented in the LaRC model includes the monoterpene measured by PTR-MS, half of the MVK and MACR measured by PTR-MS, and propene, c-2-butene, isobutylene, and t-2-butene estimated from PTR-MS measurement and canister ratios. While the fractional contributions of all the rest of the VOC reactivities were below 10% (**Figure 3.30**). Formaldehyde only took account of approximately 6% ($0.5 \pm 0.2 \text{ s}^{-1}$) of total OH reactivity, which is consistent with the increased role of isoprene and alkenes, which indicates local emission sources and limited secondary processing. The large contribution of isoprene reactivity also underscores the importance of biogenic VOC. Common oil and gas extraction indicators, such as ethane (C_2H_6), and petrochemical industry emission indicators, such as aromatics and BTEX, made only limited contributions (about 7% for aromatics, 1% for ethane, 2% for propane, 5% for alkanes other than ethane, and less than 1% for benzene). During SAFS 2017, the total OH reactivity of VOCs ($5.0 \pm 0.9 \text{ s}^{-1}$) was dominated by HCHO ($2.0 \pm 0.4 \text{ s}^{-1}$, 41%), followed by isoprene ($1.2 \pm 0.5 \text{ s}^{-1}$, 23%), alkenes ($0.7 \pm 0.0 \text{ s}^{-1}$, 14%) aromatics ($0.4 \pm 0.0 \text{ s}^{-1}$, 8%), and alkanes ($0.3 \pm 0.0 \text{ s}^{-1}$, 6%) (**Figure 3.31**). The large contribution of isoprene reactivity underscores the importance of biogenic VOC in urban pollution and HCHO could be largely secondarily formed from varied reactive species. It should also be noted that ethane made a negligible contribution (<3%) to total OH reactivity.

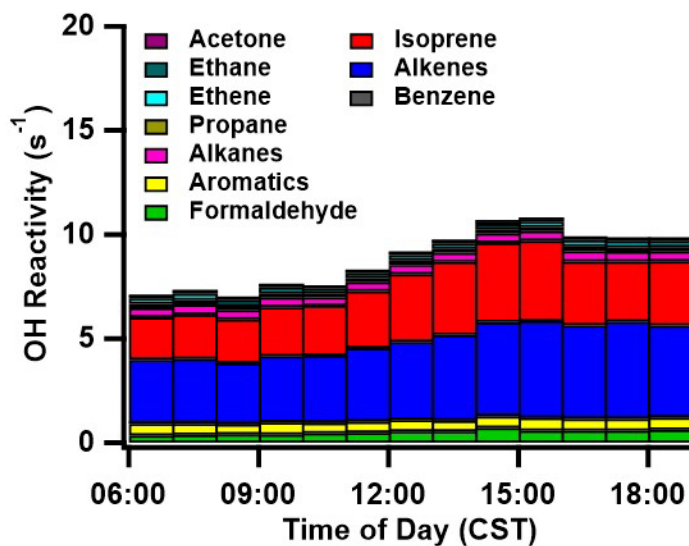


Figure 3.30: The OH reactivity of VOCs estimated at SA TW site using the LaRC model in 2021.

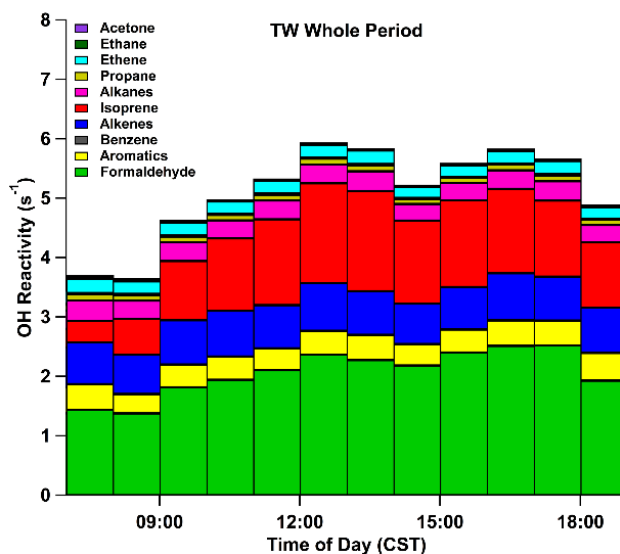


Figure 3.31: The OH reactivity of VOCs estimated at SA TW site using the LaRC model in 2017.

Based on the LRO_x/LNO_x ratio (**Figure 3.32**), 28% of the LaRC modeled period was in VOC-sensitive regime, with an average NO of 7.1 ppbv and $P(O_3)$ of 30.4 ppbv hr^{-1} , while 66% of the period was in a NO_x -sensitive regime, with an average NO of 1.2 ppbv and a higher average $P(O_3)$ of 34.1 ppbv hr^{-1} at TW during the modeling period in SAFS 2021. Approximately 6% of the period was in the transitional regime with an average NO of 1.6 ppbv and PO_3 of 32.4 ppbv hr^{-1} . The diurnal variation of LRO_x/LNO_x indicated that $P(O_3)$ initiated in NO_x -sensitive regime between 6:00 and 7:00 CST in the early morning, but quickly shifted to VOC-sensitive regime between 7:00 and 9:00 CST, likely due to the addition of NO_x from morning traffic. Then the ozone formation lingered around the transitional regime between 9:00 and 11:00 CST, until it

stabilized and stayed in NO_x -sensitive from 11:00 CST throughout the afternoon. Notice that a shift from NO_x - to VOC-sensitive regime during the afternoon traffic hour was not observed, likely due to the accumulation of VOCs throughout the day. The peak $P(\text{O}_3)$ was observed around early noon- 70.0 ppbv hr^{-1} during 13:00–15:00 CST. On average, the net ozone production rate was $35.0 \pm 25.9 \text{ ppbv hr}^{-1}$ throughout the daytime and was most active from 11:00 to 15:00 CST. During the elevated $P(\text{O}_3)$ period, the ozone formation regime stayed NO_x -sensitive, with an average $P(\text{O}_3)$ at $63.0 \pm 8.7 \text{ ppbv hr}^{-1}$.

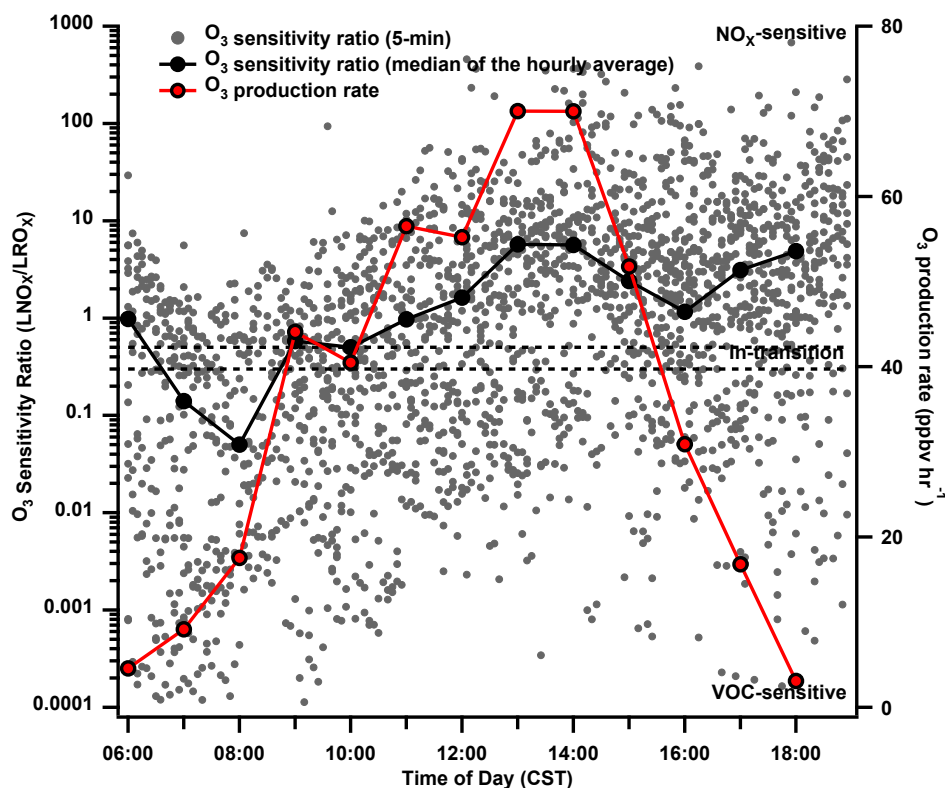


Figure 3.32: The 5-min (grey points) and median of the hourly average (black line with markers) daytime profiles of O_3 sensitivity ratio ($\text{LRO}_x/\text{LNO}_x$) on the left axis, and the modeled net ozone production rate ($P(\text{O}_3)$), red line with markers) on the right axis. The two horizontal dash lines on the left axis at values of 0.3 and 0.5 indicate the transition regime between NO_x - and VOC-sensitive regimes for SAFS 2021.

During SAFS 2017 (**Figure 3.33**), 27% of the LaRC modeled period was in VOC-sensitive regime, with an average NO of 2.0 ppbv and $P(\text{O}_3)$ of 13.9 ppbv hr^{-1} , while 68% of the period was in a NO_x -sensitive regime, with an average NO of 0.5 ppbv and a higher average $P(\text{O}_3)$ of 28.1 ppbv hr^{-1} at TW during the modeling period in SAFS 2017. Approximately 5% of the period was in the transitional regime with an average NO of 1.0 ppbv and $P(\text{O}_3)$ of 24.1 ppbv hr^{-1} . The diurnal variation of $\text{LRO}_x/\text{LNO}_x$ indicated that $P(\text{O}_3)$ was in VOC-sensitive regime in the early morning and quickly transitioned to NO_x -sensitive regime between 8:00 and 9:00 CST. It remained NO_x -sensitive thereafter throughout the daytime. The peak $P(\text{O}_3)$ was observed around noon- 38.9 ppbv hr^{-1} during 12:00-13:00 CST. On average, the net ozone production rate was $22.8 \pm 11.0 \text{ ppbv hr}^{-1}$ throughout the daytime and was most active from 10:00 to 14:00 CST. During the elevated $P(\text{O}_3)$

period, the ozone formation regime stayed NO_x -sensitive, with an average $P(\text{O}_3)$ at 33.0 ± 4.0 ppbv hr^{-1} .

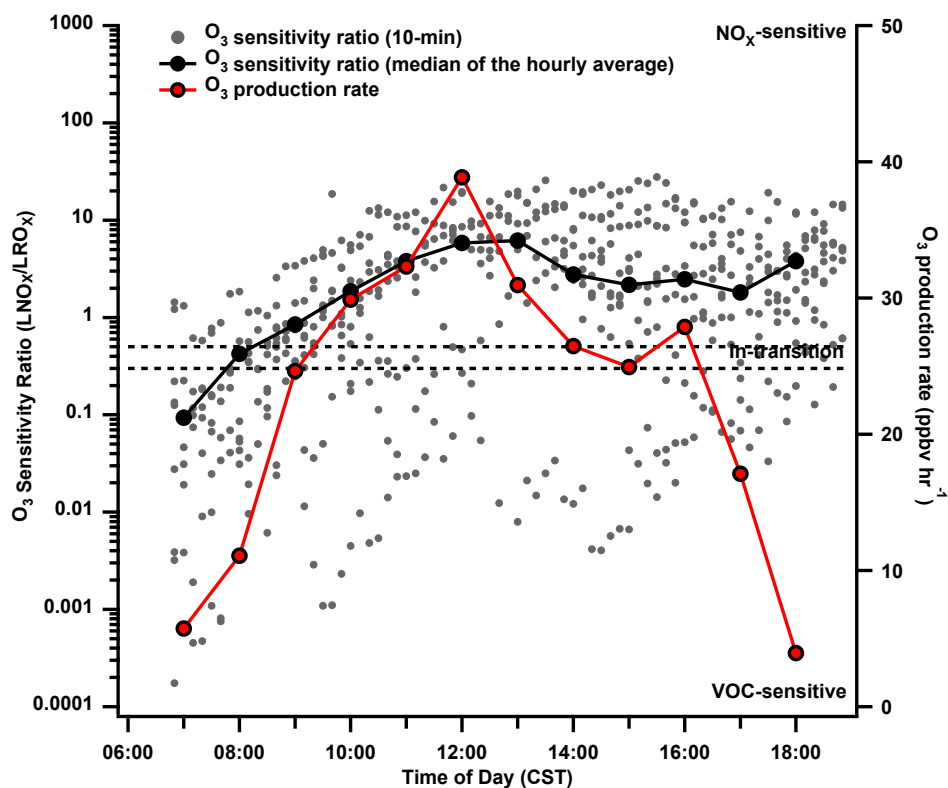


Figure 3.33: The 5-min (grey points) and median of the hourly average (black line with markers) daytime profiles of O_3 sensitivity ratio ($\text{LRO}_x/\text{LNO}_x$) on the left axis, and the modeled net ozone production rate ($P(\text{O}_3)$, red line with markers) on the right axis. The two horizontal dash lines on the left axis at values of 0.3 and 0.5 indicate the transition regime between NO_x - and VOC-sensitive regimes for SAFS 2017.

Comparing the diurnal patterns of ozone formation regime from SAFS 2021 to SAFS 2017, we discovered that even though the shift from VOC-sensitive to NO_x -sensitive regime both initiated around 9:00 CST, ozone formation remained in the transitional regime longer in 2021 (till 11:00 CST) than that in 2017 (till 10:00 CST). Moreover, the peak $P(\text{O}_3)$ was also delayed from noon (12:00–13:00 CST) in 2017 to early afternoon (13:00–15:00 CST) in 2021. As previously described in $F(\text{O}_3)$ and $D(\text{O}_3)$ paragraphs, average daytime ozone formation rate increased 45% (22.7 to 33.0 ppbv hr^{-1}) while ozone destruction rate remained unchanged from 2017 to 2021, which was also consistent with a nearly doubled peak $P(\text{O}_3)$ (33.0 to 63.0 ppbv hr^{-1}). The increase in ozone production rates could be explained by elevated precursors, since both NO_x and VOC concentrations elevated, while the photochemical condition of the ambient environment represented by jNO_2 remained similar. However, the more rapid ozone production does not necessarily translate into a higher ambient ozone concentration, since the measured O_3 level in 2021 was actually slightly lower than that of 2017, possibly due to a reduction in background regional ozone level.

3.7.3.4 Aerosol composition and chemistry

As shown in **Figure 3.34**, we observed higher loadings of non-refractory submicron aerosol during 2021 compared to 2017, including organics, sulfate, ammonium, nitrate, and chloride. After performing source apportionment, higher levels of primary and secondary organic aerosols were also observed in 2021 versus 2017 (**Figure 3.35**). No obvious changes in the diurnal patterns of the aerosol species were observed. Even though there was a prevalent increase, the overall mass concentration of each species was still at a moderate level.

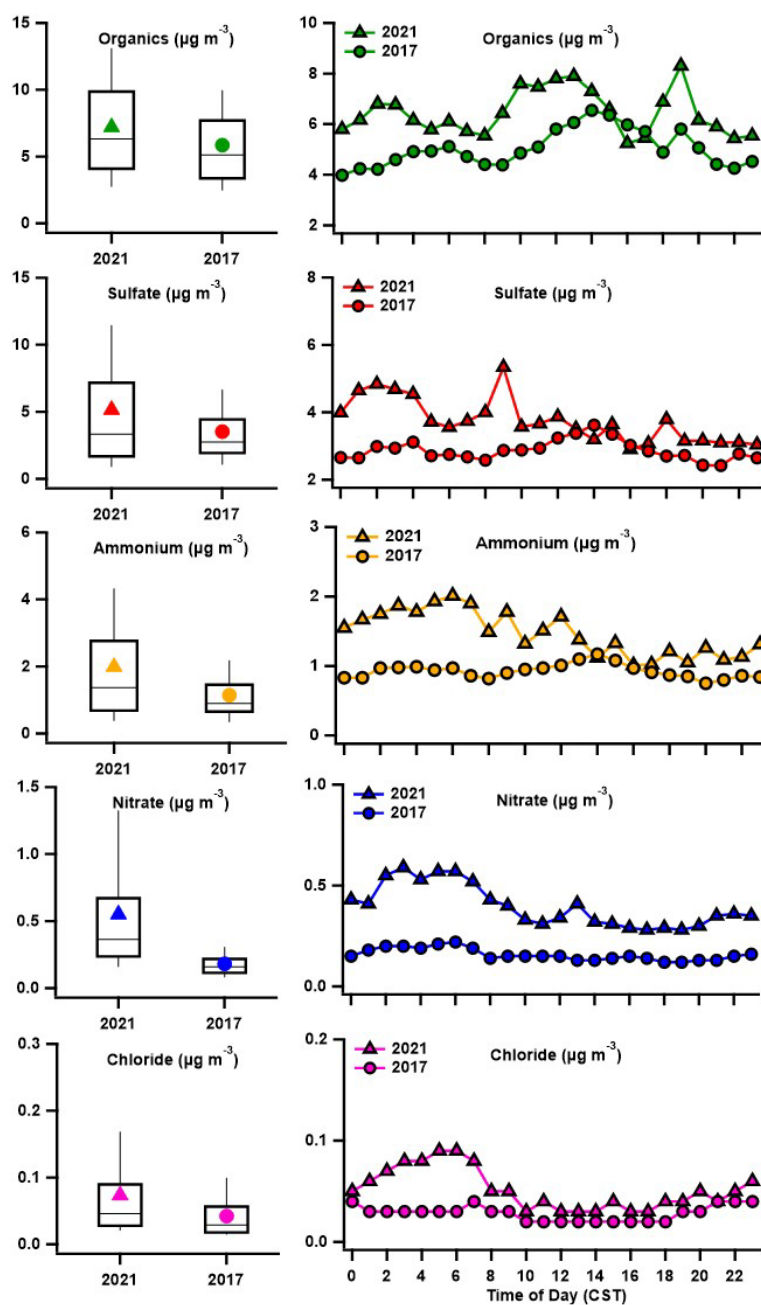


Figure 3.34: Box plots (left) and mean diurnal profiles (right) of aerosol species measured at the TW during SAFS 2021 and 2017 campaigns.

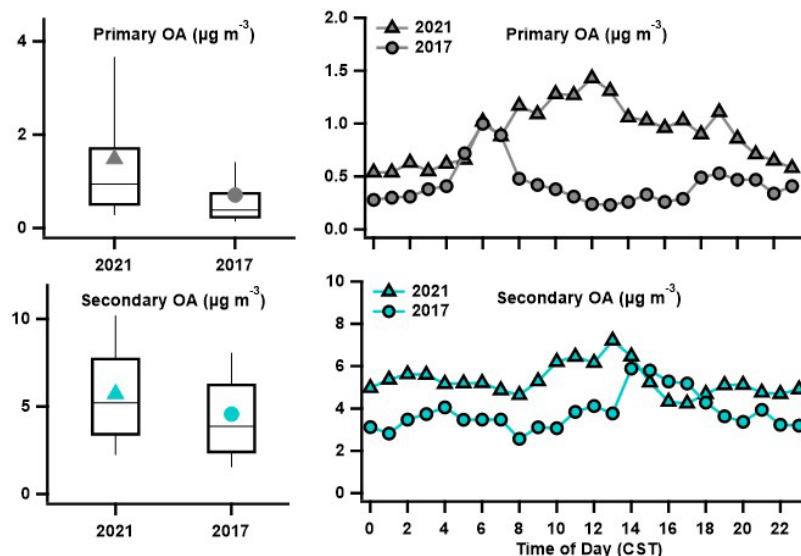


Figure 3.35: Box plots (left) and mean diurnal profiles (right) of primary and secondary organic aerosols at TW identified by PMF analysis during SAFS 2021 and 2017 campaigns.

3.8 Task 8: Spatial Distribution and Characterization of Air Pollutants (Ozone, Trace Gas, VOC, and Aerosols) from 2021 Field Study Observations

3.8.1 Summary and Key Findings

- This task was completed. We conducted the following analyses for examining spatial distributions and characterization of air pollutants. We characterized the spatial distribution of air pollutants by evaluating mobile and stationary measurements and comparing them to emission inventories. We examined mobile measurements of upwind, central, and downwind comparisons of ozone metrics and precursors, sources of VOC and aerosols, as well as aerosol chemical properties (e.g., composition, organic aerosol elemental ratio) and physical properties (e.g., size and optical scattering and absorption). Analysis of mobile measurements allowed for investigation of potential signatures of point sources, such as cement kilns, power plants, and other anthropogenic activities, in and upwind of the San Antonio area, utilizing VOC (e.g., isoprene, formaldehyde), trace gas (ozone, nitrogen oxide compounds, carbon monoxide, and sulfur dioxide), and aerosol composition (e.g., sulfate, nitrate, and organics) and optical measurements. The final data set was submitted to the TCEQ on April 15, 2023.
- Elevated ozone mixing ratios were observed downwind of urban San Antonio area on multiple mobile measurement passes.
- Applied SIBaR, a background extraction method, to the inorganic trace gas data to investigate emission hotspots.

- Observed periods of enhanced NO_x levels during multiple mobile days in the northeast of San Antonio close to cement kilns. It is challenging to conclude whether cement kilns have contributed and to what extent to the observed NO_x concentrations. We believe that a combination of wind direction, local vehicular emissions, and potential emissions from cement kilns might have posed complicated influences on the elevated NO_x levels in the area.
- Repeatedly enhanced NO_x levels were observed in southeast San Antonio downwind of the Calaveras Power Station in Bexar County. Our analysis indicates that the observed elevated NO_x levels were possibly associated with power plant emissions. There are also indications of SO₂ emissions downwind of the power plant.
- Observed higher NO_x concentrations downwind of the Eagle Ford Shale area on one of the mobile days in the region, indicating NO_x emissions associated with the anthropogenic activities in the Eagle Ford Shale area. It is inconclusive to relate CO emissions to the Eagle Ford Shale anthropogenic activities.

3.8.2 Methodology

3.8.2.1 Emission inventory

The 2021 Texas emissions inventory of CO, NO_x, and SO₂ from TCEQ were used.

3.8.2.2 State-Informed Background Removal (SIBaR) analysis

The State-Informed Background Removal (SIBaR) method developed by Actkinson et al. (2021) was used to systematically separate background versus non-background periods during the entire 2021 SAFS study, including both stationary and mobile measurement periods. Details on the method can be found in Actkinson et al. (2021). This method was applied to the high-resolution (30s) trace gas data, including CO, NO_x, SO₂, and speciated VOC data, which yielded a status wave indicating the classification of “background” versus “non-background” for each measured data point. We then evaluated the application of the classification determined from CO SIBaR to all other trace gases. We also did the SIBaR analysis of NO_x and the evaluation of applying NO_x SIBaR classification to other trace gases. We reconstructed the background concentrations of the trace gases by linear interpolation of levels during the SIBaR-identified-background periods.

3.8.3 Results

3.8.3.1 Inorganic trace gases

We observed spatial distributions of ozone on multiple passes during the mobile measurements. A few were associated with wind patterns. As shown in **Figure 3.36**, much-elevated ozone levels were observed in downwind areas of the San Antonio urban core on select days. In particular, high ozone levels exceeding 70 ppbv occurred in multiple regions in North San Antonio on April 25, whereas upwind near the urban core, ozone mixing ratios were lower by 30 ppbv. This may be related to the spatial distribution of background ozone, transport of ozone precursors, and the

spatial heterogeneity of ozone formation and destruction rates. Further analysis needs to be performed to evaluate the relative importance and contribution of various factors leading to the elevated ozone levels downwind.

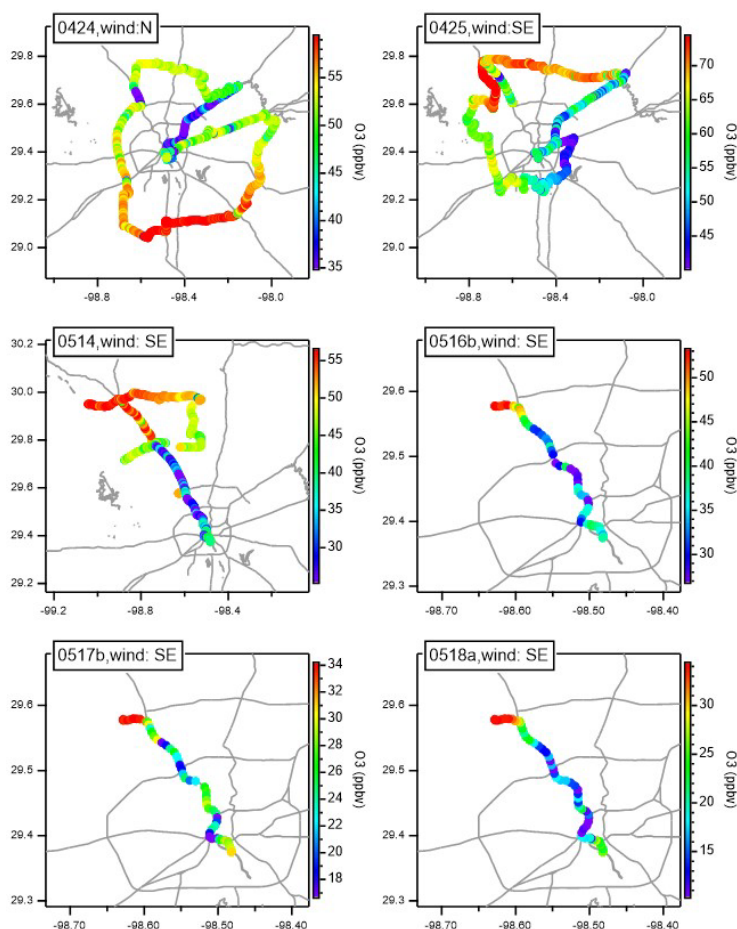


Figure 3.36: Mobile passes in the San Antonio area on select days colored by measured ozone mixing ratios.

In order to investigate potential signatures of point sources, such as cement kilns, power plants and other anthropogenic activities, in and upwind of the San Antonio areas, we performed SIBaR analysis to the primary inorganic trace gases including CO, NO_x, and SO₂. **Figure 3.37** showed that SIBaR successfully separated periods that should be classified as background versus non-background for the entire 2021 SAFS study period, including both the stationary and mobile measurement periods. The SIBaR results of NO_x were applied to all other nitrogen species (NO, NO₂, NO_y and NO_z) and appeared to work well.

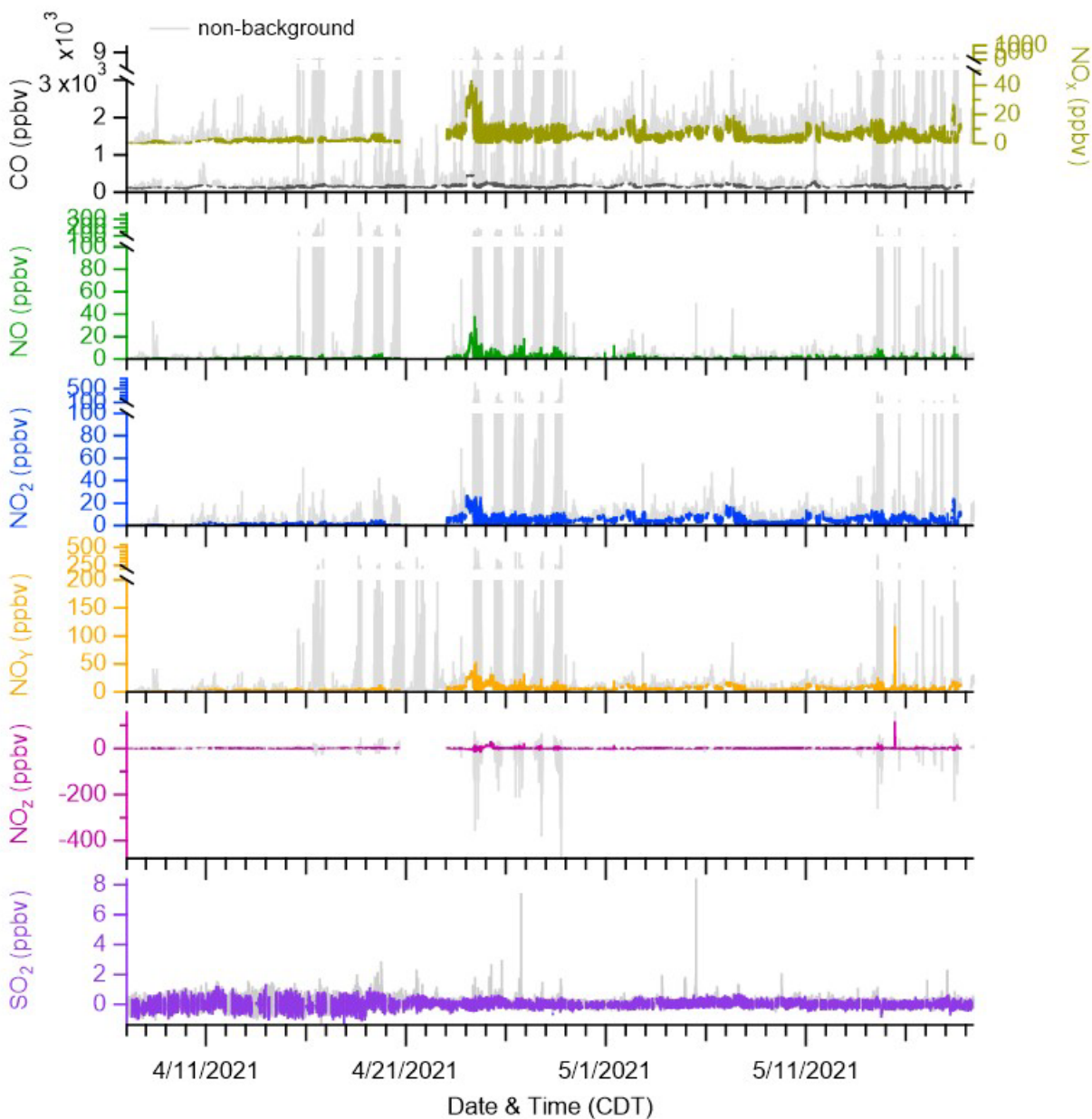


Figure 3.37: Time series of measured traces of gases during the 2021 SAFS study. The colored lines are the background periods identified by SIBaR analysis, whereas the gray lines are the non-background periods based on SIBaR results.

Based on the measured mixing ratios of the SIBaR-identified background periods, we performed linear interpolation of the background mixing ratios and obtained the interpolated background concentrations for the non-background periods. **Figure 3.38** shows the interpolated background mixing ratios of CO for the two select mobile days. The results showed that background CO levels were greatly elevated in the center of San Antonio relative to the city outskirts on April 24. Background CO levels in the center and suburban areas of San Antonio were much higher than those in the rural areas on April 27. Note that the interpolated background mixing ratios may span

a long period of time up to an hour and cover a relatively large area over miles depending on the observational data. Therefore, caution should be taken while interpreting the rainbow gradient of the interpolated background levels.

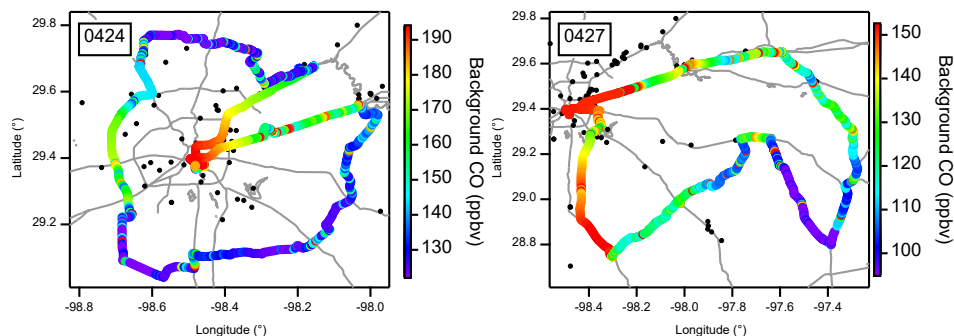


Figure 3.38: Mobile measurements of CO on select days in the San Antonio area.

Figure 3.39 show all passes ($N = 6$) we drove the mobile lab near the cement kilns in the northeast San Antonio area. The mobile trajectories are colored by four matrices of NO_x concentrations, which is a major primary pollutant emitted from cement kilns based on Texas 2021 emission inventories (also shown in the figure): a) the observed NO_x during the entire period, b) the observed NO_x during background periods identified by SIBaR analysis, c) the linear-interpolated background NO_x concentration during the entire period, and d) the background-corrected concentration during the non-background period identified by SIBaR analysis (observed NO_x minus interpolated background NO_x). Results show that concentration hotspots of NO_x were observed at multiple places along the trajectories, and identified as non-background periods. Spatial heterogeneity was observed during some passes. However, when taking into account the dominant wind direction, elevated NO_x concentrations did not always occur downwind of the cement kilns. For example, the dominant wind was from the north on April 24. On this day, the pass downwind (south) of the cement kilns had elevated NO_x concentrations than the upwind pass (north of the cement kilns). However, on April 25, the dominant wind was the opposite and from the southeast. Similarly higher NO_x concentrations were observed along the pass south of the cement kilns compared to the north side. Note that the south pass on both days was Interstate-35, a very busy highway, whereas the north passes were local roads. These results suggest that vehicular emissions likely greatly influenced the observed NO_x mixing ratios in the region. Similarly on the other days, NO_x concentrations did not always show elevated mixing ratios downwind of cement kilns. We believe that wind direction, vehicular emissions in close proximity, together with the potential direct emissions from the cement kilns might have all played a role in the observed NO_x concentrations and it is inconclusive to say if we identified point sources signatures from cement kilns in the SE San Antonio region.

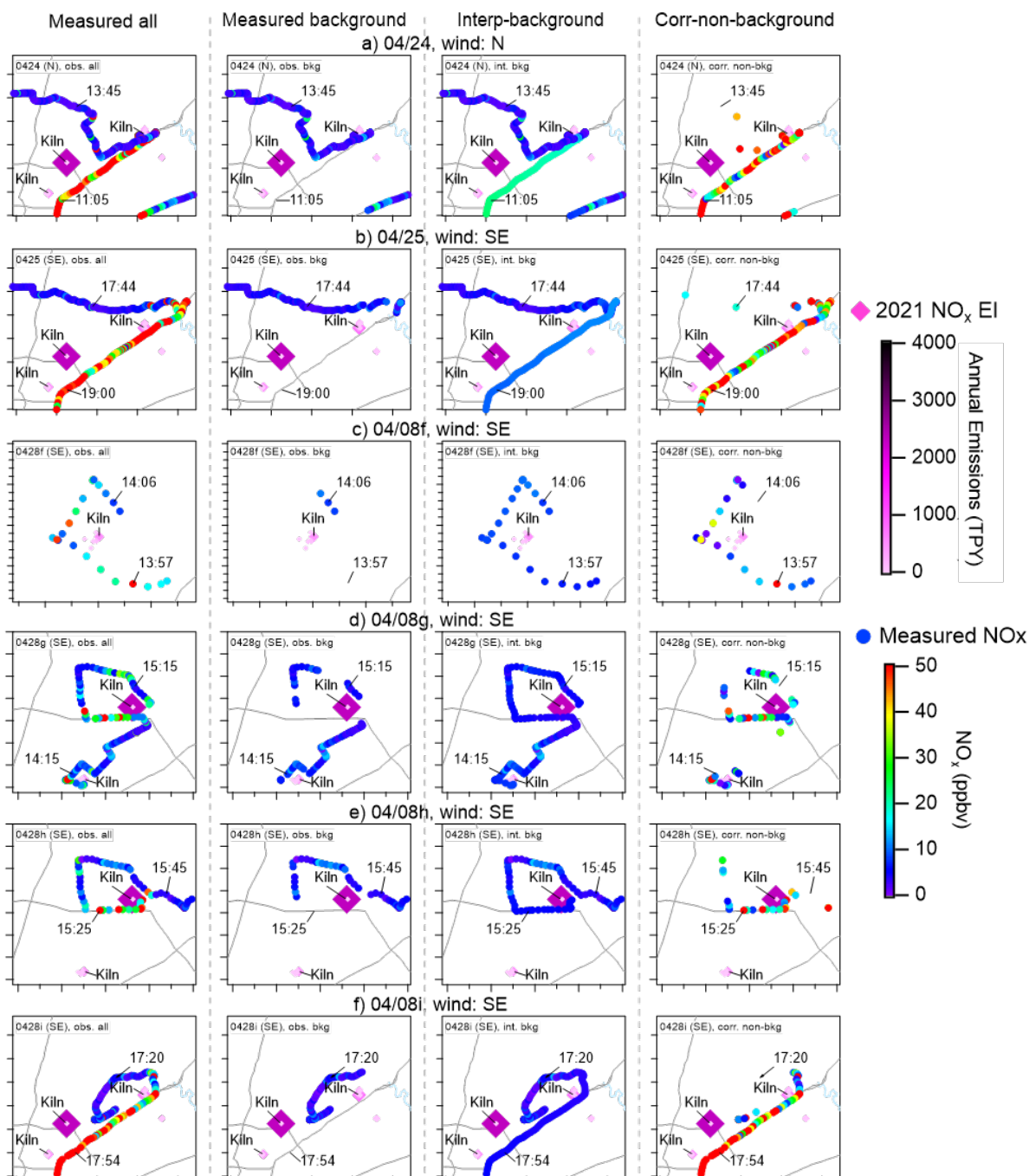


Figure 3.39: Map of the NE San Antonio area with six mobile measurement passes (a-f) colored by four metrics of NO_x concentrations: the observed NO_x (the first column on the left), the observed NO_x during the background periods identified by SIBaR analysis (the second column), c) the linear-interpolated background NO_x concentration during the entire period (the third column), and d) the background-corrected concentration during the non-background period identified by SIBaR analysis (the fourth column). The dominant wind during the drive is noted in the text. The Dimon markers indicate the NO_x point sources colored by the annual emissions of NO_x in unit of ton per year (TPY) in 2021.

We also examined NO_x concentrations in the southeast area of San Antonio near the Calaveras power station during mobile measurement periods. Analysis results indicate that we may have observed direct influences from power plant emissions on the observed NO_x concentrations during mobile measurement near the area. **Figure 3.40** shows all mobile passes (N = 5) in close proximity to the plant. We saw repeatedly elevated NO_x concentrations downwind of the power plant for extended periods of time (areas) when driving on local roads between Highway 87 and 181. SIBaR analysis also identified these data (circled in **Figure 3.40**) and classified them as non-background periods. The NO_x concentration hotspots appeared every time we passed by the power plant, despite slightly varied locations possibly associated with changing winds. These results indicate that we might have sampled the NO_x under the influence of power plant emissions.

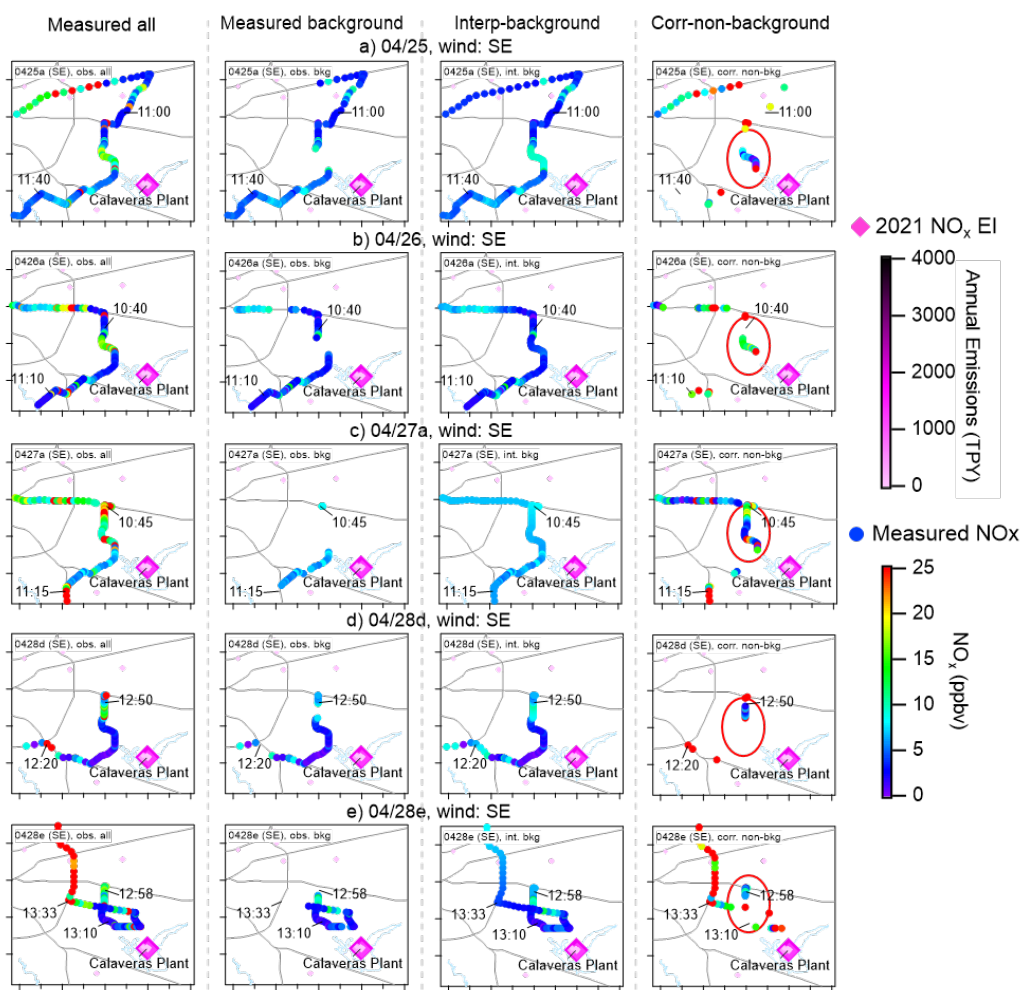


Figure 3.40: Map of the southeast San Antonio area near the Calaveras Power Station with five mobile measurement passes (a-e) colored by four metrics of NO_x concentrations: the observed NO_x (the first column on the left), the observed NO_x during the background periods identified by SIBaR analysis (the second column), c) the linear-interpolated background NO_x concentration during the entire period (the third column), and d) the background-corrected concentration during the non-background period identified by SIBaR analysis (the fourth column). The dominant wind during the drive is noted in the text. The Dimon markers indicate the NO_x point sources colored by the annual emissions of NO_x in units of tons per year (TPY) in 2021.

Power plants can also be important point sources of SO₂. In this study, we also saw indications of elevated SO₂ concentrations downwind of the Calaveras Power Station during most driving passes of the mobile measurements. As shown in **Figure 3.41**, five mobile passes were made near the Calaveras Power Station on various days. SIBaR analysis identified non-background periods (the fourth column) while sampling on the local road segments downwind of the Calaveras power plant for four out of the five passes. On April 25, SO₂ mixing ratios showed a clear concentration hotspot of up to 1 ppbv downwind of the power plant. However, SO₂ levels were noisy and generally below 0.3 ppbv for the majority of the mobile observational periods, caution should be taken while interpreting the data.

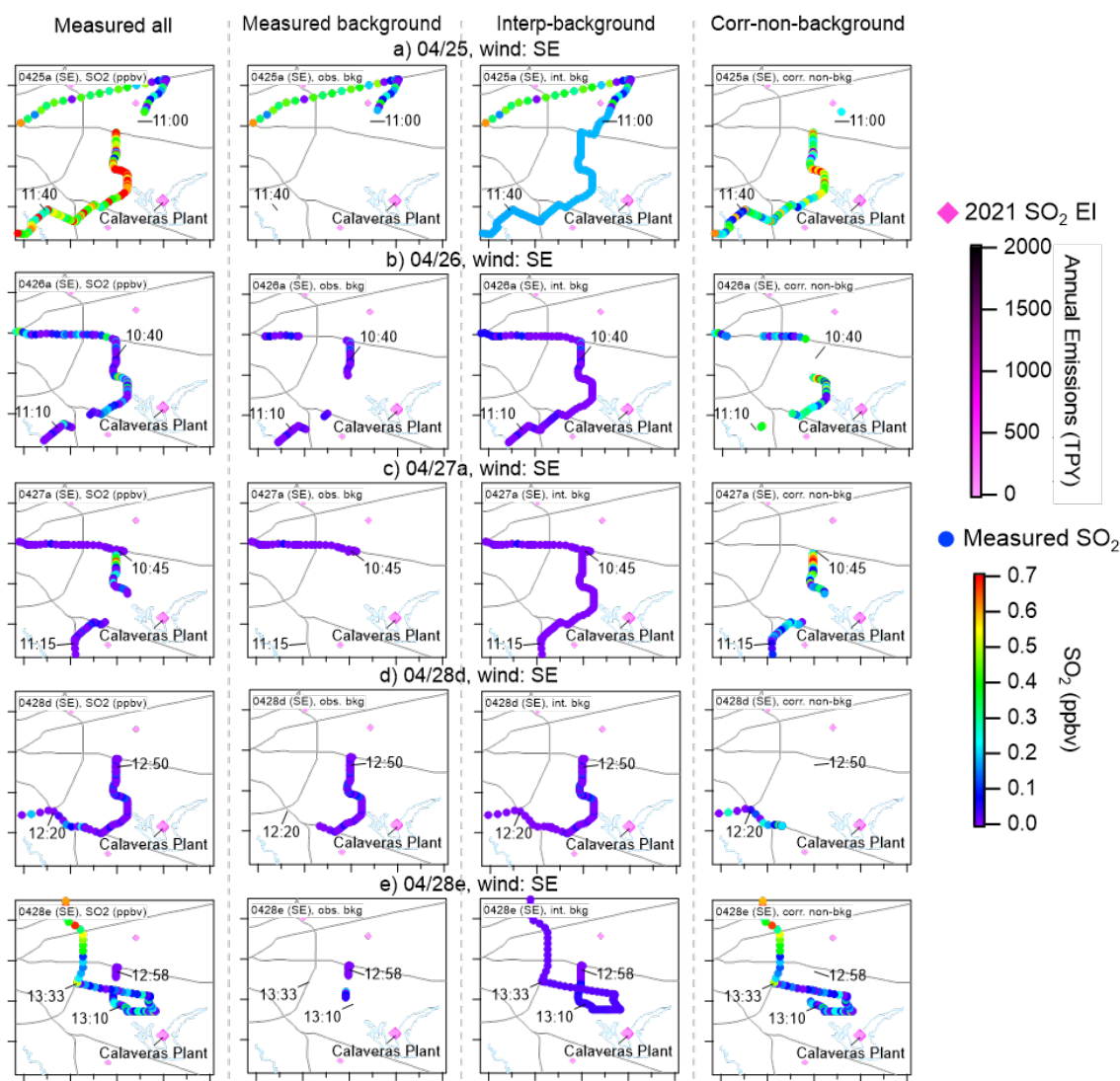


Figure 3.41: Map of the southeast San Antonio area near the Calaveras Power Station with five mobile measurement passes (a-e) colored by four metrics of SO₂ concentrations: the observed SO₂ (the first column on the left), the observed SO₂ during the background periods identified by SIBaR analysis (the second column), c) the linear-interpolated background SO₂ concentration during the entire period (the third column), and d) the background-corrected concentration during the non-background period identified by SIBaR analysis (the fourth column). The dominant wind during the drive is noted in the text.

The Dimon markers indicate the SO_2 point sources colored by the annual emissions of SO_2 in units of tons per year (TPY) in 2021.

The other anthropogenic emission sources we investigated were NO_x and CO emissions from the Eagle Ford Shale area to the southeast of San Antonio and northwest of Corpus Christi. On April 26, we made a circle around the eagle ford shale area. As shown in **Figure 3.42**, the southeast leg can be viewed as upwind, whereas the northwest leg can be considered downwind since the prevailing wind was from the SE. Note that both legs were on local roads. Vehicular emissions of NO_x in small towns along the driving routes have led to episodically high NO_x levels. SIBaR analysis successfully identified these plumes. Considering the background periods identified by SIBaR analysis on these two parallel legs, the observed NO_x mixing ratios were on average 1.7 (± 3.6) ppbv and 3.5 (± 5.4) ppbv for the upwind and downwind leg, respectively. NO_x levels also appeared to be higher in the rural sectors upwind compared to those downwind. These observations indicate that anthropogenic emissions from the Eagle Ford Shale likely contributed to increased NO_x concentrations in the rural areas downwind. Note that this was just from one mobile drive. More sampling data are needed to draw any conclusions.

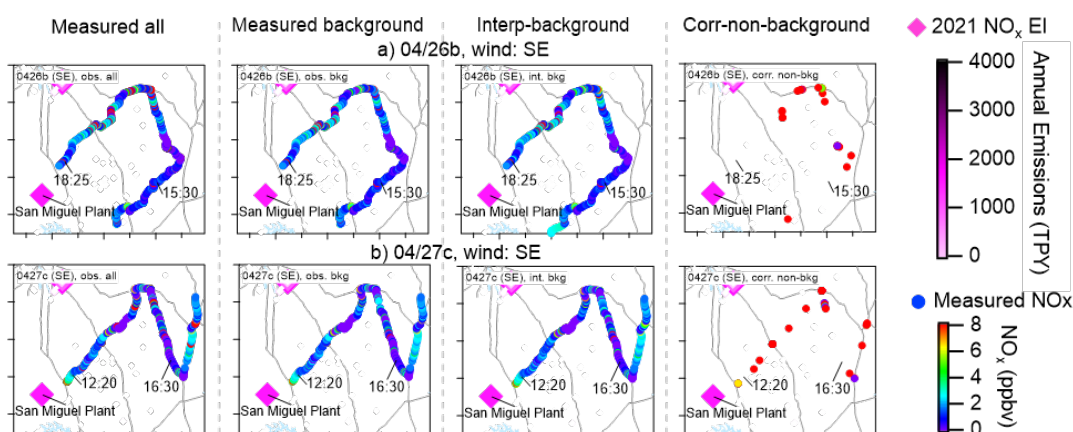


Figure 3.42: Map of the Eagle Ford Shale area with two mobile measurement passes (a-b) colored by four metrics of NO_x concentrations: the observed NO_x for the entire periods (the first column on the left), the observed NO_x during the background periods identified by SIBaR analysis (the second column), c) the linear-interpolated background NO_x concentration during the entire period (the third column), and d) the background-corrected concentration during the non-background period identified by SIBaR analysis (the fourth column). The dominant wind during the drive is noted in the text. The Dimon markers indicate the NO_x point sources colored by the annual emissions of NO_x in units of tons per year (TPY) in 2021.

Observed CO mixing ratios near the Eagle Ford Shale area during three mobile passes are shown in **Figure 3.43**. CO sampled within the Eagle Ford Shale region on April 25 appeared to be much higher than those sampled around (April 26 and 27). However, CO on the same route on the east leg of April 26 and 27 showed quite different CO levels. This indicates that there were great day-to-day variabilities in CO mixing ratios in the area. In addition, CO concentrations along the upwind and downwind legs on the same day (April 26) seemed to be rather comparable. Given the limited mobile data, it is challenging to conclude if anthropogenic emissions in the Eagle Ford Shale area contributed to elevated CO in the region.

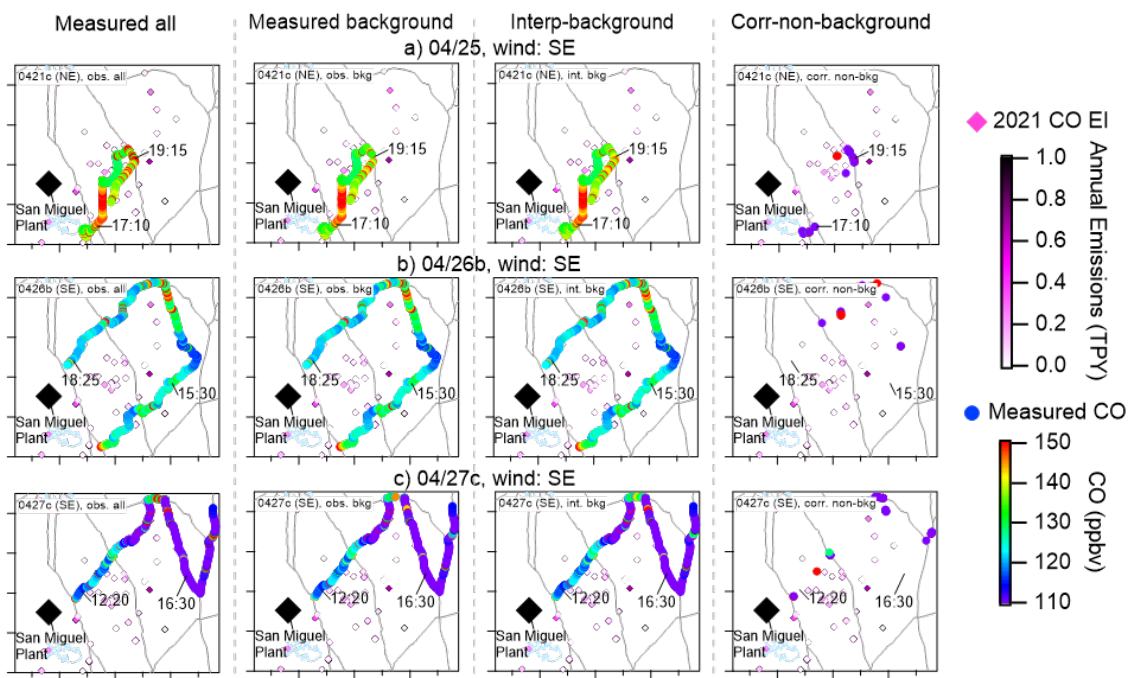


Figure 3.43: Map of the Eagle Ford Shale area with three mobile measurement passes (a-b) colored by four metrics of CO concentrations: the observed CO for the entire periods (the first column on the left), the observed CO during the background periods identified by SIBaR analysis (the second column), c) the linear-interpolated background CO concentration during the entire period (the third column), and d) the background-corrected concentration during the non-background period identified by SIBaR analysis (the fourth column). The dominant wind during the drive is noted in the text. The Dimon markers indicate the CO point sources colored by the annual emissions of CO in units of tons per year (TPY) in 2021.

3.8.3.2 VOCs

MAQL mobile times and locations are presented for select days in **Figure 3.44** to **Figure 3.48**.

Mobile PTR-MS VOC observations are presented for select days and for select VOCs in **Figure 3.49** to **Figure 3.76**.

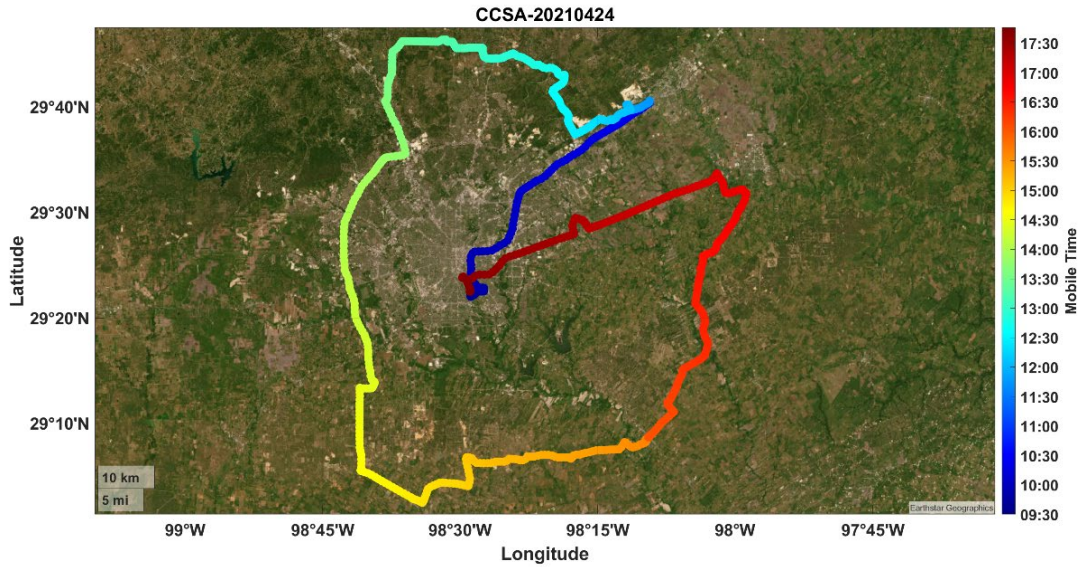


Figure 3.44: Mobile time and locations for CCSA mobile track measurements in San Antonio on April 24, 2021

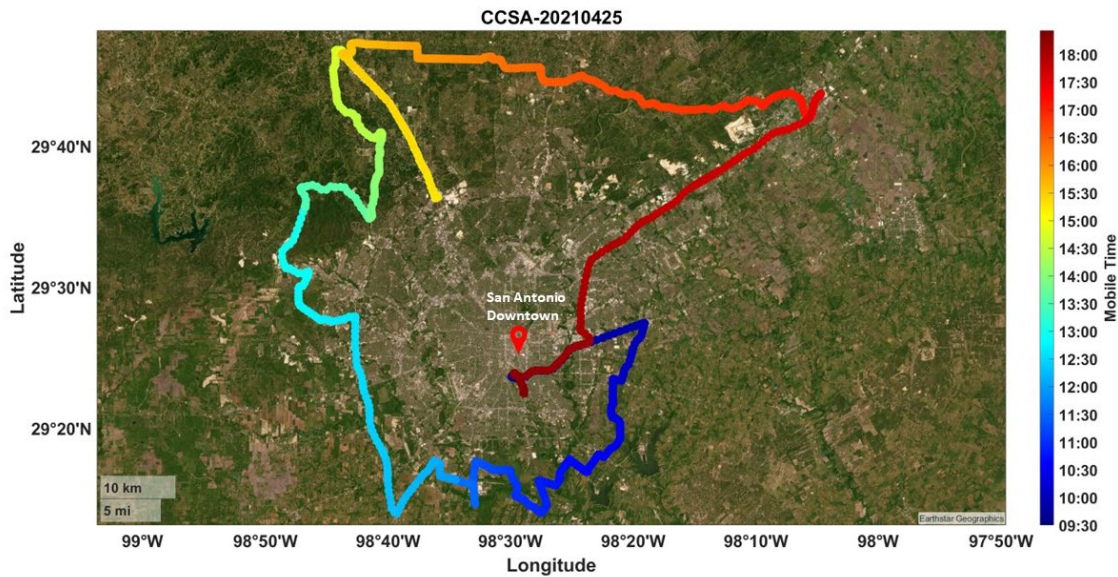


Figure 3.45: Mobile time and locations for CCSA mobile track measurements in San Antonio on April 25, 2021

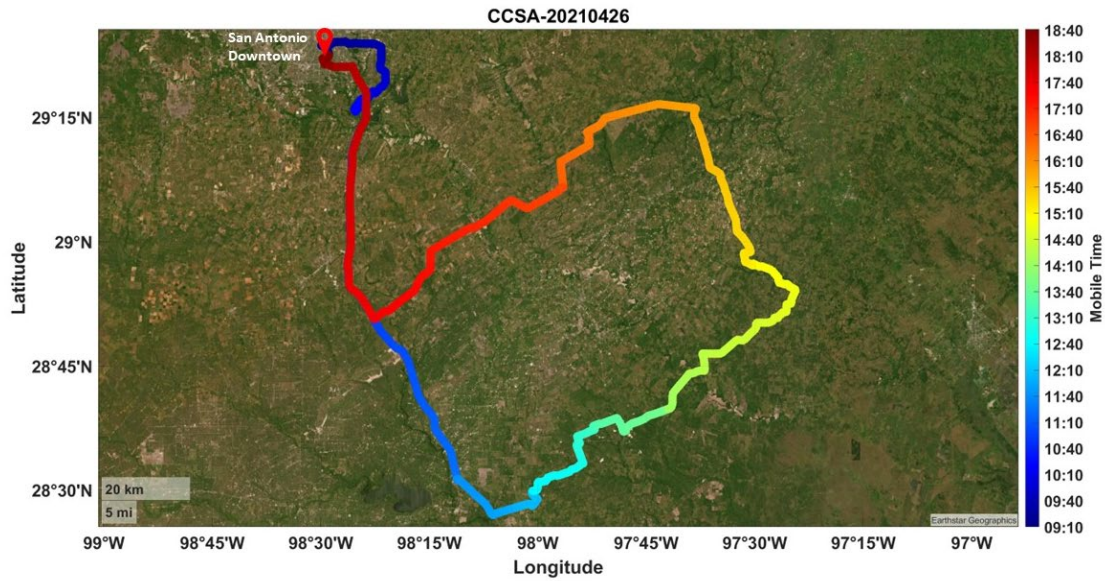


Figure 3.46: Mobile time and locations for CCSA mobile track measurements in San Antonio on April 26, 2021

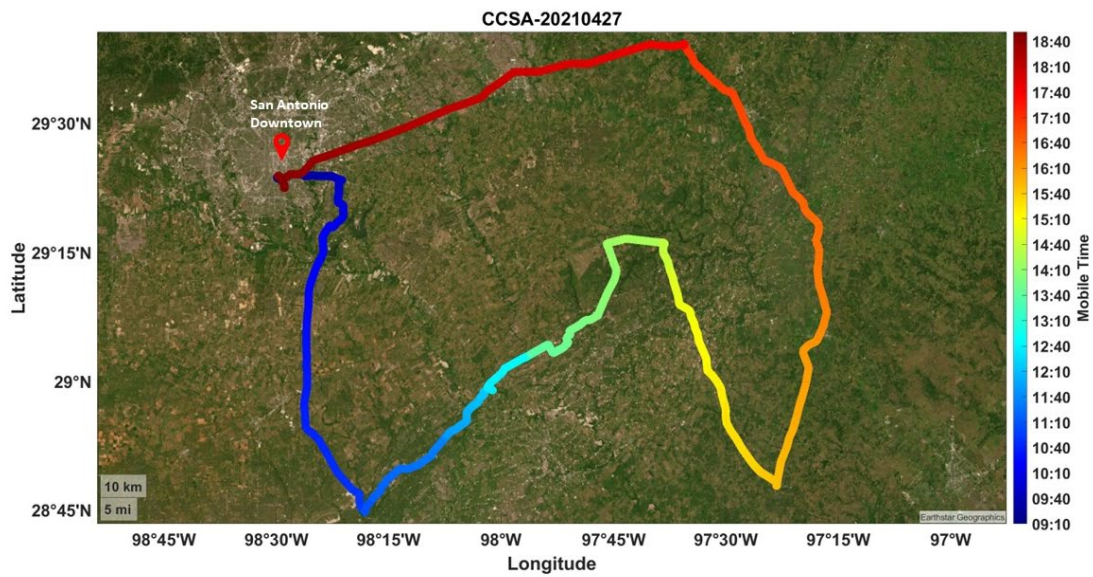


Figure 3.47: Mobile time and locations for CCSA mobile track measurements in San Antonio on April 27, 2021

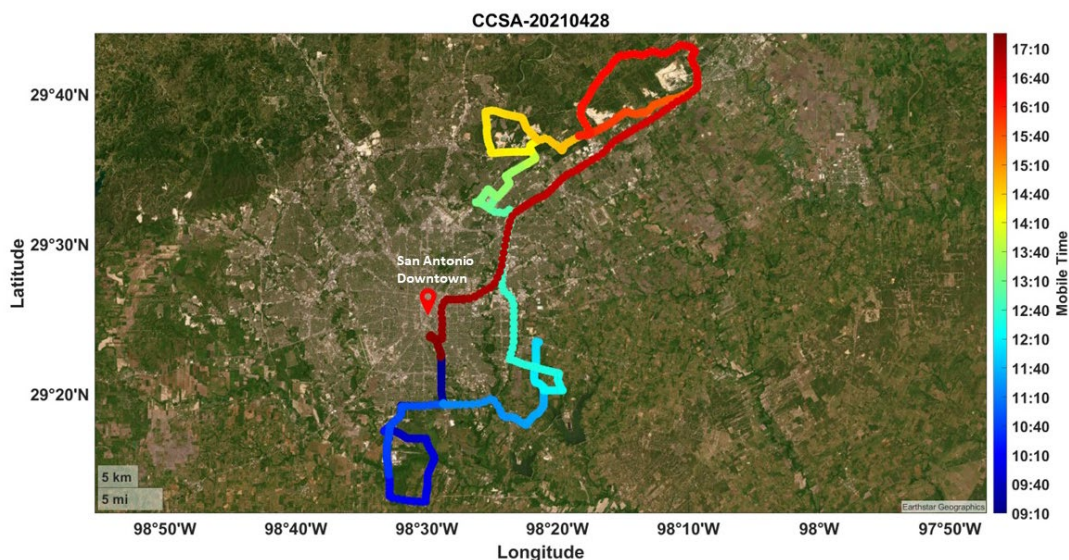


Figure 3.48: Mobile time and locations for CCSA mobile track measurements in San Antonio on April 28, 2021

Mobile PTR-MS VOC observations are presented for select days and for select VOCs. The select VOCs were measured throughout the SAFS campaign with concentrations in the low ppbv range.

- Ambient isoprene concentrations for the April 24, 2021 mobile time series demonstrate a relatively classic emission profile with lower concentrations in the morning and evening and increase during the midday peaking at 3.0 to 3.5 ppbv. This diurnal isoprene profile corresponds to increases in temperature and solar radiation, which also peak during midday. However, over the course of the afternoon, isoprene concentrations decrease periodically to ~1.5 ppbv. This decrease in ambient concentrations over the course of the days (i.e. time series) may be driven by changes in photochemistry or solar radiation (e.g., cloud cover). This BVOC example highlights the challenges of interrupting times series VOC data and the importance of additional measurements (intensity of radiant energy) and the consideration of the time of observation.
- Benzene and toluene mobile times series were relatively similar peaking during times and in areas typically associated with traffic (i.e. urban areas).
- April 26 and 27, 2021 represented mobile times series with significant periods of rural observations. During short periods of these rural maneuvers, xylene increased from ~0.75 ppbv to over 2 ppbv. The increase occurred at different locations but relatively similar times (i.e. 15:00).
- Acetone mobile times series for April 28, 2021 observed ambient concentrations ranging from 2.5 to 7 ppbv. Ambient concentrations above 6 ppbv were located in the NE just north of I-35. The dominant wind direction was SE, which, with emission inventories, may help identify a specific emission source.

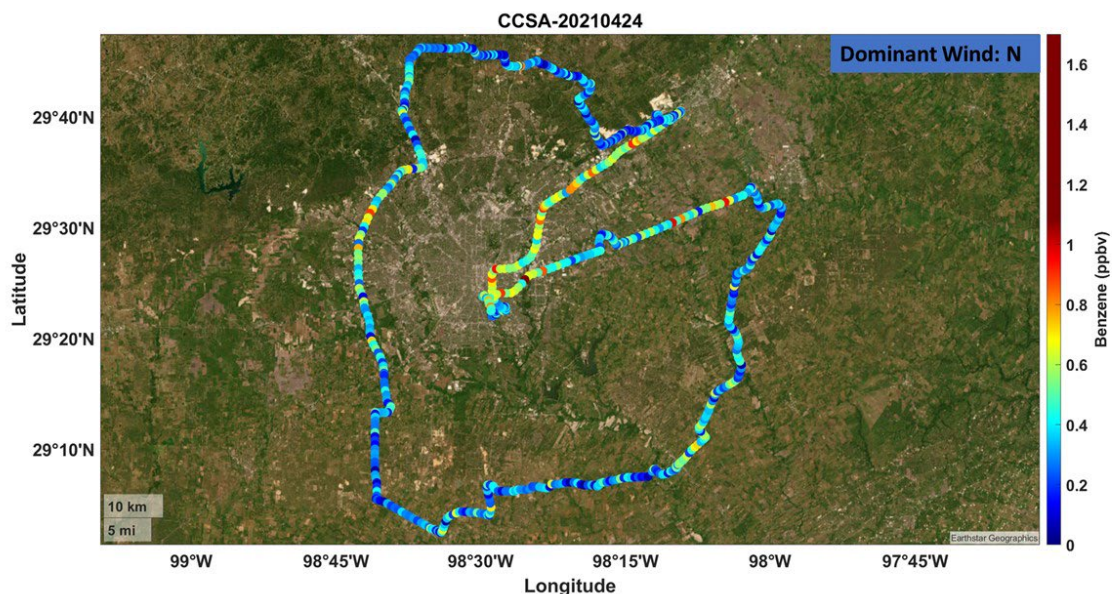


Figure 3.49: Mobile time series of benzene mass concentrations (ppbv) at m/z 79 resulting from CCSA mobile track measurements in San Antonio on April 24, 2021.

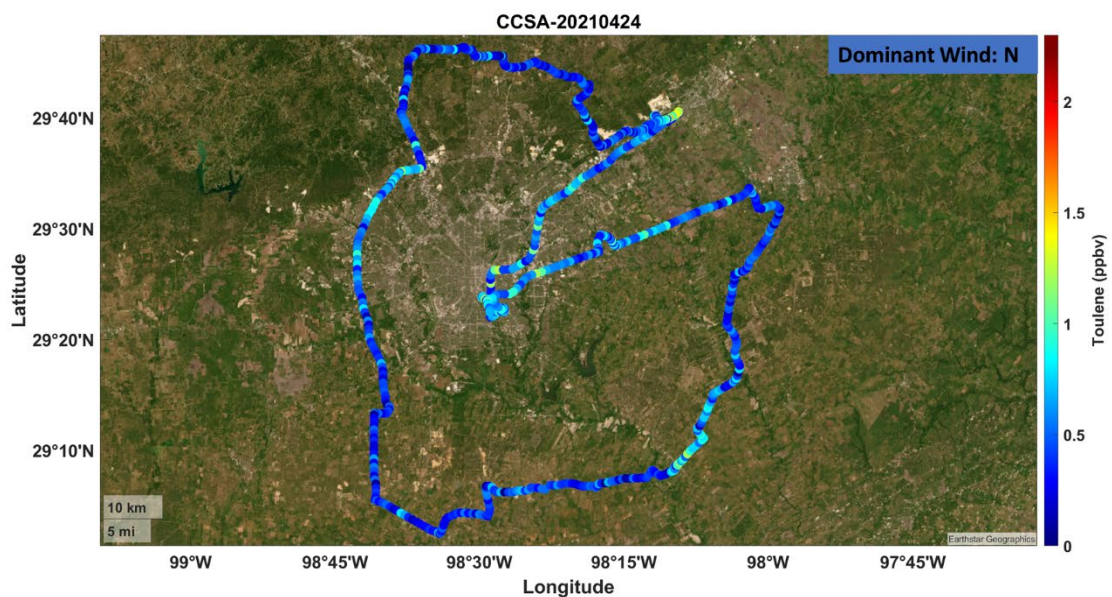


Figure 3.50: Mobile time series of toluene mass concentrations (ppbv) at m/z 93 resulting from CCSA mobile track measurements in San Antonio on April 24, 2021.

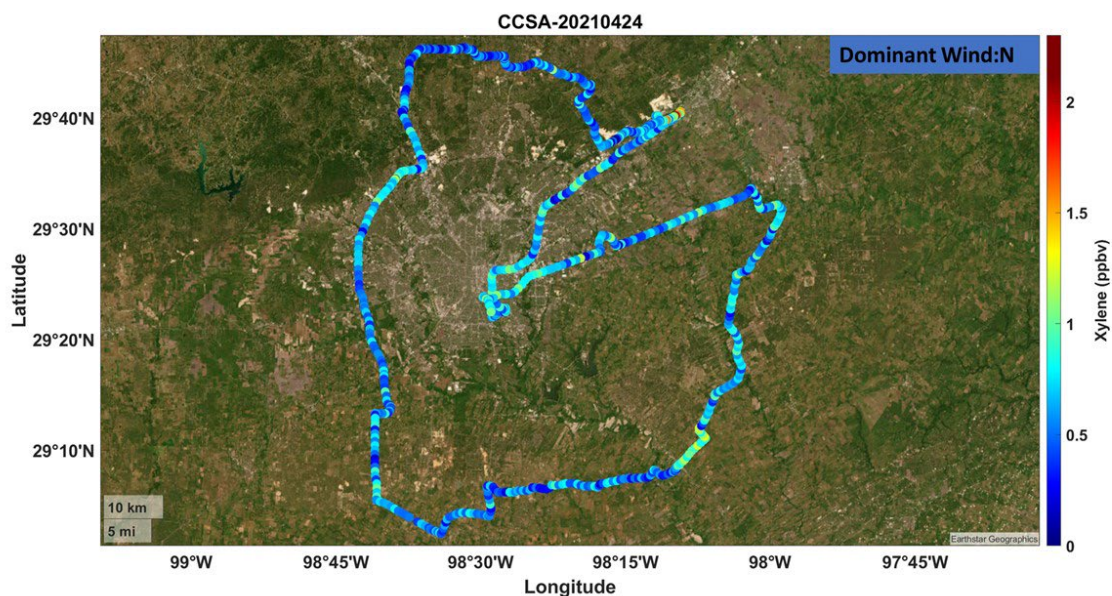


Figure 3.51. Mobile time series of xylene mass concentrations (ppbv) at m/z 107 resulting from CCSA mobile track measurements in San Antonio on April 24, 2021.

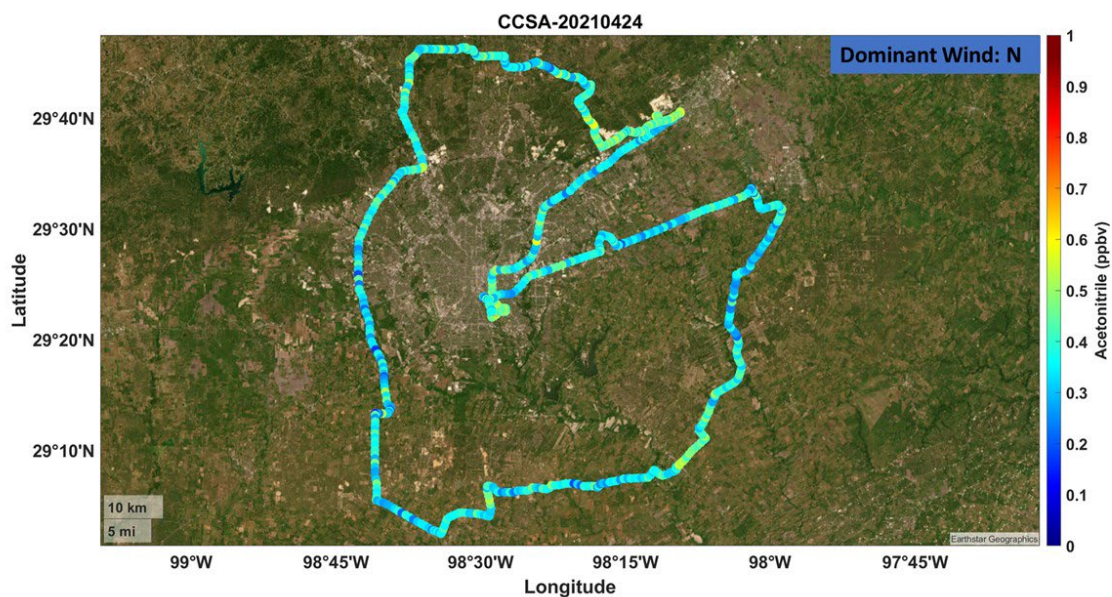


Figure 3.52. Mobile time series of acetonitrile mass concentrations (ppbv) at m/z 42 resulting from CCSA mobile track measurements in San Antonio on April 24, 2021.

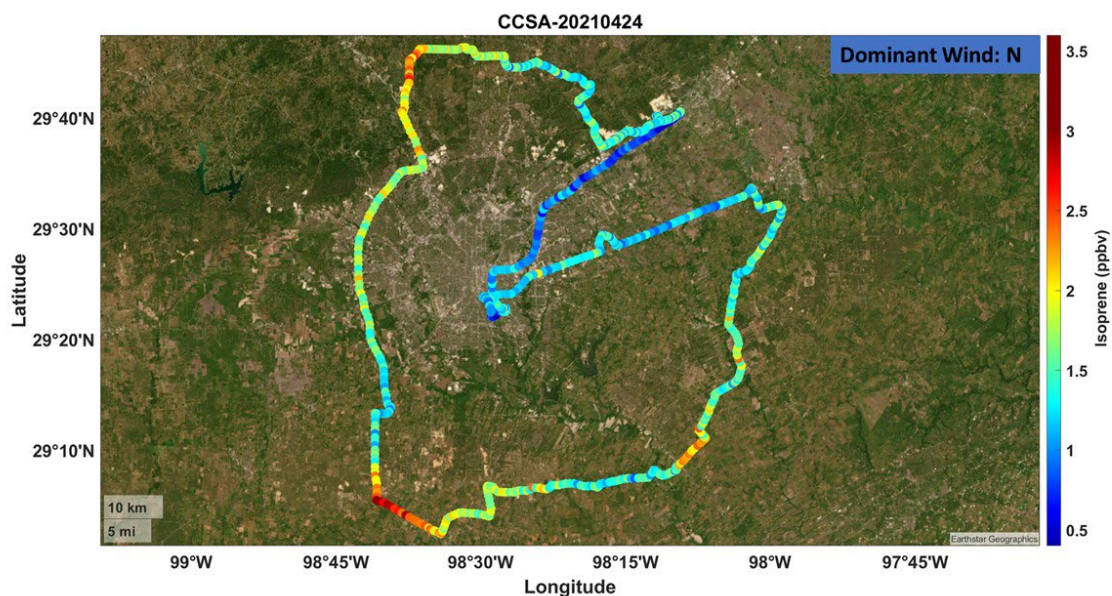


Figure 3.53. Mobile time series of isoprene mass concentrations (ppbv) at m/z 69 resulting from CCSA mobile track measurements in San Antonio on April 24, 2021.

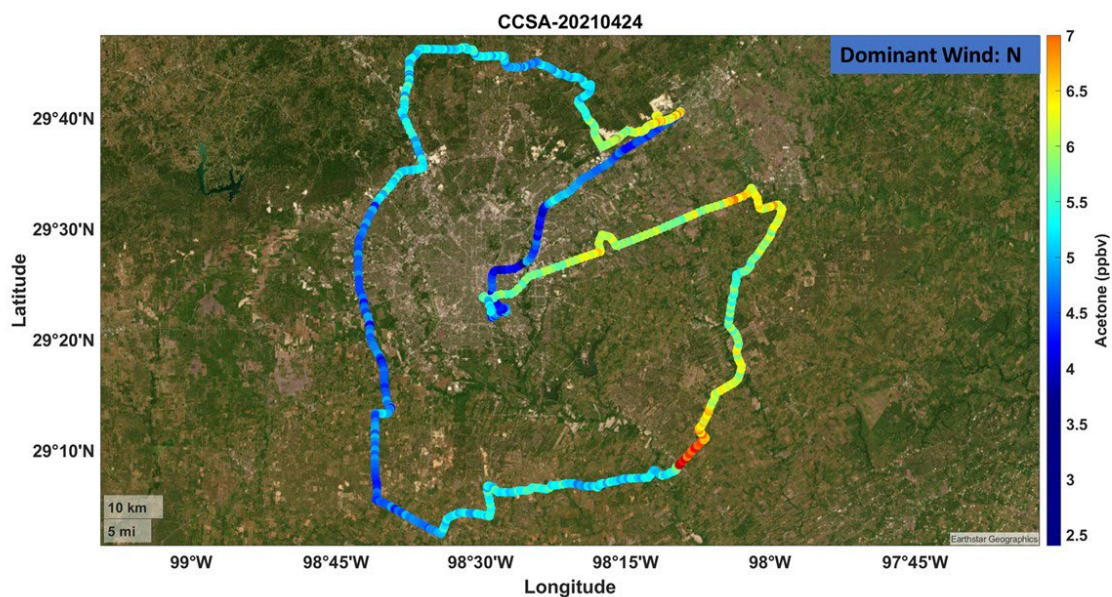


Figure 3.54. Mobile time series of acetone mass concentrations (ppbv) at m/z 59 resulting from CCSA mobile track measurements in San Antonio on April 24, 2021.

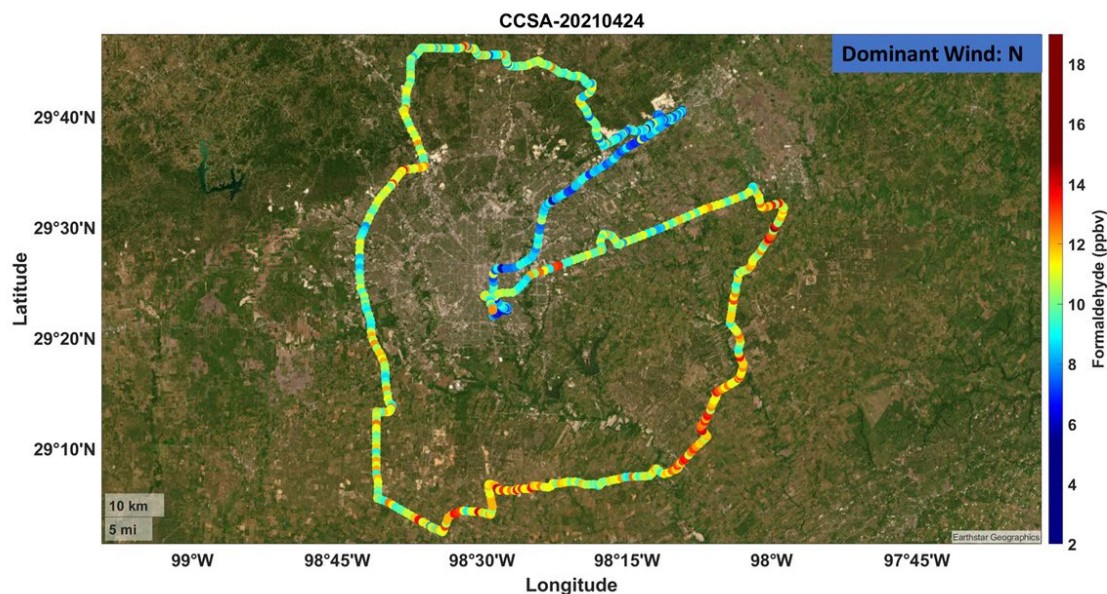


Figure 3.55. Mobile time series of formaldehyde mass concentrations (ppbv) at m/z 31 resulting from CCSA mobile track measurements in San Antonio on April 24, 2021.

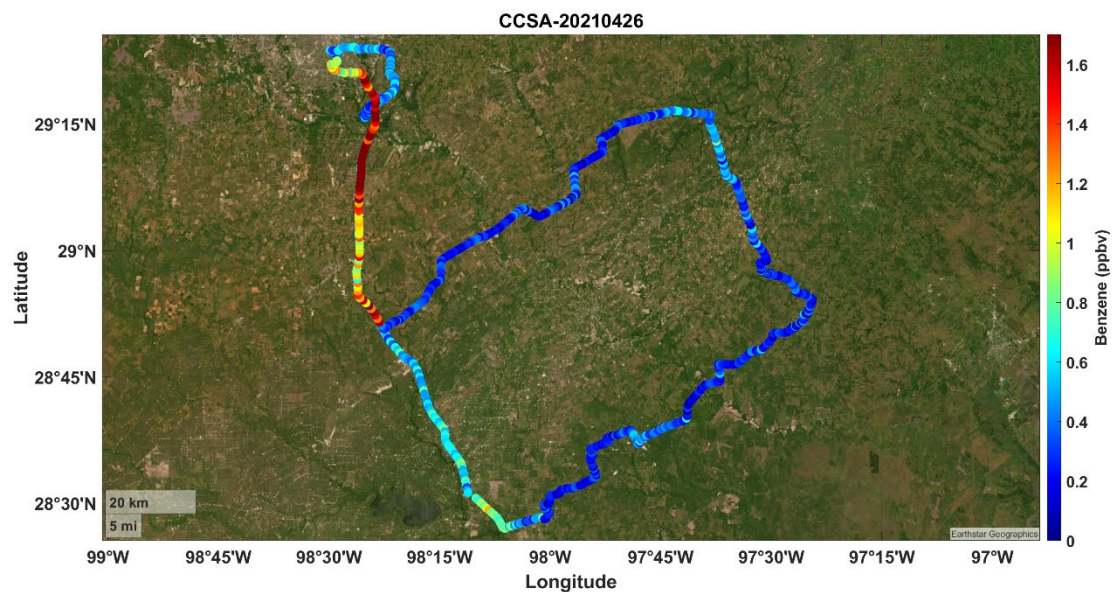


Figure 3.56. Mobile time series of benzene mass concentrations (ppbv) at m/z 79 resulting from CCSA mobile track measurements in San Antonio on April 26, 2021.

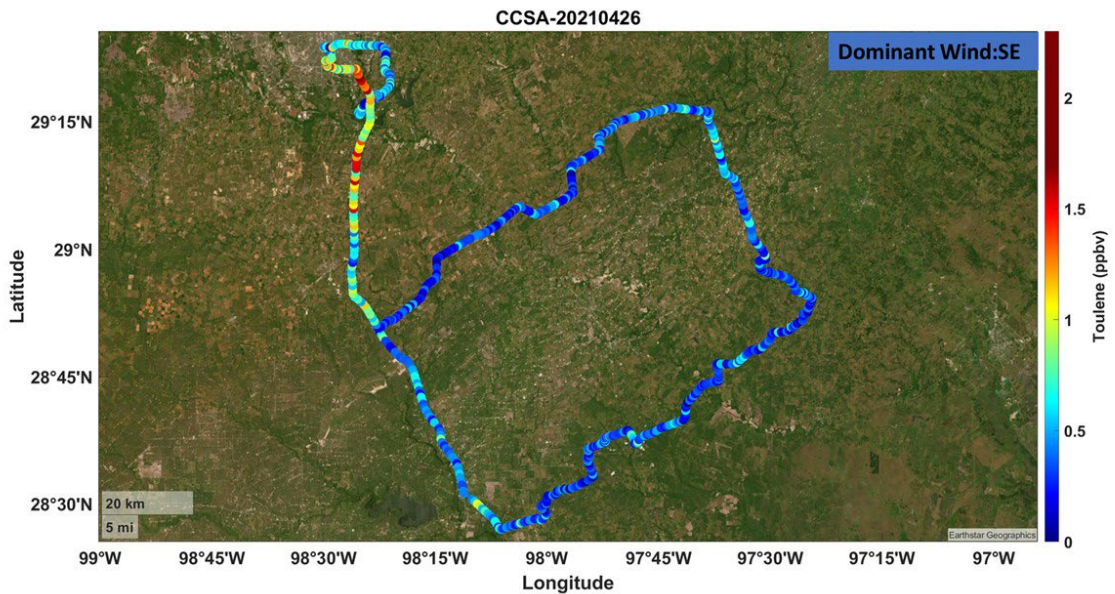


Figure 3.57. Mobile time series of toluene mass concentrations (ppbv) at m/z 93 resulting from CCSA mobile track measurements in San Antonio on April 26, 2021.

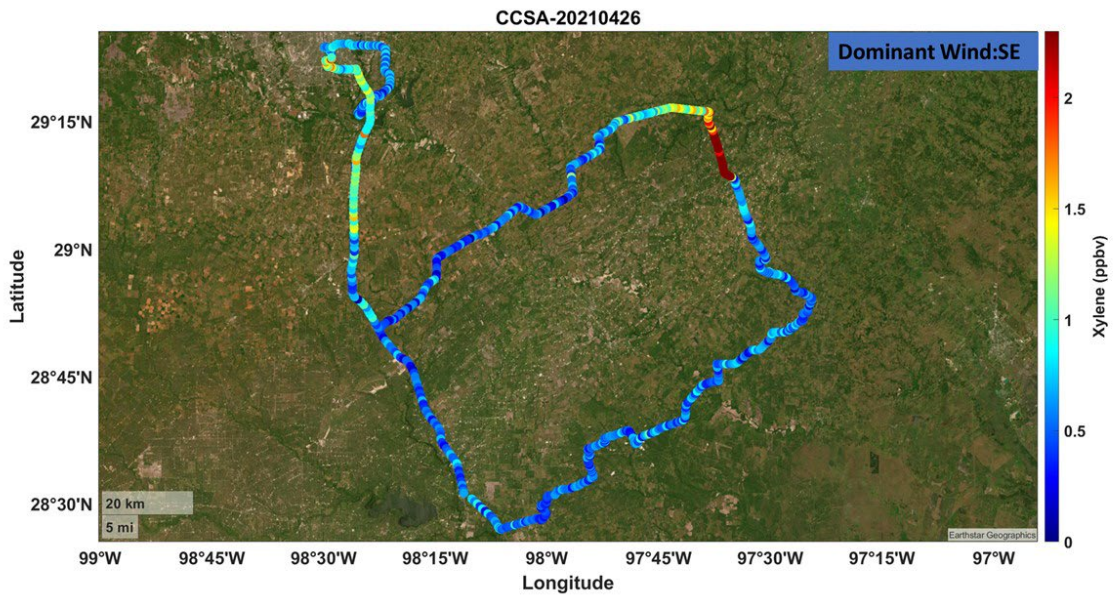


Figure 3.58. Mobile time series of xylene mass concentrations (ppbv) at m/z 107 resulting from CCSA mobile track measurements in San Antonio on April 26, 2021.

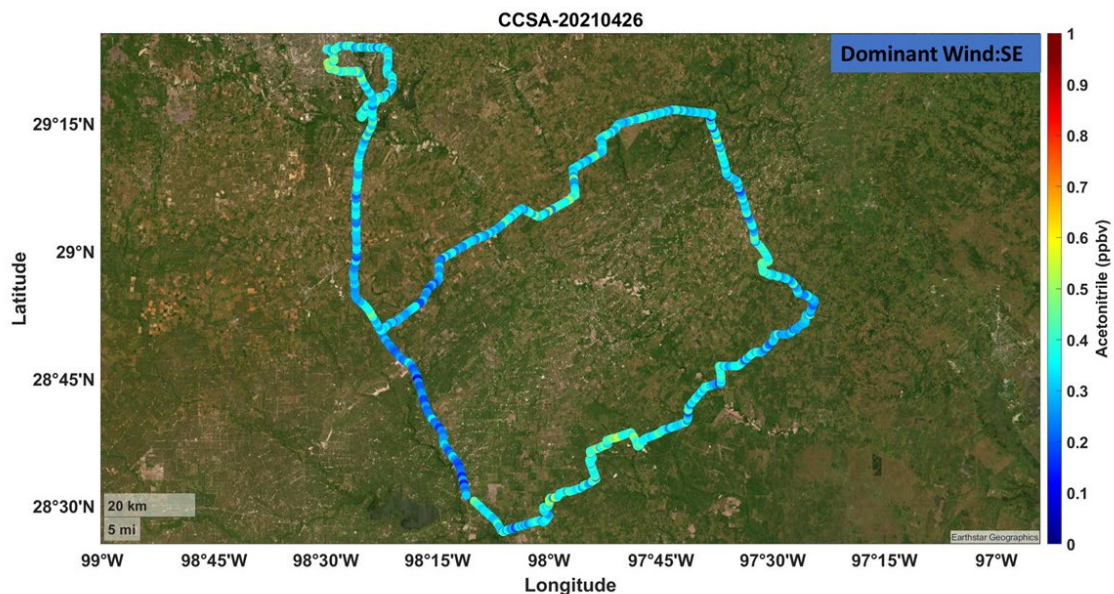


Figure 3.59. Mobile time series of acetonitrile mass concentrations (ppbv) at m/z 42 resulting from CCSA mobile track measurements in San Antonio on April 26, 2021.



Figure 3.60. Mobile time series of isoprene mass concentrations (ppbv) at m/z 69 resulting from CCSA mobile track measurements in San Antonio on April 26, 2021.



Figure 3.61. Mobile time series of formaldehyde mass concentrations (ppbv) at m/z 31 resulting from CCSA mobile track measurements in San Antonio on April 26, 2021.

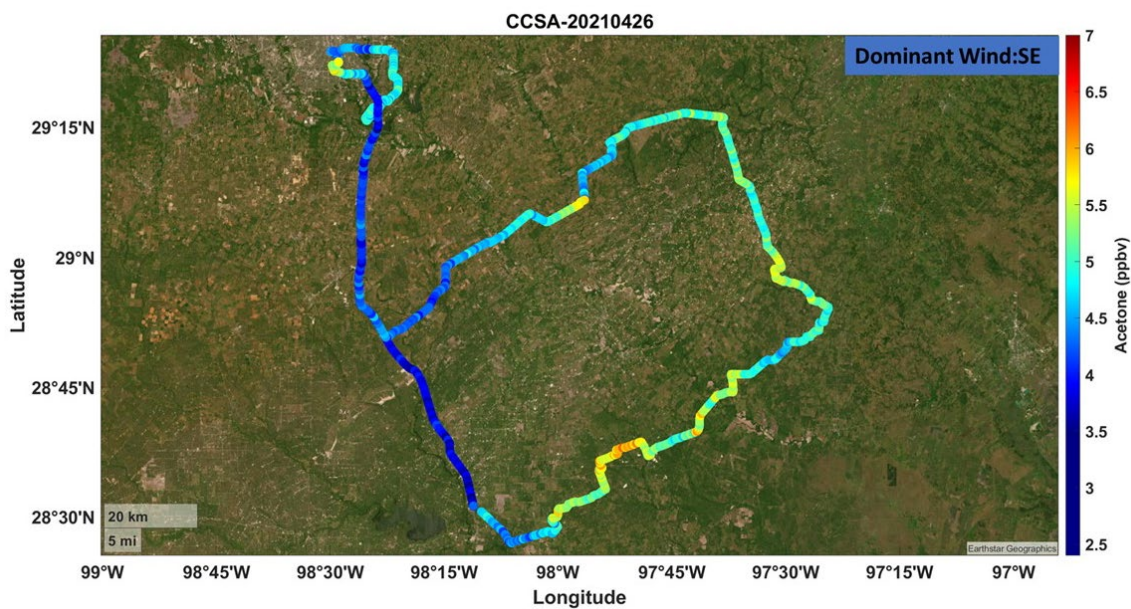


Figure 3.62. Mobile time series of acetone mass concentrations (ppbv) at m/z 59 resulting from CCSA mobile track measurements in San Antonio on April 26, 2021.

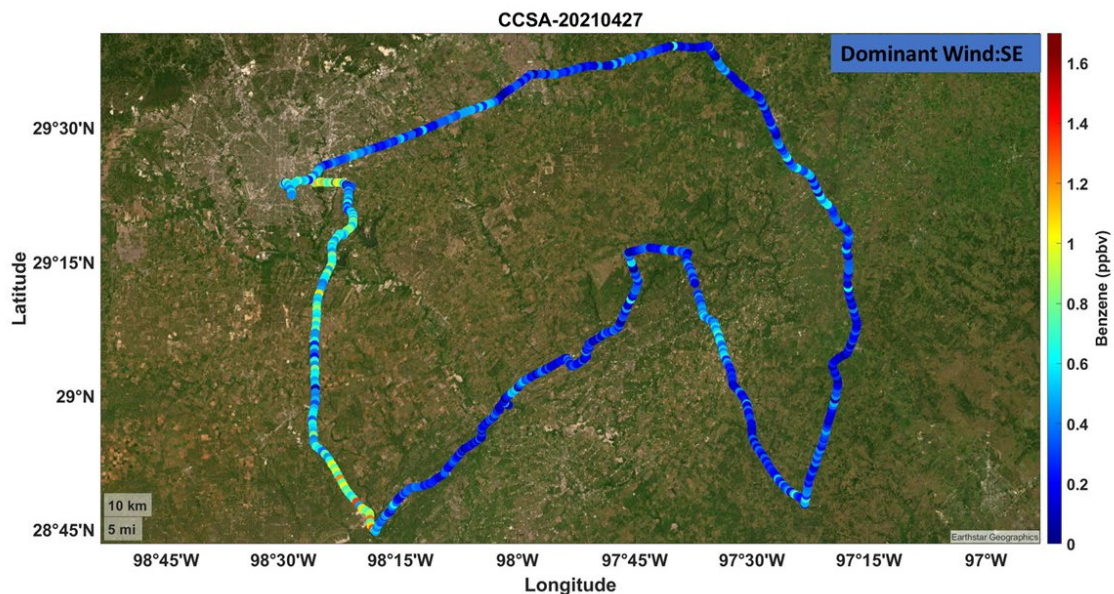


Figure 3.63. Mobile time series of benzene mass concentrations (ppbv) at m/z 79 resulting from CCSA mobile track measurements in San Antonio on April 27, 2021.

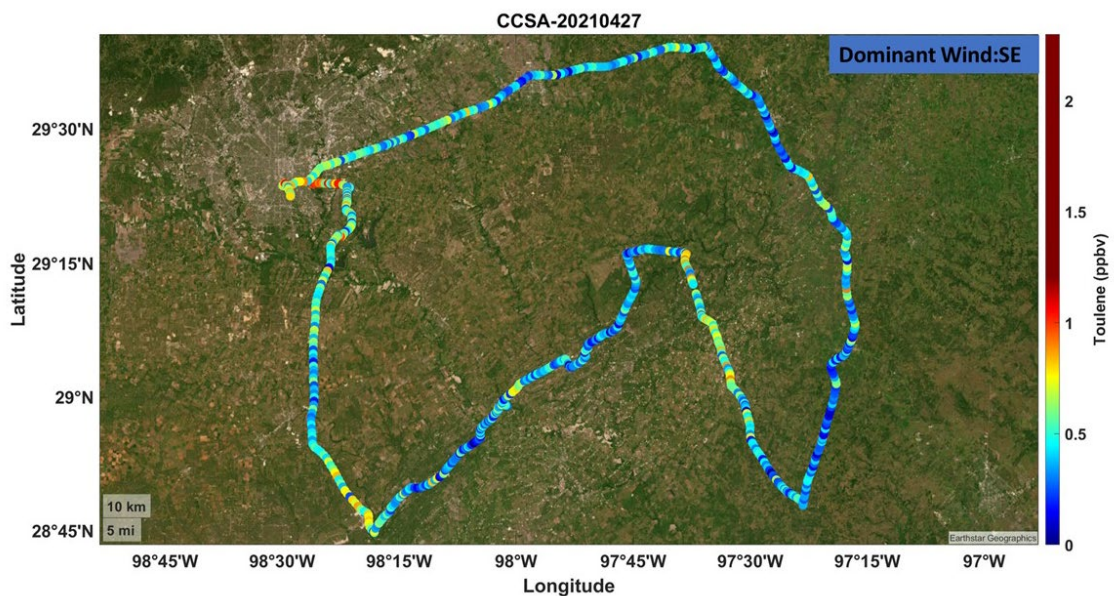


Figure 3.64. Mobile time series of toluene mass concentrations (ppbv) at m/z 93 resulting from CCSA mobile track measurements in San Antonio on April 27, 2021.

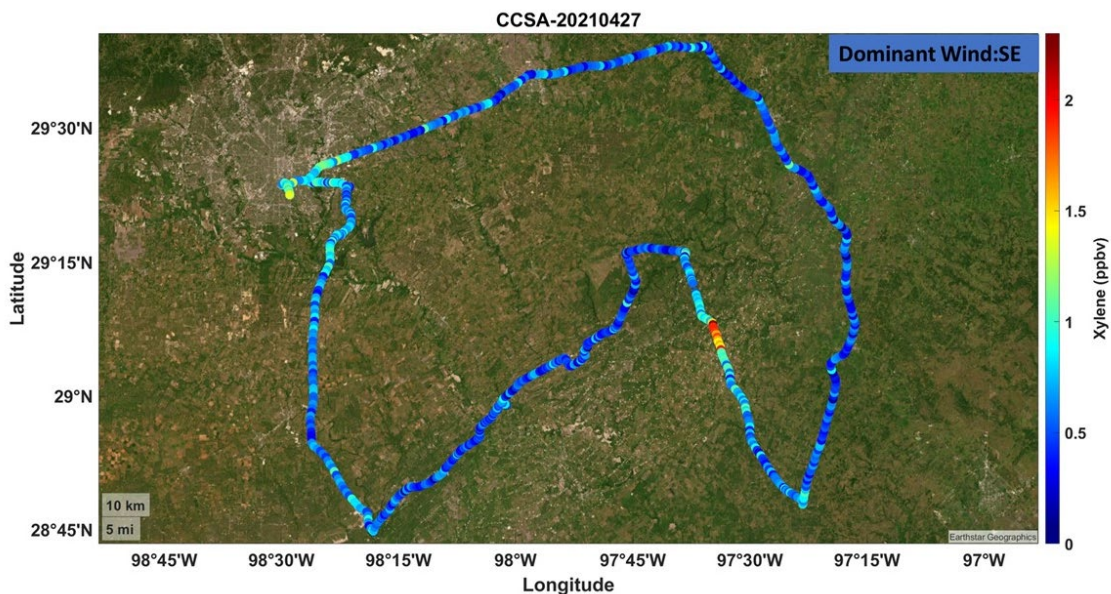


Figure 3.65. Mobile time series of xylene mass concentrations (ppbv) at m/z 107 resulting from CCSA mobile track measurements in San Antonio on April 27, 2021.

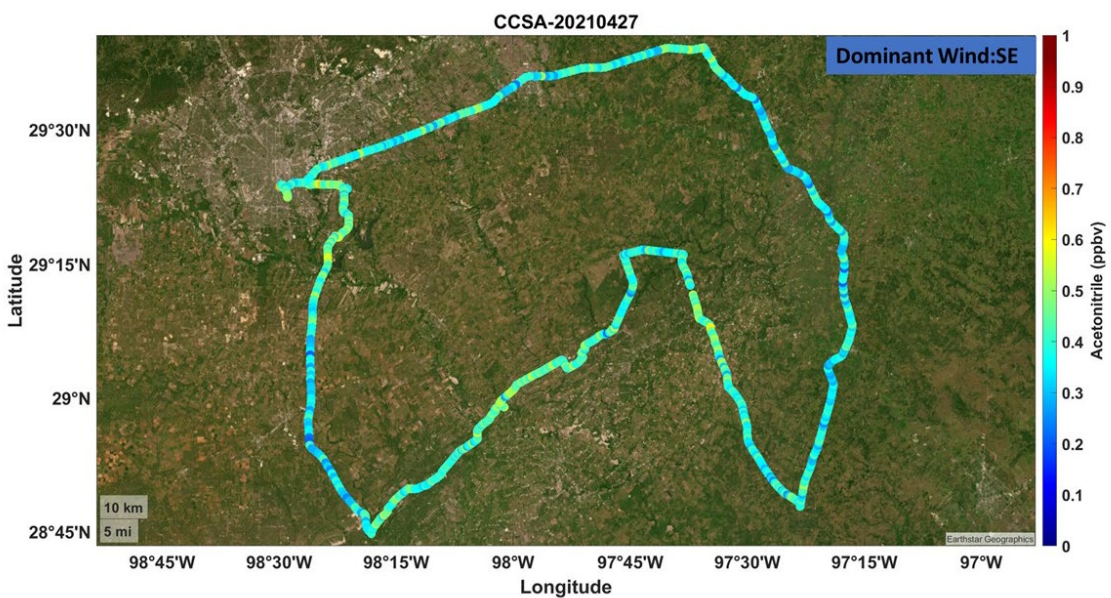


Figure 3.66. Mobile time series of acetonitrile mass concentrations (ppbv) at m/z 42 resulting from CCSA mobile track measurements in San Antonio on April 27, 2021.

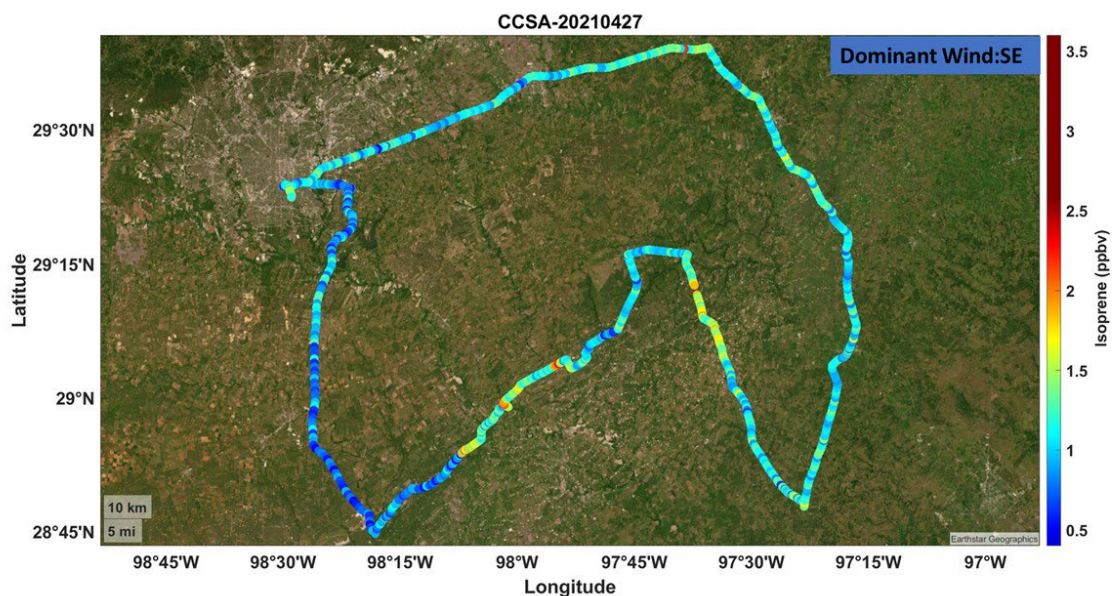


Figure 3.67. Mobile time series of isoprene mass concentrations (ppbv) at m/z 69 resulting from CCSA mobile track measurements in San Antonio on April 27, 2021.

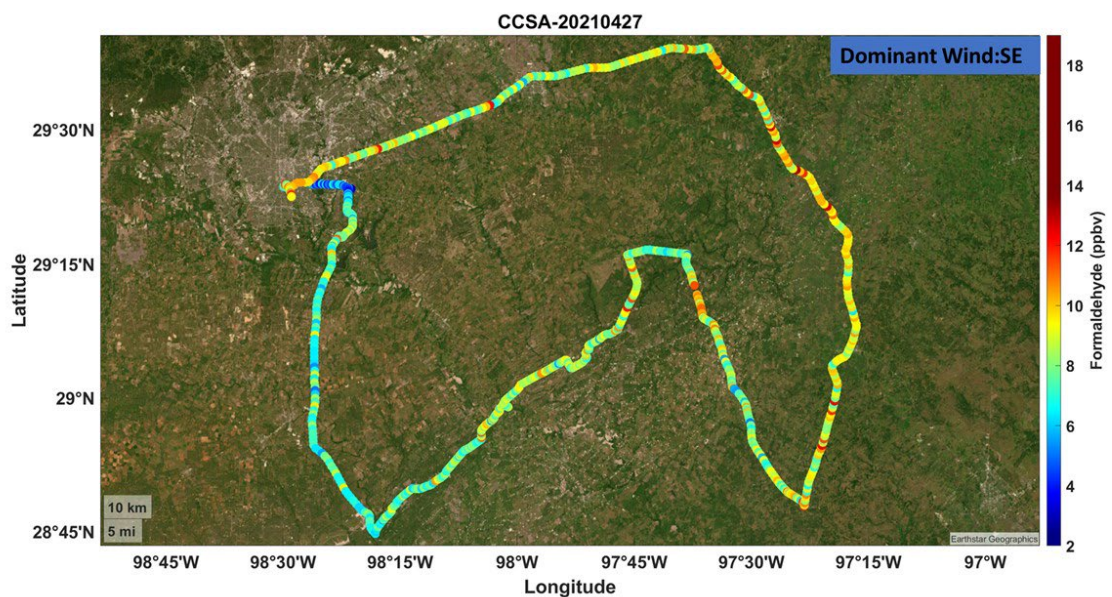


Figure 3.68. Mobile time series of formaldehyde mass concentrations (ppbv) at m/z 31 resulting from CCSA mobile track measurements in San Antonio on April 27, 2021.

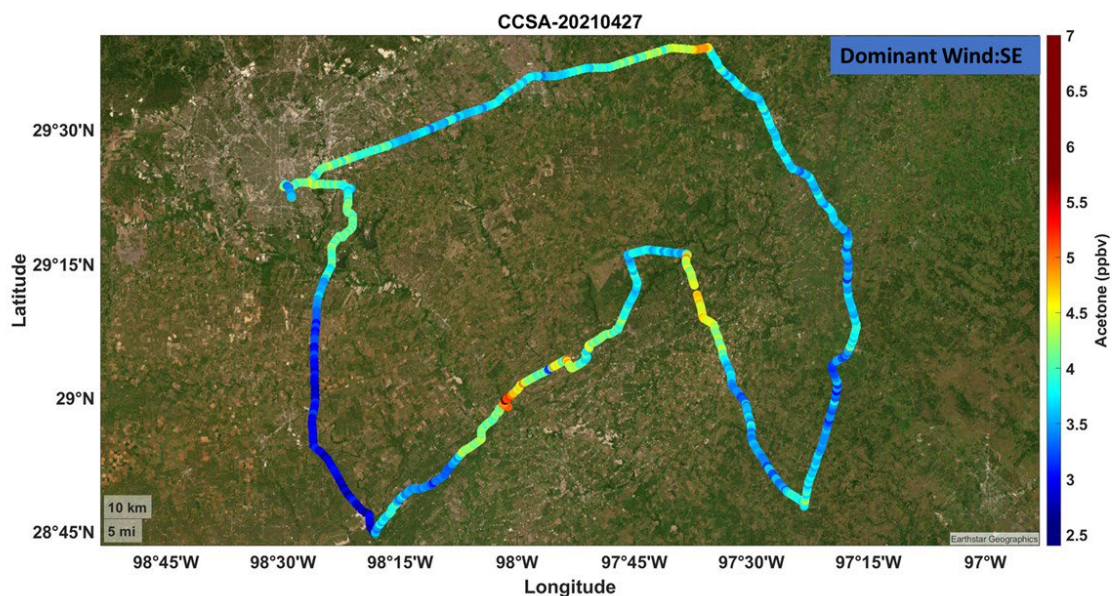


Figure 3.69. Mobile time series of acetone mass concentrations (ppbv) at m/z 59 resulting from CCSA mobile track measurements in San Antonio on April 27, 2021.

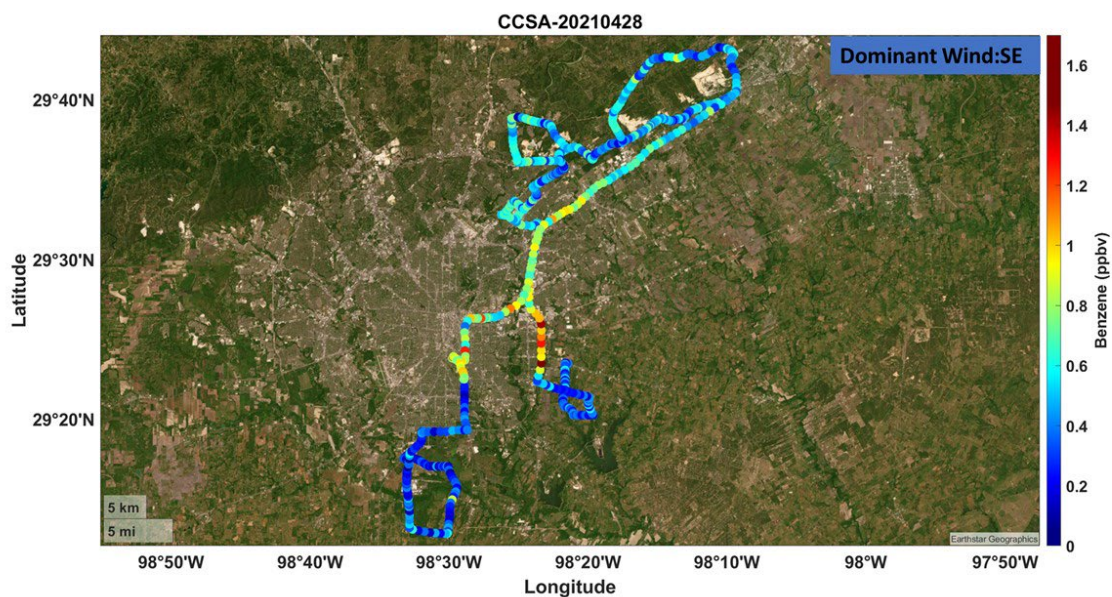


Figure 3.70. Mobile time series of benzene mass concentrations (ppbv) at m/z 79 resulting from CCSA mobile track measurements in San Antonio on April 28, 2021.

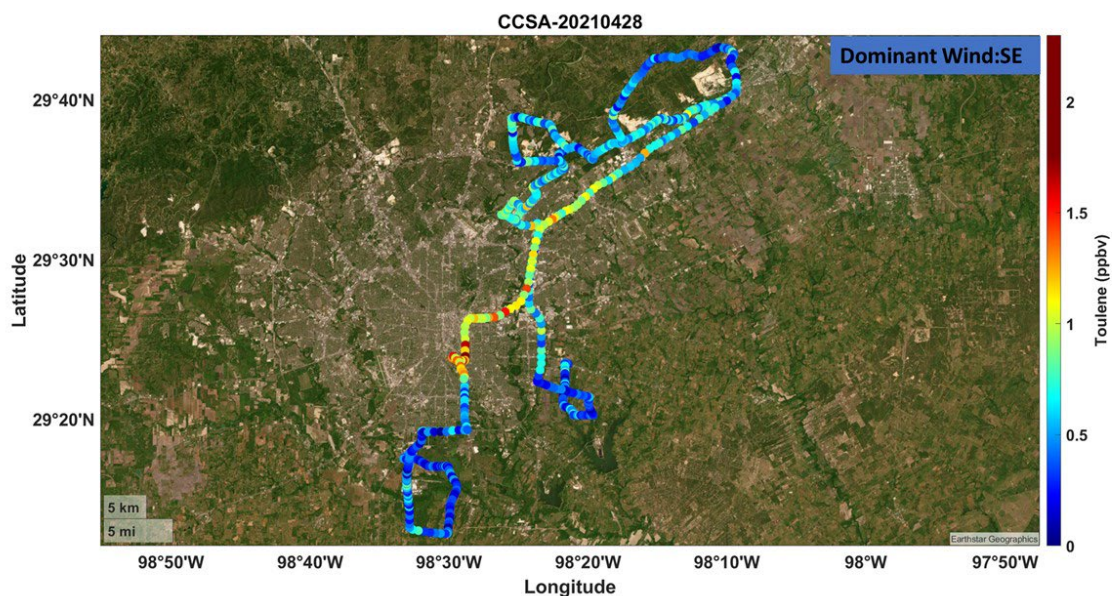


Figure 3.71. Mobile time series of toluene mass concentrations (ppbv) at m/z 93 resulting from CCSA mobile track measurements in San Antonio on April 28, 2021.

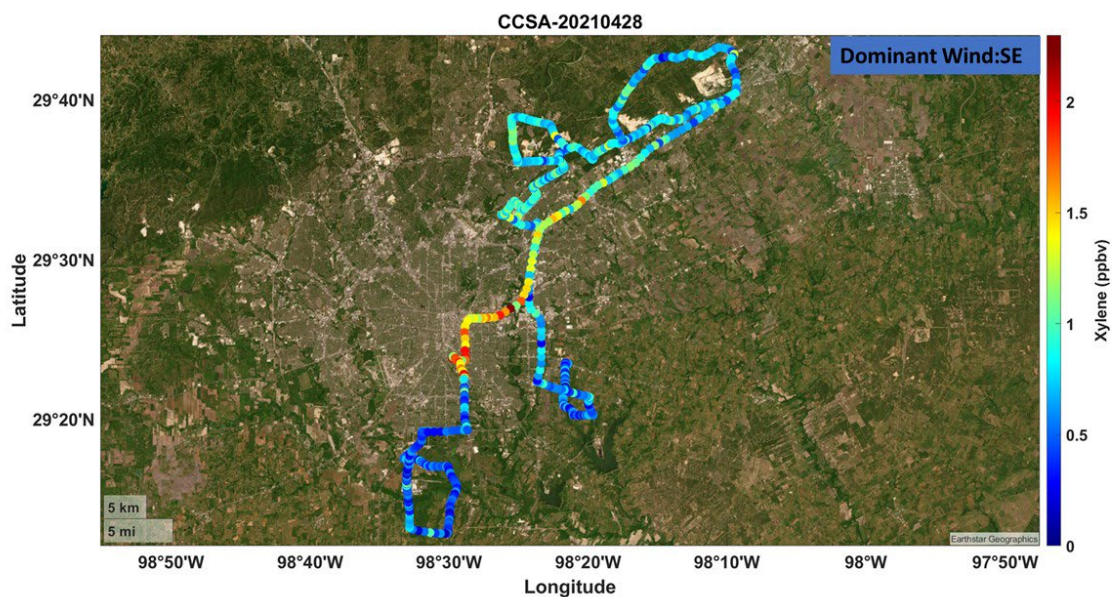


Figure 3.72. Mobile time series of xylene mass concentrations (ppbv) at m/z 107 resulting from CCSA mobile track measurements in San Antonio on April 28, 2021.

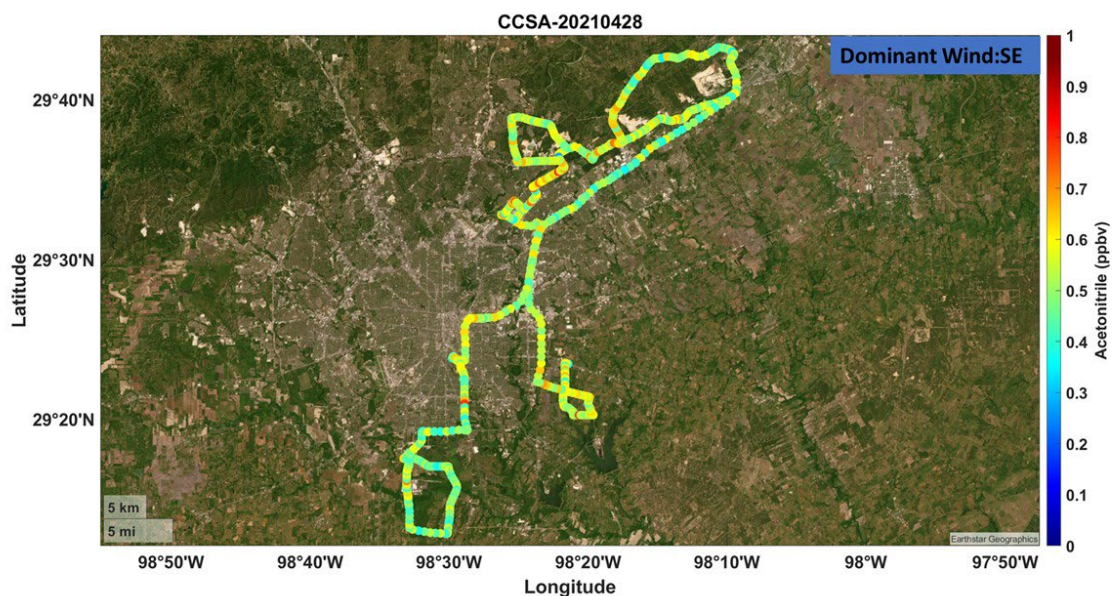


Figure 3.73. Mobile time series of acetonitrile mass concentrations (ppbv) at m/z 42 resulting from CCSA mobile track measurements in San Antonio on April 28, 2021.

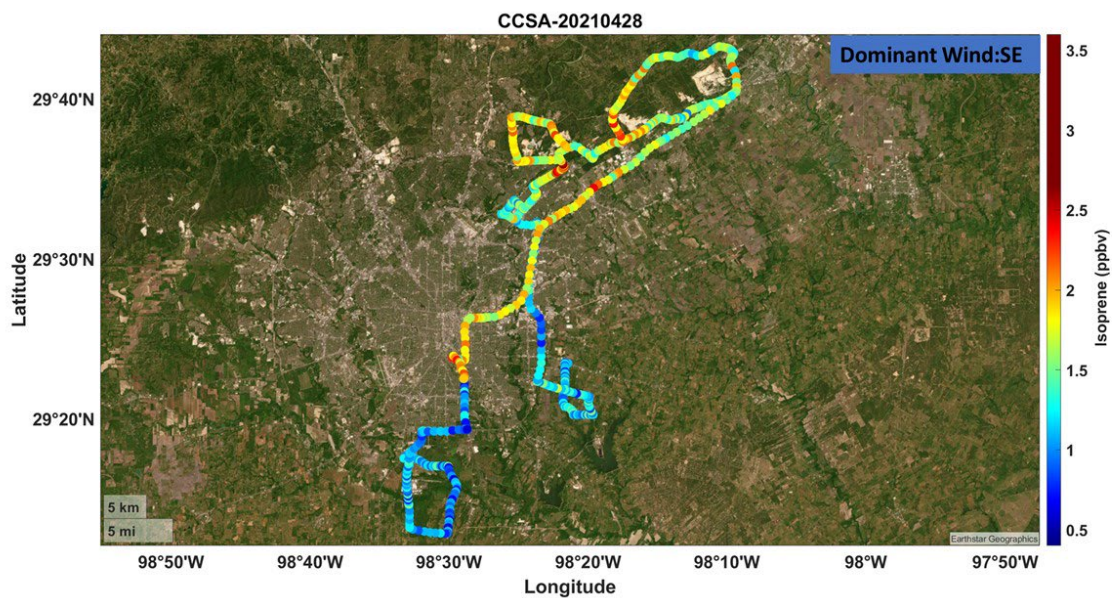


Figure 3.74. Mobile time series of isoprene mass concentrations (ppbv) at m/z 69 resulting from CCSA mobile track measurements in San Antonio on April 28, 2021.

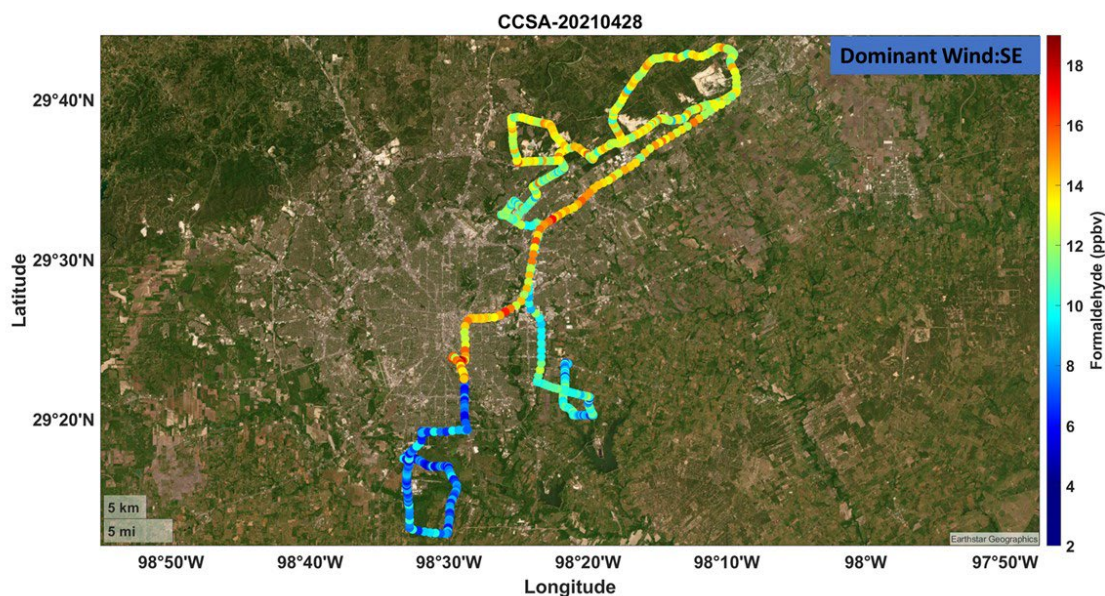


Figure 3.75. Mobile time series of formaldehyde mass concentrations (ppbv) at m/z 31 resulting from CCSA mobile track measurements in San Antonio on April 28, 2021.

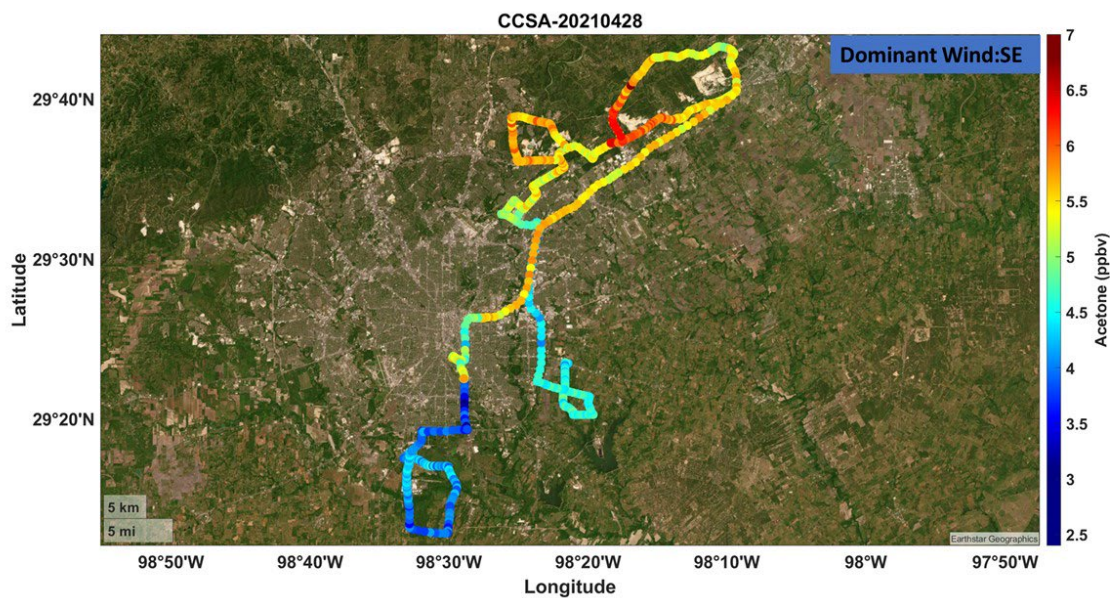


Figure 3.76. Mobile time series of acetone mass concentrations (ppbv) at m/z 59 resulting from CCSA mobile track measurements in San Antonio on April 28, 2021.

3.8.3.3 Aerosol composition and chemistry

The spatial distributions of aerosol composition and elemental ratios are presented below for select mobile measurements.

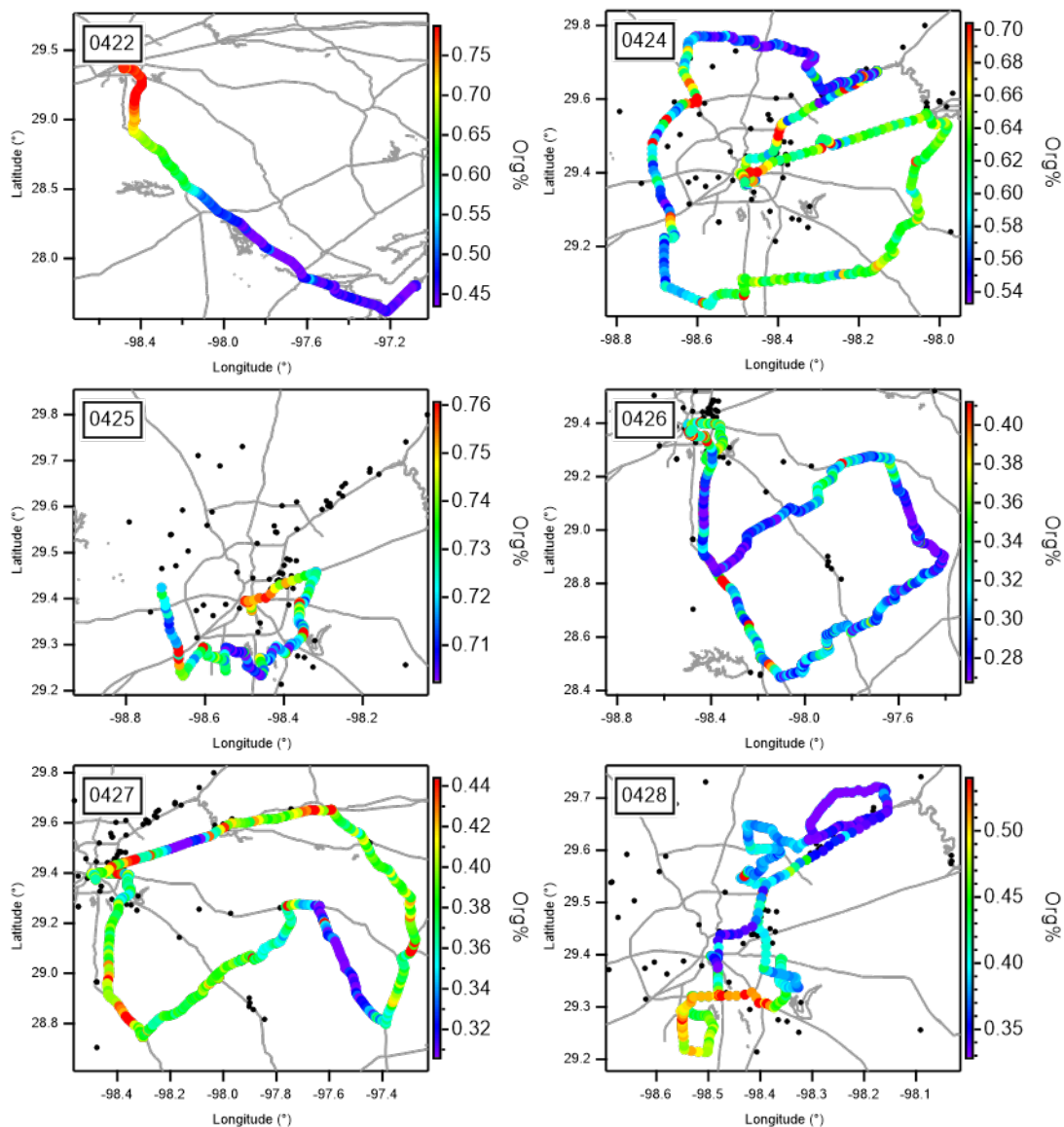


Figure 3.77: Mobile measurements in San Antonio from April 22–28, 2021 colored by mass fraction contribution of organic aerosol to total non-refractory submicron aerosols.

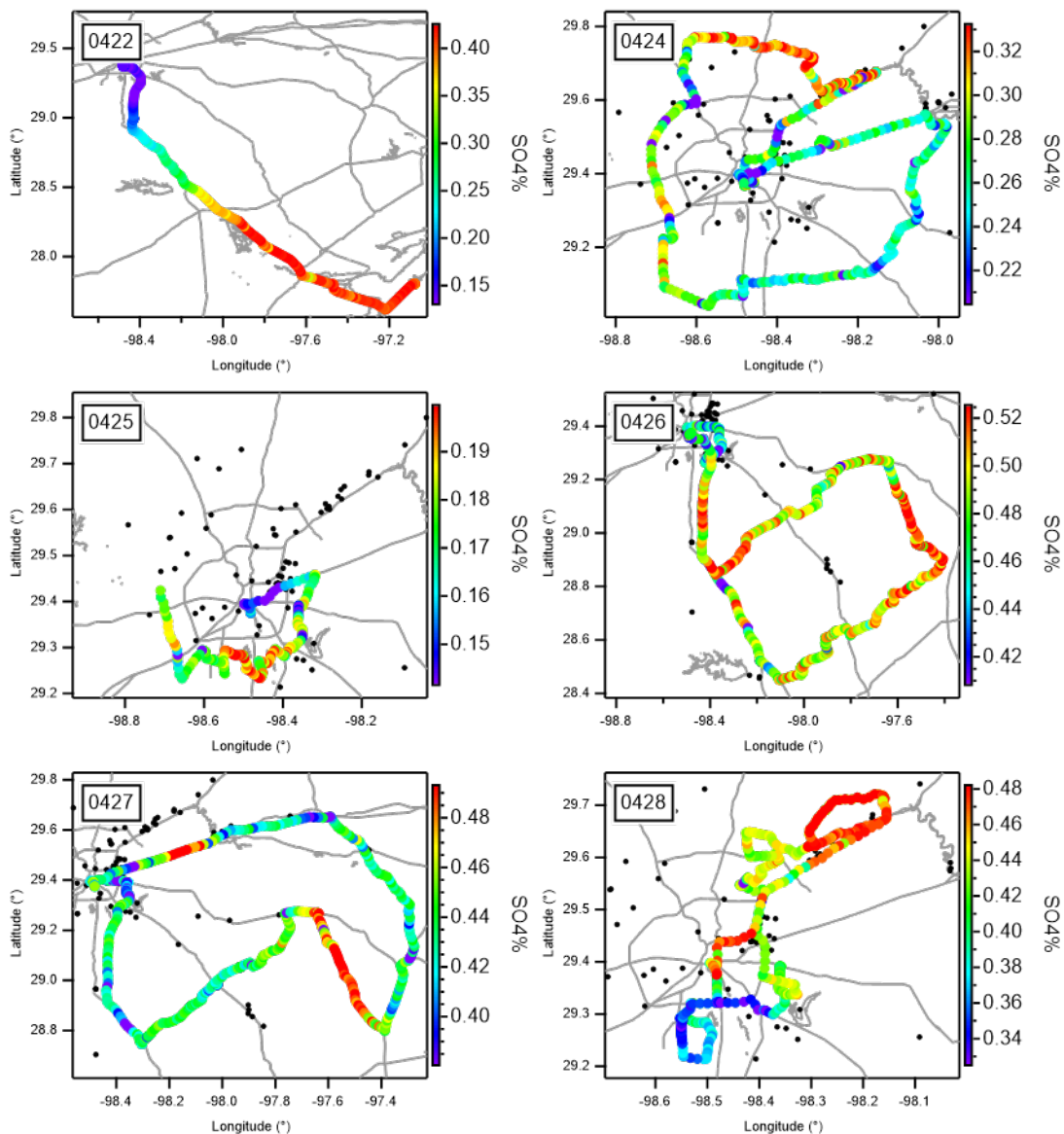


Figure 3.78: Mobile measurements in San Antonio from April 22–28, 2021 colored by mass fraction of sulfate aerosol to total non-refractory submicron aerosols.

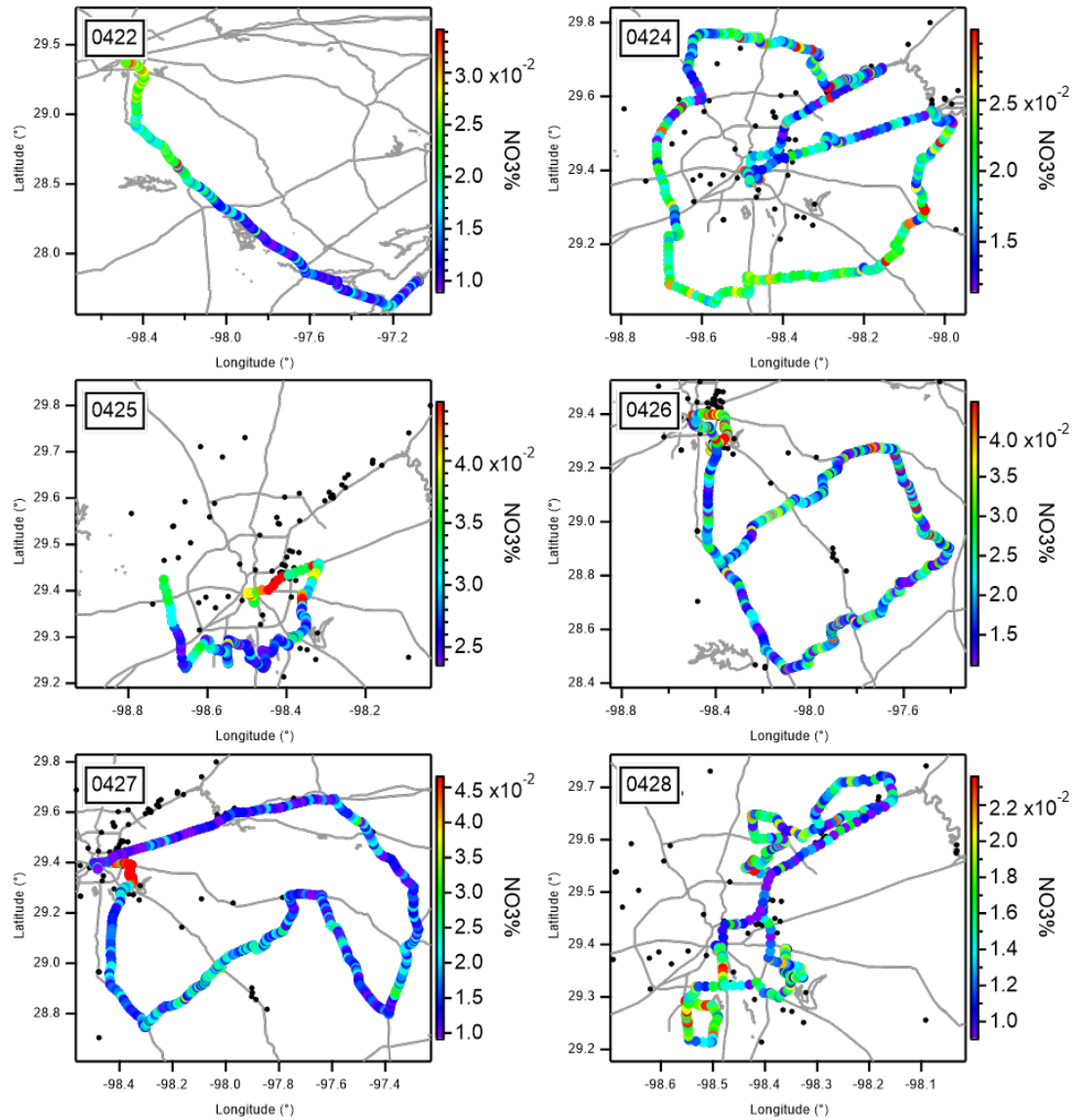


Figure 3.79: Mobile measurements in San Antonio from April 22–28, 2021 colored by mass fraction of nitrate aerosol to total non-refractory submicron aerosols.

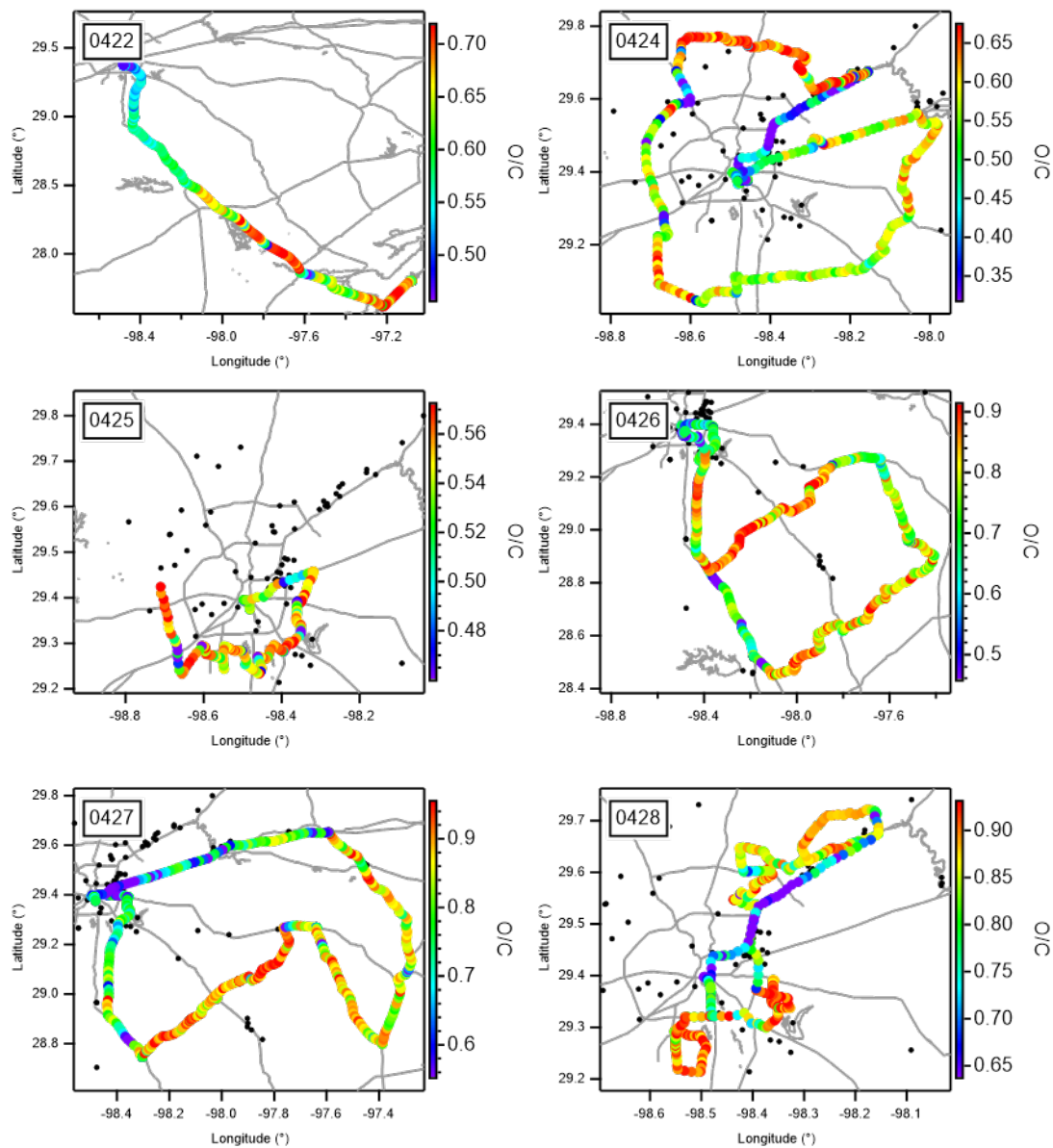


Figure 3.80: Mobile measurements in San Antonio from April 22–28, 2021 colored by oxygen-to-carbon ratio of organic aerosols.

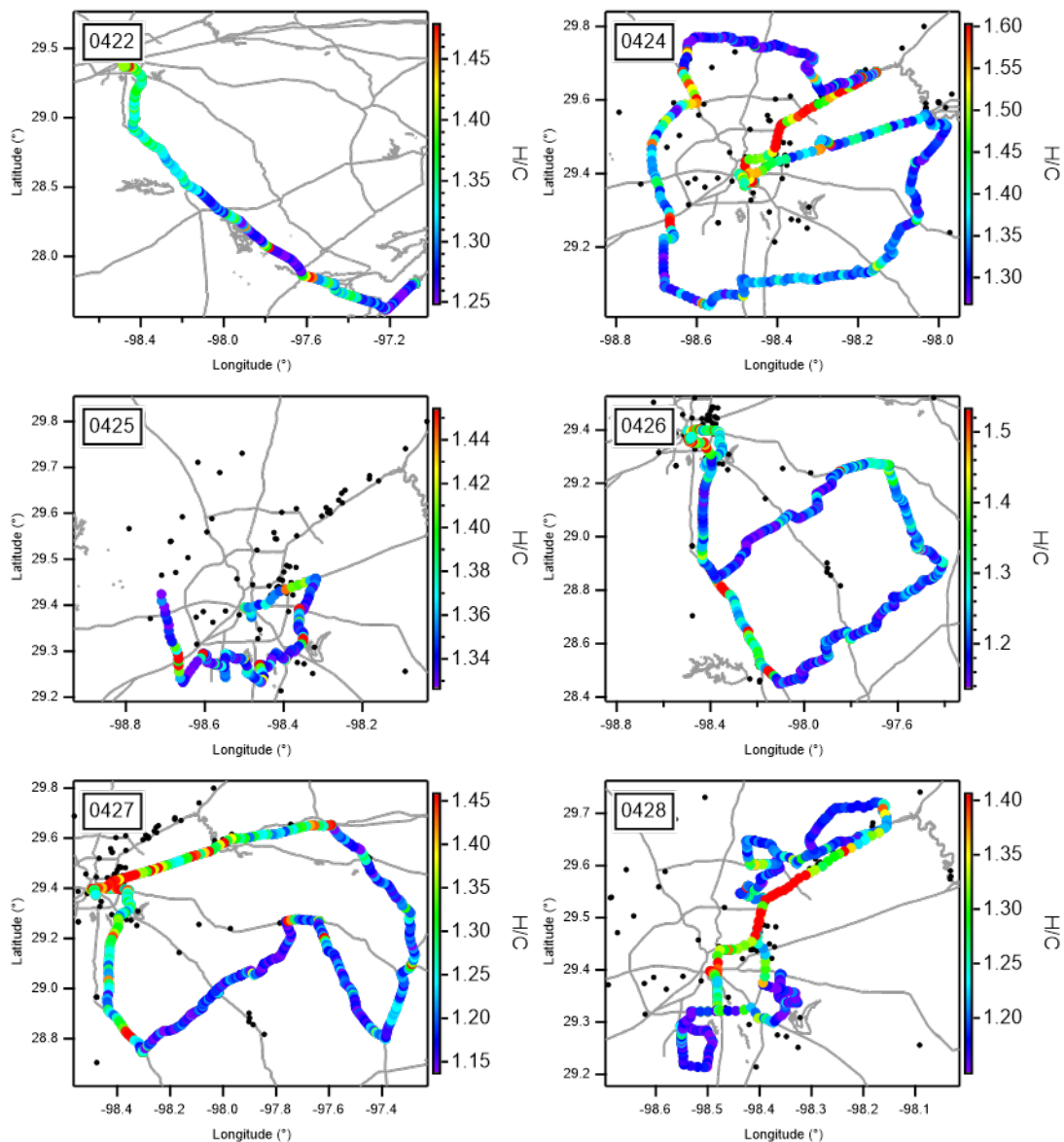


Figure 3.81: Mobile measurements in San Antonio from April 22–28, 2021 colored by hydrogen-to-carbon ratio of organic aerosols.

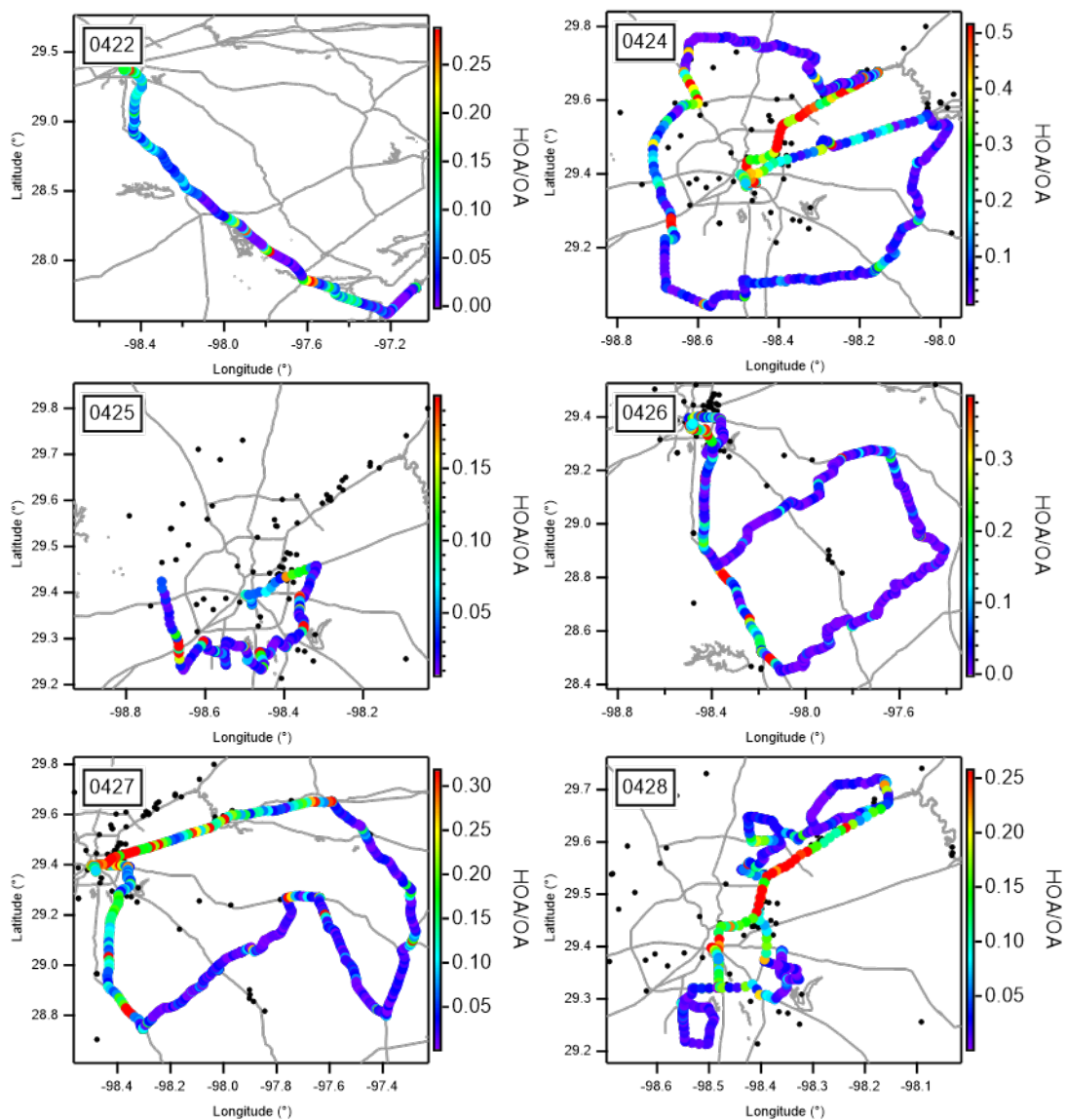


Figure 3.82: Mobile measurements in San Antonio from April 22–28, 2021 colored by mass fraction of hydrocarbon-like organic aerosol (HOA) to total organic aerosol.

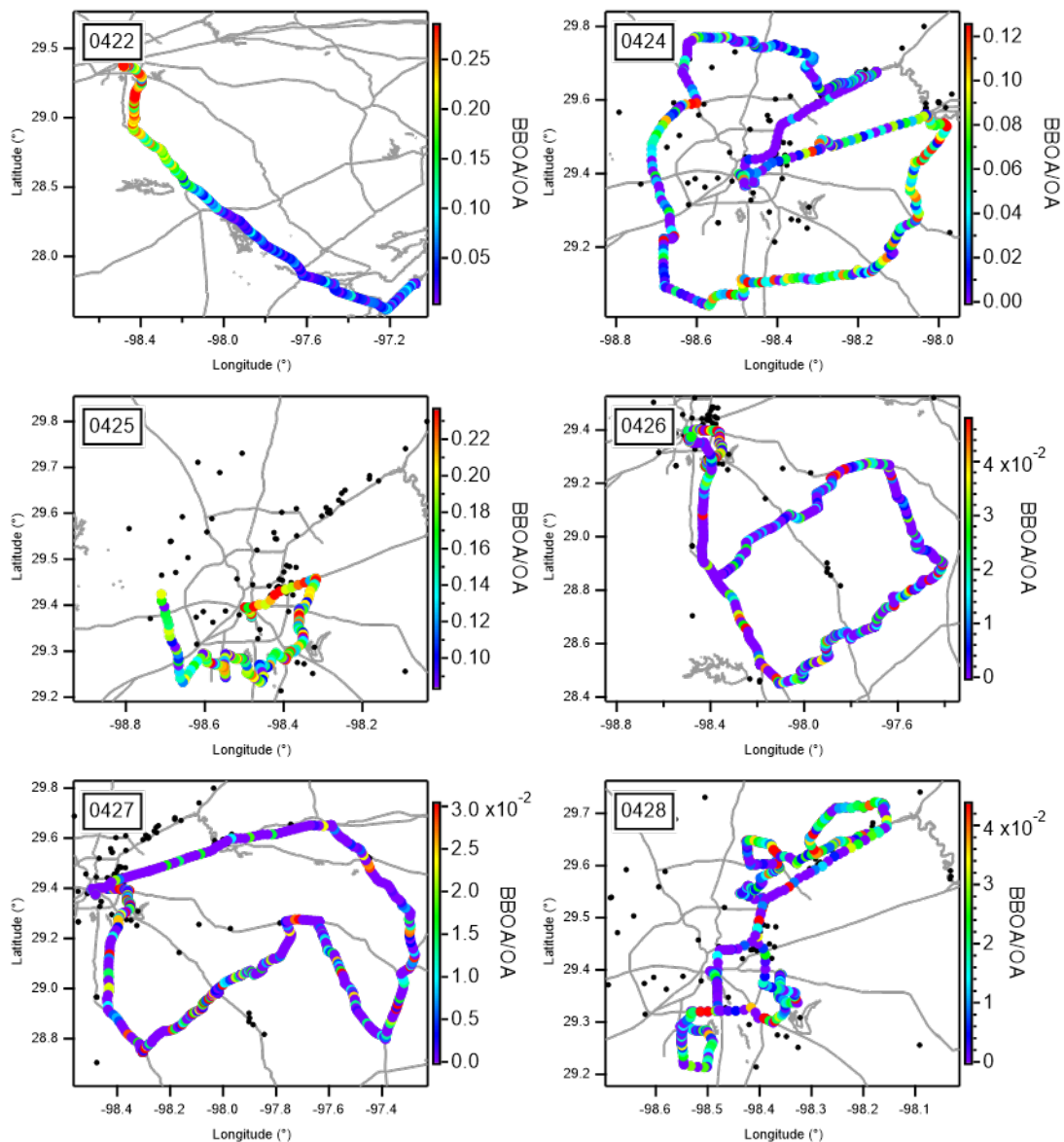


Figure 3.83: Mobile measurements in San Antonio from April 22–28, 2021 colored by mass fraction of biomass burning organic aerosol (BBOA) to total organic aerosol.

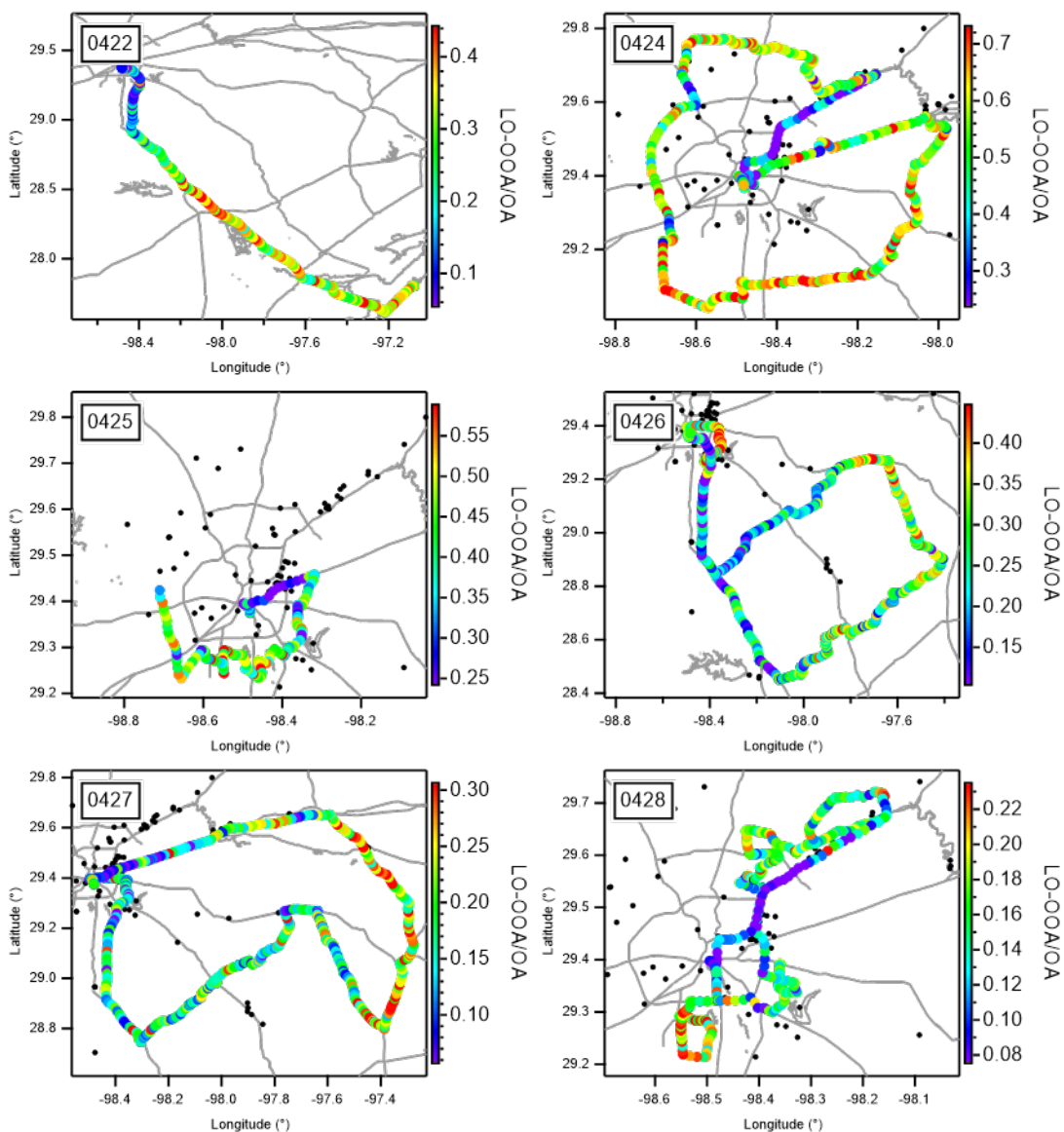


Figure 3.84: Mobile measurements in San Antonio from April 22–28, 2021 colored by mass fraction of less-oxidized oxygenated organic aerosol (LO-OOA) to total organic aerosol.

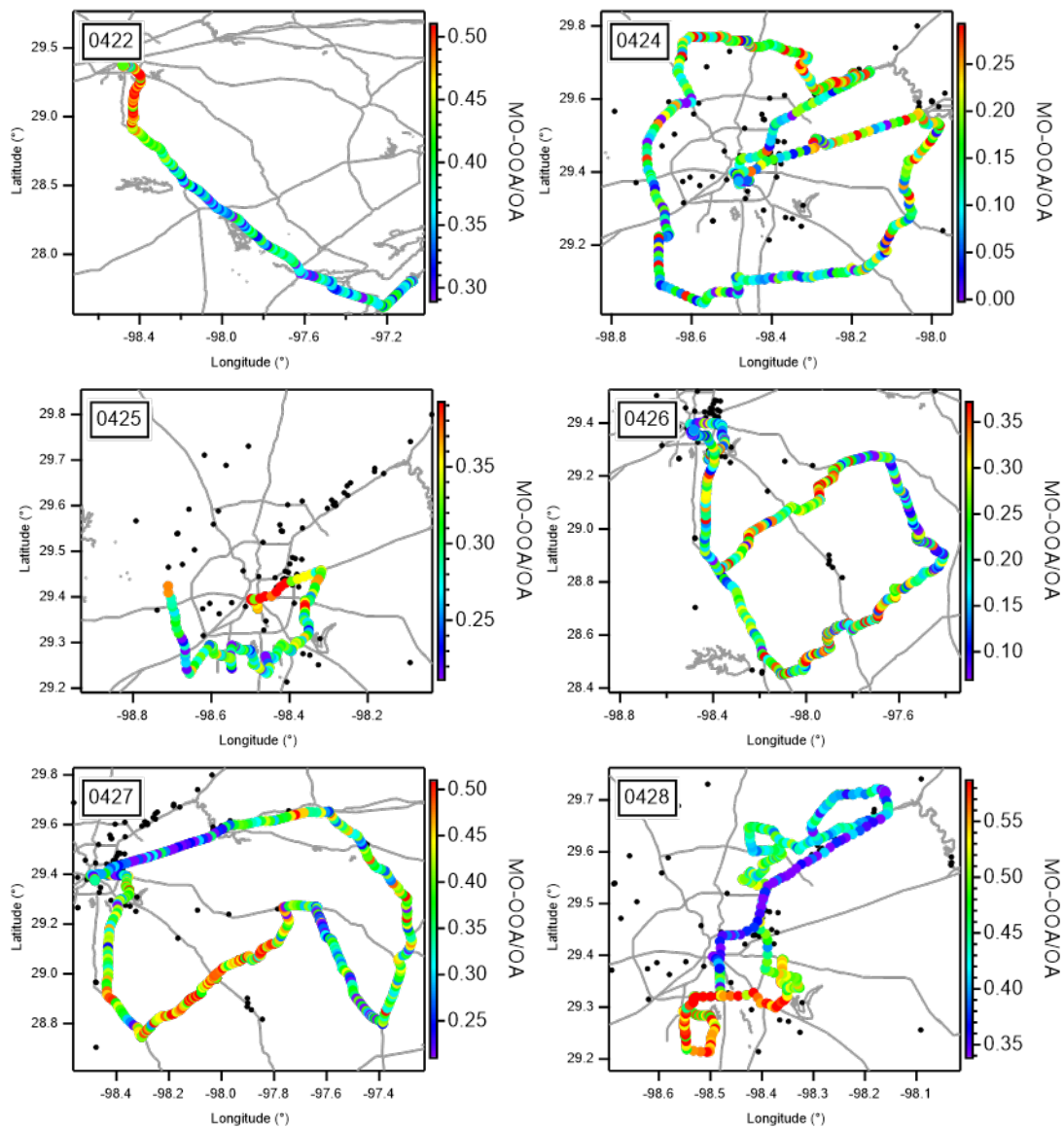


Figure 3.85: Mobile measurements in San Antonio from April 22–28, 2021 colored by mass fraction of more-oxidized oxygenated organic aerosol (MO-OOA) to total organic aerosol.

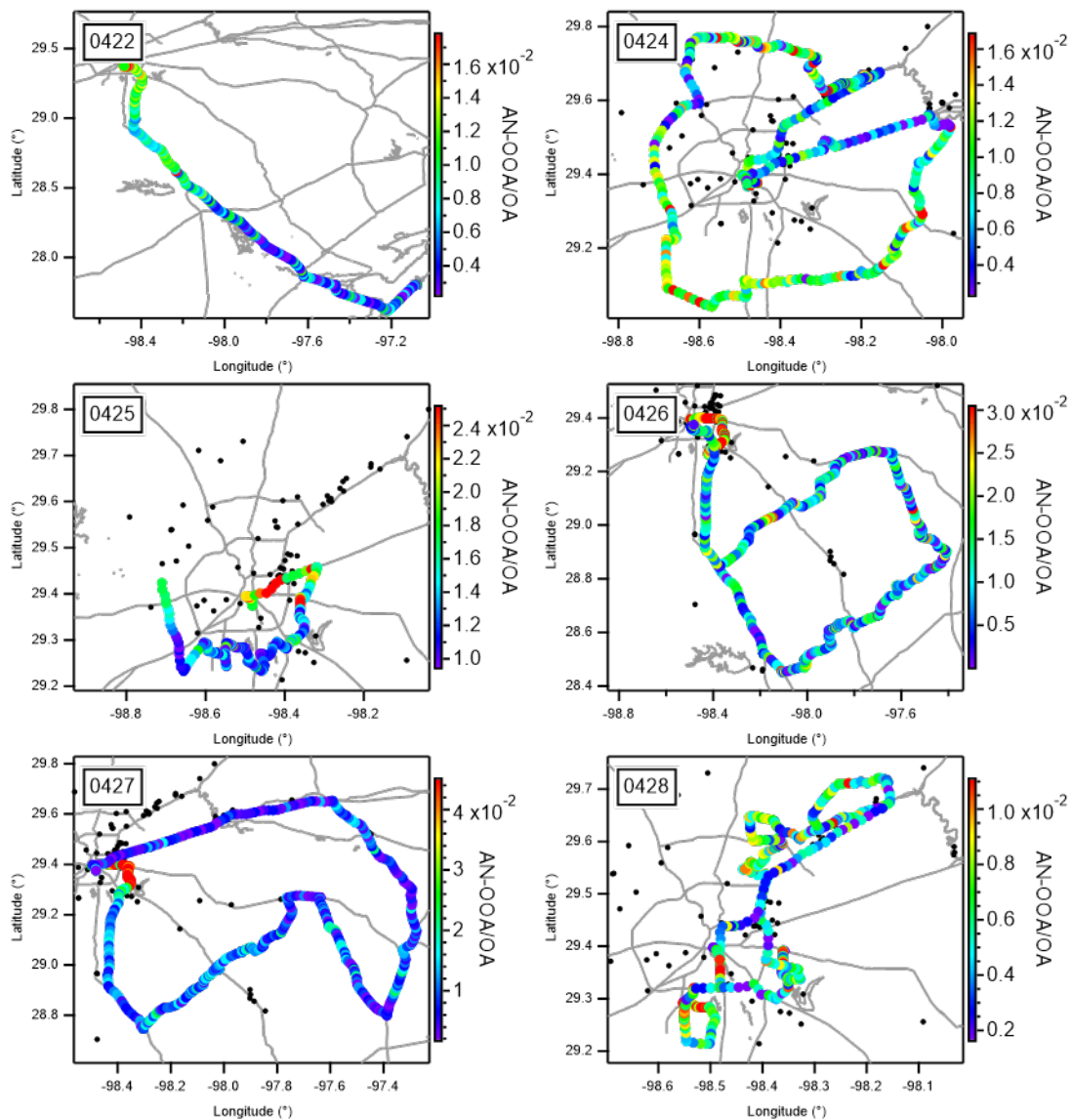


Figure 3.86: Mobile measurements in San Antonio from April 22–28, 2021 colored by mass fraction of an OOA that was associated with ammonium nitrate and biomass burning (AN-OOA) to total organic aerosol.

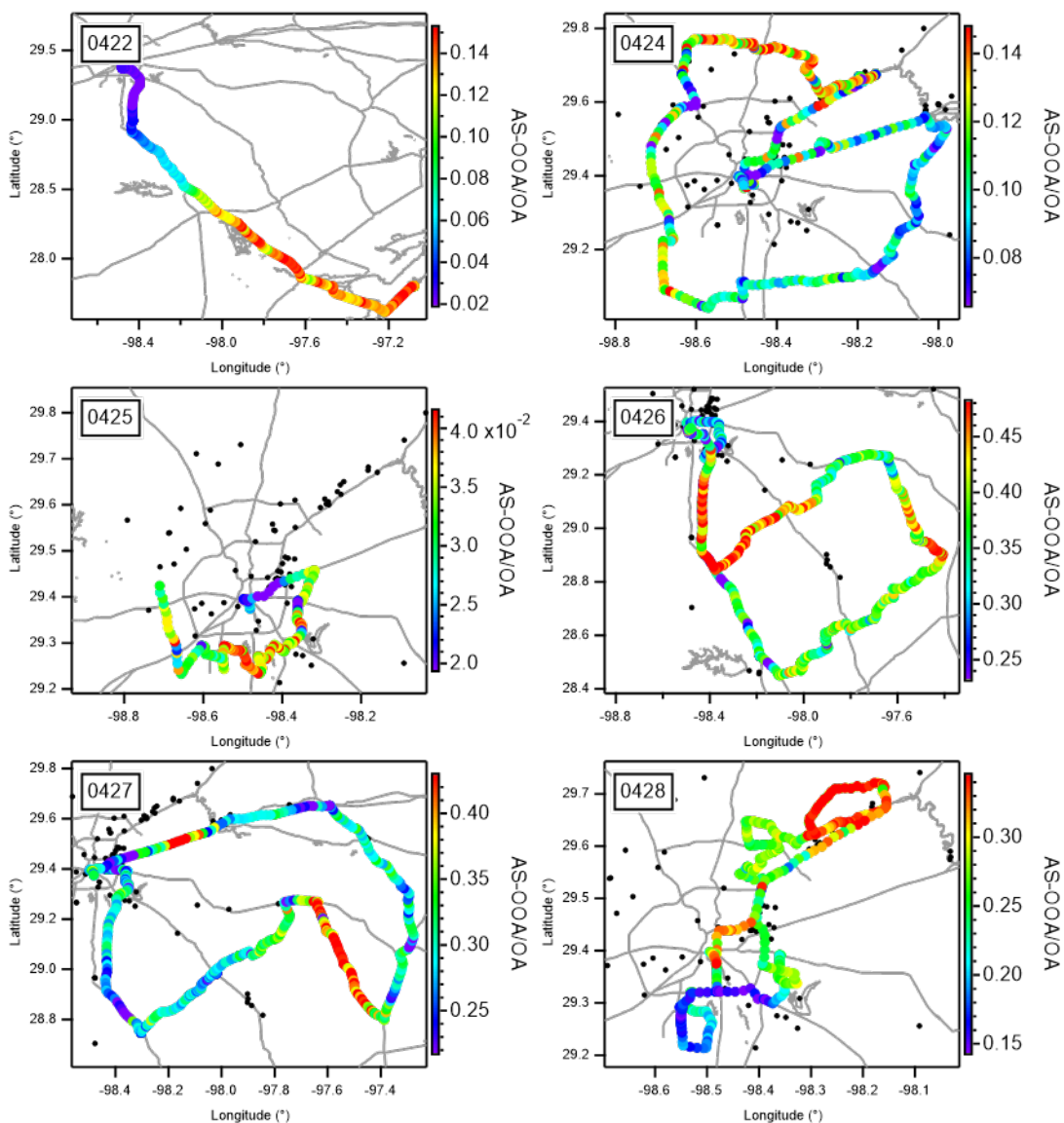


Figure 3.87: Mobile measurements in San Antonio from April 22–28, 2021 colored by mass fraction of a highly oxidized OOA associated with ammonium sulfate (AS-OOA) to total organic aerosol.

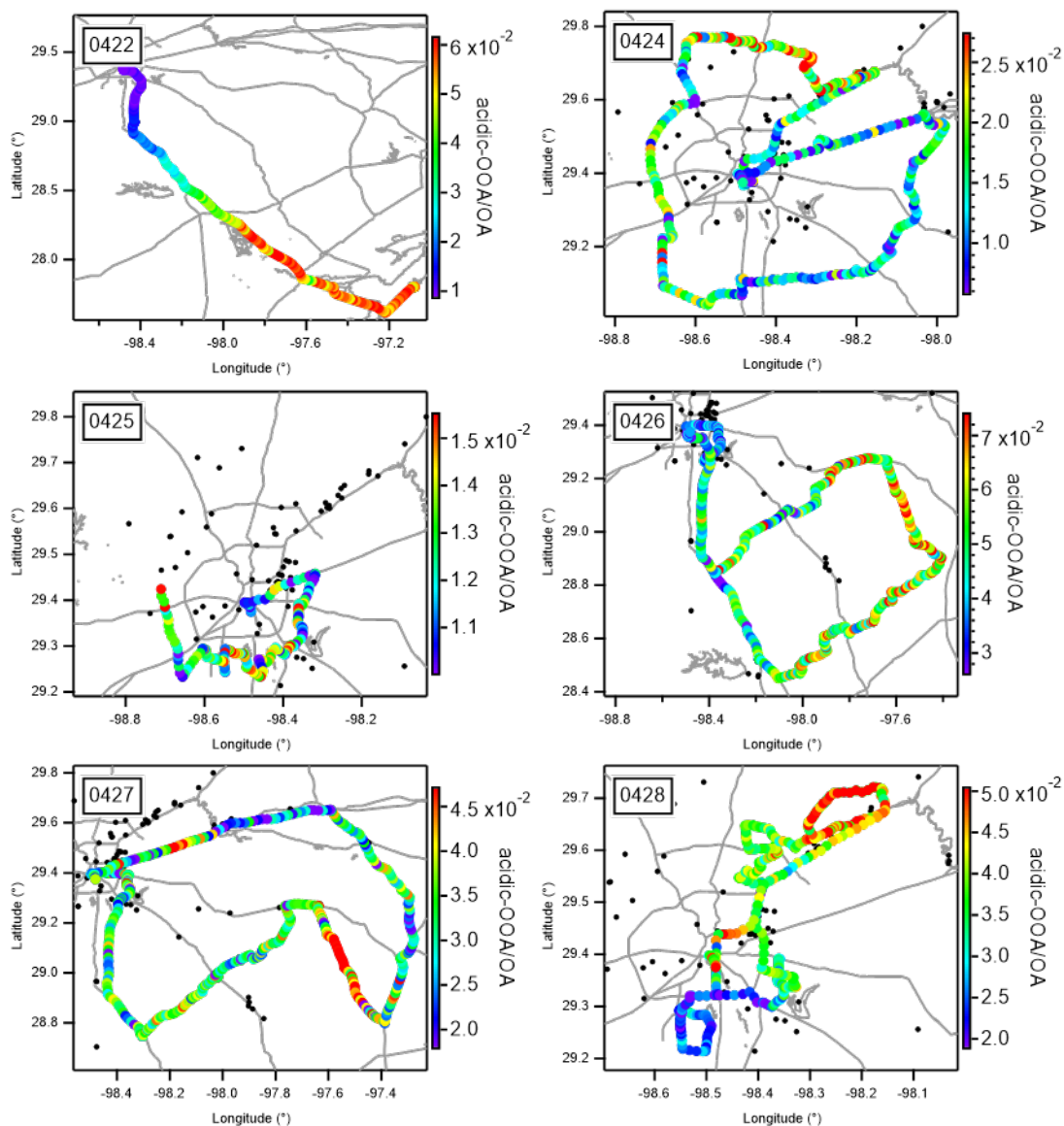


Figure 3.88: Mobile measurements in San Antonio from April 22–28, 2021 colored by mass fraction of a highly oxidized OOA associated with acidic sulfate (acidic-OOA) to total organic aerosol.

3.8.3.4 Aerosol optical properties

Aerosol absorption coefficients, Scattering absorption coefficients, and Single-scattering albedo (SSA) are presented for select days in **Figure 3.89** to **Figure 3.100**.

Mobile time series of the aerosol absorption coefficients (e.g., **Figure 3.89**) report moderate absorption coefficients with periods of portions of the times series indicating rapid increases in aerosol absorption. This highlights the spatial heterogeneity in aerosol across the domain. During the April 27, 2021 (**Figure 3.95**) deployment, the absorption coefficients tend to decrease as the MAQL 2 moved away from the city center, however, again there were short periods of increased

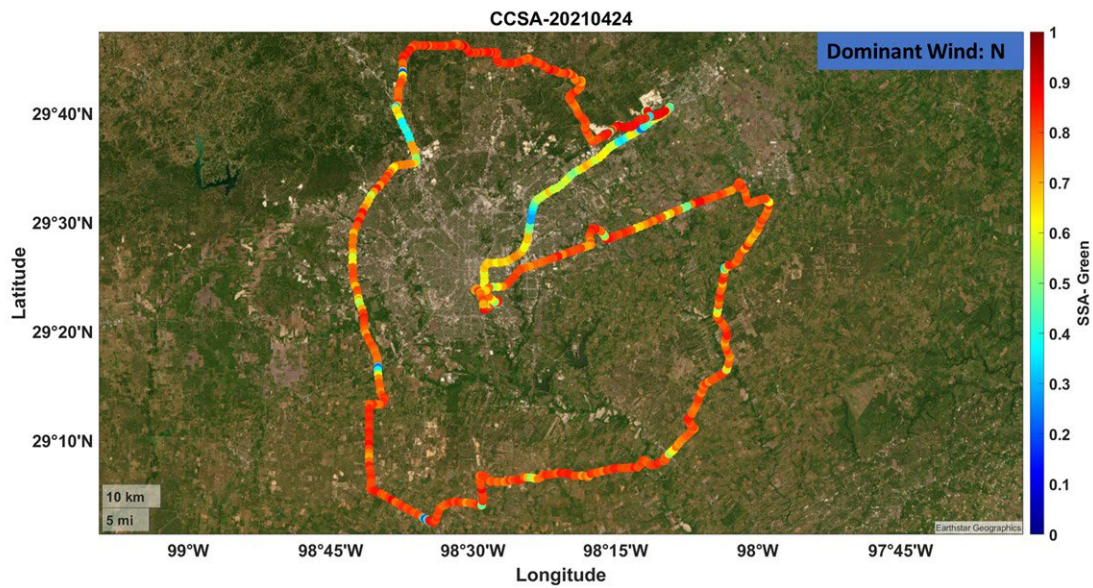


Figure 3.91: Mobile time series of single-scattering albedo (SSA; green) resulting from CCSA mobile track measurements in San Antonio on April 24, 2021.

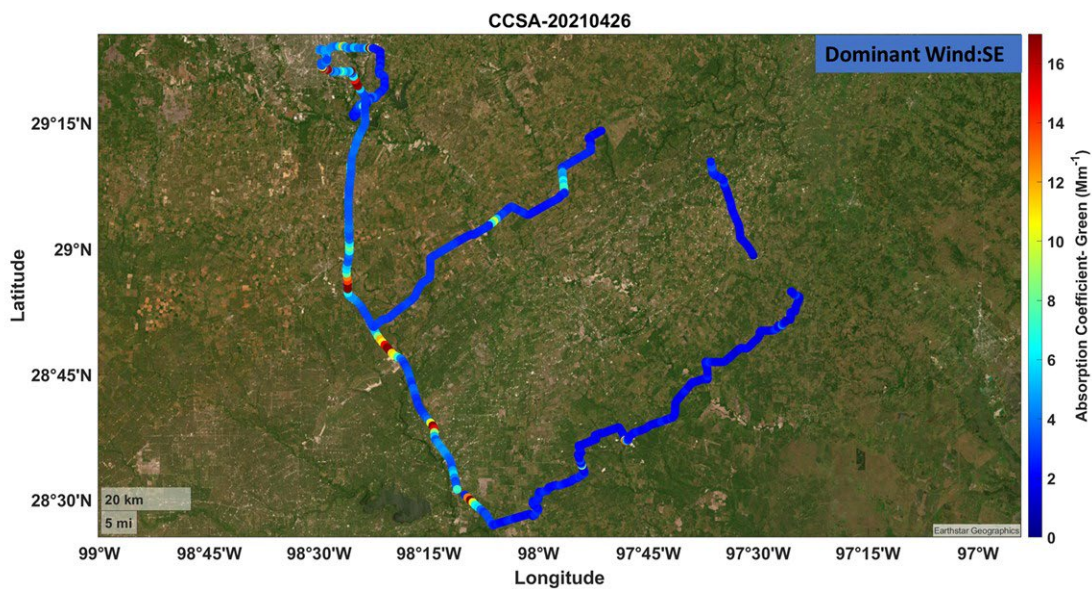


Figure 3.92: Mobile time series of aerosol absorption coefficient (green; 528 nm) resulting from CCSA mobile track measurements in San Antonio on April 26, 2021.



Figure 3.93: Mobile time series of scattering absorption coefficient (green; 525 nm) resulting from CCSA mobile track measurements in San Antonio on April 26, 2021.



Figure 3.94: Mobile time series of single-scattering albedo (SSA; green-528 nm) resulting from CCSA mobile track measurements in San Antonio on April 26, 2021.

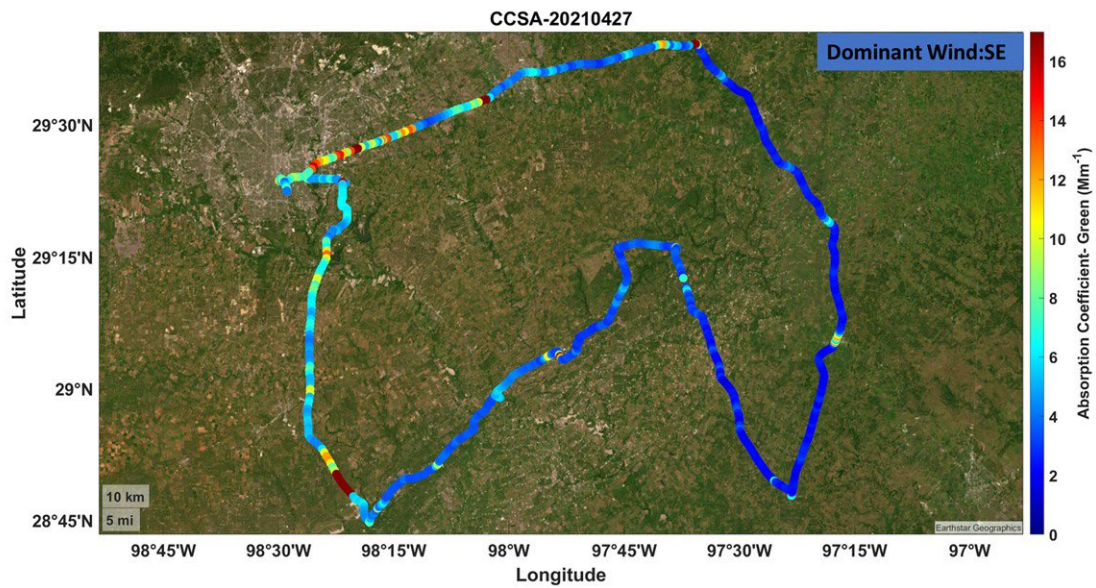


Figure 3.95: Mobile time series of aerosol absorption coefficient (green; 528 nm) resulting from CCSA mobile track measurements in San Antonio on April 27, 2021.

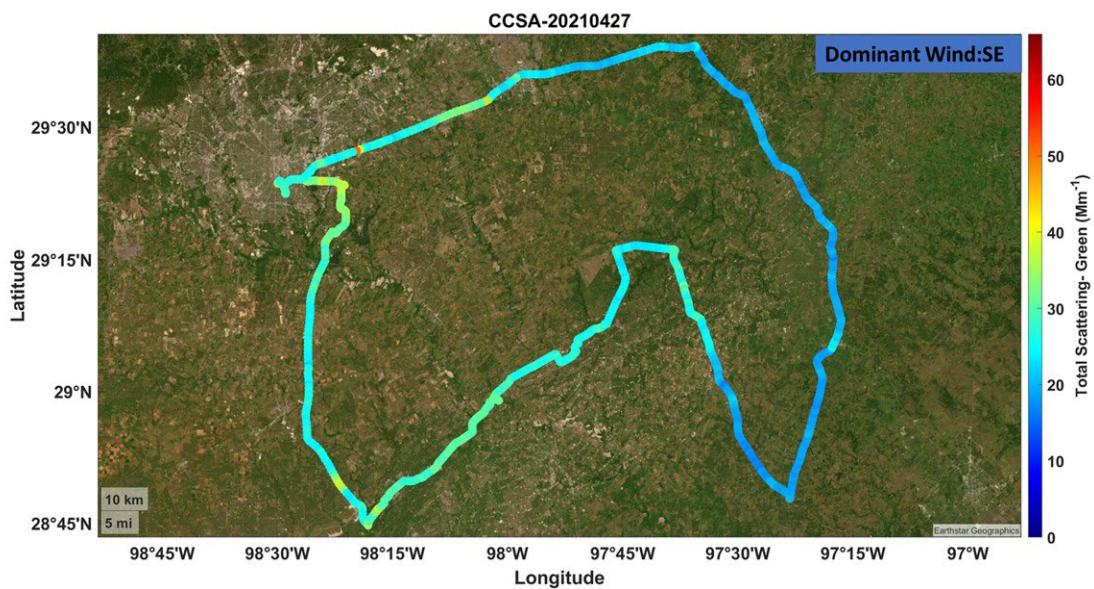


Figure 3.96: Mobile time series of scattering absorption coefficient (green; 525 nm) resulting from CCSA mobile track measurements in San Antonio on April 27, 2021.

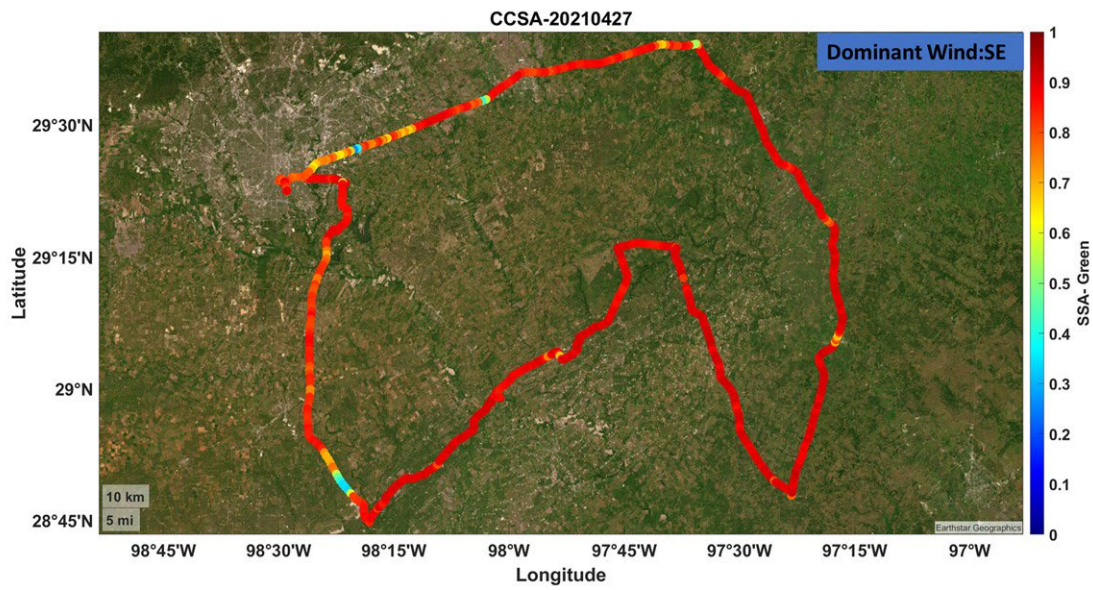


Figure 3.97: Mobile time series of single-scattering albedo (SSA; green-528 nm) resulting from CCSA mobile track measurements in San Antonio on April 27, 2021.

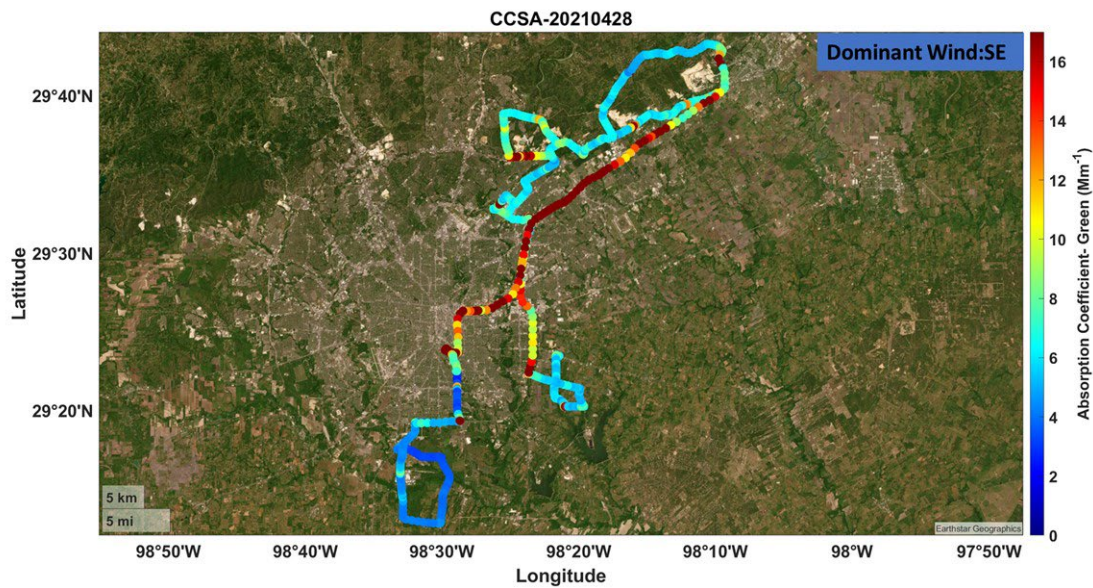


Figure 3.98: Mobile time series of aerosol absorption coefficient (green; 528 nm) resulting from CCSA mobile track measurements in San Antonio on April 28, 2021

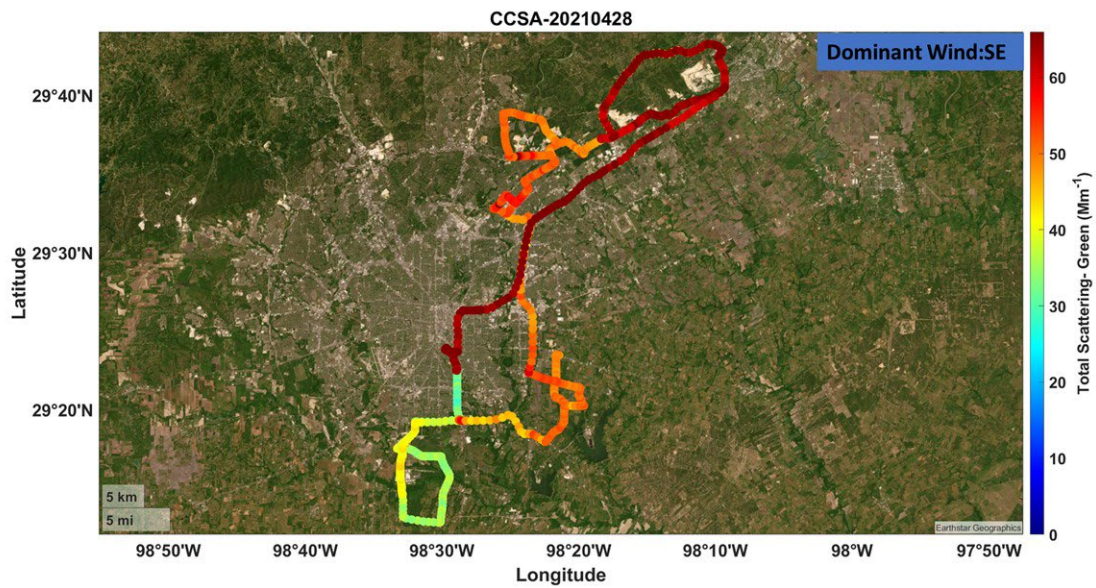


Figure 3.99: Mobile time series of scattering absorption coefficient (green; 525 nm) resulting from CCSA mobile track measurements in San Antonio on April 28, 2021.

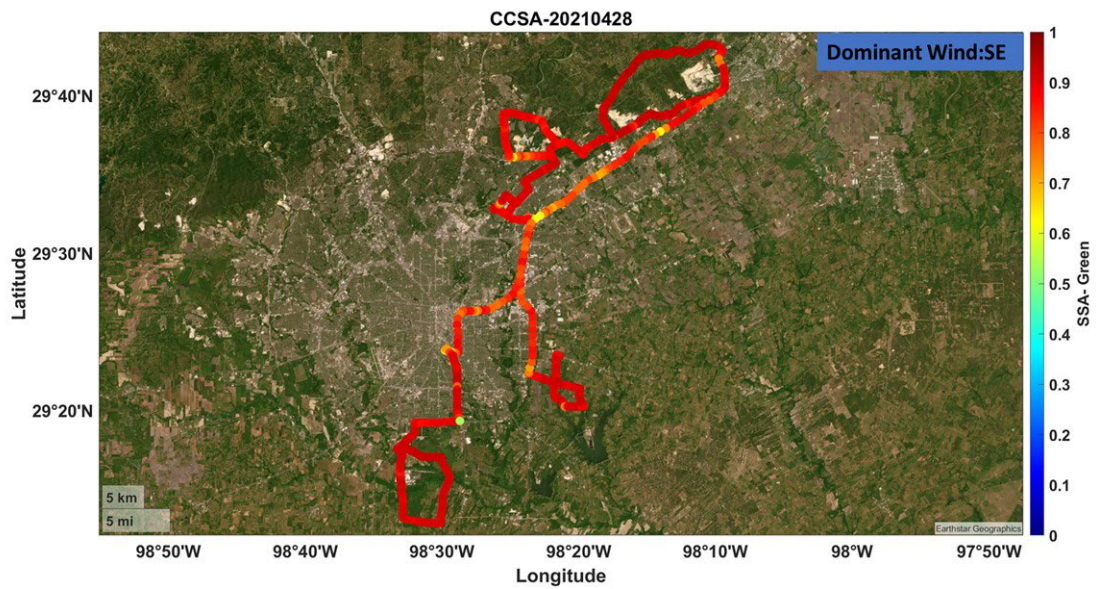


Figure 3.100: Mobile time series of single-scattering albedo (SSA; green-528 nm) resulting from CCSA mobile track measurements in San Antonio on April 28, 2021.

3.9 Task 9: Modeling Analysis to Aid the Observational Analysis

3.9.1 Summary and Key Findings

- This task was completed. We conducted modeling analyses to complement, corroborate, and/or validate the observational analyses in Tasks 3 through 7. Model sensitivity simulations were designed to investigate the separate and combined roles of local emissions, atmospheric dynamics, atmospheric chemistry, and background airmasses on high pollution events. We reviewed, proposed, and selected appropriate modeling tools best suited for analyses of interest. We also conducted comparisons of 2017 to 2021 ozone modeling results in the San Antonio area to investigate whether changes in chemistry are due to changes in emissions, changes in meteorology, or both. We assessed the sensitivity of ozone formation to nitrogen oxides and VOC. The final data set was submitted to the TCEQ on April 15, 2023.
- According to air quality standards, 2017 and 2021 show similar levels of ozone design value while 2021 has more ozone exceedance days but lower levels of health concerns.
- Using the WRF-GC air quality models, we found that the regional mean ozone in May 2021 is 2.39 ± 0.99 ppbv lower than in May 2017.
- Anthropogenic emission-induced ozone changes account for an upward change of 1.13 ± 0.28 ppbv, while meteorology-induced changes account for a downward change of -0.64 ± 0.83 ppbv over 2017–2021.
- Simulated ozone changes align with three independent observations, including ground-based measurements from TCEQ CAMS, field measurements from SAFS, and space-borne measurements from TROPOMI.
- All the results indicate that highways and urban centers (VOC-sensitive regions) are the major reasons for a positive ozone response to reduced anthropogenic NO_x emissions in 2021 compared to 2017. Lower temperature, higher humidity, stronger Bermuda High, etc., are the meteorological reasons for lower ozone in 2021 than 2017.

3.9.2 Methodology

3.9.2.1 Observations data

This study uses observations from stationary and mobile measurements from the San Antonio Field Studies (SAFS), the routine ground-based measurements from the TCEQ Continuous Ambient Monitoring Stations (CAMS), and the spaceborne TROPOspheric Monitoring Instrument (TROPOMI).

SAFS stationary and mobile measurements used for the analysis:

- For 2017, stationary measurements of ozone (May 1–30), NO_x (May 2–30), and HCHO (May 10–26) at TW as well as ozone (May 6–30), NO_x (May 6–30), and HCHO (May 28–

30) at UTSA in 2017 were used according to data availability of each measurement. The native temporal resolutions for all the variables are 5 minutes.

- For 2021, stationary measurements of ozone, NO_x, and HCHO at TW (during nighttime of April 22–29, daytime and nighttime of April 29–May 12, and nighttime of May 12-18) and UTSA (during daytime of May 16-18) are used.
- For 2021, mobile measurements were taken during daytime of both April 22–29 and May 12–18. The native temporal resolutions are 30 seconds for ozone and NO_x and 5 minutes for HCHO.

Next, routine measurements of hourly ozone and NO_x in 2017 and 2021 were obtained from the CAMS. We obtained the maximum daytime average 8-hour (MDA8) ozone (https://www.tceq.texas.gov/cgi-bin/compliance/monops/8hr_monthly.pl) and the design value (https://www.tceq.texas.gov/cgi-bin/compliance/monops/8hr_attainment.pl) from 2012 to 2022 at three TCEQ sites from TCEQ websites (TCEQ, 2023). The three sites (San Antonio Northwest C23, Camp Bullis C58, and Calaveras Lake C59) were chosen because they met EPA quality assurance criteria and were used for regulatory purposes (EPA, 2015a, 2015b).

Last, we used offline NO₂ and HCHO tropospheric vertical column densities (version 1.4) from the TROPOMI. Launched in October 2017, TROPOMI has spectrometers measuring in the UV–Vis spectral bands and is on sun-synchronous orbits with an overpass at around 13:30 local time. TROPOMI achieves daily global coverage and has a ground pixel resolution of 7 km × 3.5 km (along-track × across-track) before 6 August 2019 and 5.5 km × 3.5 km after 6 August 2019. Due to data availability, data in May 2018 were used to represent May 2017 condition in comparison with May 2021. A physical oversampling approach (Sun et al., 2018) was applied to the NO₂ and HCHO column retrievals. For quality assurance, only observations with the overall quality flag (qa_value) greater than 0.75 and retrieved cloud fraction (cloud_fraction) less than 0.3 are used.

Apart from the observations above, we used geopotential heights and winds at 850 hPa from the European Centre for Medium Range Weather Forecast (ECMWF) reanalysis version5 (ERA5) dataset to derive the synoptic conditions in Figure 3.9.3.20.

3.9.2.2 Model experiments

Table 3.1 summarizes the WRF-GC model simulations to identify the contributions from the changes in anthropogenic emission versus meteorology and associated biogenic emissions between 2017 and 2021. [Year2017] and [Year2021] are standard simulations with both anthropogenic emissions and meteorology in 2017 and 2021, respectively. [Year2021_emis] and [Year2021_met] are counterfactual simulations where [Year2021_emis] has 2017 meteorology and 2021 anthropogenic emissions and [Year2021_met] has 2021 meteorology and 2017 anthropogenic emissions. The differences in ozone concentrations between these simulations represent the contributing effects of anthropogenic emissions, meteorology, and other factors all combined. The ozone differences calculated by [Year2021] minus [Year2017] are combined effects of anthropogenic emission, meteorology and associated biogenic emissions, as well as other

changes between 2017 and 2021 (i.e., overall ozone changes). Among these, the contribution of anthropogenic emission changes can be calculated by [Year2021_emis] minus [Year2017] (i.e., anthropogenic emission-induced ozone changes) and the contribution of meteorological changes can be calculated by [Year2021_met] minus [Year2017] (i.e., meteorology-induced ozone changes).

Table 3.1: List of simulations used in this study.

Simulation	Meteorology	Emission
[Year2017]	2017	2017
[Year2021_emis]	2017	2021
[Year2021_met]	2021	2017
[Year2021]	2021	2021

3.9.3 Results

3.9.3.1 Observed ozone interannual variability in San Antonio

Design value and AQI, the two air quality standards widely used to reflect and regulate ozone concentrations, are used to show the interannual variability of ozone in San Antonio in the recent decade. We show ozone design values in San Antonio from 2012 to 2022 (**Figure 3.101a**), which can be grouped into three stages. The first stage is a rapid reduction over 2012-2016, shifting ozone status in San Antonio from moderate nonattainment ($81 \leq \text{design value} < 93$) to marginal attainment ($71 \leq \text{design value} < 81$) according to the NAAQS 2015 standard. The second stage is a relatively steady period with subtle fluctuation of ozone design values over 2016-2020. The third stage is in and after 2020 when design values start to increase. Meanwhile, **Figure 3.101b** shows the number of days exceeding the AQI standard for ozone each year. Exceedance days with MDA8 ozone greater than 85 ppbv but less than or equal to 105 ppbv are categorized into ‘unhealthy’ ($150 < \text{AQI} \leq 200$); this type of exceedance days occurs at the frequency of less than 5 times annually in and before 2017 but disappears after 2017. Exceedance days with MDA8 ozone greater than 70 ppbv but less than or equal to 85 ppbv are categorized into ‘unhealthy for sensitive groups’ ($100 < \text{AQI} \leq 150$); the numbers of this type of exceedance days fluctuate over years from 4 to 17 occurrences annually.

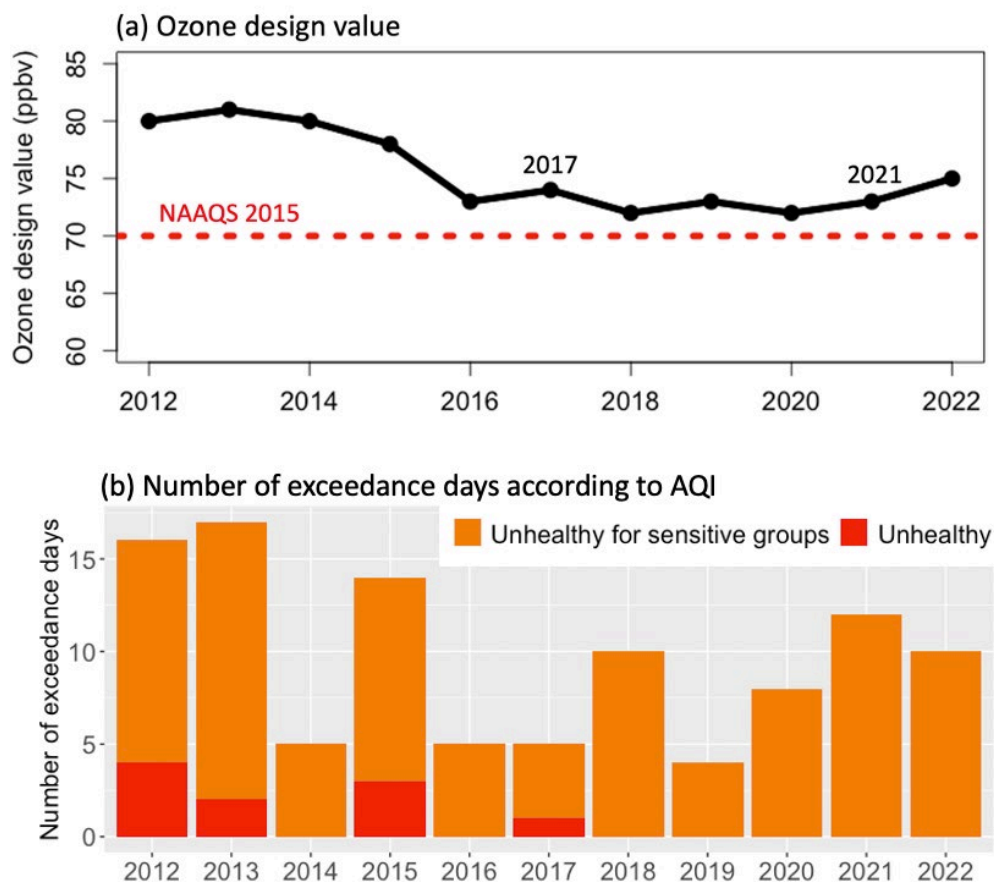


Figure 3.101: (a) The variability of ozone design value in San Antonio from 2012 to 2022. The Red dashed line shows the National Ambient Air Quality Standards (NAAQS) 2015 standard for ozone of 70 ppbv. (b) The number of days exceeding the Air Quality Index (AQI) standard for ozone each year. Orange and red colors represent two AQI categories, that is ‘unhealthy for sensitive groups’ ($100 < AQI \leq 150$; $70 < MDA8 \leq 85$) and ‘unhealthy’ ($150 < AQI \leq 200$; $85 < MDA8 \leq 105$), respectively.

The two campaign years of 2017 and 2021 have similar ozone design values (**Figure 3.101a**) but a varying number of ozone exceedance days (**Figure 3.101b**). 2021 experienced more exceedance days but lower levels of health concern while 2017 had fewer exceedance days but higher levels of health concern. Since the two abovementioned air quality standards are both based on MDA8 ozone concentrations, monthly MDA8 averaged over 2012–2022 is used to examine the representativeness of field campaign months in **Figure 3.102**. Results show that San Antonio ozone events usually occur in two peaks including a spring peak (April to May; mean MDA8 of 45 ppbv) and a summer peak (August to October; mean MDA8 of 43 ppbv). The field campaign months of May belong to the spring peak and represents the annual mean MDA8 of 40 ppbv with a slightly higher concentration of 4 ppbv.

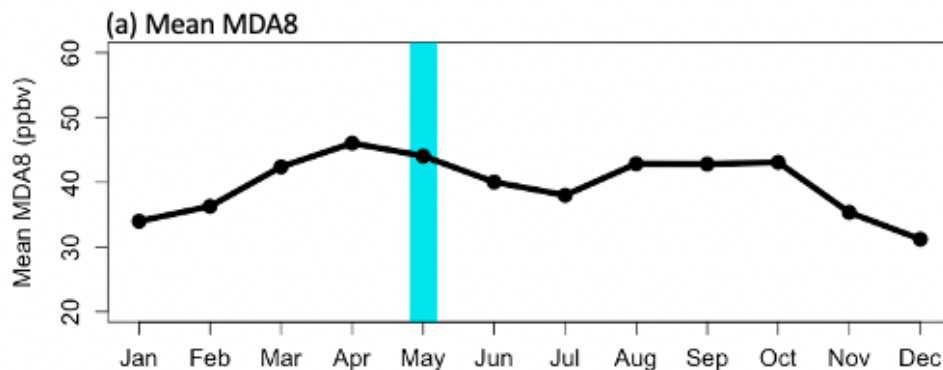


Figure 3.102: The average MDA8 in each month in San Antonio from 2012 to 2022. The blue box highlights the month of May, the intensive operation period during field campaigns in 2017 and 2021.

3.9.3.2 Model evaluation

In this section, we report the comparison of the simulated results from the model with the observation data from April-May 2021 and May 2017. We compared both the spatial (from mobile measurements) and temporal variations of ozone, trace gas, volatile organic compounds (VOCs), and meteorological variables.

3.9.3.2.1 *Simulation of ozone*

Figure 3.103 shows the simulated ozone obtained from the model compared to the observed values for the year 2021 from stationary measurements at Traveler’s World (TW). The time series shown corresponds to the period of April 22–29 (data were from nighttime only), April 29–May 9 (both day and night data), and May 13–19 (only during nighttime), 2021. The figure shows that the simulated values follow closely the changes in the observed ozone levels. However, there is some offset between the time series, as the model overestimates the ozone level particularly when observed ozone levels are low. The mean value for observed ozone is 28.83 ± 13.61 ppbv, while for the simulation the mean value is 47.54 ± 13.07 ppbv. These mean values demonstrate the overestimation from the simulation when both day and nighttime data are combined. It is to be noted that the photochemical models typically overestimate ozone during night hours. Thus, our evaluation with combined day and night measurements includes one of the most challenging modeling scenarios. During the daytime only, as observed from the mobile measurements, simulated results are quite similar to the observation data which demonstrates that during the daytime model captures the ozone variations well. But model overestimates ozone during nighttime as observed from the stationary measurements which is the combination of both day and night data. Nonetheless, the correlation between the simulated and observed ozone is 0.66 which shows that the simulated ozone values do track the changes in the observed ozone values.

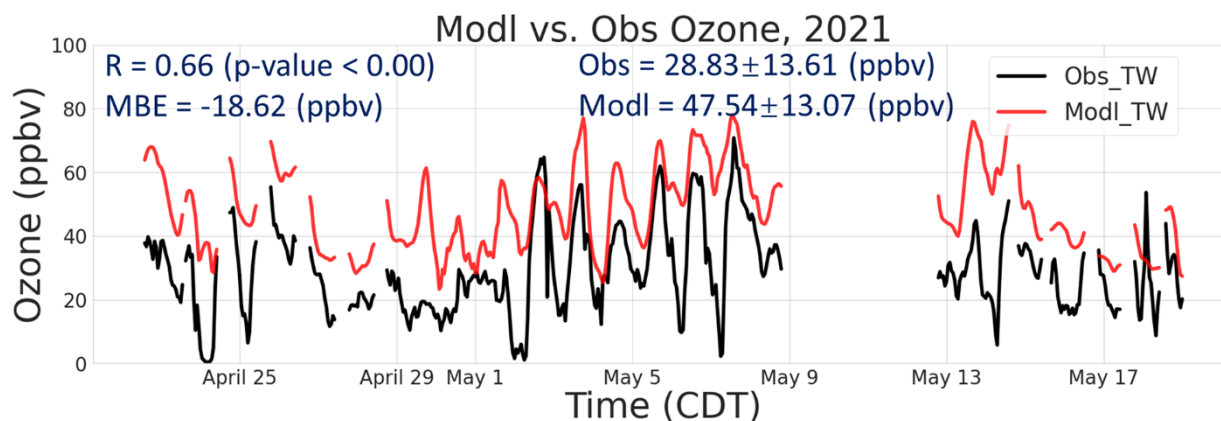


Figure 3.103: Modeled and observed hourly average ozone for stationary data from TW, 2021

In **Figure 3.104**, we show a similar comparison of the observed and simulated ozone for mobile measurements from April 22–29, and May 12–19, 2021. The figure shows that the simulated values follow the trend of the observed values in the mobile-based measurements also. The mean value for the observed values is 39.00 ± 15.69 ppbv, and it is 56.64 ± 14.24 ppbv for the simulated values. The correlation between observed and simulated values is 0.84, which is higher than the correlation obtained for the stationary measurement.

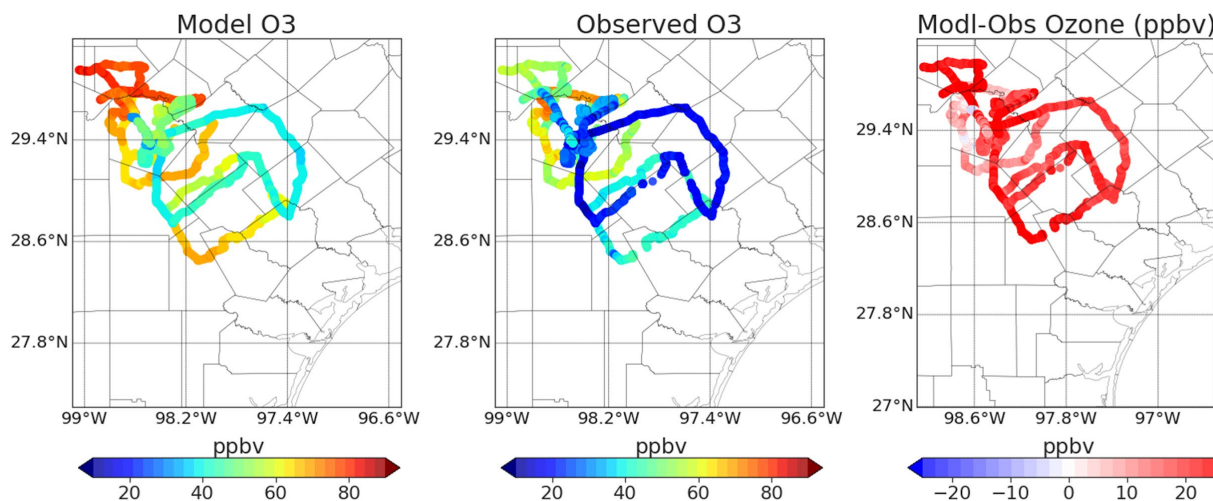


Figure 3.104: Modeled, observed, and difference of modeled and observed ozone for mobile data from SA, 2021

We also compared the simulation and observed ozone for 2017 with the stationary observation data from May 1–30, 2017. **Figure 3.105** shows the simulated and observed ozone for TW and UTSA, where simulated results show a similar trend as that in 2021. The model shows an overestimate of ozone concentration, with a mean of 46.17 ± 14.09 ppbv compared to the mean of 36.51 ± 15.12 ppbv from observation for TW (**Figure 3.105 a**). For UTSA, the mean simulated ozone and observed ozone values are 48.84 ± 14.10 ppbv and 37.84 ± 13.78 ppbv respectively (**Figure 3.105b**). The correlation between the time series of modeled and observed ozone levels

obtained for TW is 0.58 and for UTSA is 0.68. Even though there is an overestimation of ozone, the model is able to capture the trend for both stationary and mobile measurements.

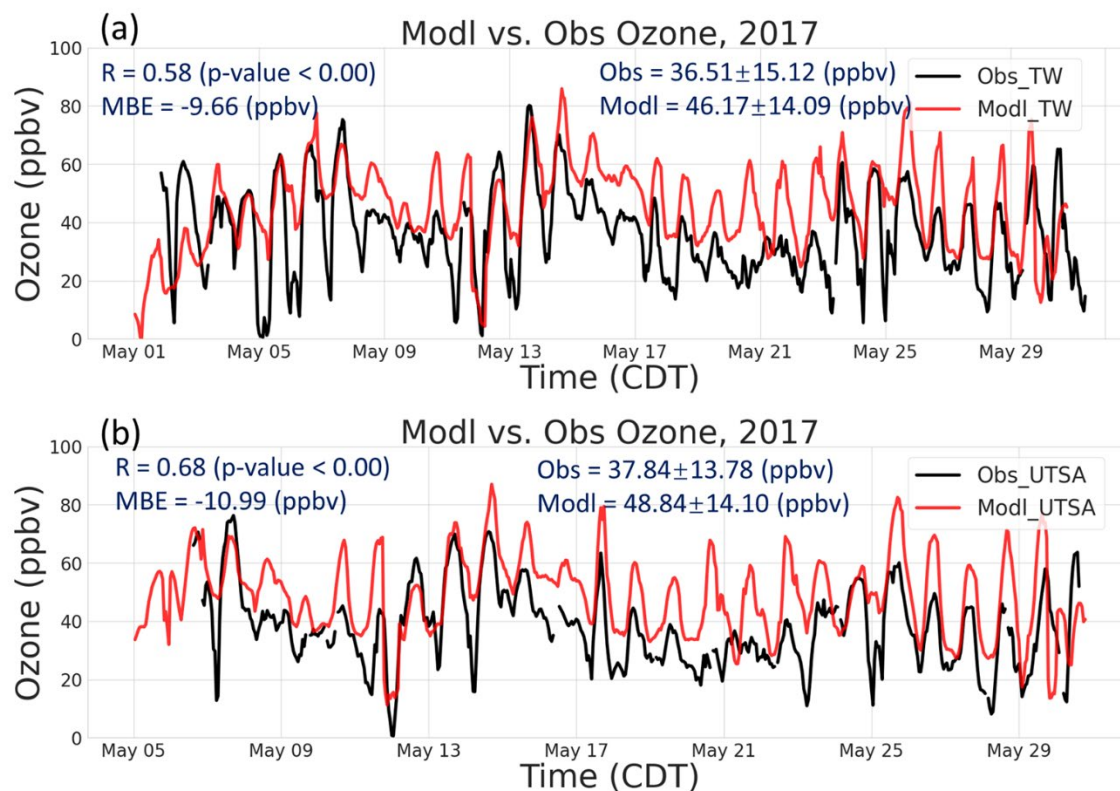


Figure 3.105: Modeled and observed hourly average ozone for stationary data from (a) TW and (b) UTSA, 2017

The scatter plot in **Figure 3.106** compares the modeled and observed ozone for both mobile and stationary data. The plot for mobile data is using the native resolution of the observation data, which is 30 seconds. The stationary data-based plot is obtained with hourly averaging data, combining both TW and UTSA datasets. In the scatter plot based on mobile observations, the modeled and observed values have a correlation of 0.84 and a mean bias error (MBE) of 17.64 ppbv. The model performance is comparable for stationary data in both 2021 and 2017, with a correlation of 0.63 between modeled and observed ozone and an MBE of 18.06 ppbv and 10.26 ppbv, respectively.

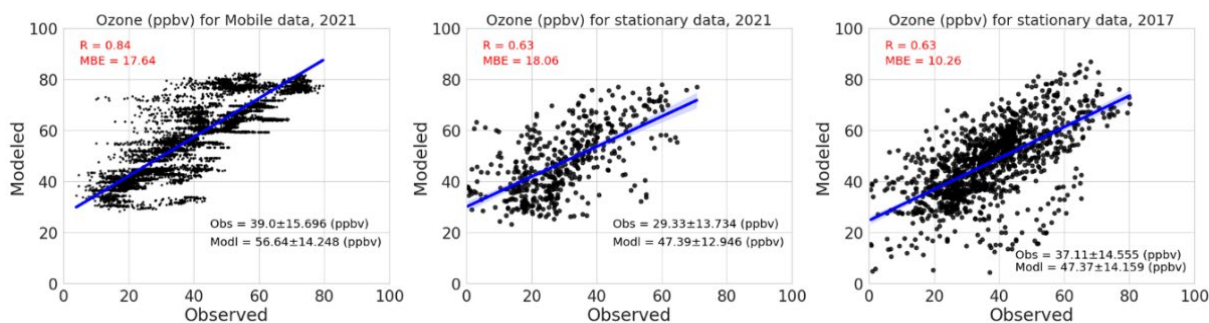


Figure 3.106: Scatter plot for mobile observation of ozone (temporal resolution of 30 seconds) from SA for 2021 and hourly average ozone of stationary data (combining both TW and UTSA data) from 2021 and 2017 respectively.

3.9.3.2.2 *Simulation of trace gases*

Considering the simulation of trace gases from the model, the model underestimates the NO_x ($\text{NO} + \text{NO}_2$) and CO while it overestimates the SO_2 for both mobile and stationary observation from 2021. **Figure 3.107a** shows the timeseries of simulated and observed NO_x for stationary measurements from TW. The model shows an underestimation of NO_x with a mean concentration of 2.86 ± 1.96 ppbv for simulated values compared to observed values which had a mean concentration of 7.79 ± 7.46 ppbv. The error in simulation occurs for both the high and low peaks of observed NO_x but the simulated values capture some variability in the observed values. **Figure 3.107 b, c, & d** shows mobile measurements for observed, simulated NO_x at the measurement locations/time, and the difference between simulated and observed. The model shows an underestimation of mobile measurements of NO_x with a mean concentration of 1.62 ± 1.19 ppbv while observed mean concentration is 20.08 ± 49.70 ppbv. This large underestimation mainly comes from onroad NO_x emissions not well represented in the model. The modeled concentration is 3.01 ± 2.05 ppbv in comparison with observed concentration of 7.87 ± 7.68 ppbv when onroad NO_x ($\text{NO}_x > 20$ ppbv) are avoided/discarded in the comparison.

NO_x underestimation is mainly along the highways stretching out from the urban center (I-37, I-35, I-10; see **Figure 3.107**). This on one hand suggests the high onroad NO_x emissions may not be well represented in the emission inventory, and on the other hand suggests the chemical time steps in the model may not be able to resolve such high- NO_x measurements at a fine temporal resolution of 30 seconds along the highways. Despite such NO_x underestimation along the highways, the levels of ozone overestimation are relatively consistent across urban (high NO_x) and rural (low NO_x) regions, indicating such overestimation is a systematic/universal bias under different chemical environments instead of a chemical-specific issue that happens in a certain type of chemical environment. Therefore, the model simulations can be further used to examine the impacts of anthropogenic emissions and meteorology on ozone levels in the following section of 3.9.3.3.

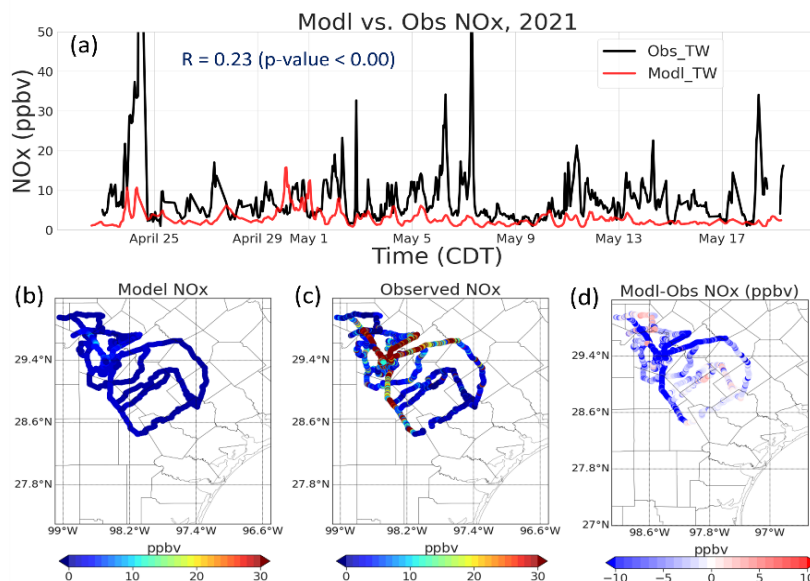


Figure 3.107: Modeled and observed hourly average NO_x for (a) stationary data from TW, 2021 and (b) modeled, (c) observed, and (d) difference of modeled and observed NO_x for mobile data from SA, 2021

Figure 3.108 shows the time series for simulated and observed NO_x of TW and UTSA for May 2017. As compared to 2021, the model is able to better estimate NO_x in 2017 with a correlation of 0.42 and 0.24 for TW and UTSA respectively. In the case of NO_x at TW, the simulated values are underestimated with a mean concentration of 3.35 ± 2.59 ppbv while the observed mean NO_x concentration is 6.32 ± 6.87 ppb. But for UTSA, both modeled and observed mean concentrations are quite close to each other with a mean value of 3.79 ± 2.73 and 3.68 ± 2.76 ppbv respectively.

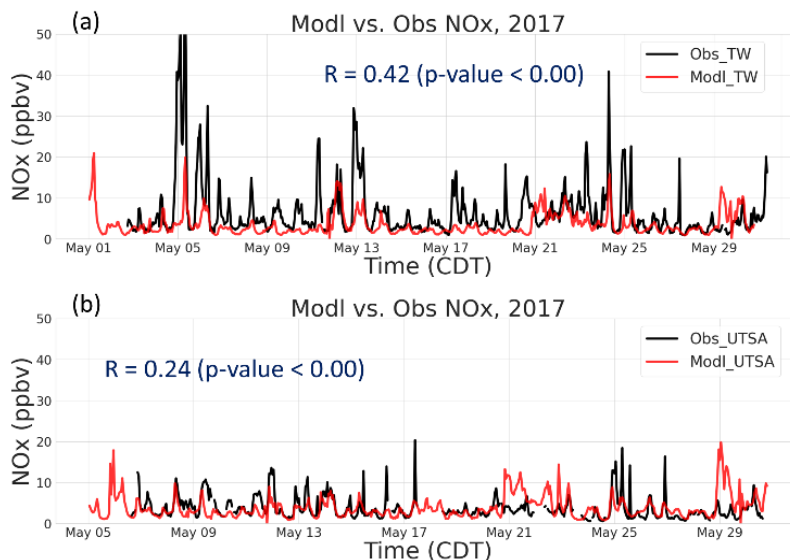


Figure 3.108: Modeled and observed hourly average NO_x for stationary data from TW and UTSA, 2017

Figure 3.109 shows a scatter plot that compares simulated and observed NO_x levels for both mobile and stationary measurements. The correlation between simulated and observed values for

mobile measurements is 0.27, and the mean bias error (MBE) is -18.4 ppbv. For stationary measurements in 2021 (combined TW and UTSA), the correlation between simulated and observed values is 0.24, while in 2017 it is 0.32. **Table 3.2** provides detailed statistics comparing simulated and observed values for all trace gases. The results suggest that the model cannot fully capture the trends in emissions for trace gases, as evidenced by lower correlations between simulated and observed values.

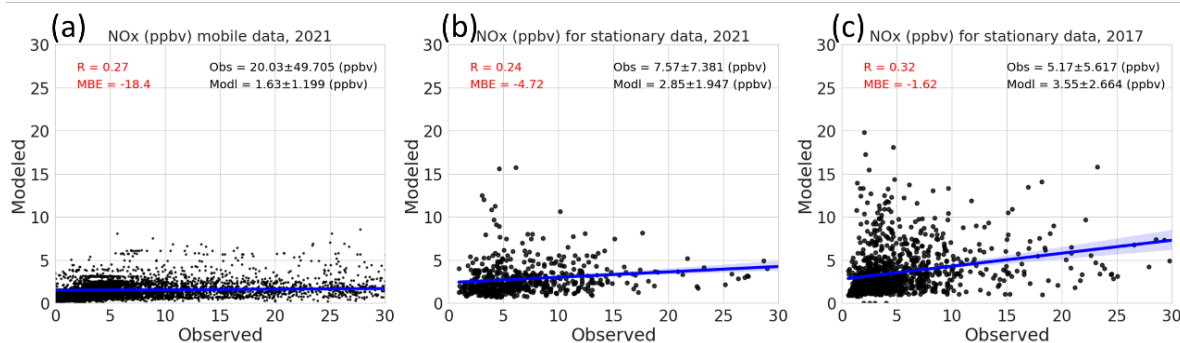


Figure 3.109: Scatter plot for (a) mobile observation of NO_x from SA for 2021 and hourly average NO_x of stationary data (combining both TW and UTSA data) from (b) 2021 and (c) 2017 respectively.

Table 3.2: Performance metrics of NO_x, CO, and SO₂ from WRF-GC simulation (1km x 1km domain) in comparison with observation data for 2021 and 2017

Variable	Region: SA	Obs	Modl	MBE	RMSE	R
NO _x (ppbv) (2021)	TW (stationary)	7.79±7.46	2.86±1.96	-4.83	8.17	0.23
	Mobile measurements	20.08±49.70	1.62±1.19	-18.04	52.71	0.26
CO (ppbv) (2021)	TW (stationary)	178.23±68.72	136.40±26.14	-41.83	80.30	0.19
	Mobile measurements	245.86±356.88	133.23±23.04	-112.63	369.30	0.25
SO ₂ (ppbv) (2021)	TW (stationary)	0.06±0.14	0.44±0.59	0.37	0.70	0.17
	Mobile measurements	0.08±0.27	0.33±0.41	0.25	0.56	-0.07
NO _x (ppbv) (2017)	TW (stationary)	6.32±6.87	3.35±2.59	-2.96	6.89	0.42
	UTSA (stationary)	3.68±2.76	3.79±2.73	0.10	3.38	0.24

Variable	Region: SA	Obs	Modl	MBE	RMSE	R
CO (ppbv) (2017)	TW (stationary)	170.91±63.35	131.11±30.70	-39.79	71.93	0.35
	UTSA (stationary)	154.40±42.24	137.13±27.55	-17.27	49.54	0.16
SO ₂ (ppbv) (2017)	TW (stationary)	0.15±0.53	0.36±57	0.20	0.72	0.22
	UTSA (stationary)	0.34±0.69	0.41±0.60	0.07	0.91	0.01

3.9.3.2.3 *Simulation of VOCs*

Figure 3.110 shows the simulated and observed HCHO for stationary and mobile observation from the SA region. The timeseries in the top pane of the figure shows the observed and simulated HCHO from the TW stationary dataset. The model underestimates HCHO with a mean value of 1.52 ± 0.97 ppbv for the simulated data compared to 2.38 ± 0.97 ppbv from the observation. As seen from the time series, during night, model has a larger underestimation of HCHO but during the daytime there is lesser offset between simulated and observed values. For the mobile measurement, the model follows a similar pattern as in the stationary case with an underestimation of HCHO by 45.29%. The mean concentration of simulated HCHO is 2.07 ± 0.92 ppbv compared to mean concentration value of 3.79 ± 0.99 ppbv for the observed values. The correlation between the observed and simulated HCHO for stationary measurement is 0.28 while the correlation is slightly higher with a value of 0.47 in the mobile case.

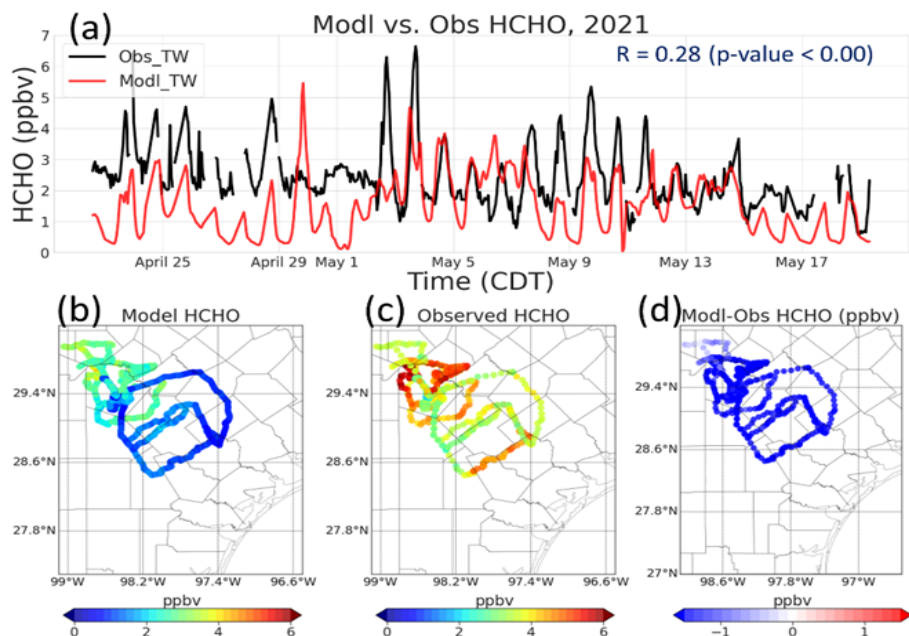


Figure 3.110: (a) Modeled and observed hourly average HCHO for stationary data from TW, 2021 and (b) modeled, (c) observed, and (d) difference of modeled and observed HCHO for mobile data from SA, 2021

As the model underestimated the HCHO, we also looked over the other VOCs such as isoprene where model shows a different trend. **Figure 3.111** shows the modeled and observed isoprene emissions for both stationary and mobile data. The time series for stationary data indicates that the model assumes isoprene emissions to be zero during nighttime but captures the trend during daytime. However, the model overestimates daytime isoprene. Combining both daytime and nighttime stationary data, the model has a mean concentration of 1.01 ± 1.34 ppbv compared to observed mean concentration of 1.03 ± 0.43 ppbv. On the other hand, for mobile measurements, the model overestimates the isoprene, with an average of 5.60 ± 3.84 ppbv compared to 1.37 ± 0.52 ppbv from the observation data. During the daytime, models overestimate the isoprene, while during the nighttime it underestimates the isoprene. The correlation between the model and observation data is higher for stationary data with a value of 0.57, compared to 0.50 for mobile measurements.

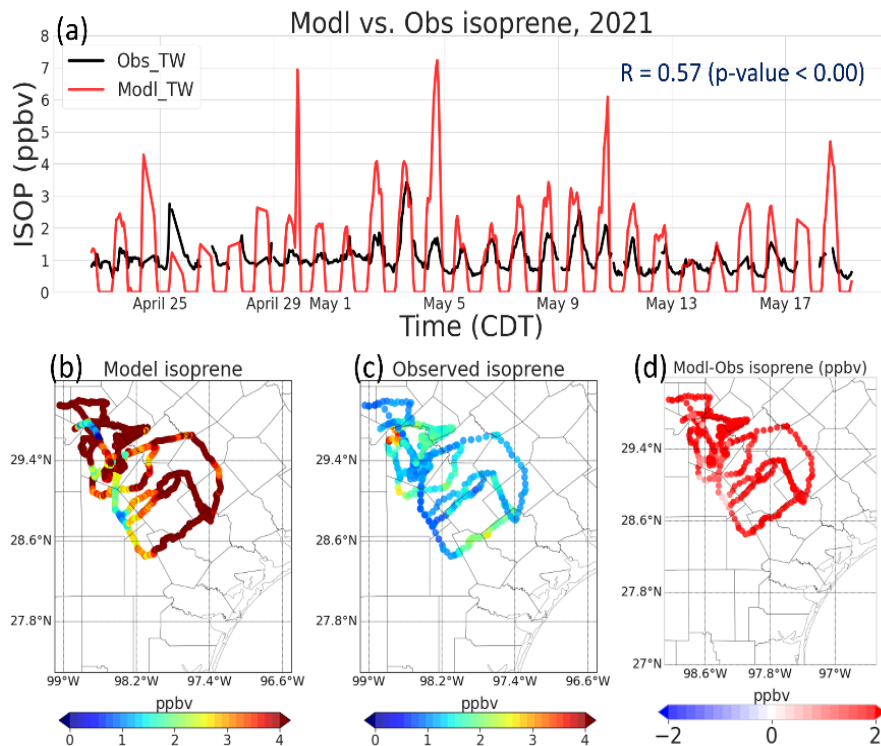


Figure 3.111: (a) Modeled and observed hourly average isoprene for stationary data from TW, 2021 and (b) modeled, (c) observed, and (d) difference of modeled and observed isoprene (lower left to right) for mobile data from SA, 2021

Figure 3.112 show the time series comparing modeled and observed HCHO and isoprene data from TW stationary site in 2017. The model's VOC prediction pattern is similar for both 2017 and 2021. The model underestimates HCHO, with an average value of 1.70 ± 1.00 ppbv compared to observed value of 2.50 ± 1.17 ppbv. The correlation between modeled and observed HCHO is 0.46, indicating that the model captures the HCHO trend reasonably well. On the other hand, the model simulates isoprene variations better in 2021 than 2017. The correlation coefficients between modeled and observed isoprene concentrations [at TW](#) are 0.57 in 2021 (**Figure 3.113**) but 0.18 in 2017. For mobile measurements, there is a systematic overestimation of less than 2 ppbv in the model.

To further compare modeled and observed values of VOCs, we examined the scatter plot between modeled and observed values. **Figure 3.113** presents the scatter plot for both mobile observation data and stationary data (combined TW and UTSA data) for 2021 and 2017. The scatter plot of HCHO for stationary data shows that for both 2021 and 2017, model performance is similar. However, for isoprene, the model prediction is better for 2021 compared to 2017. The detailed performance matrices for HCHO and isoprene are presented in **Table 3.3**.

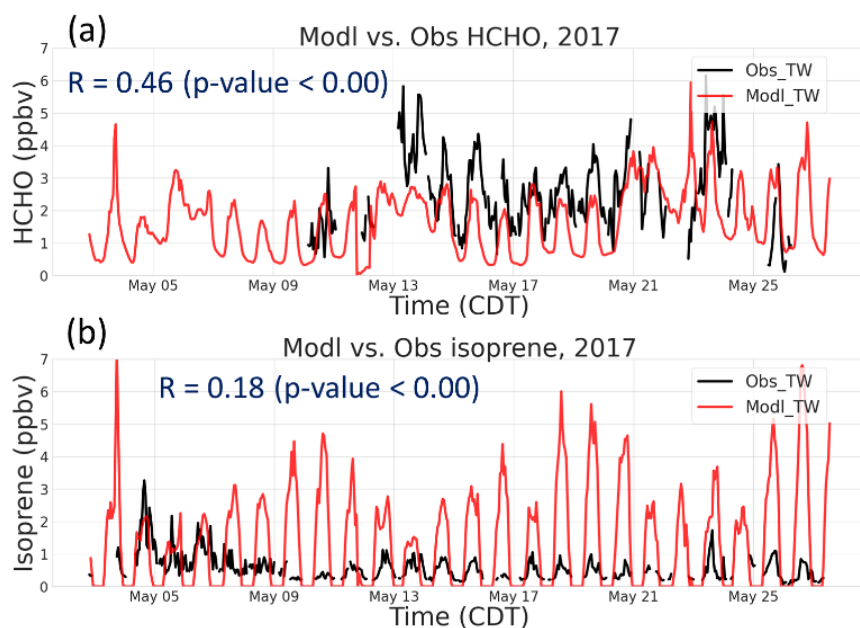


Figure 3.112: Modeled and observed hourly average HCHO (top) and isoprene (bottom) for stationary data from TW, 2017

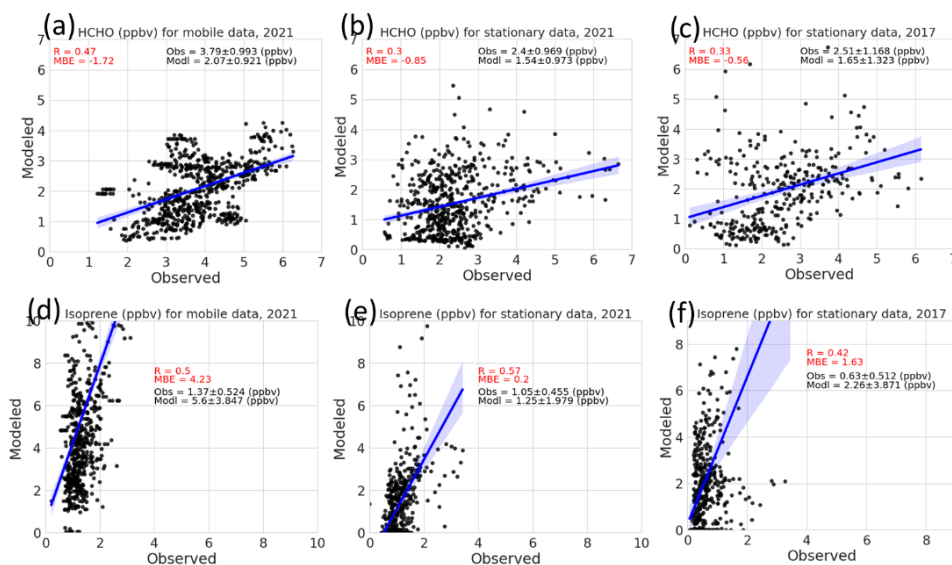


Figure 3.113: Scatter plot for mobile observation of (a) HCHO and (d) isoprene from SA for 2021 and hourly average HCHO and isoprene of stationary data (combining both TW and UTSA data) from (b&e) 2021 and (c&f) 2017 respectively.

Table 3.3: Performance metrics of HCHO and isoprene from WRF-GC simulation (1km x 1km domain) in comparison with observation data from TW and UTSA for 2021 and 2017

Variable	Region: SA	Obs	Modl	MBE	RMSE	R
HCHO (ppbv) (2021)	TW (stationary)	2.38±0.97	1.52±0.97	-0.85	1.44	0.28
	Mobile measurements	3.79±0.99	2.07±0.92	-1.71	1.98	0.47
Isoprene (ppbv) (2021)	TW (stationary)	1.03±0.43	1.01±1.34	-0.02	1.15	0.57
	Mobile measurements	1.37±0.52	5.60±3.84	4.23	5.56	0.50
HCHO (ppbv) (2017)	TW (stationary)	2.50±1.17	1.70±1.00	-0.80	1.39	0.46
	UTSA (stationary)	2.49±1.10	3.48±1.89	0.99	2.26	0.15
Isoprene (ppbv) (2017)	TW (stationary)	0.57±0.42	1.52±1.56	0.95	1.81	0.18
	UTSA (stationary)	1.12±0.85	8.59±8.88	7.47	11.34	0.45

3.9.3.2.4 Simulation of meteorological variable

Figure 3.114 shows the temperature and relative humidity data for both simulated values from the model and observed values collected from TW for 2021 and TW/UTSA in 2017. The simulated data follows the trend in the observation data for the meteorological variables. However, the temperature is slightly overestimated by the model, with an average of 24.55 ± 4.08 °C compared to the observation's average of 22.52 ± 4.46 °C for 2021 stationary data. Interestingly, the model is able to capture the observation trend better for 2017 than in 2021 with an average temperature of 25.88 ± 4.32 °C from model and 25.05 ± 4.53 °C from observation for TW, and 24.72 ± 4.69 °C and 24.24 ± 4.35 °C for UTSA respectively. The correlation between modeled and observed temperature values is 0.77 for 2021 and 0.80 and 0.84 for TW and UTSA, respectively. Additionally, both 2021 and 2017 exhibit a slight underestimation of relative humidity by the model.

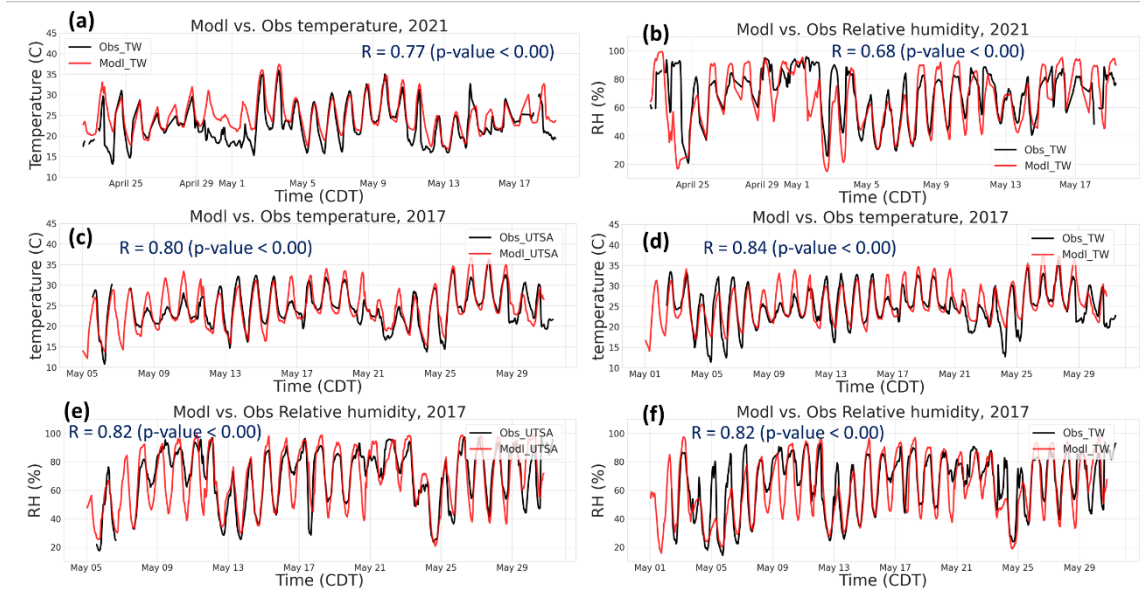


Figure 3.114: Modeled and observed hourly average temperature and relative humidity for stationary data from TW and UTSA. (a) temperature at TW, 2021, (b) RH at TW, 2021, (c) temperature at UTSA, 2017, (d) temperature at TW, 2017, (e) RH at UTSA, 2017, and (f) RH at TW, 2017

In **Figure 3.115**, the scatter plot displays the modeled and observed values for both temperature and relative humidity in mobile and stationary scenarios. The scatter plot for data from the mobile scenario shows data point with a temporal resolution of 30 seconds. Here, the model overestimated temperature with an MBE of 2.0 °C and underestimated RH with an MBE of -6.92 %. The stationary dataset, which combines TW and UTSA datasets, also shows that the model overestimated temperature with an MBE of 1.97 °C and 0.68 °C and underestimated the RH with an MBE of -3.38 % and -1.6 % for 2021 and 2017, respectively. From the scatterplot, it can be inferred that the model’s performance is better in 2017 compared to 2021 for the meteorological variables.

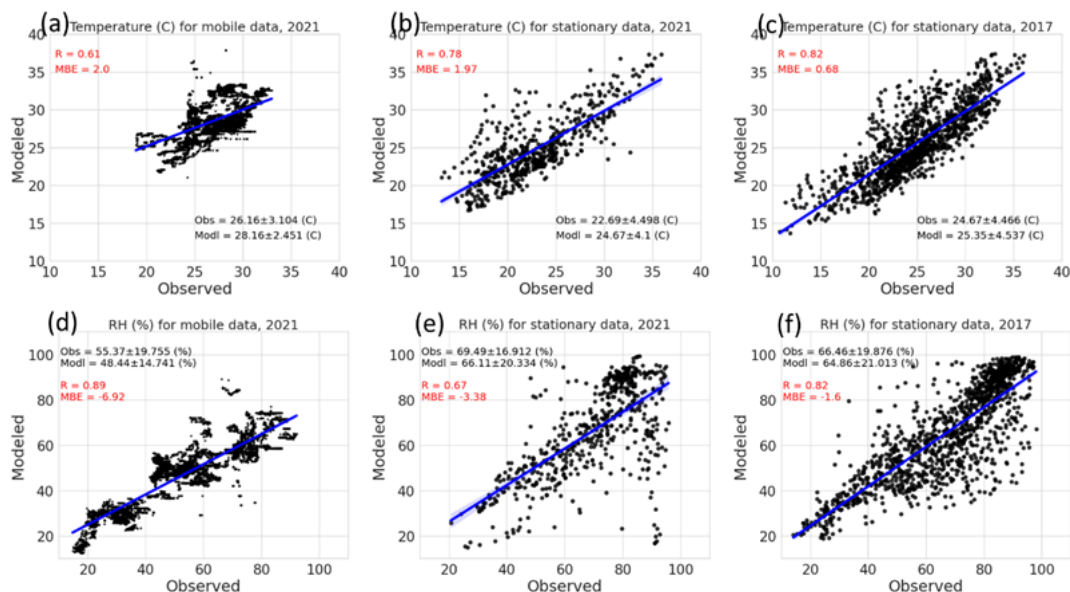


Figure 3.115: Scatter plot for mobile observation of (a) temperature and (d) relative humidity from SA for 2021 and hourly average temperature and relative humidity of stationary data (combining both TW and UTSA data) from (b&e) 2021 and (c&f) 2017 respectively.

3.9.3.3 Modeled ozone changes between 2017 and 2021

Sensitivity simulations are used to investigate the effects of different factors on the changes in the monthly mean surface ozone in May between 2017 and 2021 in San Antonio. **Figure 3.116a** shows the overall ozone changes due to the combined effects of anthropogenic emissions, meteorology and associated biogenic emissions, and other factors between 2017 and 2021, calculated by [Year2021] minus [Year2017]. The regional mean difference is -2.39 ± 0.99 ppbv (5%-95% interval: $-0.73 - -3.83$ ppbv) from 2017 to 2021 (**Figure 3.116**). Among different contributing factors, **Figure 3.116b** shows the contributions of anthropogenic emission changes to surface ozone defined by [Year2021_emis] minus [Year2017] (i.e., anthropogenic emission-induced ozone changes) while **Figure 3.116c** shows the contributions of changing meteorology and associated biogenic emissions defined by [Year2021_met] minus [Year2017] (i.e., meteorology-induced ozone changes). The regional mean differences are 1.13 ± 0.28 ppbv (5%-95% interval: $0.77 - 1.62$ ppbv) due to changes in anthropogenic emissions (**Figure 3.116b**), and -0.64 ± 0.83 ppbv (5%-95% interval: $-0.73 - -2.40$ ppbv) due to changes in meteorology and associated biogenic emissions (**Figure 3.116c**). Other factors such as different fire emissions in 2017 and 2021 are not investigated here in this project, but are worth further investigation.

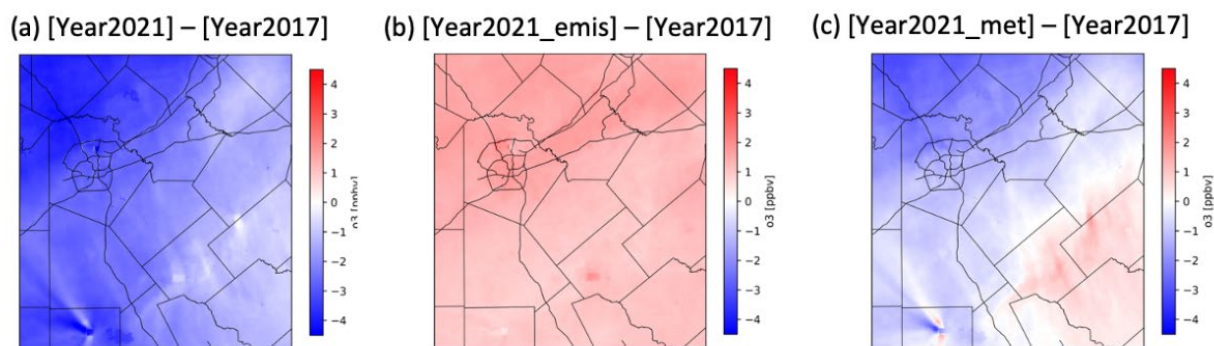


Figure 3.116: Changes in monthly mean surface ozone in May between 2017 and 2021. (a) Overall changes calculated by [Year2021] minus [Year20217]. (b) Changes due to anthropogenic emissions, calculated by [Year2021_emis] minus [Year20217]. (c) Changes due to meteorology and biogenic emissions, calculated by [Year2021_met] minus [Year20217].

3.9.3.3.1 Impact of anthropogenic emission changes on ozone

We performed sensitivity simulations to investigate the impacts of anthropogenic emissions versus meteorology on the changes in spring ozone in San Antonio between 2017 and 2021. This section shows the impacts of changes in anthropogenic emissions, defined by the [Year2021_emis] simulation minus the [Year20217] simulation. Results show that the regional averaged anthropogenic emission-induced ozone changes are 1.13 ± 0.28 ppbv from 2017 to 2021 (**Figure 3.116b**). To explain such ozone changes, NO_2 (**Figure 3.117**) and HCHO (**Figure 3.118**) concentrations in 2017 and 2021 are shown as proxies for ozone precursor NO_x and VOCs, respectively. The ratio of HCHO to NO_2 (i.e., HCHO: NO_2) is widely used as an indication of ozone formation regime that explains ozone responses to changes in emissions (Y Choi, Kim, Tong, & Lee, 2012; Yunsoo Choi & Souri, 2015; Jin et al., 2017; Martin, Fiore, & Van Donkelaar, 2004).

With a short atmospheric lifetime of about 1.8 to 7.5 hours (Liu et al., 2016), NO_2 is highly reactive and concentrated near the sources. The simulated monthly mean NO_2 concentration is 1.71 ± 0.69 ppbv in May 2021, 0.3 ± 0.2 ppbv (15%) lower than that in May 2017 (2.01 ± 0.89 ppbv), as in **Figure 3.117 a**. As comparisons, three independent sources of NO_2 observations are shown in **Figure 3.117 b** (TROPOMI), **Figure 3.117 c** (field measurements), and **Figure 3.117 d** (CAMS). The space-borne TROPOMI shows the tropospheric NO_2 vertical column density is $1.28 \pm 0.21 \times 10^{15}$ molec cm^{-2} in May 2021, 0.05 ± 0.1 molec cm^{-2} (4%) lower than that in May 2017 ($1.33 \pm 0.31 \times 10^{15}$ molec cm^{-2}), as in **Figure 3.117 b**. The field stationary measurements of NO_2 concentrations are 5.55 ± 1.96 ppbv in May 2021, 0.08 ± 0.043 ppbv (2%) lower than that in May 2017 (5.64 ± 1.87 ppbv), as in **Figure 3.117 c**. The ground-based CAMS measurements of NO_2 concentrations are 5.82 ± 5.48 ppbv in May 2021, 0.58 ± 0.96 ppbv (9%) lower than that in May 2017 (6.40 ± 5.39 ppbv), as in **Figure 3.117 d**. In summary, three independent measurements show 2%-9% lower NO_2 concentrations in 2021 compared to 2017, which is consistent with the 15% simulated by the model.

Atmospheric HCHO is one of the significant oxidization intermediates of most VOCs and thus is used widely as a proxy for VOCs. The tropospheric HCHO background concentrations are largely controlled by methane oxidation while its regional concentrations are contributed by short-lived non-methane VOCs (Zhu et al., 2020; Zhu et al., 2016). **Figure 3.118 a** shows that the simulated monthly mean HCHO concentration in May 2021 is 1.24 ± 0.27 ppbv, 0.04 ± 0.08 ppbv (3.6%) lower than that in May 2017 (1.28 ± 0.35 ppbv). As comparisons, two independent sources of HCHO observations are shown in **Figure 3.118 b** (TROPOMI) and **Figure 3.118 c** (field measurements). The CAMS measurements are not presented here because of no HCHO measurements in 2017 and 2021. The space-borne TROPOMI shows the tropospheric HCHO vertical column density in May 2021 is $6.09 \pm 1.56 \times 10^{15}$ molec cm^{-2} , 0.07 ± 0.32 molec cm^{-2} (1%) lower than that in May 2017 ($6.16 \pm 1.88 \times 10^{15}$ molec cm^{-2}), as in Figure 3.9.3.18b. The field stationary measurements of HCHO concentrations are 2.43 ± 1.06 ppbv, 0.05 ± 0.02 ppbv (2%) lower than that of 2017 (2.49 ± 1.44 ppbv), as in **Figure 3.118c**. In summary, measurements do not exhibit significant HCHO differences between the two years and show only 1%-2% lower HCHO concentrations in 2021, which is consistent with the 3.6% simulated by the model.

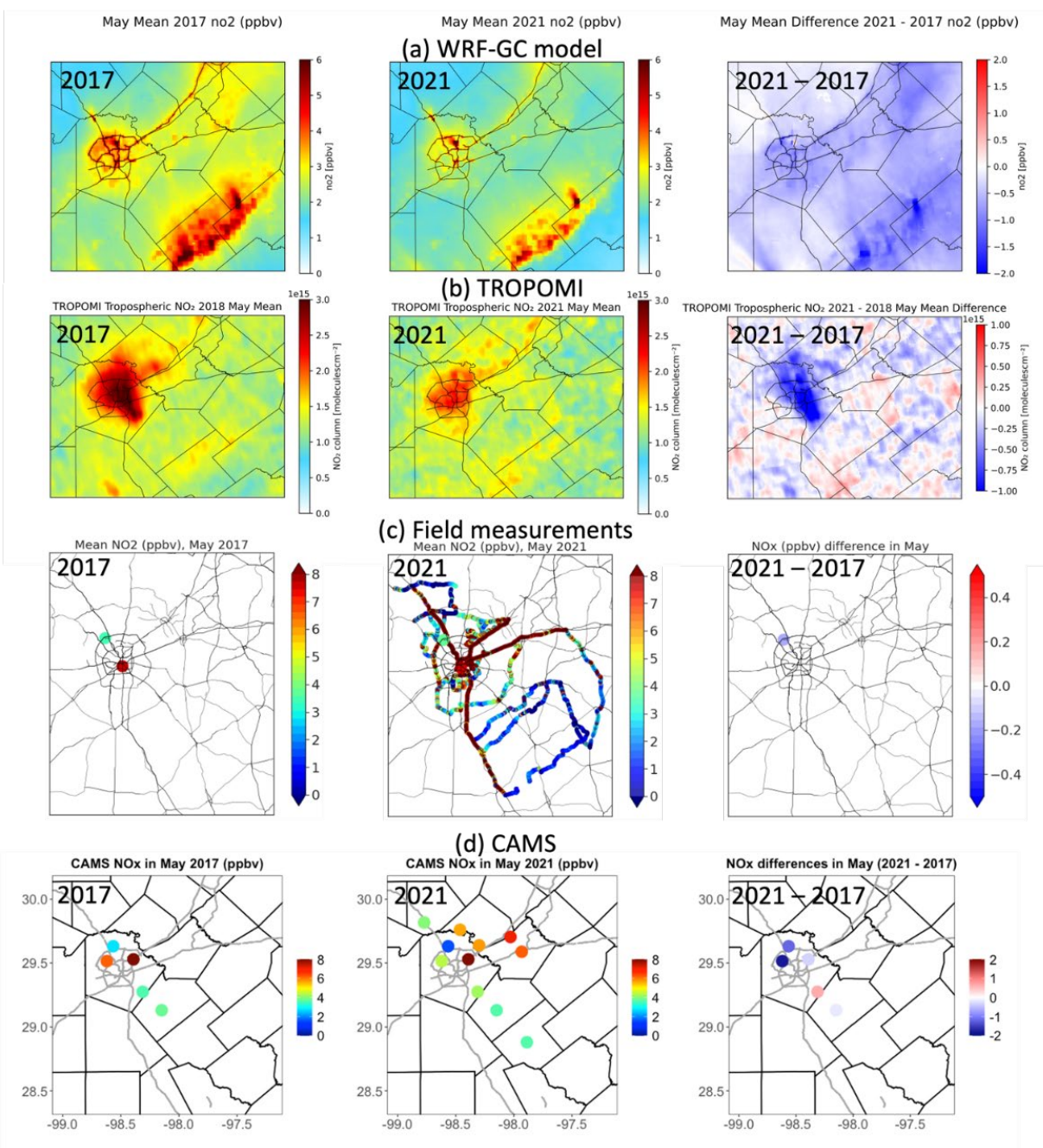


Figure 3.117: Monthly mean NO₂ concentrations in May 2017 (left) and May 2021 (middle) and the differences of 2021 minus 2017 (right) from (a) the WRF-GC model, (b) TROPOMI, (c) field measurements, and (d) CAMS.

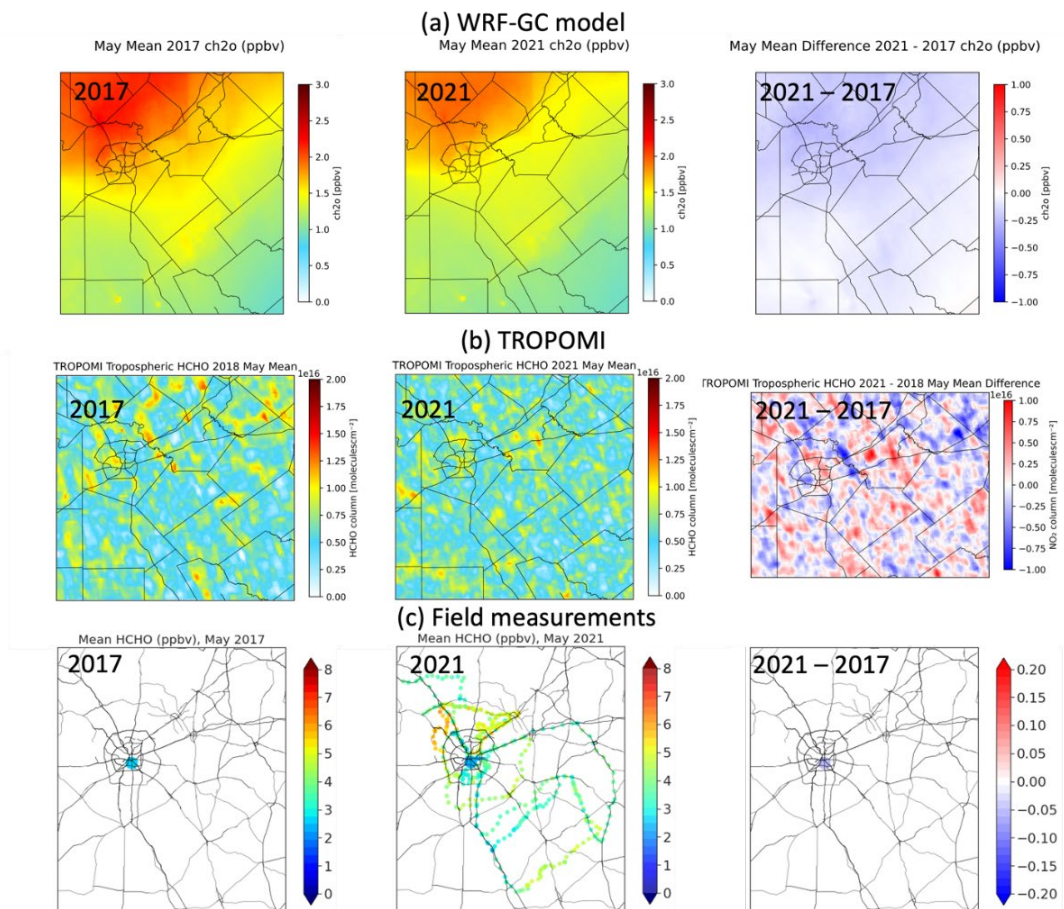


Figure 3.118: Monthly mean HCHO concentrations in May 2017 (left) and May 2021 (middle) and the differences of 2021 minus 2017 (right) from (a) the WRF-GC model, (b) TROPOMI, and (c) field measurements.

The ratio of HCHO to NO₂ is widely used as an indicator of the ozone formation regime because the relative ambient concentrations of HCHO and NO₂ reflect the reactivity-weighted concentrations of VOCs and NO_x, respectively (Valin, Fiore, Chance, & González Abad, 2016). A tropospheric column HCHO-to-NO_x ratio less than 2.6 indicates a VOC-sensitive regime, a ratio between 2.6 to 3.5 indicates a transitional regime and a ratio greater than 3.5 indicates a NO_x-sensitive regime; such thresholds were derived for the Houston region according to relationships between multi satellite observations of ozone precursors and ground-based ozone observations (Jin, Fiore, Boersma, Smedt, & Valin, 2020). Due to the close geographical distance between Houston and San Antonio, we adopt the same thresholds to indicate different ozone formation regimes in San Antonio while simultaneously noting that these values should not be static in all scenarios. For example, the same column thresholds may not work for surface ratio that is derived from field measurements of surface concentrations. Therefore, we first compare the observed (**Figure 3.119**) and modeled (**Figure 3.119b**) surface ratio to verify that the model well represents the observations, and then use the modeled tropospheric column ratio (**Figure 3.119c**) to denote ozone formation regimes. Results show that the suburban San Antonio and surrounding areas are generally

simulated to be NO_x-sensitive, which is consistent with satellite (Yunsoo Choi & Souri, 2015; Goldberg et al., 2022) and surface (Guo et al., 2021) observational findings. Yet, the major highways and urban centers remain VOC-sensitive due to the large amount of NO_x emissions due to transportation.

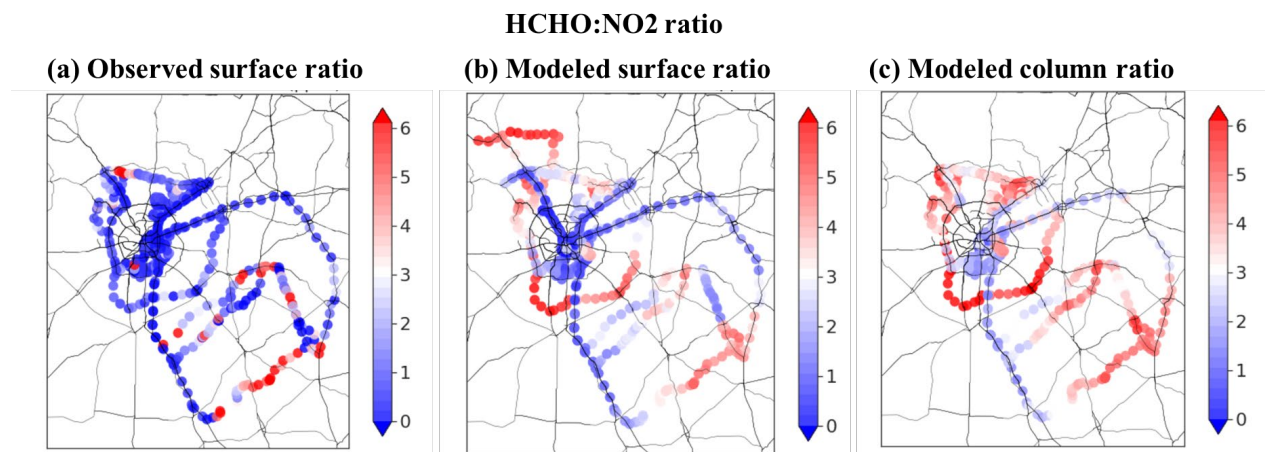


Figure 3.119: Surface HCHO:NO₂ ratio from (a) the mobile field measurements and (b) the WRF-GC model, in comparison with (c) the tropospheric column ratio from the WRF-GC model in May 2021.

3.9.3.3.2 Impact of meteorological changes on ozone

This section shows the impacts of meteorology on the changes in spring ozone in San Antonio between 2017 and 2021, defined by the [Year2021_met] simulation minus the [Year2017] simulation. Results show that the regional averaged ozone changes are -0.64 ± 0.83 ppbv from 2017 to 2021 (**Figure 3.116 c**); this is the combined impacts of meteorological changes and associated changes in biogenic emissions, chemical production and loss, etc. The simulated monthly mean air temperature in May 2021 is 23.76 ± 3.82 °C, 0.68 ± 0.3 °C lower than that in May 2017 (24.44 ± 4.12 °C), as in **Figure 3.120 a**. The simulated relative humidity in May 2021 is 77.60 ± 19.50 %, 8.1 ± 1.77 % higher than that in May 2017 (69.50 ± 21.27 %), as in **Figure 3.120b**. In 2017, higher temperature enhances ozone mainly through increased biogenic emissions and higher abundance of NO_x while lower humidity reduces the chemical loss rate of ozone (Jacob and Winner, 2009). **Figure 3.120 c** shows that the simulated monthly mean boundary layer height in May 2021 is 648 ± 410 m, 39 ± 37 m lower than that in May 2017 (687 ± 447 m). In 2021, lower boundary layers can lead to lesser vertical mixing and more ozone deposition and favor aerosol heterogeneous reactions to uptake ozone precursors, resulting in reduced ozone concentrations.

Figure 3.120 e and **f** compare the May mean wind fields and the geopotential heights at 850 hPa in 2017 versus 2021. The Bermuda High quasi-permanent pressure system is the key large-scale circulation pattern influencing weather over the eastern and southern US. The Bermuda High longitudinal index, defined as the longitude of the cross-point of the 1560 geopotential meter isoline and the 850 hPa wind ridgeline (Wang et al., 2016), shows the west extension of the Bermuda High. Comparing **Figure 3.120 e** and **Figure 3.120 f**, the Bermuda High is stronger and

extends closer to Texas in May 2021 than May 2017, indicating stronger maritime influence and thus lower surface ozone concentrations in San Antonio during May 2021 than May 2017. Meanwhile, higher wind speeds favor ozone dispersion in 2021 while low wind speeds limit ozone dispersion in 2017. All the meteorological differences (incl. temperature, humidity, winds, the Bermuda High, etc.) between 2017 and 2021 led to relatively lower spring ozone in 2021 compared to 2017.

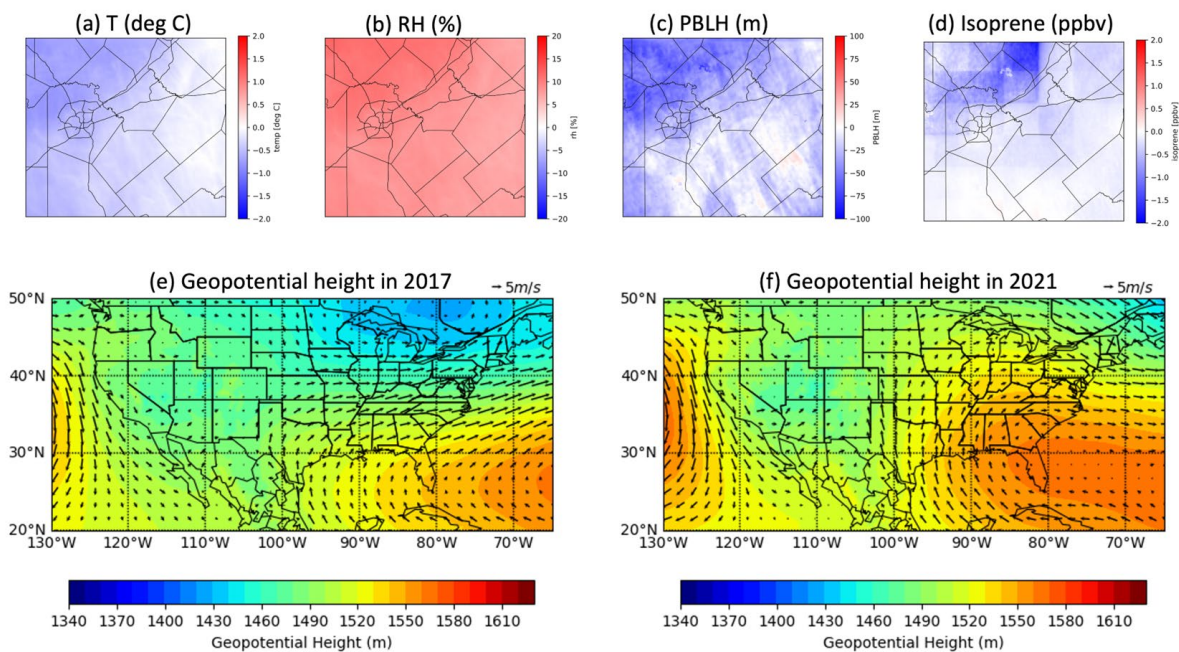


Figure 3.120: Changes in May mean (a) air temperature, (b) relative humidity, (c) planetary boundary layer height, and (d) isoprene concentration from 2017 to 2021. Monthly mean wind fields and geopotential heights at 850 hPa in (e) May 2017 and (f) May 2021.

4 Recommendations for Future Work

The 2021 San Antonio Field Study and this subsequent analysis project have developed findings that should be helpful in addressing air quality issues in the San Antonio region, however additional studies may yield new information that can be used to inform various control strategies.

- The original field study was planned to be in August/September of 2020 but had to be delayed due to COVID-related issues and was subsequently rescheduled for May 2021. It may be useful to deploy another field study to examine whether the chemistry and dynamics of ozone, and potentially PM_{2.5}, are similar between the spring and summer periods.
- This study highlighted the interactions between biogenic VOCs emissions and regional droughts in the San Antonio area and the potential implications of droughts on air quality. Specifically, future studies should seek to understand how ecosystems respond to droughts and the resulting impacts on atmospheric chemistry and subsequent air quality. This research would build on our understanding of how reactive compounds emitted by vegetation (e.g., isoprene and monoterpenes) can react with NO_x and sunlight to produce ozone. Below are additional suggestions for future studies:
 - Building on the SAFS II study, assess how under drought conditions, changes in BVOC emissions (increase in drought should increase BVOC emissions) and soil NO_x emissions (increases in drought should increase NO_x emissions) can affect the availability of ozone precursors and alter the ozone formation potential.
 - Mobile field campaign using the BU/UH Mobile Air Quality Laboratory. Investigate and measure atmospheric BVOC, NO_x, and ozone concentrations across large spatial gradients (county level) under different drought conditions. Assess how ozone is impacted by different regional drought conditions (e.g., severity and duration).
 - Multi-scale approach - understanding is critical to investigating these interactions across different scales (i.e. field-based measurements (mobile campaigns), remote sensing, satellite and modeling efforts).
 - The mobile field campaign (see above) data can be coupled with remote sensing, satellite and modeling to better predict and mitigate the impact of drought on air quality.
- Publish a paper (Shrestha et al., in preparation) using a compare and contrast approach to explore the potential impact of the 2021 drought on BVOCs emission during SAFS including increased concentrations and potential shifts in peak diurnal ambient concentrations of monoterpenes.

5 References

- Aiken, A. C., et al. (2008), O/C and OM/OC ratios of primary, secondary, and ambient organic aerosols with high-resolution time-of-flight aerosol mass spectrometry, *Environmental Science & Technology*, 42(12), 4478-4485, doi:10.1021/es703009q.
- Anderson, D. C., J. Pavelec, C. Daube, S. C. Herndon, W. B. Knighton, B. M. Lerner, J. R. Roscioli, T. I. Yacovitch, and E. C. Wood (2019), Characterization of ozone production in San Antonio, Texas, using measurements of total peroxy radicals, *Atmos. Chem. Phys.*, 19(5), 2845-2860, doi:10.5194/acp-19-2845-2019.
- Chen, S., Ren, X., Mao J., Chen, Z., Brune, W. H., Lefer, B., Rappengluck, B., Flynn J., Olson, J., and Crawford, J. H.: A comparison of chemical mechanisms based on TRAMP–2006 field data, *Atmos. Environ.*, 44, 4116–4125, <https://doi.org/10.1016/j.atmosenv.2009.05.027>, 2010.
- Byron, J. et al. (2022), *Nature*, 609, 307–312.
- Choi, Y., & Souri, A. H. (2015). Chemical condition and surface ozone in large cities of Texas during the last decade: Observational evidence from OMI, CAMS, and model analysis. *Remote Sensing of Environment*, 168, 90-101.
- Choi, Y., Kim, H., Tong, D., & Lee, P. (2012). Summertime weekly cycles of observed and modeled NO_x and O₃ concentrations as a function of satellite-derived ozone production sensitivity and land use types over the Continental United States. *Atmospheric Chemistry and Physics*, 12(14), 6291-6307.
- Collier, S., and Q. Zhang (2013), Gas-Phase CO₂ Subtraction for Improved Measurements of the Organic Aerosol Mass Concentration and Oxidation Degree by an Aerosol Mass Spectrometer, *Environmental Science & Technology*, 47(24), 14324-14331, doi:10.1021/es404024h.
- Crawford, J., Davis, D., Olson, J., Chen, G., Liu, S., Gregory, G., Barrick, J., Sachse, G., Sandholm, S., Heikes, B., Singh, H., and Blake, D.: Assessment of upper tropospheric HO_x sources over the tropical Pacific based on NASA GTE/PEM data: Net effect on HO_x and other photochemical parameters, *J. Geophys. Res.*, 104, 16255–16273, <https://doi.org/10.1029/1999JD900106>, 1999.
- de Gouw, J.A., Warneke, C., 2007. Measurements of volatile organic compounds in the earth's atmosphere using proton-transfer-reaction mass spectrometry. *Mass Spectrom. Rev.* 26, 223–257. <https://doi.org/10.1002/mas.20119>.
- de Gouw, J.A., Warneke, C., Karl, T., Eerdekens, G., van der Veen, C., Fall, R., 2003a. Sensitivity and specificity of atmospheric trace gas detection by proton-transfer-reaction mass spectrometry. *Int. J. Mass Spectrom.* 223–224, 365–382. [https://doi.org/10.1016/S1387-3806\(02\)00926-0](https://doi.org/10.1016/S1387-3806(02)00926-0).

- de Gouw, J.A., Warneke, C., Parrish, D.D., Holloway, J.S., Trainer, M., Fehsenfeld, F.C., 2003b. Emission sources and ocean uptake of acetonitrile (CH₃CN) in the atmosphere. *J. Geophys. Res. Atmos.* 108, 1–8. <https://doi.org/10.1029/2002jd002897>.
- EPA. (2015a). Air Quality Guide for Ozone. . https://www.airnow.gov/sites/default/files/2021-03/air-quality-guide_ozone_2015.pdf (accessed 29 March 2023).
- EPA. (2015b). The National Ambient Air Quality Standards. https://www.epa.gov/sites/default/files/2015-10/documents/overview_of_2015_rule.pdf (accessed 29 March 2023).
- Ervens, B., B. J. Turpin, and R. J. Weber (2011), Secondary organic aerosol formation in cloud droplets and aqueous particles (aqSOA): a review of laboratory, field and model studies, *Atmospheric Chemistry and Physics*, 11(21), 11069-11102, doi:10.5194/acp-11-11069-2011.
- Farmer, D. K., A. Matsunaga, K. S. Docherty, J. D. Surratt, J. H. Seinfeld, P. J. Ziemann, and J. L. Jimenez (2010), Response of an aerosol mass spectrometer to organonitrates and organosulfates and implications for atmospheric chemistry, *Proceedings of the National Academy of Sciences*, 107(15), 6670-6675, doi:10.1073/pnas.0912340107.
- Feng, X., Lin, H., Fu, T.-M., Sulprizio, M. P., Zhuang, J., Jacob, D. J., . . . Wang, X. (2021). WRF-GC (v2. 0): online two-way coupling of WRF (v3. 9.1. 1) and GEOS-Chem (v12. 7.2) for modeling regional atmospheric chemistry–meteorology interactions. *Geoscientific Model Development*, 14(6), 3741-3768.
- Fry, J. L., et al. (2009), Organic nitrate and secondary organic aerosol yield from NO₃ oxidation of beta-pinene evaluated using a gas-phase kinetics/aerosol partitioning model, *Atmospheric Chemistry and Physics*, 9(4), 1431-1449.
- Fry, J. L., et al. (2013), Observations of gas- and aerosol-phase organic nitrates at BEACHON-RoMBAS 2011, *Atmospheric Chemistry and Physics*, 13(17), 8585-8605, doi:10.5194/acp-13-8585-2013.
- Goldberg, D. L., Harkey, M., de Foy, B., Judd, L., Johnson, J., Yarwood, G., & Holloway, T. (2022). Evaluating NO_x emissions and their effect on O₃ production in Texas using TROPOMI NO₂ and HCHO. *Atmospheric Chemistry and Physics*, 22(16), 10875-10900.
- Guenther, A., Jiang, X., Heald, C. L., Sakulyanontvittaya, T., Duhl, T. a., Emmons, L., & Wang, X. (2012). The Model of Emissions of Gases and Aerosols from Nature version 2.1 (MEGAN2. 1): an extended and updated framework for modeling biogenic emissions. *Geoscientific Model Development*, 5(6), 1471-1492.
- Guo, F., Bui, A. A., Schulze, B. C., Yoon, S., Shrestha, S., Wallace, H. W., . . . Alvarez, S. (2021). Urban core-downwind differences and relationships related to ozone production in a major urban area in Texas. *Atmospheric Environment*, 262, 118624.

- Guo, F., et al. (2021), Urban core-downwind differences and relationships related to ozone production in a major urban area in Texas, *Atmospheric Environment*, 262, 118624, doi:<https://doi.org/10.1016/j.atmosenv.2021.118624>.
- Hudman, R., Moore, N., Mebust, A., Martin, R., Russell, A., Valin, L., & Cohen, R. (2012). Steps towards a mechanistic model of global soil nitric oxide emissions: implementation and space based-constraints. *Atmospheric Chemistry and Physics*, 12(16), 7779-7795.
- Jin, X., Fiore, A., Boersma, K. F., Smedt, I. D., & Valin, L. (2020). Inferring changes in summertime surface Ozone–NO_x–VOC chemistry over US urban areas from two decades of satellite and ground-based observations. *Environmental science & technology*, 54(11), 6518-6529.
- Jobson, B.T.; McCoskey, J.K. Sample drying to improve HCHO measurements by PTR-MS instruments: laboratory and field measurements. *Atmos. Chem. Phys.* 2010, 10, 1821-1835, doi:DOI 10.5194/acp-10-1821-2010.
- Kleinman, L. I.: Low and high NO_x tropospheric photochemistry, *J. Geophys. Res.*, 99(94), 831–838, <https://doi.org/10.1029/94JD01028>, 1994.
- Kleinman, L. I., Daum, P. H., Lee, Y.-N., Nunnermacker, L. J., Springston, S. R., Weinstein-Lloyd, J., and Rudolph, J.: Ozone production efficiency in an urban area, *J. Geophys. Res.*, 107, 4733, <https://doi.org/10.1029/2002JD002529>, 2002.
- Kleinman, L. I.: The dependence of tropospheric ozone production rate on ozone precursors,
- Lefer, B., Rappenglück, B., Flynn, J., Haman, C., 2010. Photochemical and meteorological relationships during the Texas-II Radical and Aerosol Measurement Project (TRAMP). *Atmos. Environ.* 44, 4005–4013. <https://doi.org/10.1016/j.atmosenv.2010.03.011>.
- Lin, H., Feng, X., Fu, T.-M., Tian, H., Ma, Y., Zhang, L., Lundgren, E. W. (2020). WRF-GC (v1.0): online coupling of WRF (v3. 9.1. 1) and GEOS-Chem (v12. 2.1) for regional atmospheric chemistry modeling–Part 1: Description of the one-way model. *Geoscientific Model Development*, 13(7), 3241-3265.
- Lindinger, W., Hansel, A., Jordan, A., 1998. On-line monitoring of volatile organic compounds at pptv levels by means of proton-transfer-reaction mass spectrometry (PTR-MS) medical applications, food control and environmental research. *Int. J. Mass Spectrom. Ion Process.* 173, 191–241. [https://doi.org/10.1016/S0168-1176\(97\)00281-4](https://doi.org/10.1016/S0168-1176(97)00281-4).
- Liu, F., Beirle, S., Joiner, J., Choi, S., Tao, Z., Knowland, K. E., . . . Wagner, T. (2023). High-resolution mapping of nitrogen oxides emissions in US large cities from TROPOMI retrievals of tropospheric nitrogen dioxide columns. Retrieved from
- Martin, R. V., Fiore, A. M., & Van Donkelaar, A. (2004). Space-based diagnosis of surface ozone sensitivity to anthropogenic emissions. *Geophysical Research Letters*, 31(6).
- Mazzuca, G. M., Ren, X., Loughner, C. P., Estes, M., Crawford, J. H., Pickering, K. E.,

- Weinheimer, A. J., and Dickerson, R. R.: Ozone production and its sensitivity to NO_x and VOCs: results from the DISCOVER-AQ field experiment, Houston 2013, *Atmos. Chem. Phys.*, 16, 14463–14474, <https://doi.org/10.5194/acp-16-14463-2016>, 2016.
- Middlebrook, A. M., R. Bahreini, J. L. Jimenez, and M. R. Canagaratna (2012), Evaluation of Composition-Dependent Collection Efficiencies for the Aerodyne Aerosol Mass Spectrometer using Field Data, *Aerosol Science and Technology*, 46(3), 258-271, doi:10.1080/02786826.2011.620041.
- Murray, L. T., Jacob, D. J., Logan, J. A., Hudman, R. C., & Koshak, W. J. (2012). Optimized regional and interannual variability of lightning in a global chemical transport model constrained by LIS/OTD satellite data. *Journal of Geophysical Research: Atmospheres*, 117(D20).
- Olson, J. R., Crawford, J. H., Chen, G., Brune, W. H., Faloon, I. C., Tan, D., Harder, H., and Martinez, M.: A reevaluation of airborne HO_x observations from NASA field campaigns, *J. Geophys. Res.*, 111(D10), 12, <https://doi.org/10.1029/2005JD006617>, 2006.
- Paatero, P. and Tapper, U., Positive matrix factorization - a nonnegative factor model with optimal utilization of error-estimates of data values. *Environmetrics* **1994**, 5 (2), 111-126.
- Schroeder, J. R., Crawford, J. H., Fried, A., Walega, J., Weinheimer, A., Wisthaler, A., Wisthaler, A., Müller, M., Mikoviny, T., Chen, G., Shook, M., Blake, D., and Tonesen, G. S.: New insights into the column CH₂O/NO₂ ratio as an indicator of near-surface ozone sensitivity, *J. Geophys. Res. Atmos.*, 122, 8885–8907, <https://doi.org/10.1002/2017JD026781>, 2017.
- Shrestha, S., et al. (2022), Traffic, transport, and vegetation drive VOC concentrations in a major urban area in Texas, *Science of The Total Environment*, 838, 155861, doi:<https://doi.org/10.1016/j.scitotenv.2022.155861>.
- Sillman, S.: The use of NO_y, H₂O₂, and HNO₃ as indicators for ozone-NO_x-hydrocarbon sensitivity in urban locations, *J. Geophys. Res.*, 100(D7), 14,175–14,188, <https://doi.org/10.1029/94JD02953>, 1995.
- Sun, K., Zhu, L., Cady-Pereira, K., Chan Miller, C., Chance, K., Clarisse, L., . . . Liu, X. (2018). A physics-based approach to oversample multi-satellite, multispecies observations to a common grid. *Atmospheric Measurement Techniques*, 11(12), 6679-6701.
- TCEQ. (2023). San Antonio: Current Attainment Status. <https://www.tceq.texas.gov/airquality/sip/san/san-status> (accessed 29 March 2023).
- Ulbrich, I. M., M. R. Canagaratna, Q. Zhang, D. R. Worsnop, and J. L. Jimenez (2009), Interpretation of organic components from Positive Matrix Factorization of aerosol mass spectrometric data, *Atmospheric Chemistry and Physics*, 9(9), 2891-2918.

- Valin, L., Fiore, A., Chance, K., & González Abad, G. (2016). The role of OH production in interpreting the variability of CH₂O columns in the southeast US. *Journal of Geophysical Research: Atmospheres*, 121(1), 478-493.
- Wang, Y., Jia, B., Wang, S.-C., Estes, M., Shen, L., & Xie, Y. (2016). Influence of the Bermuda High on interannual variability of summertime ozone in the Houston–Galveston–Brazoria region. *Atmospheric Chemistry and Physics*, 16(23), 15265-15276.
- Zhang, Q., J. L. Jimenez, M. R. Canagaratna, I. M. Ulbrich, N. L. Ng, D. R. Worsnop, and Y. L. Sun (2011), Understanding atmospheric organic aerosols via factor analysis of aerosol mass spectrometry: a review, *Anal. Bioanal. Chem.*, 401(10), 3045-3067, doi:10.1007/s00216-011-5355-y.
- Zhou, S., S. Collier, D. A. Jaffe, and Q. Zhang (2019), Free tropospheric aerosols at the Mt. Bachelor Observatory: more oxidized and higher sulfate content compared to boundary layer aerosols, *Atmospheric Chemistry and Physics*, 19(3), 1571-1585, doi:10.5194/acp-19-1571-2019.
- Zhou, S., S. Collier, D. A. Jaffe, N. L. Briggs, J. Hee, A. J. Sedlacek, L. Kleinman, T. B. Onasch, and Q. Zhang (2017), Regional influence of wildfires on aerosol chemistry in the western US and insights into atmospheric aging of biomass burning organic aerosol, *Atmospheric Chemistry and Physics*, 17(3), 2477-2493, doi:10.5194/acp-17-2477-2017.
- Zhou, S., S. Collier, J. Xu, F. Mei, J. Wang, Y.-N. Lee, A. J. Sedlacek, S. R. Springston, Y. Sun, and Q. Zhang (2016), Influences of upwind emission sources and atmospheric processing on aerosol chemistry and properties at a rural location in the Northeastern U.S, *Journal of Geophysical Research: Atmospheres*, 121(10), 6049-6065, doi:10.1002/2015jd024568.
- Zhou, S., Guo, F., Chao, C.Y., Yoon, S., Alvarez, S., Shrestha, S., Flynn, J., Usenko, S., Sheesley, R., Griffin, R., Marine submicron aerosols from the Gulf of Mexico: polluted and acidic with rapid production of sulfate and organosulfates, *Environ Sci Technol*, <https://doi.org/10.1021/acs.est.2c05469>
- Zhu, L., González Abad, G., Nowlan, C. R., Chan Miller, C., Chance, K., Apel, E. C., . . . Hornbrook, R. S. (2020). Validation of satellite formaldehyde (HCHO) retrievals using observations from 12 aircraft campaigns. *Atmospheric Chemistry and Physics*, 20(20), 12329-12345.
- Zhu, L., Jacob, D. J., Kim, P. S., Fisher, J. A., Yu, K., Travis, K. R., . . . De Smedt, I. (2016). Observing atmospheric formaldehyde (HCHO) from space: validation and intercomparison of six retrievals from four satellites (OMI, GOME2A, GOME2B, OMPS) with SEAC 4 RS aircraft observations over the southeast US. *Atmospheric Chemistry and Physics*, 16(21), 13477-13490.